

Yolk-Shell Nanostructures Prepared via Block Copolymer Self-Assembly for Catalytic Applications

DISSERTATION

zur Erlangung des akademischen Grades

**Doctor rerum naturalium
(Dr. rer. nat.)**

vorgelegt

**der Fakultät Mathematik und Naturwissenschaften
der Technischen Universität Dresden**

von

M.S. Aruni Shajkumar
geboren am 16.12.1988 in Kerala, Indien

Eingereicht am 28.09.2017

Die Dissertation wurde in der Zeit von Oktober 2013 bis September 2017
in der Professur für Physikalische Chemie polymerer Materialien am
Leibniz-Institut für Polymerforschung Dresden e.V. angefertigt.

Gutacher : **Prof. Dr. Manfred Stamm**
Technische Universität Dresden
Institut Physikalische Chemie und Physik der Polymere
(Professur im Ruhestand)
Leibniz-Institut für Polymerforschung Dresden

Prof. Dr. Alexander Eychmüller
Technische Universität Dresden
Institut Physikalische Chemie
Professur für Physikalische Chemie

Tag der Verteidigung : **19.01.2018**

To my parents

Preface

This work was carried out at the Leibniz Institute of Polymer Research Dresden (Leibniz-Institut für Polymerforschung Dresden e.V.), in the Institute of Physical Chemistry and Polymer Physics, in the years 2013 - 2017 under the supervision of Prof. Dr. Manfred Stamm and Dr. Andriy Horechyy. All the experiments and analysis were carried out in the Institute. The research was made possible by funding from the Leibniz Institute of Polymer Research Dresden e.V., Graduate Academy, Gesellschaft von Freunden und Förderern TU Dresden e.V., and DAAD, which is gratefully acknowledged.

Abstract

Yolk-shell nanostructures/yolk-shell nanoparticles are defined as a hybrid structure, a mixture of core/shell and hollow particles, where a core particle is encapsulated inside the hollow shell and may move freely inside the shell. Of the various classifications of yolk-shell nanostructures, a structure with an inorganic core and inorganic shell (inorganic/inorganic) has been studied widely due to their unique optical, magnetic, electrical, mechanical, and catalytic properties. In the work presented here, among the different inorganic/inorganic yolk-shell nanostructures noble metal@silica yolk-shell nanostructures has been chosen as the topic of interest. Silica shell possesses many advantages such as chemical inertness, tunable pore sizes, diverse surface morphologies, increasing suspension stability, no reduction in LSPR properties of noble metal nanoparticles when used as a coating for such particles. Noble metal nanoparticles such as AgNPs and AuNPs, on the other hand, possess unique structural, optical, catalytic, and quantum properties. Hence yolk-shell nanostructures with a combination of Ag or Au core and a silica shell (Ag@SiO_2 and Au@SiO_2) would open to endless possibilities.

In this study, four areas were mainly explored: mechanism of silica shell formation over a given template, the synthetic modifications of Ag@SiO_2 and Au@SiO_2 yolk-shell nanostructures, their application as a potential catalyst, and devising of a flow type catalytic reactor. Despite the growing number of contributions on the topic of yolk-shell nanostructures, particularly Au@SiO_2 and Ag@SiO_2 yolk-shell nanostructures, a potential for improvement lies in all four aforementioned areas.

As an initial study, the effect of different processing conditions as well as the mechanism of silica shell formation over reactive block copolymer templates was investigated. An asymmetric PS-*b*-P4VP block copolymer was chosen as a structure directing component to deposit silica shell. In order to deposit silica shell, PS-*b*-P4VP micelles with a collapsed PS core and a swollen P4VP corona was prepared via a solvent exchange method. The growth of silica shell over the PS-*b*-P4VP micelles (reactive template) was done using *in-situ* DLS and TEM. The experimental data obtained revealed the 4 distinct stages involved in the silica shell formation over the reactive BCP micellar template starting from the accumulation of silica precursor around the P4VP corona followed by a reactive template mediated hydrolysis-condensation reaction of the silica precursor which eventually lead to the shell densification and shell growth around the micelles. An understanding of the mechanism of silica shell formation over reactive templates provides a direct way to encapsulate various active species such as metal nanoparticles and quantum dots and paves the way for the template mediated synthesis of hybrid nanostructures such as yolk-shell nanoparticles. These studies also serve as a platform to fine-tune the properties of such hybrid nanostructures by varying the reaction parameters during silica shell deposition and reaction time.

The next part of the work focused mainly on the synthesis, process optimisation and characterization of Ag@SiO_2 and Au@SiO_2 yolk-shell nanostructures, and their potential use

as a nanocatalyst. A well-known soft template mediated synthesis of the yolk-shell nanostructure was adopted for the present work. For this PS-*b*-P4VP micelle was used as a dual template for both encapsulation of nanoparticle and the deposition of silica shell. The nanoparticles were entrapped selectively to the BCP micellar core and silica deposition was done by reacting the nanoparticle-loaded micelles with an acidic silica sol which lead to the formation of Ag@PS-*b*-P4VP@SiO₂ or Au@PS-*b*-P4VP@SiO₂ particles with respect to the nanoparticle used. In the case of Ag@PS-*b*-P4VP particles, upon silica deposition, a partial dissolution of AgNPs was observed whereas AuNPs were stable against dissolution. Hence yolk-shell nanostructures with AuNPs were studied further. As-prepared Au@PS-*b*-P4VP@SiO₂ particles were then subjected to pyrolysis to remove the BCP template. The resulting yolk-shell nanostructures comprised of an AuNP core and a hollow mesoporous silica shell. Upon removal of the BCP template, the Au@SiO₂ particles fused together and formed large aggregates. The catalytic properties of Au@SiO₂ yolk-shell nanoparticles were explored using a model reaction of reduction of 4-nitrophenol and proved to have good catalytic activity and efficient recyclability. It was observed that catalytic efficiency was hindered by the particle aggregates formed after pyrolysis by creating an inhomogeneity in the system and inaccessibility of the catalytic surface for the reactants. Hence synthetic modifications were needed to overcome such drawbacks.

Next part of the work deals with the synthetic modification of Au@SiO₂ yolk-shell nanoparticles done by embedding them in a porous silica structure (PSS). Such structural morphology was attained by gelating the excess silica precursor while synthesising the Au@PS-*b*-P4VP@SiO₂ particles. The pyrolytic removal of block copolymer results in the formation of Au@SiO₂@PSS catalyst and the porous nature of both the shell and the silica structure provides an easy access for the reactants to the nanocatalyst surface located inside. The catalytic properties of Au@SiO₂@PSS were studied using a model reaction of catalytic reduction of 4-nitrophenol (4-NP) and reductive degradation of different dyes. Kinetic studies show that Au@SiO₂@PSS catalyst possesses enhanced catalytic activity as compared to other analogous systems reported in the literature so far. Furthermore, catalytic experiments on the reductive degradation of different dyes show that Au@SiO₂@PSS catalyst can be considered as a very promising candidate for wastewater treatment.

Another proposed direction of applying the Au@SiO₂ yolk-shells is by devising a continuous flow catalytic system composed of Au@SiO₂ yolk-shell nanoparticles for the effective degradation of azo dyes as a promising candidate for wastewater treatment. This was done by infiltrating the Au@PS-*b*-P4VP@SiO₂ particles inside a porous glass substrate (frits) and the subsequent pyrolytic removal of the BCP template resulting in the formation of Au@SiO₂ yolk-shell nanostructures sintered inside the frit pores. The flow catalytic reactor was exploited in terms of studying its catalytic activity in the degradation of azo dyes and 4-nitrophenol and proved to have a catalytic efficiency of ca. 99% in terms of reagent conversion and has a long-term stability under flow. Thus, with a few modifications, these flow type systems can open the doors to a very promising continuous flow catalytic reactor in the future.

Table of Contents

1	INTRODUCTION	1
1.1	Motivation.....	2
1.2	Objective of Thesis	5
1.3	Outline of Thesis.....	6
2	THEORY AND FUNDAMENTALS	7
2.1	Block Copolymers	8
2.1.1	Types of Block Copolymers	8
2.1.2	Self-Assembly of Block Copolymers	9
2.1.3	Self-Assembly of Block Copolymers in Solution	11
2.1.4	Block Copolymer Micelles	12
2.1.5	Critical Micelle Concentration (CMC).....	13
2.1.6	Preparation and Characterization of BCP Micelles	15
2.1.7	Micellization of Cationic Amphiphilic Block Copolymers.....	15
2.1.8	Application of Block Copolymer Micelles in Nanotechnology	17
2.2	Controlled Localisation of Nanoparticles in Block Copolymer Domains.....	18
2.2.1	Controlled Localisation of Nanoparticles Modified with Polymeric Ligands	19
2.2.2	Controlled Localisation of Nanoparticles in Colloidal Block Copolymer Self-Assembly	21
2.2.3	Applications of Nanoparticle encapsulated Block Copolymer Self- Assembly	26
2.3	Yolk-Shell NanoStructures	27
2.3.1	How are They Different from Core/Shells?	28
2.3.2	Type of Yolk-Shell Nanostructures	28
2.3.3	Routes for Synthesis of Yolk-Shell Nanostructures	31
2.3.4	Characterization of Yolk-Shell Nanostructures.....	35
2.3.5	Application of Yolk-Shell Nanostructures	37
3	EXPERIMENTAL.....	39
3.1	Characterization Techniques	40
3.1.1	Scanning Electron Microscopy (SEM).....	40

Table of Contents

3.1.2	Transmission Electron Microscopy (TEM)	40
3.1.3	UV-VIS Absorbance Spectroscopy	41
3.1.4	Dynamic Light Scattering (DLS).....	41
3.1.5	Gas Adsorption Measurements	42
3.1.6	Inductively Coupled Plasma Optical Emission Spectroscopy (ICP-OES)	42
3.1.7	Atomic Force Microscopy (AFM)	42
3.1.8	Thermogravimetric Analysis (TGA).....	43
3.2	Chemicals.....	43
3.3	Synthetic Procedures.....	45
3.3.1	Synthesis of PS- <i>b</i> -P4VP@SiO ₂ Particles.....	45
3.3.2	Synthesis of PS-stabilized Silver Nanoparticles (AgNP-PS).....	45
3.3.3	Synthesis of PS-stabilized Gold Nanoparticles (AuNP-PS).....	46
3.3.4	Synthesis of Ag@SiO ₂ and Au@SiO ₂ Yolk-Shell Nanostructures	47
3.3.5	Synthesis of Porous Silica-supported Yolk-Shell Catalyst (Au@SiO ₂ @PSS)	48
3.3.6	Fabrication of Flow-Type Catalytic Reactors by Infiltration of Au@PS- <i>b</i> -P4VP@SiO ₂ in Porous Glass Frit.....	48
3.4	In-situ monitoring of silica shell formation	48
3.5	Catalytic studies	49
3.5.1	Catalytic Reactions using Ag@SiO ₂ , Au@SiO ₂ Yolk-Shell Nanoparticles, and Au@SiO ₂ @PSS Catalyst	49
3.5.2	Continuous Flow Catalytic Studies.....	49
4	RESULTS AND DISCUSSION	51
4.1	In-Situ Monitoring of Silica Shell Formation	52
4.1.1	Motivation.....	52
4.1.2	Synthesis of PS- <i>b</i> -P4VP@SiO ₂ Particles.....	54
4.1.3	Effect of Processing Conditions on the Morphology of PS- <i>b</i> - P4VP@SiO ₂	55
4.1.4	Mechanism of Silica Shell Formation in the Presence of Reactive Block Copolymer Templates	58
4.1.5	Conclusion	65
4.2	Yolk-Shell Nanostructures as Bifunctional Catalysts.....	66
4.2.1	Motivation.....	66
4.2.2	Fabrication of Ag@SiO ₂ and Au@SiO ₂ Yolk-Shell Nanostructures	68
4.2.3	Ag@SiO ₂ Yolk-Shell Nanostructures.....	69

4.2.4	Au@SiO ₂ Yolk-Shell Nanostructures	74
4.2.5	Catalysis Studies using Au@SiO ₂ Yolk-Shell Nanoparticles	80
4.2.6	Reduction of 4-Nitrophenol using Au@SiO ₂ Yolk-Shell Nanoparticles	80
4.2.7	Conclusion	84
4.3	Silica encapsulated Gold Nanoparticle Yolk-Shells embedded in Porous Silica Structure (Au@SiO ₂ @PSS)	85
4.3.1	Motivation	85
4.3.2	Synthesis of Au@SiO ₂ @PSS Catalyst	85
4.3.3	Characterization of Au@SiO ₂ @PSS Catalyst	86
4.3.4	Reduction of 4-Nitrophenol using Au@SiO ₂ @PSS catalyst	88
4.3.5	Reduction of Organic Dyes – Congo Red, Methyl Orange, and Methylene Blue.....	92
4.3.6	Conclusion	97
4.4	Continuous Catalysis	98
4.4.1	Motivation	98
4.4.2	Fabrication	99
4.4.3	Flux Experiments on Frits Infiltrated with Au@SiO ₂ Yolk-Shell Nanoparticles	107
4.4.4	Continuous Flow Catalysis	109
4.4.5	Conclusion	117
5	SUMMARY	119
6	FUTURE OUTLOOK	125
7	REFERENCE.....	127
8	APPENDIX.....	153
8.1	Heterogeneous Catalyst	154
8.1.1	Adsorption Isotherms	154
8.1.2	Eley-Rideal Mechanism	157
8.1.3	Langmuir-Hinshelwood Mechanism (LH)	157
8.2	Techniques	159
8.2.1	Scanning Electron Microscopy (SEM).....	159
8.2.2	Transmission Electron Microscopy (TEM).....	161
8.2.3	UV-VIS Absorbance Spectroscopy	161
8.2.4	Dynamic Light Scattering (DLS)	164
8.2.5	Gas Adsorption measurements	166

Table of Contents

8.2.6	Atomic Force Microscopy (AFM)	168
8.3	Determination of the content and specific surface area of gold in Au@SiO ₂ @PSS catalyst	169
8.4	Blank Experiment to study the reaction of CR + NaBH ₄ in the absence of catalyst	170
8.5	List of Abbreviations and Symbols.....	171
8.6	List of Figures	174
8.7	List of Tables	182
8.8	List of Publications	183
9	ACKNOWLEDGEMENTS.....	185

1 INTRODUCTION

1.1 MOTIVATION

Nanoparticles (NPs) are considered as the building blocks for various applications of nanotechnology. The ability to tune the size, shape and morphology of nanoparticles help to develop new and advanced physicochemical properties such as increased stability, surface area, optical, magnetic, and catalytic properties. Nanoparticles have a high surface to volume ratio and improved functionality compared to their bulk counterparts. The unique structural, optical, magnetic, catalytic, and quantum properties of metal nanoparticles are used in the fields of photovoltaics, optoelectronics,¹ water purification,² catalysis,³ sensors,⁴ photonics, rechargeable batteries,⁵ biomedicine,^{4,6} etc. Among different metal nanoparticles, noble metal nanoparticles and magnetic nanoparticles are most commonly used in the aforementioned applications. One of the challenges in using pure noble metal nanoparticles is the poor stability caused by their high surface energy. Driven by changes in reaction environment, loss of capping agents or at high temperatures the nanoparticles have a tendency to aggregate, reshape or sinter during their use.

In order to overcome the disadvantages of naked metal nanoparticles, and to develop new properties, functionalized polymers, polyelectrolyte brushes, dendrimers, polymeric membranes, resins or metal oxides, have been used to coat, embed or support nanoparticles.⁷⁻¹⁰ To combine the advantages of both the support and the metal nanoparticle, and to improve the stability of nanoparticles, the metal nanoparticles can be enclosed inside the support shell with a hollow space separating the shell and the nanoparticle core. Such systems are known as yolk-shell nanostructures or simply yolk-shell nanoparticles or nanorattles.

Yolk-shell nanoparticles were first reported in the late 2002.^{11,12} They are defined as a hybrid structure between core-shell and hollow particles where the enclosed core particle may or may not move freely inside the shell which is generally represented as a core@void@shell or core@shell.¹³ These structures must be distinguished from solid nanoparticles (composed of one or many elements but with a uniform structure),¹⁴ Janus particles (two parts of the same particle have different chemical or physical properties),¹⁵ hollow particles (with an empty interior),¹⁶ core-shell particles (comprising smaller solid particle(s) coated with a tight layer of other element(s)),¹⁷ and reverse bumpy balls (encapsulated cores attached to the shell)¹⁸ (Figure 1.1). The main feature differentiating yolk-shell nanostructures from the aforementioned structures is the presence of a void between the encapsulated core and the surrounding shell. The hollow space can be loaded with one or more particles.¹⁹ Additionally, the shell can be constituted of multiple layers^{20,21} and contain functional groups²² or targeting moieties.²³

A large number of possible building blocks provide a number of compositions for the construction of yolk-shell nanoparticles. The core is usually made of metals (Au,²⁴ Ag,²⁵ Cu,²⁶ Pt,²⁷ Pd,²⁸ Ni³) metalloids (Si),²⁹ oxides (SiO₂,³⁰ Fe₂O₃,³¹ SnO₂,²⁰ Co₃O₄,³²) doped oxides (Gd₂O₃:Eu³⁺)³³ or sulphides (Ag₂S, CdS, PbS, ZnS, AgInS₂),³⁴ where the shell can be composed of metal (Pt³⁵), oxides (SiO₂,³⁰ MgSiO₃,³⁶ CuSiO₃,³⁷ NiSiO₃,³⁷ NiTiO₃,³⁸ CeO₂,²⁸ ZrO₂,¹⁷

TiO₂,³⁹ SnO₂,²¹ Fe₂O₃,⁴⁰) polymers (P(NIPAm-coAAM),³³ PMAA,⁸ PANi⁴¹) or carbon¹² (C¹⁸ groups,⁴² nitrogen-doped carbon²⁹). The properties of the yolk-shell nanoparticles are largely dependent on their chemical composition.

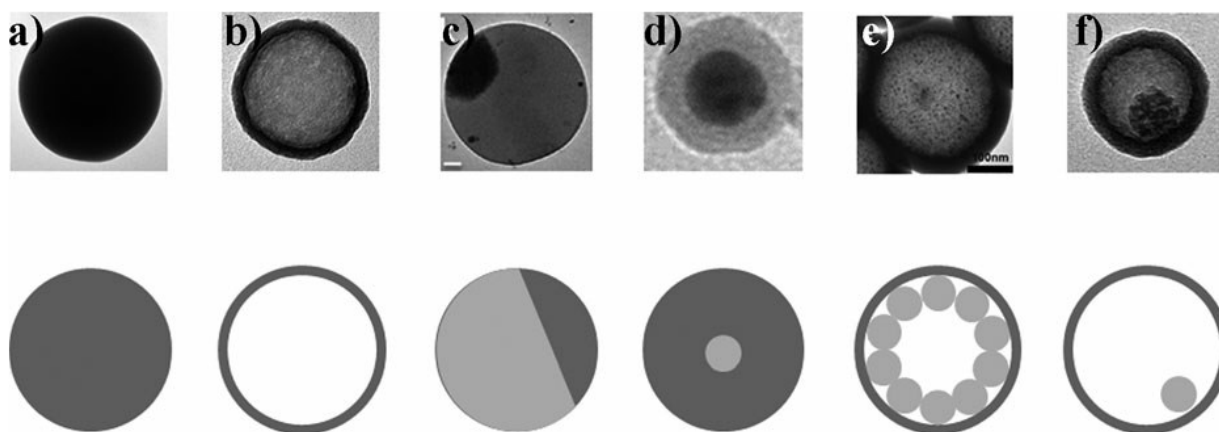


Figure 1.1 TEM images and schematic representation of the common types of nanoparticles: (a) Solid; (b) Hollow; (c) Janus; (d) Core-Shell; (e) Reverse Bumpy Ball; and (f) Yolk-Shells or Nanorattle. Reproduced from Ref. 13.

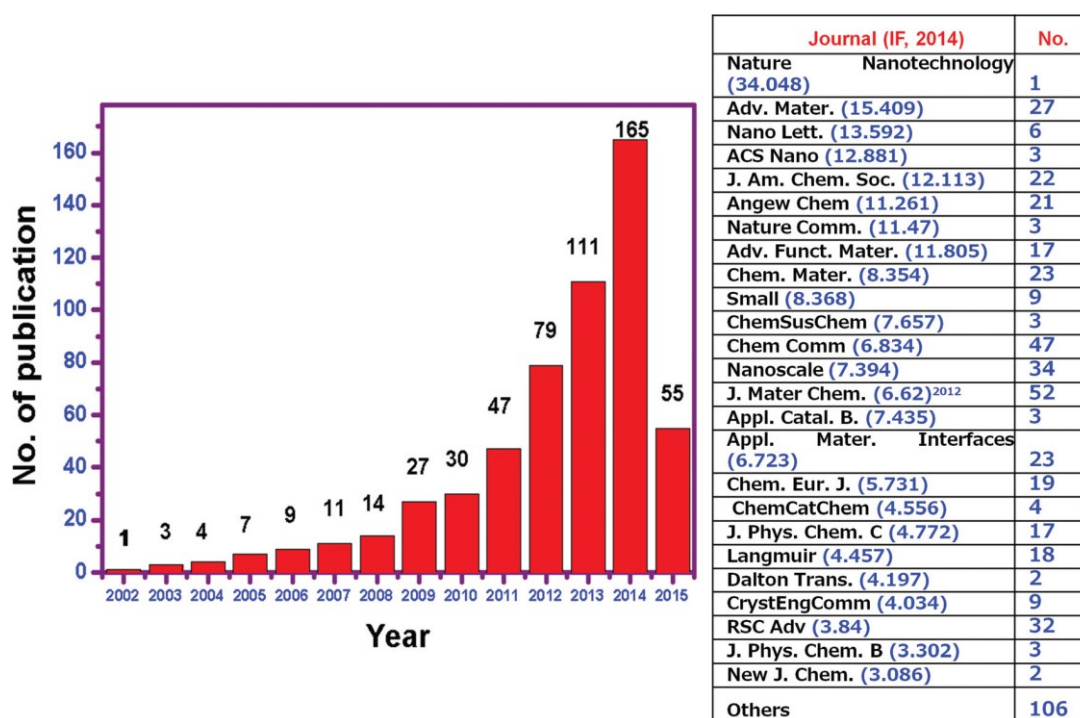


Figure 1.2 Publications per year for yolk-shell nanoparticles during the period of 2002 to 2015 and list of published documents in journals. Reproduced from Ref. 43.

Over the last decade, there is a considerable increase in the quantity and quality of research papers on yolk-shell nanoparticles as shown in Figure 1.2.⁴³ Most of the studies on yolk-shell nanoparticles have focused on the improvement of different catalytic applications. In such systems, the catalytic reactions occur on the surface of the nanocatalyst located in the cavity or attached to the inner wall of the shell. Thus, encapsulated nanocatalyst is exposed to a homogeneous environment, which makes them act as nanoreactors.¹⁰ The encapsulated nanocatalyst is largely protected from aggregation and mechanical leaching during the reaction and catalyst recovery. This makes yolk-shell nanocatalysts more robust as compared to the catalysts on supports. Furthermore, yolk-shell nanocatalysts were found more stable in harsh conditions, and hence, better suitable for high-temperature catalytic reactions.^{3,22}

The size, shape, and surface properties of encapsulated nanocatalyst can be tuned by various methods.²² Yolk-shell particles could be designed such that enclosed nanocatalyst surface is free from stabilising ligands, which makes them catalytically highly active. In addition to the ligand-free nanoparticle core surface, the presence of free space or voids separating the core from the shell is crucial for particular systems to become catalytically active.⁴⁴ In yolk-shell systems, reactants, products, and solvents should be able to pass through the permeable shell and reach catalytically active sites located inside. Diffusion rate can be controlled by adjusting shell porosity. Pore size and pore density can be tuned by controlling reaction conditions during shell formation, by incorporation of porogen²² or by chemical etching⁴⁴. Hence and not surprisingly, there is a large interest in the design of novel yolk-shell type structures for the catalytic application.

1.2 OBJECTIVE OF THESIS

Owing to the beneficial characteristics of yolk-shell nanostructures, such as increased particle stability, combined properties of shell material and core particles, ease of reactants to diffuse into the hollow interior, property tuning by altering the shell and core characteristics, the objective of this thesis is to explore the catalytic properties of yolk-shell nanoparticles.

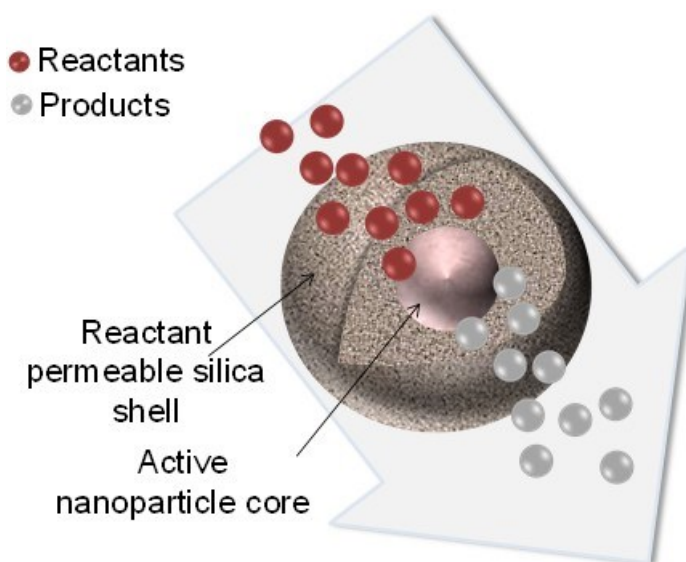


Figure 1.3 Schematic showing the yolk-shell nanoparticle as a nanocatalyst.

The main objectives of the work are:

1. Design and synthesis of yolk-shell nanoparticles using silica as a shell material and using noble metal nanoparticles as a core (Ag, Au) via a sacrificial block copolymer template method.
2. Studying the mechanism of formation of silica shell around the block copolymer template.
3. Studying the catalytic activity of the yolk-shell nanoparticles using various model reaction.
4. Devising the particles to a continuous flow catalyst by entrapping them in an appropriate flow channel template.

1.3 OUTLINE OF THESIS

The present thesis is divided into four major chapters, which are outlined as follows:

Chapter 1: A general introduction to the topic of yolk-shell nanoparticles is provided, highlighting the importance of their investigation and their potential application in nanocatalysis followed by major goals of the work.

Chapter 2: An extensive theoretical background is provided, covering the topics of block copolymers, assembly of nanoparticles in block copolymers, and yolk-shell nanostructures.

Chapter 3: An overview of the characterization techniques used and synthetic and experimental procedures used for the present work are discussed in detail.

Chapter 4: The results on each part of the work are presented and discussed. A short motivation is included for each part, as well as additional experimental procedures used. A summary providing the conclusions drawn from the results is presented at the end of each part. The chapter starts from the mechanism of silica shell formation over the block copolymer template and later explores the synthesis and synthetic modifications of yolk-shell nanoparticles and their application as a catalyst using different model reactions.

Chapter 5: This chapter provides a summary and conclusion of the present work as well as ideas for further exploration.

2 THEORY AND FUNDAMENTALS

2.1 BLOCK COPOLYMERS

A copolymer is formed when at least two different monomers comprise to form a single chain. When the different monomers are arranged as alternating blocks of various lengths in a polymer chain, they are called as block copolymers.^{45,46}

Block Copolymers are always a field of interest for the molecular engineers, as they can combine distinct monomers to obtain new polymers with new and superior physical properties. The distinct blocks in a block copolymer are usually incompatible with one another and hence they prefer to exist in a de-mixed state rather than in a mixed state.

2.1.1 Types of Block Copolymers

In block copolymers, the different monomers are organised into distinct segments or blocks. Depending on the number of different monomer blocks, they can be classified into diblock, triblock and multiblocks or depend on the arrangement of the blocks, into linear or star block copolymers (Figure 2.1). The simplest type of block copolymer is the diblock copolymers (-AB-) which consist of a sequential arrangement of two different types of monomers which are covalently linked together. As the name indicates, tri-block copolymers (-ABC- or -ABA-) consist of three different blocks which are covalently linked with each other and multiblock copolymers consist of three or more different monomer blocks.

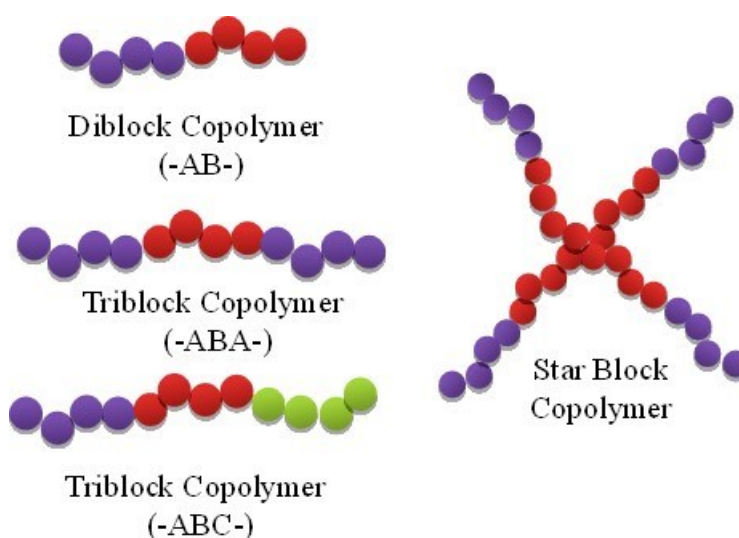


Figure 2.1 Schematic showing the different types of block copolymers.

Based on the chain arrangements, block copolymers are classified into linear block copolymers where the blocks are connected end to end. Another type of arrangement is the star block copolymers, where individual monomer chains are connected via one of their ends at a single junction. Block copolymers can be synthesized by the living polymerization techniques, such as Living Anionic or Cationic Polymerization, Atom Transfer Free Radical Polymerization (ATRP), Reversible Addition-Fragmentation Chain Transfer Polymerization (RAFT), or Group Transfer Polymerization (GTP), etc., which efficiently enable a control over the chain polydispersity (PDI).^{47,48}

2.1.2 Self-Assembly of Block Copolymers

Block copolymers are defined as macromolecules with a linear or radial arrangement of two or more different blocks of the varying monomer composition.⁴⁹ They have been the focus of interest during the last 30 years due to the arrangement of chemically distinct blocks into microdomains, which leads to a microphase separation. Since the different blocks are linked together by covalent bonds, the microphase separation is spatially limited and results in self-assembled structures including spheres, cylinders, gyroids, and lamellae as depicted in Figure 2.2 (a).^{50,51} The length scale of these structures generally ranges from 1 to 100 nm.⁵² Since these structures are of the same order as the exciton diffusion length or the thickness of tunnelling barriers, they are used in various physicochemical devices.

For the formation of such nanostructures, certain parameters such as the total degree of polymerization, $N=N_A + N_B$, the volume fraction of the constituent blocks, f_A and f_B ($f_A + f_B = 1$), and the Flory-Huggins interaction parameter, χ_{AB} , are important.^{51,53} The phase separation is driven by the degree of incompatibility between A and B blocks and is defined by the χ parameter. For diblock copolymers with no strong specific interactions, χ_{AB} is normally positive and small, follows an inverse dependence on temperature. The degree of microphase separation of the diblocks is determined by the segregation product, χN . The incompatibility between the constituent blocks decreases with decreasing χN and increasing temperature. At the same time, the combinatorial entropy increases. With respect to variations in entropy or incompatibility, the copolymer will undergo order-to-disorder transition (ODT) and become disordered i.e., homogeneous. The temperature at which the ODT occurs is referred to as T_{ODT} .^{50,54-57}

The plot of the product χN vs. the volume fraction, f , of one of the blocks expresses the phase balance between entropy and enthalpy of the block. Figure 2.2 (b) shows the phase diagram of diblock copolymers predicted by self-consistent mean field (SCMF) theory.^{50,58} With increasing the volume fraction, f_A , at a fixed χN above the ODT, the order-to-order transition (OOT) starts from closely packed spheres, CPS, which separates the disordered state (Dis) and S phase, passing through the body-centered cubic spheres (S), hexagonally packed cylinders (C) and bicontinuous gyroids (G), to lamellae (L). When the block copolymer composition is inverted morphological inversion ($L \rightarrow G' \rightarrow C' \rightarrow S' \rightarrow CPS' \rightarrow Dis$) takes place. Figure 2.2 (c) shows an experimental phase diagram of PI-*b*-PS block copolymers reported by Bates and co-workers. Experimentally obtained phase diagram display certain dissimilarities compared to that of theoretically predicted. These differences could be explained by the effect of additional parameters that are not considered in theoretical models. First, an overall asymmetry is present in the experimental phase portrait of PI-*b*-PS copolymer with respect to the volume fraction of PI block, $f_A = 1/2$. This arises partially due to the differences in the shape and the size between the isoprene and styrene monomers, $a_A \neq a_B$. The experimental diagram, in addition to the G phase, contains a transient structure between C and L phase, a thermodynamically unstable

perforated layer (PL). Another discrepancy between the theoretical and experimental phase diagram is the region near the ODT in the phase diagram. In the experimental phase diagram, not only the disordered phase is stable beyond $\chi_{AB}N = 10.5$ (for $f_A = 1/2$) but also the direct transitions between the disordered phase and the various ordered phases are clearly evident. In contrast, theoretical phase (SCMF theory) diagram shows the order-order lines converging to a critical point at $\chi_{AB}N = 10.5$ and $f_A = 1/2$. This allows only a direct phase transition between the disordered phase and the spherical ordered phases.

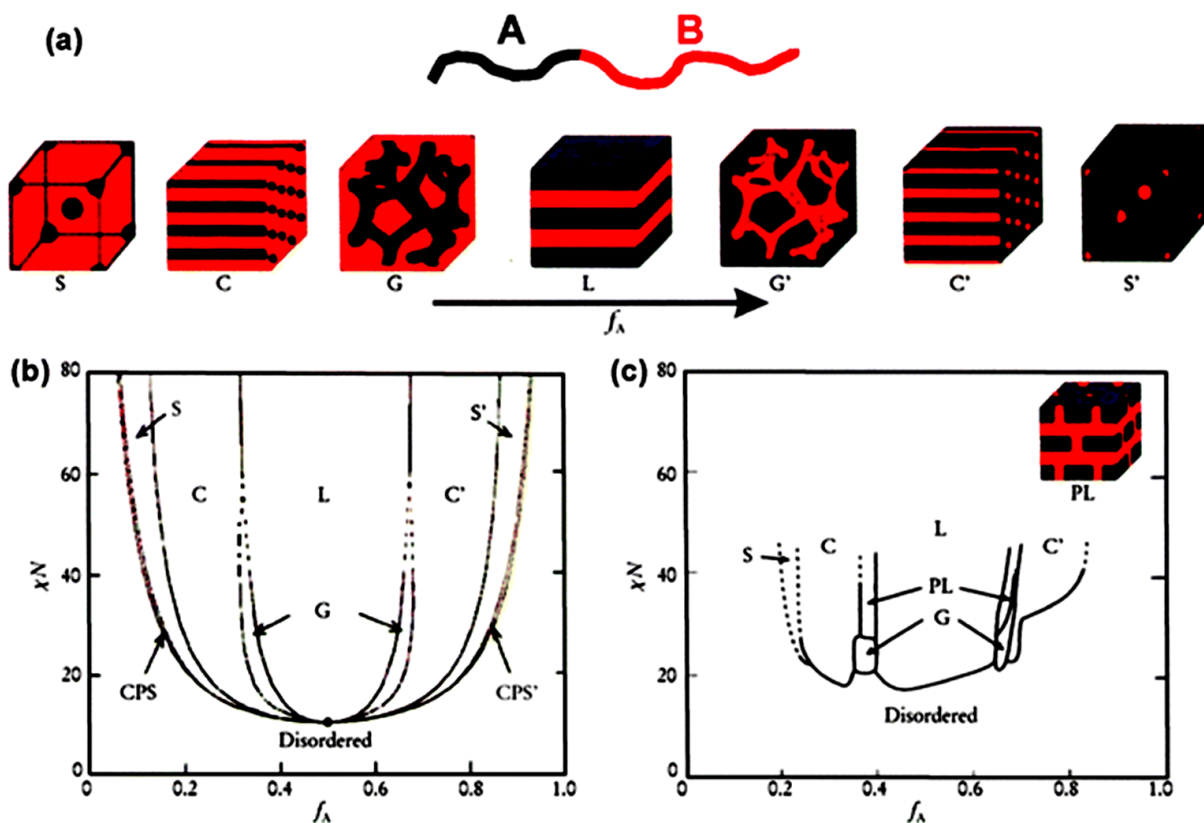


Figure 2.2 (a) Equilibrium microdomain structures of AB diblock copolymers in bulk: S and S' = body centered cubic spheres, C and C' = hexagonally packed cylinders, G and G' = bicontinuous gyroids, and L = lamellae; (b) Theoretical phase diagram of AB diblock copolymers predicted by the SCMF theory, depending on volume fraction (f) of the blocks and the segregation parameter, χN , where χ is the Flory-Huggins segment-segment interaction energy and N is the degree of polymerization. CPS and CPS' = closely packed spheres; (c) Experimental phase portrait of PI-b-PS copolymers, in which f_A represents the volume fraction of polyisoprene. PL = perforated lamellae. Reproduced from Ref. 50 and 51.

The various morphologies can be attributed to two major factors: (1) the interfacial energy between two blocks (an enthalpic contribution) and (2) chain stretching (an entropic contribution). During microphase separation, the two blocks separate from each other to minimise interfacial area in order to lower the interfacial energy. Phase separation induces the stretching away of chains from the coiled polymer conformation and the volume fraction of the constituent

block being the factor which determines the degree of stretching. As in the case of highly asymmetric diblocks, the block with the smaller volume fraction assembles to spherical microdomains whereas the one with higher volume fraction forms a matrix. This conformation allows the system to attain to the lowest interfacial area and increased configurational entropy which makes them energetically more stable. With an increase in volume fraction at a fixed temperature, the volume fraction of the block that forms the matrix decreases resulting in the formation of less curved interfaces which leads to a morphological transition from spheres to cylinders to lamellae.

2.1.3 Self-Assembly of Block Copolymers in Solution

The self-assembly of block copolymers in solution is much more complex than that in bulk. Amphiphilic block copolymers have gained much focus in the last 15 years. The structures formed by amphiphilic block copolymers in solution include spherical micelles, rods, bicontinuous structures, lamellae, vesicles, hexagonally packed hollow hoops (HHHs), large compound micelles (LCMs), large compound vesicles (LCVs), tubules, onions, eggshells, baroclinic tubules, pincushions etc., (Figure 2.3).⁵¹

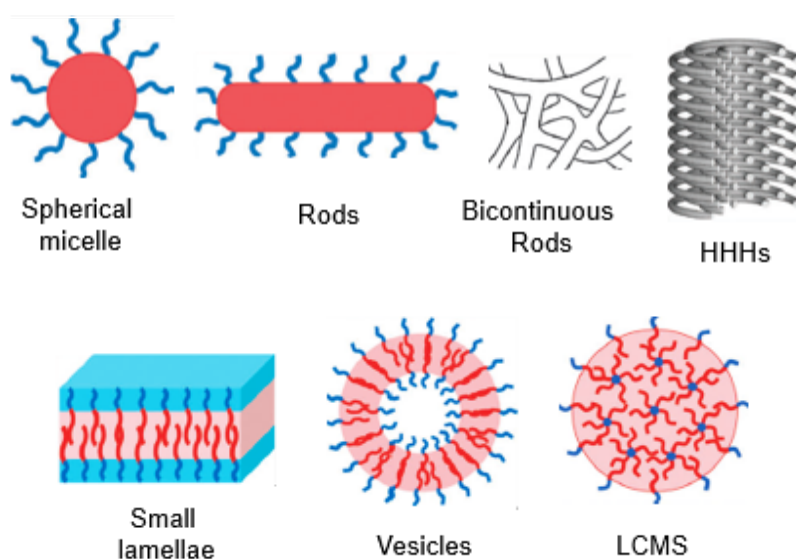


Figure 2.3 Schematic diagram showing various morphologies formed by amphiphilic block copolymers in solution. Reproduced from Ref. 51.

Simple spherical micelles, usually being the first type of aggregates to form, consist of a spherical core surrounded by coronal chains and the radius of the core cannot exceed the longest corona chain in their planar zigzag configuration. On the other hand rods (cylindrical or worm-like micelles) are composed of a cylindrical core and a corona surrounding the core. They are characterized by diameters of the same order of magnitude as those of primary spheres but can have varying length.⁵¹ A three-dimensional network of interconnected branched rods

constitutes the bicontinuous rods whereas phase inverted counterparts of rods comprise the hexagonally packed hollow hoop. Lamellae (flat or slightly curved bilayer) and vesicles (closed bilayers) are another two types of structures formed by block copolymers in solution. An aggregation of inverse micelles, the outer surface of which is stabilised in solution by a thin layer of hydrophilic chains form the large compound micelles (LCMs).^{51,54}

2.1.4 Block Copolymer Micelles

Block copolymers with different blocks having different affinities for solvents which consist of a polar (hydrophilic) and a non-polar (hydrophobic) blocks are known as amphiphilic block copolymers. When an amphiphilic block copolymer is dissolved in a solvent, which is thermodynamically good for one block and a precipitant for the other, micellar structures will be formed with one block on the exterior of the structure forming the corona, and the other block on the interior, ‘protected’ from the solvent, forming the core.^{52,59,60}

The important parameters that control the size of micelles are the degree of polymerization of the polymer blocks, N_A and N_B , and the Flory-Huggins interaction parameter χ .⁶¹ The micellar structure is characterised by the core radius R_c , the overall radius of the micelle R_m , and the distance between adjacent blocks at the core-corona interface known as grafting distance, b , (Figure 2.4). The process of micellization is characterized by the aggregation of a given number of block copolymer chains, defined as the aggregation number, Z .⁶⁰ In the case of spherical micelles, the core radius, R_c , and the area occupied by one chain at the core-corona interface, b^2 , are directly related to the number of polymers per micelles. Therefore, the aggregation number, Z , can be expressed:⁶¹

$$Z = \frac{4\pi R_c^2}{b^2} \quad (2.1)$$

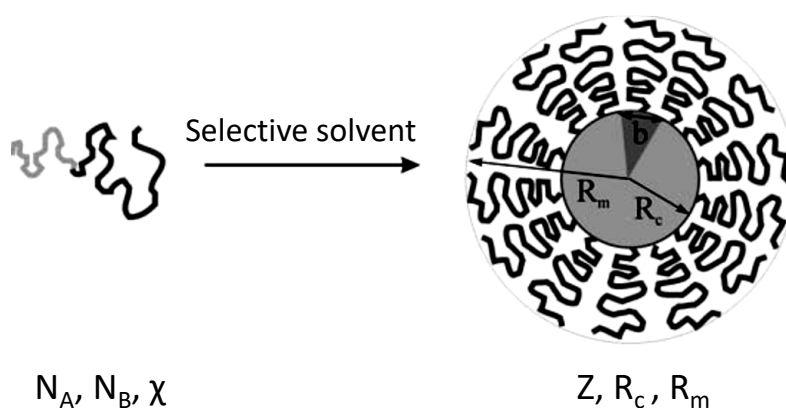


Figure 2.4 Schematic representation of A-B diblock copolymer micelle in a solvent selective for one of the blocks and the important characteristics of BCP micelles. Reproduced from Ref. 61.

The factors that influence the morphology of such micellar aggregates are copolymer composition, initial copolymer concentration in solution, added solvent content, and the nature

of the common solvent. The force balance between the stretching of the core, surface tension between the core and the outside solvent and the repulsion among the corona chains, that prevents the unlimited growth of the micelle into a distinct macroscopic phase, determines the morphology of the aggregates. Such micellar aggregates are formed when an amphiphilic block copolymer is dissolved in a solvent which is selective only for one of the blocks. The interaction between the soluble blocks and solvent stabilises the micelles in solution.^{62,63} The general classification of micelles includes regular micelles and inverse micelles. When dispersed in a polar solvent, the blocks rearrange to form a regular micelle which has a hydrophobic core and hydrophilic corona. On the contrary, when they are dispersed in an apolar solvent the blocks will rearrange to form reverse micelles which have a hydrophilic core and hydrophobic corona.⁶² Micelles can be further divided into a star and crew-cut micelles depending on the composition of the block copolymers. When the length of corona forming block is much longer than that of the core forming ones, star micelles are formed. When the corona-forming block is shorter (thin corona) than that of the core forming ones (bulky core), crew-cut micelles are formed.

2.1.5 Critical Micelle Concentration (CMC)

The concentration at which the first micelle is formed is called the critical micelle concentration (CMC). With the increase in the concentration of block copolymer chains in solution, more micelles are formed while the concentration of non-associated chains, unimers, remains constant and is equal to the value of CMC. This corresponds to an ideal system under thermodynamic equilibrium. The critical micelle concentration can be determined, for instance, from the plots of surface tension as a function of the logarithm of the concentration. CMC can then be defined as the concentration at which the surface tension reaches a stable plateau value.^{60,64} Surface tension is independent of the concentration above the CMC and shows little or no dependency with changes in temperature whereas the critical micelle concentration follows an inverse dependence on temperature. Tsunashima et al. studied the micellization of PS-*b*-PB diblock copolymers in various solvents.⁶⁵ They used DLS to measure the hydrodynamic radius, in solvents having the same refractive index of either the PS or PB chains. In a solvent selective for PB block, unimers with collapsed PS segments were observed at low concentration and micelles were observed at higher concentrations, thus defining the CMC. For PEO-*b*-PPO-*b*-PEO triblock copolymer in aqueous solution, CMC varies with the composition of the copolymer.⁶⁰ At a constant PPO/PEO ratio, the CMC decreased with increase in total MW of the copolymer. Faust et al. used the fluorescence of a probe (pyrene) in order to determine CMC.⁶⁰ In this technique, the fluorescence intensity ratios of two different bands of pyrene are measured as a function of copolymer concentration. An increase in this ratio at a given copolymer concentration indicates the formation of micelles and thus the CMC.

Micelles can form spontaneously from a balance between the entropy and enthalpy. For block copolymers in organic selective solvents, the micellar assembly is driven by enthalpic forces, as it is entropically unfavourable to form these ordered structures.⁶⁰ For block copolymers in an aqueous media, such as PEO-*b*-PPO-*b*-PEO, the transfer of a unimer to micelle is

entropy driven.^{60,64} The exchange of block copolymer molecules between micelles and solution is very slow compared to the exchange kinetics observed for low molecular weight surfactant micelles. Moreover, the critical micellar concentration is much lower for block copolymers in comparison with low molecular weight surfactants.^{60,66} Because of the slow exchange kinetics, these structures are often kinetically trapped and this allows the opportunity to vary structural parameters such as the characteristic shape, size and spacing of the array features. However, macromolecular chains possess some dissolution problems when they are placed in a selective solvent, resulting in a large insoluble block, which is mainly arising due to the presence of blocks with high T_g . In order to eliminate this problem usually, they are dissolved in a common good solvent which is then replaced with a selective solvent.⁶⁰ The core of the micelle formed can serve as a reservoir in which various functional species, such as metal or semiconductor nanoparticles, quantum dots, dyes or drug molecules, etc. can be incorporated by means of chemical, physical or electrostatic interactions depending on their physicochemical properties.⁶⁷ These intensify the interest in using BCP micelles as scaffolds for fabricating nano-containers or nanoreactors. Recent progress in novel micellar structures includes three main categories (1) amphiphilic micelles which are formed by hydrophobic interactions, (2) polyion complex micelles which result from electrostatic interaction, and (3) micelles stemming from metal complexation.^{68,69}

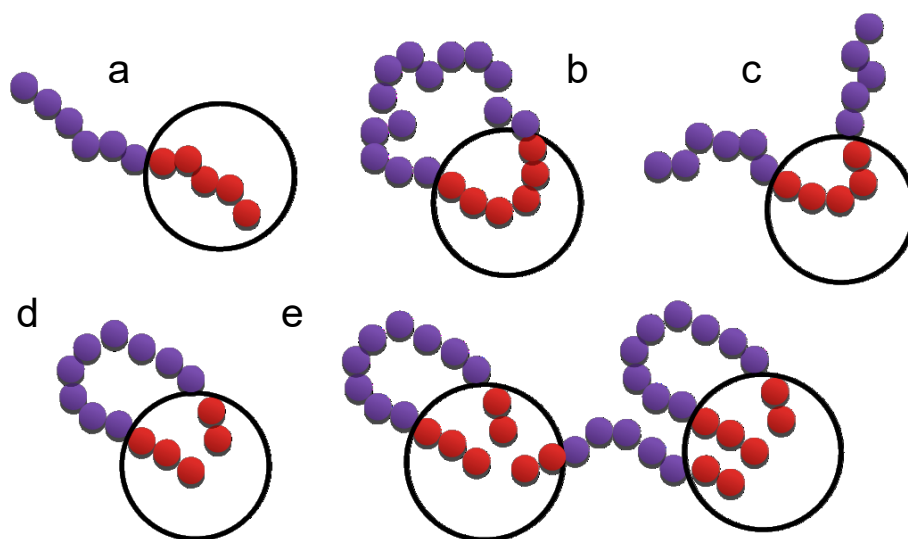


Figure 2.5 Schematic representation of chain conformations of (a) Linear diblock; (b) Cyclic diblock copolymers; (c, d, e) Linear triblock copolymers in a micellar state. Adapted from Ref. 60 and 70.

The diblock copolymers are entropically more favoured to form micelles compared to triblock and cyclic ones. For cyclic copolymers, the two block junctions per molecule must reside at the core-corona interface while for triblock copolymers a fraction of chains will be looped (Figure 2.5).^{60,70} For a linear diblock copolymer, assuming that the composition and N are constant, the CMC is significantly lower than for other architectures. Moreover, the association number and radius of the micelles formed from diblock copolymers will be larger compared to copolymers of other architectures.^{59,66,67} On the other hand, cyclic copolymers

experience the highest conformational restriction as both blocks must loop producing a flower micelle.^{73,74}

2.1.6 Preparation and Characterization of BCP Micelles

One of the simplest ways to produce block copolymer micelle is the direct dissolution of the bulk sample in a selective solvent for one of the blocks. But this works best for low molecular weight copolymers having a shorter insoluble block. Another method is the dissolution of the blocks in a non-selective solvent which results in the formation of molecularly dissolved chains. In order to initiate micellization, a selective solvent for one of the blocks and a precipitate for the other are added in excess to this. Apart from these, in the case of stimuli-responsive BCP, micellization can also be achieved by varying external parameters, such as pH, temperature, ionic strength, etc.⁵⁹

Although these methods can result in the formation of polydisperse micelles, there are several advantages including the exclusion of large aggregates, the formation of ‘crew-cut’ micelles etc. ‘Crew-cut’ micelles are prepared from highly asymmetric diblock copolymers containing very short blocks initially dissolved in non-selective solvents, which later on addition of a selective solvents form crew-cut micelles.⁶⁰

Different instrumental techniques can be used to visualise block copolymer micelles among which scanning electron microscopy (SEM) and transmission electron microscopy (TEM) being widely used.^{60,75} Direct visualisation of block copolymer micelles can also be achieved by atomic force microscopy (AFM). However, the shape and size of the micelles can be affected by tip convolution effects, by specific interactions between the substrate and some moieties of the block copolymer, or by relaxation of a low T_g micellar core resulting in the flattening of the micelles on the substrate.^{60,75} The micellar morphology can also be studied using scattering techniques such as static light scattering (SLS) and dynamic light scattering technique (DLS). SLS allows the determination of absolute weight-averaged M_w , Z and R_g of the micelles whereas from DLS the hydrodynamic radius, R_h , can be measured.⁷⁶ Although the size of the micelle can be calculated by taking a mean value over a large number of micelles, this method is model dependent and can vary from the real value.⁶⁰ Apart from these commonly used techniques, small angle X-ray scattering (SAXS),⁷⁷ small angle neutron scattering (SANS),^{78,79} analytical ultracentrifugation (AUC),⁸⁰ size exclusion chromatography (SEC)⁸¹ are also used to analyse micellar structures.

2.1.7 Micellization of Cationic Amphiphilic Block Copolymers

Block copolymer micelles with a polyelectrolyte corona are an important class of colloidal particles and are often referred to as polyelectrolyte block copolymer micelles.⁶⁰ They combine the structural features of polyelectrolytes, block copolymers and surfactants. As a result, such polymers possess unusual and unique properties which make them fascinating and challenging subject for researchers.

The intrinsic properties of the polyelectrolyte block are strongly influenced by pH, salt concentration and polar interactions. The free energy of a micelle is mainly determined by (1) the interfacial energy of the core/corona interface, (2) the energy needed to stretch the block copolymer chains, and (3) the repulsion among the coronal chains. The minimum free energy corresponds to an equilibrium grafting distance b (N_A , N_B , χ) which depends on block lengths and salt concentration (via χ). The aggregation number, Z , can be calculated from the mathematical expression:

$$Z = N_A^\alpha N_B^{-\beta} \quad (2.2)$$

For non-ionic or neutral block copolymers the grafting distance, b , depends on the soluble block length as $b_0 N_B^{\beta/6}$ with $b_0 \approx 1$ nm. Hence, the aggregation number Z can be written as a function of N_A and N_B ,

$$Z = Z_0 N_A^2 N_B^{-\beta} \quad (2.3)$$

where $Z_0 \approx 1$ and $\beta \approx 0.8$. While for ionic block copolymers the micellization behaviour is strongly influenced by the polyelectrolyte block. For a strongly segregated amphiphilic system such as ionic block copolymers, taking PS-*b*-P4VP as an example, the aggregation number can be expressed as:

$$Z \propto N_A^{1.93} N_B^{-0.79} \quad (2.4)$$

Thus, a qualitatively different behaviour is experimentally observed compared to uncharged block copolymers. The grafting distance shows a characteristic $b = b_0 N^{1/2}$ dependency and an increase in salt concentration lowers the value of the overall radius, R_m . This indicates that mutual repulsion of the polyelectrolyte chains leads to strong stretching of the core blocks.⁶¹

The amount of added salt has a strong influence on the conformation and interactions of polyelectrolyte chains due to the screening of electrostatic interactions between them. Depending on the salt concentration, two regimes can be established for polyelectrolyte block copolymer micellar shells namely ‘osmotic brush’ and ‘salted brush’ regimes. If the added salt concentration is larger than the internal counter ions a ‘salted brush’ regime is established whereas if the added salt concentration is lower than the internal counter ions then an ‘osmotic brush’ regime is obtained. In the ‘osmotic brush’, the osmotic pressure of the counter ions leads to strong stretching of the polyelectrolyte chains and is independent of the added salt concentration. On the other hand, in the ‘salt brush’ regime the polyelectrolyte chains shrink with an increase in added salt concentration. These two concepts have been used to study the properties of polyelectrolyte block copolymer micelles.

In dilute solutions, polyelectrolyte block copolymers form regular micelles with a hydrophobic core and a polyelectrolyte shell. Block copolymers containing anionic polyelectrolyte blocks were studied by Eisenberg et al. and Tuzar et al. in PS-*b*-PAA and PS-*b*-PMAA systems respectively.^{63,66} They showed that at low pH, the PMAA sequence is in the acidic form while at higher pH it is partially or totally ionised i.e., the ionisation degree of these anionic blocks is strongly dependent on pH.⁶⁰ However, the first systematic investigation of micelle formation of cationic polyelectrolyte block copolymers in aqueous solution was carried out by Gallot and Selb.^{61,80} In their work, Selb and Gallot studied the micellization of cationic PS-*b*-P4QVP and other quaternized P2VP and P4VP containing block copolymers. They noted that most of these polymers when directly dissolved in a solvent selective for one of the blocks (eg. water) exhibit low solubility. As the hydrophobic domains were in the glassy state, the thermal energy was insufficient for immediate dissolution. Hence organic co-solvents such as DMF, dioxane, THF, chloroform etc. were used to dissolve these polymers, then by dialysis to obtain stable frozen micelles in pure aqueous solutions.⁶¹

The PS-*b*-P4VP block copolymer is well known for their polyelectrolytic properties due to the presence of cationic P4VP block. The studies conducted by Gohy et al. and Khanal et al. on the micellization of P4VP containing block copolymer systems, have proved that in a solvent selective for P4VP, PS forms glassy cores and P4VP chains extend at low pH (> 5) owing to repulsive forces among the protonated 4VP species.^{60,82} The addition of the anionic species to these micelles cancels the positive charges of the 4VP units, resulting in a morphological change in the P4VP shell from an extended to a shrunken form. Thus, a morphological change can be brought to PS-*b*-P4VP micelles by changing the pH. This property of PS-*b*-P4VP micelles can be made use in creating nano-aggregates which can be utilised for the controlled release of drugs.^{82,83}

2.1.8 Application of Block Copolymer Micelles in Nanotechnology

Block copolymers are gaining interest in use as templates for various nanomaterials with targeted functionalities and properties. Owing to their self-assembling behaviour, the block copolymers form periodic structures with spherical, cylindrical, lamellar, and gyroid morphologies in nanometer scale. These self-assembled structures have been widely used as templates for fabrication of hybrid organic/inorganic nanostructures. Amphiphilic block copolymer micelles can be used in lithography, to generate nanostructured interfaces and the pattern dimension can be controlled by the self-assembly of block copolymer micelles.⁸² Block copolymer micelles can be functionalized to provide higher target selectivity thereby applying them in selective drug delivery, especially for chemotherapeutic drugs.⁸³ Various other applications include using block copolymer micelles for synthesising nanostructured membranes, as a template for nanoparticle synthesis,⁸⁶ for synthesising core/shell particles or yolk/shells⁸⁷ and, as a sacrificial template to create hollow nanostructures.⁸⁸

Lately, using block copolymer micelles directly as nanoreactors or as a template for its synthesis has gained a great deal of interest. Weberskirch and co-workers used hydrophobic

segments of amphiphilic block copolymers in metal-catalyzed transformations.^{89,90} Experiments conducted by M. Lee and J.-H. Ryu studied the application of PEO-*b*-HPP-*b*-PEO micelles as nanoreactors in aqueous solution.^{91,92} This micellar structure exhibited supramolecular properties and was used for the room-temperature Suzuki coupling between aryl halides and aryl boronic acid.^{91,92} Liang et al. used PS-*b*-P4VP block copolymers as reactive templates to deposit the silica shell via an acid catalyzed sol-gel synthesis.⁹³ By varying the solvent selectivity for one of the blocks, they deposited silica shell in the P4VP core or in the P4VP corona to obtain PS-*b*-P4VP/SiO₂ core-shell particles. A similar work was done by Cho et al. dealt with PS-*b*-P4VP micellar templates for the fabrication of various nano-objects.⁹⁴ By varying the solvent ratios (THF/ethanol and THF/water) they obtained different morphologies such as cylindrical or spherical micelles, vesicles or reverse spherical micelles.

2.2 CONTROLLED LOCALISATION OF NANOPARTICLES IN BLOCK COPOLYMER DOMAINS

Block copolymers form ordered nanodomain structures whose morphology can be tailored by their molecular weight and composition.⁹⁵ On the other hand, block copolymers, owing to their rich diversity of structures at the nanometre scale, are an effective means for patterning and controlling particle location. Incorporation of nanoparticles into a polymer matrix can bring a significant impact on the material properties such as mechanical strength, conductivity, permeability, catalytic activity and optical and magnetic properties.^{96,97} The performance of such systems depends on the precise control of the spatial organisation of the nanoparticles.⁹⁸ The selective inclusion of metal nanoparticles in block copolymers can be executed in several ways. One involves the incorporation of pre-synthesized nanoparticles in one of the nanodomains of the block copolymer. Another involves the reduction of metal ions in one of the nanodomains.⁹⁵ Nevertheless, bare metal nanoparticles, due to the high interfacial energy, tend to agglomerate and disperse poorly in (co)polymer matrices.

Precise control of nanoparticle location in A-*b*-B block copolymers can be achieved by synthesising or modifying the nanoparticles with different ligands, A or B homopolymers, a mixture of A and B homopolymers, and A-*r*-B random copolymers.⁹⁹ By modifying the nanoparticle surface with ligands, their stability and compatibility can be improved. The chemical composition, grafting density and molecular weight of the ligands influence the location and dispersion of the nanoparticles and thus the final morphology of the nanocomposites. By fine-tuning the ligand properties nanoparticles can be selectively localised in either A or B domains or at the A/B interface. For example, in order to localise the particles within the A- or B-domain of an A-B diblock copolymer, particles need to be coated with either A or B-type homopolymer. To localise particles at the interfaces between the two blocks, particles have to be coated with a mixture of A- and B-type homopolymers.¹⁰⁰ These approaches are based on minimising the enthalpic interaction of mixing of nanoparticles into block copolymer matrices by modifying the nanoparticle surface with components similar to the respective block copolymer domains.⁹⁹

2.2.1 Controlled Localisation of Nanoparticles Modified with Polymeric Ligands

Kim et al. controlled the location of gold nanoparticles in PS-*b*-P2VP block copolymer thin films by varying the grafting density and chain length of the polymeric ligands within the block copolymer domains.^{101–106} In their experiments, they observed that the final morphology of the block copolymer is affected by the location and concentration of gold nanoparticles. But when studying the localisation of nanoparticles in thin films, the orientation of microdomains with respect to the used substrate has also been taken into account. In a theoretical investigation done by Balazs et al. they studied the effects of neutral and selective nanoparticles in diblock copolymer thin film on the orientation of BCP microdomains confined between two hard plates.¹⁰⁷ Their studies showed that, on a substrate that has a low interfacial energy with only one of the block, symmetric diblock copolymer form parallel-oriented lamellae at equilibrium. The orientation of the block copolymer changed from parallel to perpendicular upon addition of neutral nanoparticle to the thin film. The neutral nanoparticles were located at the interface of the self-assembled block copolymers and near the substrate to reduce the entropy loss of the polymer chains. The addition of neutral nanoparticles to the block copolymer domains that are parallel to the substrate (hard plates) reduced the interfacial tension and neutralises the substrate and hence the orientation of block copolymer changed from parallel to perpendicular. In agreement with the theoretical model proposed by Balazs, experimentally Yoo et al. described a general method for controlling the localisation of gold nanoparticles in the microdomains of PS-*b*-PMMA diblock copolymer thin films.¹⁰⁶ The gold nanoparticles were coated with different compositions of PS and PMMA which are either neutral for the PS-*b*-PMMA domains or selective for either PS or PMMA. The selective nanoparticles produced a parallel domain orientation whereas the neutral nanoparticle-induced a perpendicular domain orientation (Figure 2.6).

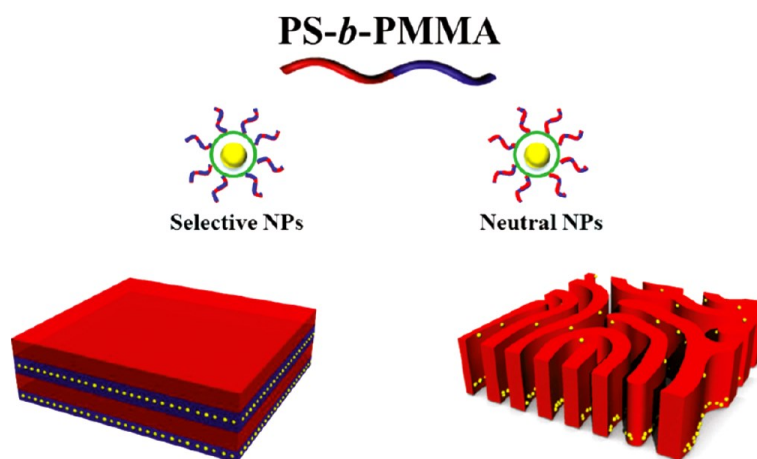


Figure 2.6 Schematic showing the controlled orientation of block copolymer thin films by introducing selective and neutral nanoparticles. Reproduced from Ref. 106.

The studies conducted by Kramer et al. in PS-*b*-PVP/Au thin films, dealt with the controlled localisation of gold nanoparticles within different PS-*b*-PVP block copolymer domains.¹⁰⁰ They have controlled the location of gold nanoparticle in the PS or PVP domains by coating the nanoparticle with the respective homopolymer. Particles coated with PS homopolymer have selectively segregated into the PS domain, whereas, those coated with PVP, on the other hand, have segregated into the PVP domains (Figure 2.7). Therefore, it can be clearly stated that particles coated with a short homopolymer lower their enthalpy by segregating into the corresponding domain of the block copolymer. Moreover, by concentrating the particles near the centre of the compatible domain where the polymer chain ends are located, the chain can accommodate particles by moving apart rather than stretching.

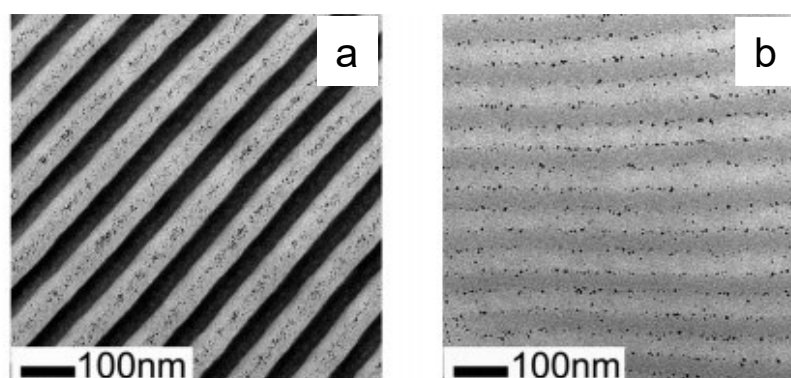


Figure 2.7 TEM image of (a) PS-coated particles segregated to the centre of the PS domains (light region) in a PS-*b*-PVP lamellar diblock copolymer phase; (b) PS/PVP coated particles segregated at the interface between PS/PVP blocks. Reproduced from Ref. 100.

According to a model proposed by Balazs and coworkers, the variation in the size and volume fraction of particles can be varied to control the particle distribution inside the composite.¹⁰⁸ They presented a method to calculate the morphological and thermodynamic behaviour of AB diblock copolymer - spherical particle mixtures without requiring a prior knowledge of the equilibrium structure. For small volume fractions of large particles, the A sub chains must stretch to get around the dispersed particles, incurring a loss in conformational entropy. As the local particle volume fraction is increased, stretching of the A segments is reduced by the segregation of the particles into a central core. This free energy gain for the polymers results in the loss of translational entropy for the particles. On the other hand, for the same volume fraction of small particles, the stretching required by the polymers to circumvent the spheres is less significant. In this case, the translational entropy of the particles dominates the behaviour of the system. As more small particles are added to the system, the spheres are more uniformly dispersed and the entropic free energy per A block increases.

It is described that by coating the nanoparticles with a mixture of PS and PVP homopolymers the gold nanoparticles were localised at the interface between two blocks.¹⁰⁰ This interfacial adsorption was not observed for pure PS or PVP coated particles. This selective

segregation could be explained based on the interfacial energies of the PS-*b*-PVP diblock (γ_{SV}), the nanoparticle-PS (γ_{nS}) and the nanoparticle-PVP interfaces (γ_{nV}). They also explained that the adsorption energy of nanoparticles at an interface is given by $E_a = \pi r^2 \gamma_{SV} (1 - |\cos\theta|)^2$ where r is the radius of the particle and $|\cos\theta| = |\gamma_{nV} - \gamma_{nS}| / \gamma_{SV}$.^{100,109} For particles coated with both the homopolymers, the total interfacial energy ($\Delta\gamma$) is much less than the interfacial energies of the PS-*b*-PVP diblock (γ_{SV}). As a result $\cos\theta \ll 1$ and the adsorption energy, $E_a \approx \pi r^2 \gamma_{SV}$. Therefore, in this case it is expected that the particles are bound to the PS-PVP interface if the values of $|\cos\theta|$ is small.¹⁰⁰ Thus, in order to selectively localize particles within the A- or B- block of the A-B diblock copolymer, particles are either coated with A- or B-type homopolymer respectively. To localize particles at the interfaces between the blocks, particles are coated with a mixture of A- and B-type homopolymers. With this approach, particles can be localized completely within one copolymer domain or the other, or they can be arranged at the interfaces between the blocks.

2.2.2 Controlled Localisation of Nanoparticles in Colloidal Block Copolymer Self-Assembly

In solution, the solvent-polymer interaction dictates the ability to form well-defined structures. Amphiphilic block copolymers can self-assemble into various nanostructures such as spherical, cylindrical micelles, or vesicles depending on the block ratio, solubility of the blocks in the solvents, solvent composition, and immiscibility of the solvents and temperature / pH of the solutions. The micellar aggregates are extremely stable if the core-forming block is in a glassy state.⁶² As a result, they are the most studied example of self-assembling structures in selective solvents. Encapsulation of nanoparticles into BCP micellar aggregates can have the following advantages: (1) Improving the stability of nanoparticles: - the stability of nanoparticles is highly dependent on the ligand structure that is bound to the nanoparticle surface.¹¹⁰ But over a long period of time, these ligands can dissociate under high-temperature or chemical cleaving agents.¹¹¹ Encapsulating nanoparticles in BCP micellar aggregates provide a suitable environment for the stabilisation of nanoparticles. Additionally, after crosslinking the micelles, nanoparticles will be stable against heat and other environmental conditions.¹¹² (2) Reducing toxicity: - the as-synthesized nanoparticles are normally coated with surfactant molecules, for example, AuNPs stabilised with cetyltrimethylammonium bromide (CTAB).¹¹³ Hence, the biological applications of these nanoparticles are limited due to the cytotoxicity of CTAB. The potential toxicity can be reduced by encapsulating ligand-free nanoparticles in biocompatible BCP micelles; as such micellar structures provide an environment for stabilising the nanoparticles.¹¹⁴ (3) Easy to be multi-functionalized: - multifunctionality can be induced by the simultaneous incorporation of different NPs within a single micellar carrier.¹¹⁵ (4) Templates for functional cavity formation: - the encapsulated nanoparticles can act as a sacrificial nanotemplate for hollow polymer capsule formation by crosslinking the resulting polymer shell and by the removal of the nanoparticle template.¹¹⁶

However, to control the location of nanoparticles in colloidal self-assemblies of amphiphilic block copolymers is challenging when compared to that in BCP bulk or thin films. On the other hand, colloidal self-assembly of amphiphilic block copolymers and inorganic nanoparticles create versatile functional materials with unique chemical and mechanical properties for various applications such as nanoreactors, drug delivery and medical imaging. As mentioned above, the distribution of nanoparticles can determine the final properties of the block copolymer structures; controlled arrangement of nanoparticles in such colloidal polymer assemblies is important. By varying the types of the nanoparticle, the properties of such colloidal structures can be varied. Micelles containing a single nanoparticle are termed as ‘cherry micelles’^{54,117} whereas micelles containing multiple NPs are ‘raspberry micelles’.⁵⁴ Each BCP micellar aggregate contains three different domains, namely, the core, corona, and the interface, which allows the selective localisation of nanoparticles amongst these domains.^{54,118–120}

Encapsulation of nanoparticles in the micellar core improves the stability of the nanoparticle and preserves its characteristic properties. Besides, the encapsulated particle will be protected uniformly by the corona on all sides. This might be useful in the area of labelling or catalysis. Locating the nanoparticle in the core and the corona facilitates the encapsulation of different types of particles with a tailored spacing. The arrangement of separated electron-donor and electron-acceptor in different domains with controlled spacing is used in optical applications. For example, an assembly with QDs in the core and AuNPs in the corona with an interparticle spacing of 20 nm facilitated an enhancement of QD PL emission relative to the QD emissions from micelles without AuNPs.¹²¹

The controlled loading of nanoparticles in micellar aggregates can be achieved via the *in-situ* synthesis of nanoparticles within the micelle or by incorporating preformed nanoparticles into the micellar assembly. The latter approach offers an effective means to precisely control the location and size of nanoparticles in BCP micelles. Depending on the required properties and application, nanoparticles can be either located in the core, corona, and interface of the micelle. Kramer et al. synthesised novel core-shell nanoparticles with a hydroxylated ligand modified gold core and a PS outer shell.¹⁰⁴ The nanoparticles were functionalized using thiol-terminated PS-*b*-PI diblock copolymer ligands. The double bonds of PI blocks were then hydroxylated which resulted in a multi-layered core-shell assembly with a gold core, inner hydroxylated block and an outer PS shell.

Luo et al. also demonstrated a method to control the location of gold nanoparticles in colloidal polymer assemblies by tuning the nature of the nanoparticle surface.⁹⁷ They controlled the arrangement of nanoparticles in PS-*b*-PAA polymer micelles, from the micellar core to the A/B polymer interface using mixed nanoparticle ligands as shown in Figure 2.8. By varying the ratio between hydrophilic and hydrophobic surface ligands the nanoparticles were selectively localized at the interface between PS and PAA block or aggregated in the centre of the assembly.

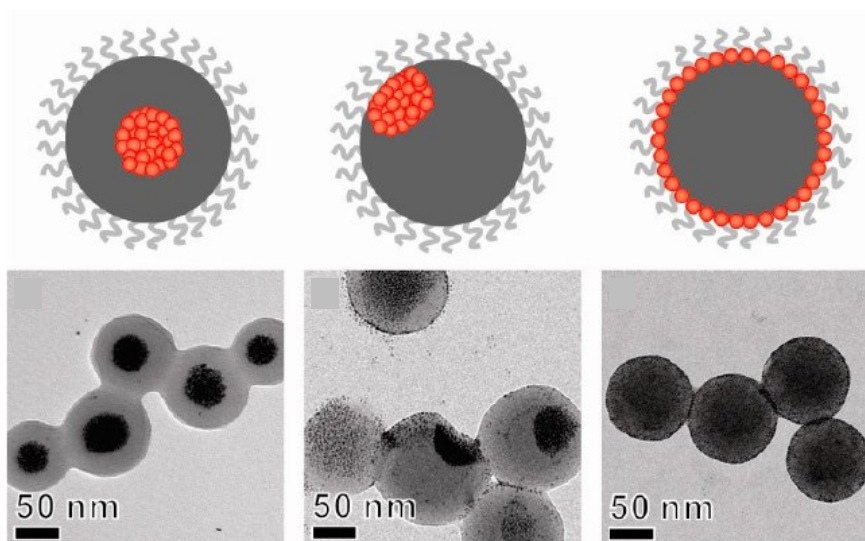


Figure 2.8 Schematic representation of selective localisation of gold nanoparticle in the core of the micelles (a) As free-standing; (b) Attached to the inner walls of the core; (c) At the interface between PS-*b*-PAA diblock copolymer and the corresponding TEM images. Reproduced from Ref. 97.

Encapsulation of preformed inorganic nanoparticles into micellar aggregates can be attained by various strategies. Some of the widely studied methods are described below.

Co-precipitation method: Preformed inorganic nanoparticles can be encapsulated into BCP micellar core through the co-assembly of NPs and amphiphilic BCPs in a selective solvent. Eisenberg and co-workers conducted experiments with the controlled incorporation of gold nanoparticles into the centre of the micelles by coating the particles with diblock copolymers (PS-*b*-PAA) of the same or similar composition.¹¹⁸ Taton and co-workers have synthesised nanoparticle loaded polymer micelles where alkyl terminated nanoparticles were uniformly embedded in the hydrophobic polymer core.¹²² In another work by Taton et al., the authors demonstrated selective encapsulation of dodecanethiol functionalized gold nanoparticle to the micellar core of PS in (PS-*b*-PAA) diblock copolymer.¹¹⁹ In a typical procedure, homogeneous solutions of PS-*b*-PAA and dodecanethiol functionalized AuNPs were first prepared in a good solvent such as N, N-dimethylformamide. A solvent selective for the PAA block (eg. Water) simultaneously desolvated the PS blocks and NPs, leading to the aggregation of the NPs with the PS blocks, forming micellar cores, which were protected by the hydrophilic corona. This approach can be used to prepare multifunctional particles possessing different properties in a single hybrid micelle with various morphologies. Using this method NPs can either be dispersed uniformly in the micellar aggregates or can be localised in the core of the micelles. Another method followed by Park et al. allowed the radial distribution of nanoparticles in the BCP micelle by simply changing the copolymers to nanoparticle ratio.¹²³

Interfacial instabilities of emulsion droplets: Another method to encapsulate nanoparticles into the micellar aggregates is through the interfacial-assisted assembly of the emulsion droplets.

Instead of dissolving the copolymer in water-miscible solvent, Zhu and Hayward used a water-immiscible organic solvent which is a good solvent for both the blocks of the BCP.¹²⁴ The polymer solution was then dispersed as an emulsion in a continuous aqueous phase with a stabiliser followed by the removal of solvent from the droplets by diffusion through the aqueous phase and evaporation. An increase of the BCP concentration within the droplets resulted in the self-assembly of the polymer through a series of interfacial instabilities. This gave rise to an increase in surface area of the droplets and ejected micellar assemblies to the aqueous phase. An advantage of this approach is the ability to produce either spherical or worm-like hybrid micelles, where the micellar morphology depends on the composition of the copolymer. This method can be applied to a wide range of block copolymer with different hydrophobic blocks. In addition, this method can be utilised in the production of multifunctional micelles by simultaneous encapsulation of different type of nanoparticles.

Heating-cooling method: In the heating-cooling method, hybrid micelles are generated using longer hydrophilic chains and short hydrophobic segments. Chen et al. employed this method to encapsulate single AuNPs in hairy micelles of PS-*b*-PGA and PS-*b*-PAA BCPs with a narrow polydispersity.¹²⁵ In a typical synthesis, a mixture of BCP and hydrophobically functionalized AuNP solution was heated to 110°C and then slowly cooled down to induce the self-assembly of the BCPs. Homogeneous micelles were formed as the CMC of the polymer slowly decreased with temperature. An advantage of this route is the use of BCPs with longer hydrophilic chains to prepare stable micellar aggregates without cross-linking them. It aids not only the encapsulation of single nanoparticles per micelles but also avoids the mixing of two solution phases which could induce regional inhomogeneity and aggregation. Moreover, the micelles resulting from this method possesses a thick hydrophilic shell which enables the attachment of biomolecules. Two or three AuNPs of the same or of different kinds can also be encapsulated using this method.^{126,127}

Other approaches for the encapsulation of NPs into the micelles include supramolecular assembly/disassembly route, via electrostatic interactions, film rehydration, nano flash precipitation, microfluidic processing, hydrogen bonding of the NPs with the host BCPs, mini-emulsion polymerization, and thiol-end functionalization.

Factors that govern the precise localisation of NP in micelles: To optimise the optical, magnetic, and mechanical properties it is important to tune the position of NPs within the micelles. But it is difficult due to the strong enthalpy incompatibility ($\Delta H_{\text{NP-polymer}}$) of the NP with a polymer, long distance van der Waals attractions between the NPs ($\Delta G_{\text{NP-to-NP}}$), and the conformational entropy loss of the polymer ($\Delta S_{\text{polymer}}$) resulted from polymer chain deformation induced by the insertion of NPs. The nanoparticle aggregation in polymer micelles can be avoided by reducing the NP-NP attraction and employing favourable interactions between NPs and the host polymers. By changing the surface chemistry, size, and shape of the NPs one can control their position within the micellar aggregates. For a stable incorporation of NPs within the BCP matrix, the compatibility of NPs with BCP microstructures is the key factor. The compatibility

of nanoparticles can, in turn, be controlled by considering the symmetry of both the NPs and the BCP matrix. A general method used is to modify NPs with polymeric ligands that favourably interact with the polymer host and reduces the NP-NP attractive interactions. As stated before, Eisenberg and co-workers incorporated AuNPs coated with PS-*b*-PAA selectively to the central portion of the BCP as shown in Figure 2.9.¹¹⁸

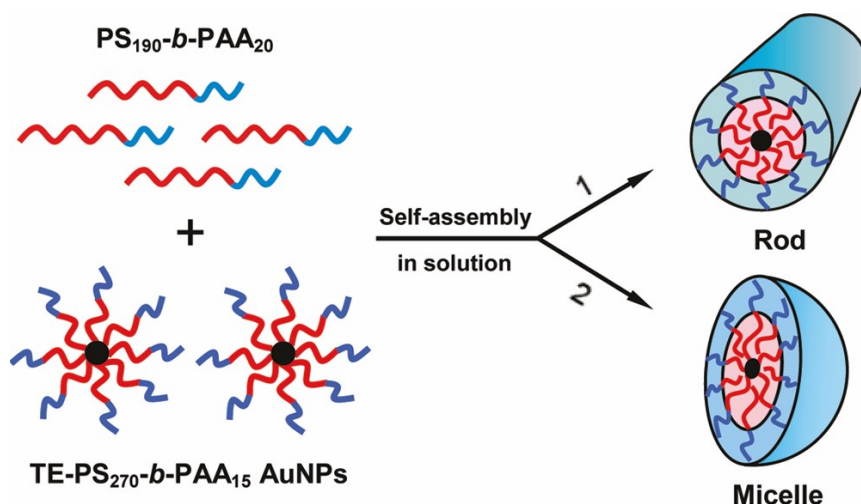


Figure 2.9 Schematic illustrations of the selective incorporation of PS-*b*-PAA (PS-red and PAA-blue) coated AuNPs into the central portion of the BCP micelles or rods. Reproduced from Ref. 118.

The uniform dispersion of nanoparticles in polymer micelles is also determined by the wettability of the polymeric ligands by the host polymer. In addition, the molecular weight, different grafting density, and composition of the polymer that is attached to the nanoparticles can affect the distribution and localisation of nanoparticles in the micellar aggregates. The size of the nanoparticles can also affect their spatial distribution in the polymer matrix. Smaller particles disperse freely within the polymer matrix as the stretching effect required by the block phase to circumvent the particles is less significant for smaller particles than for large-sized particles. In order to study the effect of particle size on the number of encapsulated particles, Taton and co-workers encapsulated AuNPs of a size larger than 10 nm into a PS-*b*-PAA micelle, where they obtained single AuNPs in the PS core per each micelle.¹¹⁹ For particles with 4 nm diameter, multiple particles were present within each micellar core, even at a very low particle-polymer ratio.¹²⁸ On the other hand, Chen et al. encapsulated single AuNPs with 5 nm diameter per each hairy micelle following a heating-cooling method.¹²⁵ Thus, apart from nanoparticles surface modifications and size, the encapsulation method also plays a role in determining the assembly of particles in a micelle. Still another parameter that affects the localisation of nanoparticles in micelles is the nanoparticle shape. Anisotropic particles display remarkable properties than spherical particles.¹²⁹ For example, irregularly shaped particles show plasmonic “hot spots” at high-curvature corners, which may exhibit strong plasmonic coupling between the

particles. On the other hand, anisotropic particles pose an additional challenge in directed assemblies compared to isotropic particles, as their anisotropy in shape and possible chemical composition has to be taken into account during directed assemblies. Nanoparticles with different shapes, such as nanorods (NR), have various facets and different curvature on their surfaces which in turn allows the polymeric ligands to attach more easily to curved surfaces.¹³⁰ Li et al. demonstrated a method to disperse and orient NR within cylindrical micelles by tethering brushes of same homopolymers with different lengths onto the NR surface.¹³¹ The additional void space created on the NR surface due to the mismatch of different polymer brushes provides sufficient conformational freedom for the matrix polymers close to the NR surface. This improves the wettability of the brushes and polymer matrix. Nanoparticles with other shapes, such as nanoplatelets,¹³² nanowires¹³³, and nano dumbbells¹³⁴ can also be encapsulated into BCP micelles and produce materials with novel and complex properties. Nanoplatelets can stand vertically or pack horizontally on the polymer scaffold, which brings anisotropic properties. Nanowires, when encapsulated in block copolymer micelles, may form circular spring-like coils. The mechanism of transformation from straight wires to circular rings results from the contraction of encapsulating polymer shells and energy minimization of the combined NW-polymer system.^{133,135} On the other hand, when nano dumbbells are incorporated into the polymer micelles, they form spherical clusters whose internal distribution is defined by packing of the dumbbell-like shape.

2.2.3 Applications of Nanoparticle encapsulated Block Copolymer Self-Assembly

Biomedical application: Biological applications of hybrid micelles mainly depend on the properties of the NPs encapsulated in BCP micelles. The hydrophobic core of the micelle acts as an ideal nanocarrier compartment for hydrophobic agents and the shell consists of a protective corona that stabilises the NPs. For instance, QDs can be used to perform in vivo or in vitro imaging due to their unique optical properties, including wideband excitation, narrow emission, phenomenal photostability, and high quantum yield.^{136,137}

SERS probes: Surface-Enhanced Raman Scattering (SERS) is a surface-sensitive technique that enhances Raman scattering by molecules adsorbed on rough metal surfaces. The principle of SERS is based on two major enhancements: (1) the long-range electromagnetic enhancement and (2) short-range chemical enhancement. These result in an increase in the Raman scattering cross-section of the adsorbed molecules. AuNPs are widely used as SERS substrates. Biomolecules, polymers, or inorganic layers have been used to coat metal NPs to improve the stability of the nanoprobcs. Hybrid micelles were loaded with AuNPs and Raman reporters, where the polymer shells can protect the encapsulated nanoprobcs.¹²⁷ A large variety of reporters could be incorporated into the polymer micelles by different encapsulation methods for realisation of multiplexed detection of target molecules.

Catalysis: One of the promising application for inorganic/polymer hybrid colloids is to develop catalysts with special catalysing behaviour in reactivity, stability and selectivity. Thermoresponsive polymer micelles can be used to enclose metal nanoparticle catalyst to prepare

responsive catalysts. The temperature responsiveness of the polymer corona chains can be used to adjust the catalytic activity.¹³⁸ For example, Zhang et al. synthesised AuNPs inside the core of thermoresponsive micelles of PNIPAM-*co*-P4VP.¹³⁸ Temperature responsive solubility of the PNIPAM corona chain was used to adjust the catalytic activity. Below the LCST, the extended hydrophilic PNIPAM chains expose the AuNPs to the hydrophilic reagents and accelerate the reaction. On the other hand, above LCST, the solubility of the PNIPAM chains decreases and the AuNPs were covered by the collapsed PNIPAM chains, which decelerated the reaction. Also, block copolymer micelles can be used as a reactive template to create nanoreactors to be used as high-performance catalysts.¹³⁹ The authors used PS-*b*-P4VP micelles as a sacrificial template, to encapsulate catalytically active AgNPs and AuNPs into the micellar core in order to prepare Au@SiO₂ yolk-shell catalyst.

2.3 YOLK-SHELL NANOSTRUCTURES

For the past few decades, scientists have been exploring the advantages of structurally different NPs, rather than those of simple spherical particles, such as anisotropic shape,^{140,141} hollow,^{142–147} core-shell (CS),^{148–150} yolk-shell (YS),^{18,144,147,151,152} Janus particles,^{153,154} composites,¹⁵⁵ doped^{156–158} etc. Yolk-shell nanostructures/ yolk-shell nanoparticles (YS NS / YS NPs) are defined as a hybrid structure, a mixture of core/shell and hollow, where a core particle is encapsulated inside the hollow shell and may move freely inside the shell.⁴³ Yolk-shell nanoparticles have been first reported in 2002 by Kim et al. and Kamata et al.^{11,12} In their work, Kim et al. fabricated hollow carbon and polymer capsules containing gold nanoparticles by using spherical silica templates.¹² Kamata et al. synthesised spherical hollow colloids of poly benzyl methacrylate with movable cores of gold nanoparticles.¹¹ They have stated that such structures can be tailored to have different shell/core materials to impart different properties. They are generally represented as a core/void/shell. Yolk-shell nanostructures are also termed as movable core/shell or rattle-type nanoparticles. These structures are distinguished from solid nanoparticles,^{3,30,159–161} Janus particles,^{15,154,162} hollow particles,^{16,161} and core-shell particles.^{3,17,159}

In order to represent such structures, different terminologies such as (1) nano rattles (as the core particles were encapsulated inside the hollow shells),¹² (2) movable core/shell (as the entrapped core was movable when dispersed in a liquid and stick on the wall surface in air),¹¹ (3) yolk-shell (since the core particle behave like a movable yolk inside the hollow shell),^{163,164} and (4) core/shell with hollow interiors,⁴³ have been used so far. Generally, yolk-shell nanoparticles are denoted as core@shell, for example, Au@MgSiO₃,³⁶ Au@HSNs¹⁶⁰. They can also be represented as core@void@shell^{29,165,166} such as Si@void@C²⁹ or Pt@void@TiO₂.¹⁶⁷ In the presence of multiple shells, they are represented as core@shell1@shell^{20,168}. In the present work, we adopted the yolk-shell nanoparticles (YS NPs) as a general terminology and core@shell as the representation to describe the yolk-shell nanostructures under study.

2.3.1 How are They Different from Core/Shells?

The properties of the core/shell nanoparticles mainly depend on the sequence of core and shell, the size of both the core and the shell, and the type of material. On the other hand, yolk-shell nanoparticles are hybrid structures with a movable core inside the hollow shell of the same or different materials. And they can be derived from the core/shell structure via selective etching of the core and or the shell. Yolk-shell nanostructures, being a hybrid of hollow and core/shell structure, enable them to possess the advantages of both the structures. There are certain specific advantages of yolk-shell nanostructures over core/shell structures. (1) yolk-shell nanostructures can be synthesised from a single material to enhance specific surface area,^{169–178} (2) the core surface is unblocked compared to the core/shell nanoparticles providing more active sites and higher surface area,^{179–184} (3) the void space is suitable to accommodate the guest molecules,^{22,185–188} (4) the shell layer provides more active inner and outer surfaces,^{189–191} and (5) the void provides space for the expansion of core nanoparticles in many applications.^{192–195}

2.3.2 Type of Yolk-Shell Nanostructures

Yolk-shell nanostructures are broadly classified into spherical and nonspherical depending on their core and shell morphologies irrespective of their material properties. In spherical structures, both the core and the shell are spherical in shape whereas, in the case of non-spherical structures, at least one of the structures should be non-spherical. By varying the synthetic procedure, core or shell compositions and depending on the end application one could synthesise different yolk-shell particles.

The non-spherical yolk-shell nanostructures are further classified into two types based on their geometry (1) complete non-spherical shape and (2) partially nonspherical yolk-shell nanostructures, where either the core or the shell of the yolk-shell has a non-spherical shape. The spherical yolk-shell nanostructures can further be classified into different categories such as (1) single core@hollow shell (Figure 2.10 a),³⁰ (2) multiple cores@single shell (Figure 2.10 b),¹⁵¹ (3) single core@multi-shell (Figure 2.10 c),¹⁹⁶ (4) multi core@multi-shell,¹⁹⁷ and (5) yolk-shell structures with a raspberry core (Figure 2.10 d).^{151,187} Depending on the end-use and by varying the shell composition a yolk-shell structure with multi-layered shells can be obtained while the yolk-shell structures with a raspberry core can be created using different type and composition of the nanoparticle.

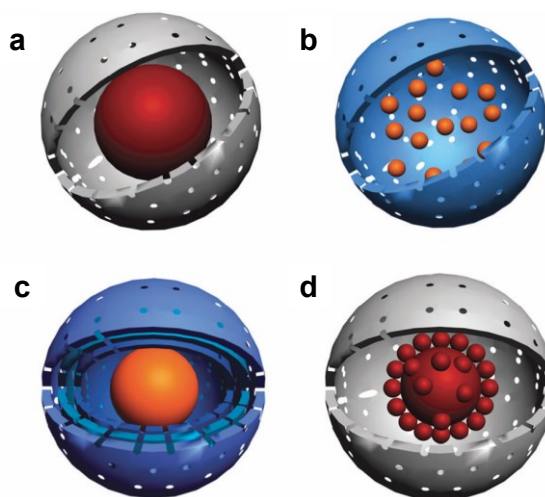


Figure 2.10 Different yolk-shell structures: (a) YS NPs with a single core; (b) YS NPs with multiple cores; (c) YS NPs with multiple shells; (d) YS NPs with a raspberry-like core. Reproduced from Ref. 151.

Single core@hollow shell nanoparticles are the simplest and the most studied structures among all the other yolk-shell nanostructures. They are made of either the same or different materials, one as the core and the other as the shell. Depending on the type of core and shell materials, they can be further classified into (1) inorganic/inorganic, (2) inorganic/polymer, and (3) polymer/polymer. Among the above-mentioned classifications, the inorganic/inorganic combinations of different materials have been studied the most. They possess unique optical, magnetic, electrical, photoelectrochemical, electrochemical, mechanical, thermal, and catalytic properties of different inorganic materials.⁴³ By fine-tuning the shell and/or core properties and characteristics they can be devised for high-performance applications. Among the inorganic/inorganic yolk-shell nanostructures, noble metal@silica yolk-shell nanoparticles are studied widely.

Noble Metal@Silica Yolk-Shell Nanoparticles: Among the various inorganic materials, silica is the most studied material because of its wide range of applications in the field of biomedicine, chemistry, and electronics. Silica shell possesses many advantages such as (1) simplicity of the sol-gel reaction to synthesise silica, (2) chemically inert and non-toxic nature which is suitable for biological and chemical applications,¹⁹⁸ (3) coating on noble metal cores does not affect the LSPR properties of noble metallic nanoparticles (because of the reduction of electromagnetic coupling between metallic nanoparticles),¹⁹⁹ (4) optical transparency towards electromagnetic radiation of the wavelength range 300-800 nm,¹⁹⁹ (5) transparency towards a magnetic field,²⁰⁰ (6) versatility in the design of diverse surface morphologies and functionalization via surface modification for improved biocompatibility,^{198,199} (7) acting as a catalyst support leading to high catalytic activity,²⁰¹ (8) increase in the suspension stability of core particles by reducing the bulk conductivity¹⁵⁰ and increasing the steric repulsion,¹⁸⁴ (9) acting as a sacrificial layer for creating a YS structure,^{147,202} (10) tunable pore diameter leads to the high specific surface area,²² and (11) sinter stable nature or tolerance of high temperature.^{198,199} Due to these advantages, the yolk-shell nanoparticles with a silica shell are used in different fields such as catalysis,^{151,184,203,204} separation,²⁰⁵ sensors,¹⁹⁹ biomedical,²⁰⁶ and microwave absorption.²⁰⁷

To obtain the combined advantages of both silica and metal nanoparticles, and to develop new properties, yolk-shell nanostructures of these combinations have been studied extensively. Noble metal nanoparticles provide the unique structural, optical, magnetic, catalytic, and quantum properties to the yolk-shell nanoparticles. Most of the studies were carried out in exploiting the SPR and catalytic properties of noble metal@silica yolk-shell nanoparticles. The optical properties of the noble metal (Au, Ag) NPs are described in terms of SPR.²⁰⁸ It is the resonant, collective oscillation of valence electrons in a solid stimulated by incident light.

Figure 2.11 shows the interaction between the electric field of incident light and the free electrons of a metal sphere whose size is smaller than the wavelength of light.²⁰⁹ The electric field of incident light displaces electrons from equilibrium in one direction, creating a dipole that can switch direction with the change in electric field. Generated restoring

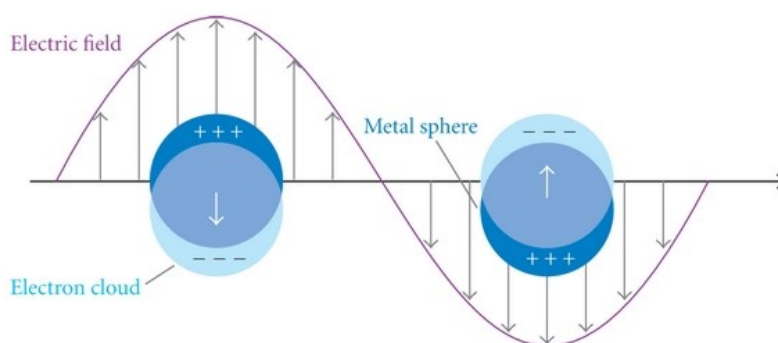


Figure 2.11 Schematic illustration of a localised surface plasmon of a metal sphere. Reproduced from Ref. 209.

force tends to recombine charges, thus resulting in oscillatory motion of electrons. When the frequency of the dipole oscillation approaches that of an incident light, a resonance condition is reached. This leads to constructive interference and the strongest signal for the plasmon. Such a condition is referred as surface plasmon resonance (SPR).²⁰⁹

In the case of confined surfaces, as in nanoparticles, this phenomenon is termed as localised surface plasmon resonance (LSPR). It occurs within metallic NPs of a size comparable to or smaller than the wavelength of light used to excite plasmon. The resonant frequency of LSPR strongly depends on the composition, size, geometry, dielectric environment, and particle-particle separation distance of NPs.²¹⁰ In the case of noble metals like Au and Ag, due to the energy levels of d-d transitions, LSPR is exhibited in the visible range of the spectrum.²¹¹ Although Ag exhibits the strongest plasmon among all noble metals, Au is preferred for biological applications mainly due to its inert nature and biocompatibility.²¹² Moreover, AuNPs have better compatibility with thiol compounds which help the easy immobilisation of biomolecules to them. Also, noble metal nanoparticles show Surface-Enhanced Raman Scattering (SERS).²¹³

As stated above, the SPR properties of AuNPs are highly dependent on its size, shape, and the dielectric constant of the surrounding medium. As a result, the agglomeration of NPs in the application media significantly changes SPR properties. The aggregation of NPs also leads to the coupling of LSPR resulting in a new excitation band with a lower energy. This, in turn, affects the intensity of SERS signal. The agglomeration of nanoparticles can be omitted by using capping agents to stabilise the nanoparticles. But these capping agents tend to undergo chemical degradation, reaction with the metal, or affected by surrounding environment, with time. This results in destabilising the particles which lead to particle agglomeration after some time.^{199,214} The problem of agglomeration can be solved on a large scale by enclosing the nanoparticles in the porous silica shell.^{22,184,199}

Apart from the optical properties, most of the studies on noble metal@SiO₂ yolk-shell nanoparticles are focused on improving the catalytic applications. Noble metal nanoparticles

exhibit high catalytic activity for different chemical reactions due to their high surface to volume ratio and a large fraction of active sites on the surface. Bare nanoparticles and nanoparticles stabilised with capping agents suffer various limitations such as agglomeration, low catalytic activity, and instability in solution phase in presence of target molecules, due to the degradation of capping agents etc. Core/shell particles, on the other hand, show improved catalytic activity when compared to pristine nanoparticles. But in such structures, core surface is blocked by the protecting shell thereby reducing the available contact area between the metal surface and the reactant molecule. This, in turn, reduces the reaction rate. On the contrary, yolk-shell nanoparticles show catalytic properties superior to core/shell nanoparticles. Due to the hollow space present between the core and the shell, the core surface is available to the reactant molecule without any masking effect from the surrounding shell.

Wang et al. demonstrated the catalytic activity of yolk-shell nanoparticles containing a single Au core and a hollow mesoporous silica microsphere (Au@HMSM) (Figure 2.14) using a model reaction with 4-nitrophenol as the reactant molecule.²¹⁵ They demonstrated that the catalytic activity can be controlled by varying the core size. Another work was done by Priebe et al. dealt with the synthesis of Ag@SiO₂ yolk-shell nanoparticles and studying their catalytic activity.²¹⁶ They proved that these structures can be used in the degradation of Methylene Blue. They also stated that the shell thickness can be controlled by varying the precursor used for shell formation. Lee and co-workers studied the effect of tuning the shell porosity and core surface functionality of Au@SiO₂ yolk-shell nanoparticles in their catalytic activity.²² The shell porosity was tuned by varying the molar ratio of porogen (octadecyltrimethoxysilane, C₁₈TMS) to the silica precursor. It was observed that the diffusion coefficient and turnover frequency increased significantly for the catalytic reduction reaction of o-nitroaniline because of the presence of pores. The functionalization of the gold core with 3-mercaptopropionic acid (3-MPA) enhanced the catalytic activity of Au@SiO₂ in the reduction of o-nitroaniline. Thus, the catalytic activity of noble metal@SiO₂ yolk-shell nanoparticles can be varied by fine-tuning the shell porosity²² and thickness,²¹⁶ core size²¹⁵ and core surface functionality.²² The porosity of the silica shell can also be tuned by changing the reaction temperature during the synthesis. Besides, Au,^{184,217} Ag,²¹⁸ Pd,²¹⁹ Pt,¹⁴ and Cu²⁶ are also used as core materials. Porous silicates are also used as shell materials with metal cores, which show a periodic size controllable pore system and high surface area. These types of yolk-shell nanoparticles have been synthesised mostly from hard^{24,31,42} and soft^{147,151,196,215,220} sacrificial template methods, and galvanic replacement reactions.^{221–223}

2.3.3 Routes for Synthesis of Yolk-Shell Nanostructures

In yolk-shell nanostructures, the core is encapsulated in a shell in order to provide protection for the core so that its functionalities are not diminished and do not vanish upon aggregation and sintering or through interaction with the surrounding environment. Besides, these structures benefit both from core and shell functionalities. The shell functionalities include the presence of reactive sites, such as –NH₂ groups, for the attachment of targeting molecules for

drug delivery or sites for the adsorption of target molecules, such as groups aimed at the extraction of organic targets.¹³ However, synthesis routes play an important role in determining the properties of these structures thereby precise tuning of the multiple possible applications. Some of the common synthesis routes include selective etching or hard templating method,^{10,30,143,147,184} soft templating,^{88,215} and template-free methods.^{10,151}

Hard Template Method: Selective etching or hard templating method is the most common method for the synthesis of hollow spheres and nano rattles. As depicted in Figure 2.12, in a typical process, the core (eg. metal nanoparticles,¹⁷ oxides,²³ polymer²²⁴) is coated with one or a few layers of either the template material or the shell material or both. This coating can be done via the hydrolysis and condensation of silica,²⁴ seeded distillation-precipitation polymerization,⁴² or a hydrothermal reaction.³¹ Subsequently, the core or the template or the middle layer (shell) is selectively removed by dissolving them in a suitable solvent²²⁵ or via calcination²²⁶ leading to the formation of yolk-shell nanostructures. This approach can be used to remove the core or the shell partially from the core-shell nanoparticles or carry out a surface protective etching where the shell surface is protected and the inner layer of the shell or the outer layer of the core is removed.²⁰²

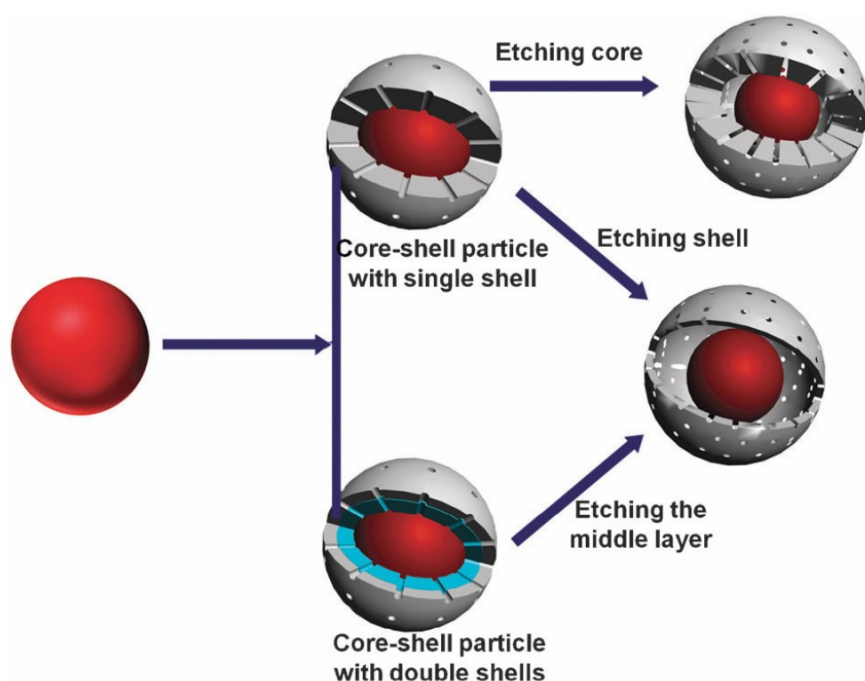


Figure 2.12 Selective etching strategies for the preparation of yolk-shell nanoparticles. Reproduced from Ref. 151.

Using the hard template method, Wu et al. demonstrated the multi-step preparation of Fe_3O_4 inside mesoporous silica spheres.²³ They coated hematite nanoparticles (Fe_3O_4) with sil-

ica precursors (TEOS and $C_{18}TMS$) and then the void between the core and the shell was obtained via ammonia etching of intermediate silica layer. Similarly, Linley et al. used silica as an intermediate layer in the synthesis of $Fe_3O_4@TiO_2$ yolk-shell nanostructures.²²⁷ The intermediate silica shell was later removed by hydrothermal treatment at $180^\circ C$. In another work done by Lee et al. they synthesised $Au@SiO_2$ yolk-shell nanostructures via selective etching of the silica shell from Au/SiO_2 core-shell particles (Figure 2.13).¹⁸⁴

The main advantages of the hard templating method are the tunability of the compartment and the scaling up of the synthesis. The size of the core, the void, and the wall thickness can be tuned by varying the synthesis parameters. Despite the fact that hard templating can be used to fabricate yolk-shell nanoparticles with controllable structures, sizes and compositions, this method has some inherent limitations as it involves long reaction time and multiple tedious steps, which often pose problems in the large-scale production of yolk-shell nanostructures. Moreover, with this method, it is quite tedious to encapsulate the hollow interior with guest molecules especially in biological applications.

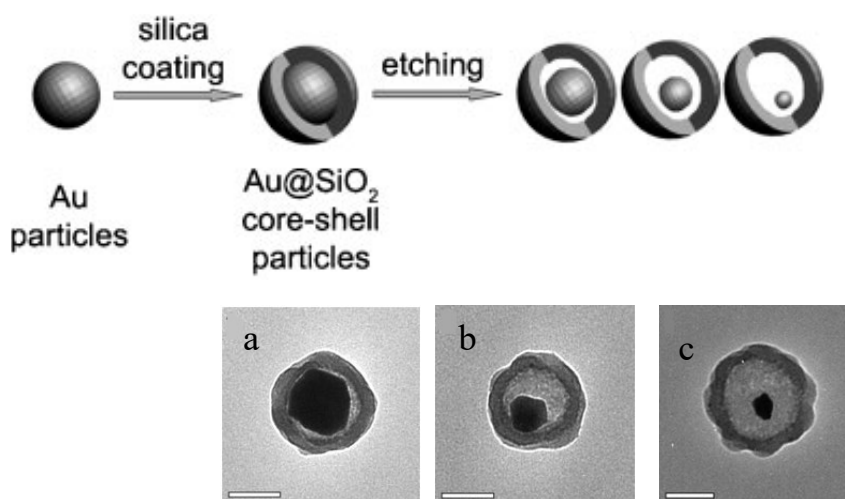


Figure 2.13 Synthetic procedure and corresponding TEM micrographs (scale bar 100nm) of $Au@SiO_2$ yolk-shell nanoparticle. Reproduced from Ref. 184.

Soft Template Methods: Soft templating has been widely used for the preparation of fine homogeneous inorganic hollow nanomaterials. It includes the use of microemulsions, surfactants, co-templates, and polymers as template materials to assemble inorganic nanomaterials. These materials may organise spontaneously into well-defined assemblies such as normal and reverse micelles, emulsions, vesicles, or liquid crystal phases, which restrict the noble metal nanoparticles as the core and the direct growth of metal oxide around the noble metal core.^{196,202} Among the different soft templating methods mentioned above, polymers constitute an important means of the soft template that can be used to prepare nano rattles with organic/inorganic shells. Li et al. used block copolymer as a soft template to construct $Au@TiO_2$ yolk-shell nanostructures.²²⁰

In a typical synthetic procedure, gold nanoparticles with poly(2-vinyl pyridine)-block-poly(ethylene oxide) (PVP-*b*-PEO) block copolymer shells were prepared by ultraviolet irradiation of a solution of PVP-*b*-PEO/HAuCl₄ complexes. Titania shell is deposited from the sol-gel reaction of titanium tetraisopropoxide on the surface of the Au@BCP core-shell. The polymer template was later removed by UV treatment to obtain Au@TiO₂ yolk-shell nanostructures.

In another work done by Wang et al. dealt with the synthesis of gold nanoparticle-loaded hollow mesoporous silica microspheres (Au@HMSM) (Figure 2.14).²¹⁵ The synthetic procedure deals with the encapsulation of pre-synthesized gold nanoparticle into PS-*b*-P4VP micelles. The silica shell was then deposited onto these micelles via sol-gel reaction. The polymer sacrificial template was removed by the calcination of Au@BCP@HMSM core-shell particles at 550 °C for 4 hours, which leads to the formation of Au@HMSM yolk-shell nanostructures. Soft-templating is useful for the synthesis of yolk-shell nanostructures with a porous shell but it is limited by the challenges in choosing appropriate template materials and the preparation of such macromolecular architectures.

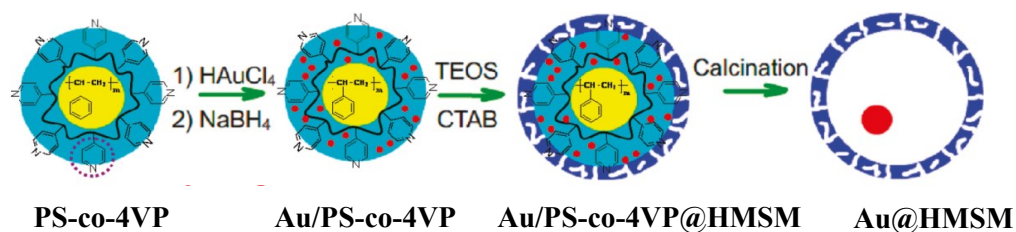


Figure 2.14 Stepwise synthesis of Au@HMSM yolk-shell nanostructures via a soft-template method. Reproduced from Ref. 215.

The other commonly used synthetic procedures involve the template-free synthesis methods such as Ship-in-bottle method,^{228,229} the Ostwald ripening method,^{177,230} Kirkendall diffusion method,^{34,164} and the Galvanic replacement method.^{35,222,223}

The Ship-in-Bottle Method: Through the ship-in-bottle method yolk-shell nanostructures with large cores can be formed via chemical reactions or self-assembly. Lou et al. were the first to prepare yolk-shell nanostructures through this method.²²⁸ They prepared silica yolk-shell nanostructures functionalized with multiple Au / Pt NPs. Shi and co-workers synthesised Fe₂O₃@SiO₂ and Fe₂O₄@C yolk-shell nanostructures using the ship-in-bottle method.²²⁹ At first, the iron nitrate solution was introduced into the hollow mesoporous silica spheres. The iron nitrate solution was transformed into hematite particles of the core via calcination resulting in Fe₂O₃@SiO₂ yolk-shell nanostructures. With the further introduction of furfuryl alcohol into the mesoporous channels of the shell, polymerization, carbonisation of poly furfuryl alcohol, the reduction of hematite into magnetite particles and the removal of silica template results in the formation of Fe₃O₄@C yolk-shell nanostructures.

Ostwald Ripening Method: It is a physical phenomenon which involves recrystallization process in solution. Liu and Zeng synthesised ZnS yolk-shell nanostructures by symmetric Ostwald ripening method.¹⁷⁷ They first assembled tiny ZnS nanocrystallites into solid spheres. Then, the loosely packed crystallites on the outer surface of the particles act as seeds for the recrystallization process. With the consumption of the crystallites from the inner layers and the recrystallization of shell creates a void inside. Adopting the symmetric and asymmetric Ostwald ripening method more complex internal structures can be achieved.

Kirkendall Diffusion Method: Kirkendall method involves the mechanism of void formation at the interface between different materials due to different interdiffusion rates in a bulk diffusion couple. Yin et al. were the first to employ the Kirkendall method to create hollow compound nanocrystals of cobalt oxide and chalcogenides (CoS and CoSe) with a size between 10-20 nm.¹⁶⁴

Galvanic Replacement Method: It is generally employed to fabricate metal nanostructures with controllable hollow interiors and porous walls.²²¹⁻²²³ The important step involves the replacement reaction between a suspension of nanoscale metal templates and a salt of a less active metal. This method can be used in fabricating gold-based hollow nanostructures with a wide range of morphologies including cubic nanocages, cubic nano boxes, triangular nanoring, single-walled nanotubes, prism-shaped nano boxes, and multiple-walled nanoshells or nanotubes. Huang et al. synthesised hydrophobic yolk-shell nanostructures with an alloy core of less than 20 nm in an organic solvent through the galvanic reaction between Au@AgNPs and HAuCl₄.²²³ The net flow of mass in one direction is balanced by a flux of vacancies which may coalesce into voids at the interface.

2.3.4 Characterization of Yolk-Shell Nanostructures

The Composition of the Yolk-Shell Nanoparticles: There are several methods to characterise yolk-shell nanoparticles by their composition. The best-suited method depends on the nature of the yolk-shell properties, such as crystallinity, magnetism, or luminescence. The presence of noble metal, such as Ag²¹⁶ and Au,^{160,231} can be detected by UV-Vis due to their surface plasmon resonance. The content of the metallic core in the yolk-shell nanoparticles can be determined by inductively coupled plasma optical emission spectroscopy (ICP-OES). The crystalline composition of yolk-shell nanoparticles is normally determined by X-ray diffraction (XRD),^{3,160} energy-dispersive X-ray spectroscopy (EDS or EDX),⁸ and wide-angle XRD.²³¹ But it is difficult to detect a few metal nanoparticles with XRD. In this case, the presence of metal nanoparticle can only be detected by UV-Vis spectroscopy.

In the case of yolk-shell nanoparticles containing organic residues, their content can be determined using various thermal analysis namely thermogravimetric analysis (TGA) and differential thermal analysis (DTA).^{23,30} Fourier transform infrared spectroscopy (FTIR) is generally used to detect functional groups that are present or attached to the surface of the

core.^{41,165,232} However, this technique cannot detect if they are present in a small amount. In the case of a core material containing $-NH_2$ as a functional group, Kaiser assay³⁰ or a fluorenylmethyloxycarbonyl (Fmoc)²³² quantification protocol can be used to determine their content. Rarely, some powerful methods such as UV-Raman spectroscopy,¹⁶⁵ ^{13}C cross-polarization magic angle spinning (CP-MAS),²³³ Nuclear Magnetic Resonance (NMR) spectroscopy,¹⁶⁵ and ^{29}Si CP-MAS NMR spectroscopy²³³ can also be used.

In the case of magnetic yolk-shell nanoparticles (those with Fe_3O_4 , Fe_2O_4),^{31,185} a magnetisation hysteresis loop is frequently measured. The presence of fluorescent dyes²³² and folic acid²³ can be detected by UV-Vis spectroscopy whereas FTIC²³² and luminescent particles such as Gd_2O_3 ³³ are measured by photoluminescence spectroscopy. The surface charge of the particles depends on the presence of functional groups³⁰ and coatings²³⁴ on them. This influences the zeta potential (ζ -potential) and the stability of the yolk-shell nanoparticles. In order to measure the ζ -potential, dynamic light scattering (DLS) is frequently used.^{234,235}

Proof of Core Encapsulation: Transmission electron microscopy (TEM) is the most commonly used method to confirm the yolk-shell morphology.^{30,152,232} As electrons transmit through the specimen, it is possible to distinguish between regions of varying electron density. It is well established that regions with higher electron density appear darker compared to those of lower electron density.²³⁶ In the case of $Ag@SiO_2$ yolk-shell nanoparticles, it is composed of a darker core and a brighter shell.²¹⁶ In situ TEM is used to study the progress of reactions by Liu et al.²⁹ They successfully used TEM to show the electrochemical lithiation of $Si@C$ yolk-shell nanoparticles and for monitoring the size expansion of the core.

Scanning electron microscopy (SEM) is usually used to study the morphology of yolk-shell nanoparticles. Although, under normal voltage, the core is normally invisible. Elevated acceleration voltages (5kV²³², 10kV³⁰) may enable visualisation of the core. In contrast to TEM, in SEM the more electron dense elements appear bright and less electron dense elements appear dark. EDS coupled with SEM or TEM is used to do elemental mapping (chemical composition) of yolk-shell nanoparticles. X-ray photoelectron spectroscopy (XPS) allows the characterization of surface composition with a detection depth limit of approximately 10 nm.²³¹

Surface Area and Porosity: Nitrogen adsorption-desorption isotherms allow the determination of the specific surface area (SSA) of the yolk-shell nanoparticles whereas the pore distribution can be estimated by the Barrett-Joyner-Halenda (BJH) method. The specific surface area is usually related to the size of the pore volume. This largely depends on the presence of molecules attached to or adsorbed on the surface. Liu et al. encapsulated magnetic iron oxide in mesoporous silica.³¹ The specific surface area of the yolk-shell nanoparticles was measured to be 494.5 $m^2 g^{-1}$ which decreased to 120.3 $m^2 g^{-1}$ after attachment of PEG and folic acid (FA) conjugates. Similarly, Kang et al. showed a gradual decrease in pore volume, surface area, and pore diameter as a result of step-wise loading of hollow mesoporous silica spheres with a thermoresponsive polymer ($Gd_2O_3: Eu^{+3}$) core, and subsequently with a drug.³³

2.3.5 Application of Yolk-Shell Nanostructures

Core-shell particles exhibit a strong electron transfer interaction between the core and the shell due to the maximised interfacial area of the nanoparticle core and the shell. Meanwhile, the yolk-shell structure comprises a nanoparticle core inside a hollow shell which allow the complete exposure of all active sites to be in contact with the reactant, whereas strong interactions between the metal core and the shell are maintained through physical or chemical contacts in the structure.¹⁰ Various combinations of the core and shell provide opportunities to tune not only the shell morphology but also chemical and physical properties of the system as a whole. Recently, yolk-shell structures are gaining a lot of interest as promising candidates for catalysis,^{151,204,237} lithium ion batteries,^{5,29,151,192} and in biomedicine.^{23,151,238}

One of the major applications of yolk-shell structures is their use as an anode material in lithium-ion batteries. Liu et al. have developed a yolk-shell structure which comprises the commercially available silica nanoparticles enclosed in a hollow carbon shell and proved that such an assembly can be used as an anode material with high capacity and long cycle life.²⁹ Moreover, the void between the shell and the core allowed the silica particles to expand freely without breaking the shell thereby stabilising the solid electrolyte interface on the shell surface.²⁹ Similarly, Sn@C yolk-shell structures have been integrated into a 3D nanofibrous conducting structures to use them as free-standing materials for gel-type lithium-ion batteries.²³⁹ Recently, Li et al. developed Al@TiO₂ yolk shells with tunable interspace and ultra-high capacity and long charging/discharging cycle life.⁵

Specially designed yolk-shell structures can be used as intelligent drug delivery vehicles due to their stability, controllable size, large hollow space, and good biocompatibility. Besides, both core and shell can be functionalized with desired functional groups to achieve controlled drug delivery and release. Yolk-shell structures with magnetic cores (Fe₃O₄ or Fe₂O₃ nanoparticles) have been shown to have a very high drug loading capacity and tested as a model system to deliver ibuprofen.²³⁸ Such structures possess enhanced drug loading capacities as well as significant magnetisation strength ($> 20 \text{ emu g}^{-1}$). Xu et al. studied the cytotoxicity of FePt@CoS₂ yolk shells and observed to have a high toxicity against HeLa cells.¹⁶³ In a similar study conducted by Y. Zhu et al. dealt with the cytotoxic effects of Fe₃O₄@SiO₂ loaded with Doxorubicin Hydrochloride (DOX) on HeLa cells.²⁴⁰ They found that the drug-loaded Fe₃O₄@SiO₂ exhibited relatively greater cell cytotoxicity than that free of DOX. As said earlier, with a combination of shell and the optical and/or the magnetic properties of the core, yolk-shell structures can serve both as an imaging agent as well as an anticancer drug.^{151,163,240-242}

The yolk-shell particles can be considered as nano-reactors when used for catalysis.^{3,184,203,243} The presence of the shell provides the nanoparticle with a homogeneous environment around and prevents their agglomeration and sintering. For example, Priebe et al. have shown the use of Ag@SiO₂ yolk shells as an effective catalyst for the degradation of Methylene Blue using sodium borohydride.¹³ Similarly, Au@SiO₂ yolk-shell structures were used as a model catalyst for the reduction of 4-nitrophenol in presence of sodium borohydride.¹⁸⁴ The

shell protects the catalyst core from leaching out. At the same time, the porous nature of the shell allows the reactants to come into contact with the catalyst. In general, catalytic nanoreactors should possess fast diffusion of reactants and products, a structure suitable to protect the enclosed catalyst and long-term stability. Moreover, the yolk-shell catalysts may possess catalyst selectivity. Ballauf and coworkers showed that Au@PNIPAM yolk-shell nanostructures possess catalytic selectivity for borohydride assisted the reduction of nitroarenes.²⁴⁴

The rate of diffusion can be controlled by tuning the shell porosity. Pore size and pore density can be altered by controlling reaction conditions during shell formation, by incorporation of porogen or by chemical etching. Lee et.al, demonstrated that precise structural and functional control can be made both to the shell and the core by chemical modification. They controlled the porosity of the silica shell by incorporation of a porogen upon shell formation. This altered the shell porosity which in turn improved the diffusion rate of reactants through the silica shells thereby enhancing the rate of the reaction. Also, they showed that by fine-tuning the surface functionality of Au@SiO₂ yolk shells, the catalytic activity can be varied.²² Further to varying the shell porosity varying the number of cores inside the shell could also bring significant changes in their catalytic activity.^{215,231}

3 EXPERIMENTAL

3.1 CHARACTERIZATION TECHNIQUES

3.1.1 Scanning Electron Microscopy (SEM)

Scanning Electron Microscope (SEM) uses an electron beam in a raster scan pattern to image a sample. The electrons interact with the atoms that make up the sample, producing signals which contain information about the sample's surface topography, morphology and chemical composition.²⁴⁵ (Additional instrumental details are discussed in Section 8.2.1.)

The samples for the SEM measurements were prepared by drop casting the respective dispersions onto silica wafers. The samples prepared on silicon substrates were viewed under the SEM without any additional coating. The cut wafers were pre-cleaned by sonication in ethanol and dried under nitrogen flow.

In order to study the frit surface and cross-section, the frit was broken into smaller pieces using a razor blade and a hammer. Suitable pieces were glued onto a SEM holder using a 2 component putty (UHU repair all power kit, UHU GmbH & Co KG, Bühl / Baden, Germany). A conductive connection was painted with a silver ink between the SEM holder and the frit piece. Finally, the whole assembly was coated with 20 nm conductive carbon layer using a carbon evaporator (Leica SCD500, Leica Microsystems GmbH, Wetzlar, Germany). The SEM images were recorded in NEON40 or Ultra 55 SEM (Carl Zeiss Microscopy GmbH, Germany). The EDX data were recorded with XFlash 5060 Spectrometer (Bruker Nano GmbH, Germany) in Ultra 55 SEM.

3.1.2 Transmission Electron Microscopy (TEM)

A Transmission Electron Microscope (TEM) works on the basic principle of a light microscope but uses electrons instead of light. Due to the significantly shorter wavelength of electrons (~2.5 pm at 200 kV) compared to visible light (400-700 nm), the angstrom resolution is reached, which is thousand times higher than in conventional light microscopes.²⁴⁶ (Additional instrumental details are discussed in Section 8.2.2.)

In the present work, Libra 120 (Carl Zeiss AG, Germany) operated at 120 kV was used to perform TEM imaging of prepared samples. Conventional and energy filtered TEM images (EFTEM) were obtained using Libra120 transmission electron microscope (Carl Zeiss Microscopy GmbH, Germany) equipped with an Omega type energy filter and operated at 120 kV. EFTEM imaging was performed by a 3-windows method using 20 eV window widths. For elemental mapping, K-ionization edges of N and C, and L23-ionization edge of Si were used. Specimens for TEM imaging were prepared by drop-casting ca. 5 μ L of sample dispersed in an appropriate solvent on the carbon coated copper grids and allowed to dry on a bloating paper.

3.1.3 UV-VIS Absorbance Spectroscopy

The absorbance of light is a phenomenon which involves the energy transfer from light to matter most in the form of thermal energy. Electromagnetic waves in the ultraviolet (200 - 400 nm) and visible range (400 - 800 nm) are able to induce electronic transitions in molecules.²⁴⁷ Most absorption spectroscopy of organic compounds is based on transitions of n or π electrons to the π^* excited state. This is because the absorption peaks for these transitions fall in an experimentally convenient region of the spectrum (200 – 700 nm).²⁴⁸ UV spectroscopy obeys the Beer-Lambert law which relates the absorbance of a solution to the concentration of the absorbing species by the following equation,

$$A = -\log \left(\frac{I_0}{I} \right) = \epsilon cl \quad (3.1)$$

where A is the absorbance, I_0 is the intensity of light incident on the sample cell, I , is the intensity of the transmitted light after passing through the sample, ϵ is extinction coefficient, c is the concentration of the absorbing species in the solution, l is the path length of the light through the sample.²⁴⁹ (Additional instrumental details are discussed in Section 8.2.3.)

In the present work, SPECORD 40 UV-Vis spectrophotometer (single beam, fixed slit width) was used to study the kinetics of catalytic reactions and performance of the catalyst, as well as for measuring of plasmonic spectra of samples containing silver and gold nanoparticles.

3.1.4 Dynamic Light Scattering (DLS)

Dynamic Light Scattering (DLS) is one of the most widely used techniques to study the properties of suspensions and solutions of colloids.^{250,251} Shining a monochromatic light beam on particles in Brownian motion results in Doppler shift as the light hit the moving particle. This, in turn, results in changing the wavelength of the incoming light. This change can be related to the size of the particle. From the diffusion coefficient, the size of the particles can be determined from Stokes-Einstein equation:

$$d_{(H)} = \frac{kT}{3\pi\eta D} \quad (3.2)$$

where $d_{(H)}$ is the hydrodynamic particle diameter, D – translational diffusion coefficient, k – Boltzmann constant, T – absolute temperature, and η – viscosity.²⁵² (Additional instrumental details are discussed in Section 8.2.4.)

In this work, Dynamic light scattering (DLS) measurements were performed at 25 °C using Zetasizer Nano S (ZEN 1600, NIBS Technology, Malvern Instruments, UK) equipped with 4 mW He-Ne-laser (632.8 nm, scattering angle 173°).

3.1.5 Gas Adsorption Measurements

As a result of more reactive surface atoms, the solid surfaces attract gases, vapours and liquids to balance atomic forces. As a consequence of imbalanced surface energy, gas adsorption takes place where molecules from a gas phase (adsorbate) are taken up by a solid surface (adsorbent).^{253,254} The adsorbed gas molecules temporarily depart from the gas phase and form a film at the surface for a certain period of time and then return to the gas phase. The duration depends on the nature of both adsorbent and the adsorbate. (Section 8.2.5.)

Here, the porosity of synthesised samples was analysed at the temperature of liquid nitrogen (77 K). N₂ adsorption experiments were carried out employing the automatically working absorptiometer Autosorb-1 (Quantachrome GmbH & Co. KG, Odelzhausen, Germany), which is a volumetrically operating instrument. The evaluation of the specific surface area was carried out according to Brunauer, Emmett, and Teller (BET) method. The pore size distributions were determined according to the Barrett-Joyner-Halenda (BJH) method for the mesopores and Saito-Foley (SF) method for the micropores.

3.1.6 Inductively Coupled Plasma Optical Emission Spectroscopy (ICP-OES)

ICP-OES is a trace level elemental analysis which uses the emission spectra of a sample to identify and quantify the elements present.²⁵⁵ The technique involves the introduction of sample solutions into the plasma that desolvates ionises and excites them. By identifying and quantifying the intensity of the characteristic emission lines, constituent elements can be identified.

The content of gold in Au@SiO₂@PSS catalyst was determined by using Agilent 5100 SVDV ICP-OES. Four portions of catalyst sample (ca. 10 mg each) were accurately (± 0.0001 mg) weighed and individually digested in 2 mL aqua regia. Each solution was adjusted to a total volume of 25 mL with Millipore water and further used for determination of gold content. To estimate the content of gold in the frit, Au@PS-b-P4VP micellar solution, Au@PS-b-P4VP@SiO₂ feed solution, as well as filtrate solution collected after the infiltration into P5 frit was analysed. For this purpose, 1.0 g of each solution was placed into a glass vial and solvents were evaporated on a rotary evaporator. The dried sample was digested in 2 mL aqua regia, heated for 1 h (boiling point). After cooling the solution was transferred to a volumetric flask. The solution was filled up to 25 mL with ultrapure water. This solution was measured with ICP-OES. All calibration procedure standard solutions were matrix matched.

3.1.7 Atomic Force Microscopy (AFM)

Atomic Force Microscope uses mechanical springs to sense forces and piezoelectric transducers for scanning.^{256,257} The AFM measures the forces acting on the tip and sample. (Section 8.2.6.) In the present work, tapping mode imaging was used to study the silica deposited BCP micelles. Height and phase images were simultaneously obtained using single beam

silicon tip with a resonant frequency of 60 – 70 kHz and a tip radius of ~ 10 nm. All the experiments were performed using Dimension 3100 AFM instrument (Digital Instruments, Inc., Santa Barbara, USA). The samples were prepared by drop casting from respective solutions onto pre-cleaned silicon wafers.

3.1.8 Thermogravimetric Analysis (TGA)

TGA is a technique which measures the amount of weight change of a material as a function of increasing temperature or isothermally as a function of time.²⁵⁸ Inorganic materials, metals, polymers and plastics, ceramics, glasses and composite materials can be analysed in the form of powder or small pieces.²⁵⁹ In the present work, samples were measured as a powder to detect the degradation temperature of the polymer. TGA measurements were performed using TA Q 5000 thermal analyser at a heating rate of 10 K / min in air.

3.2 CHEMICALS

Table 3.1 List of Polymers Used (All polymers were procured from Polymer Source Inc. Canada)

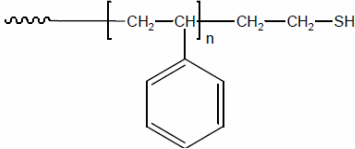
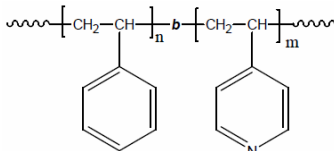
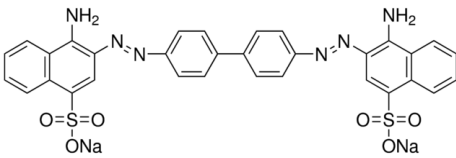
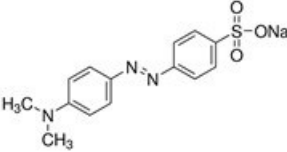
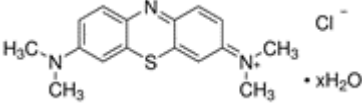
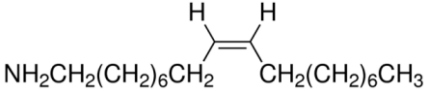
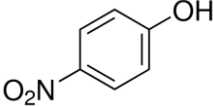
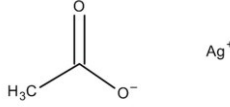
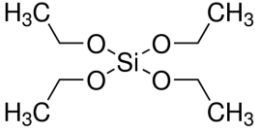
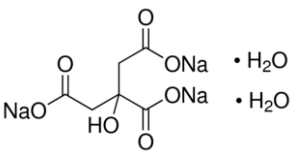
Polymer (Commercial Name)	Structure	$M_n \times 10^3$ g mol ⁻¹	PDI	ϕ / Functionality
PS-SH (P4430-SSH)		5.3	1.10	SH functionality > 95%
PS- <i>b</i> -P4VP (P9849-S4VP)		18.5- <i>b</i> -40.5	1.10	ϕ (P4VP) \approx 0.3 ϕ (P4VP) \approx 0.7

Table 3.2 List of Chemicals and Solvents

Name	Structure	M_w g mol ⁻¹	Supplier
Ammonium hydroxide (28 - 30 %)	NH ₄ OH	35.04	Fischer Chemicals
Congo Red (CR, \geq 35 % dye content)		696.66	Sigma Aldrich

Experimental

Ethanol (EtOH, absolute)	C_2H_5OH	46.07	VWR PROLABO
Hydrochloric acid (37 %)	HCl	36.46	Fischer Chemicals
Methanol (MeOH)	$\begin{array}{c} H \\ \\ H-C-OH \\ \\ H \end{array}$	32.04	Acros Organics
Methyl Orange (MO, 85 % dye content)		327.33	Sigma Aldrich
Methylene Blue (MB, ≥ 97 % dye content)		319.85	Sigma Aldrich
Millipore water (18.2 $M\Omega$ – cm at 25 °C)	H_2O	18.01	Pure Lab Plus®
Oleylamine (OlAm)		267.49	Sigma Aldrich
4 – Nitrophenol (4-NP, $\geq 99\%$)		139.11	Sigma Aldrich
Silver acetate, (AgAc, 99.99 %)		166.91	Sigma Aldrich
Sodium borohydride	$NaBH_4$	37.83	Sigma Aldrich
Sodium tetrachloroaurate (III) dihydrate, 99 %	$NaAuCl_4 \cdot 2H_2O$	397.80	Sigma Aldrich
Tetraethyl orthosilicate (TEOS, 98 %)		208.33	Sigma Aldrich
Tetraoctylammonium bromide (TOAB, 98 %)	$\begin{array}{c} CH_3(CH_2)_6CH_2 \\ \\ CH_3(CH_2)_6CH_2-N^+ \\ \\ CH_3(CH_2)_6CH_2 \\ \\ CH_3(CH_2)_6CH_2 \end{array} Br^-$	546.79	Sigma Aldrich

Trisodium citrate dihydrate (99 %)		294.10	Sigma Aldrich
Xylene	C ₈ H ₁₀	106.16	Acros Organics

3.3 SYNTHETIC PROCEDURES

3.3.1 Synthesis of PS-*b*-P4VP@SiO₂ Particles

The block copolymer micelles were prepared by dissolving the PS-*b*-P4VP block copolymer in chloroform to give a homogeneous dispersion at a BCP concentration of 0.5 mg mL⁻¹. It was then filtered through a 0.2 μm pore size PTFE membrane filter. In order to induce the micellization, a solvent exchange was done by adding an equivalent volume of methanol dropwise to the BCP solution in chloroform. The mixture was stirred for 1 hour. Next, both solvents were slowly removed on a rotary evaporator until constant mass was attained. The solid residue was redispersed in methanol to give a PS-*b*-P4VP micellar stock solution with a BCP concentration of 0.1 mg g⁻¹. It was then refluxed for 24 hours to obtain stable spherical PS-*b*-P4VP micelles in methanol. If required, the BCP concentration was adjusted by adding methanol (minor weight loss during reflux). The PS-*b*-P4VP micellar solution with the BCP concentration of 0.5 mg and 2.0 mg g⁻¹ were prepared by concentrating 0.1 mg g⁻¹ stock solution on a rotary evaporator to a desired residual mass.

Silica sol was prepared separately by mixing 1.2 mL of TEOS with 1.25 mL of methanol, 1.5 mL of deionized water, and 0.75 mL of 0.2 M aqueous HCl.²⁶⁰ The mixture was stirred for 30 min at room temperature and filtered through a 0.2 μm pore size PTFE membrane filter before mixing with the PS-*b*-P4VP micellar solution. Deposition of silica shell on PS-*b*-P4VP micelles was done by adding a measured amount of freshly prepared silica sol to a BCP micellar solution under stirring, maintaining a certain molar ratio between TEOS and 4VP. Upon completion of the reaction, the reaction mixture was collected and washed multiple times using ethanol at 13,500 rpm with a high-speed centrifuge. Then the collected sediment was dried in vacuum at 50 °C for 3 hours. The 4VP: TEOS ratio can be varied to attain particles with different morphologies. By removing the BCP template hollow silica particles can be prepared.

3.3.2 Synthesis of PS-stabilized Silver Nanoparticles (AgNP-PS)

Silver nanoparticles were synthesised using a method described by Hiramatsu with some modifications.²⁶¹ For the particular synthesis, 0.3 mmol of silver acetate (AgAc) was mixed with 2.5 mL of OlAm and injected to 50 mL of boiling xylene at 160 °C under the inert condition and refluxed for 24 hours. The colour of the mixture gradually changed from light yellow

to dark yellow, indicating the formation of silver colloids. OIAm simultaneously serves the function of both mild reducing agent and particle stabiliser.

In next step, 15 mL of the reaction mixture containing ca. 10 mg of as-synthesized silver nanoparticles were subjected to drying in a rotary evaporator to remove solvents. The dried nanoparticles were then dissolved in 5 mL of chloroform. Separately, 10 mg of PS-SH was dissolved in 10 mL of chloroform. The PS-SH solution was then added to silver nanoparticle dispersion in chloroform drop by drop under continuous stirring. Next, 5 mL more chloroform was added to the AgNP/PS mixture and left to stir for 24 hours. Thereafter PS-coated AgNP was flocculated by adding 10 mL of methanol and centrifuged at 13,500 rpm for 10 minutes. To remove the rest of OIAm and excess of PS-SH, repeated (6-8 times) centrifugation/redispersion steps were performed by adding chloroform as a solvent (ca. 5 mL) and methanol as flocculating agent (ca. 10 mL for each step). The final product was collected and dried in vacuum oven at 50 °C overnight to give a fine metallic powder of ca. 11 mg. Finally, PS-capped AgNP were dissolved in chloroform to give a stock solution, which has been used for further experiments.

3.3.3 Synthesis of PS-stabilized Gold Nanoparticles (AuNP-PS)

Gold nanoparticles coated with stabilising polystyrene (PS) shell was synthesised via two-step method. In the first step, water-soluble AuNP stabilised with citrate ligand were synthesised using a similar procedure described by Brown et al. with some modifications.²⁶² In the typical synthesis, 0.27 mmol (107.4 mg) of sodium tetrachloroaurate (III) trihydrate was added to a flask with deionized water. After one minute, 11 mL of aqueous solution of 1.0 wt. % trisodium citrate was added. Another 30 s later, 5.5 mL of freshly prepared ice-cold aqueous solutions of 0.08 wt. % sodium borohydride and 1.0 wt. % sodium citrate was quickly injected. The resulting volume of the reaction mixture was 500 mL. After 10 minutes of stirring, the solution was cooled down to room temperature.

To modify AuNP surface with PS shell, ligand exchange step was implemented. Tetraoctylammonium bromide (TOAB) was used as phase transfer agent, whereas thiol-terminated polystyrene was used as polymer ligand. In a typical experiment, 50 mg of TOAB was dissolved in 50 mL chloroform. Separately, 10.6 mg PSSH (double excess relative to the Au⁰ by weight) was dissolved in 10 mL of chloroform and mixed with the TOAB solution. Then this mixture was added to a separation funnel containing 50 mL of aqueous solution of citrate-stabilized AuNP. The two-phase mixture was shaken intensively until the upper aqueous phase appeared colourless. Organic phase with gold nanoparticles was separated and concentrated on rotary evaporator to the volume of ca. 10 mL. The reaction mixture was left under stirring for the next 24 hours at RT to ensure exchange of TOAB with PSSH. PS-stabilized Au nanoparticles were flocculated by adding 100 mL of ethanol, collected by centrifugation and then purified by repeated centrifugation/redispersion cycles with ethanol and, subsequently, with acetone (three cycles with each solvent). After removal of excess of TOAB and PS-SH, PS-capped gold nanoparticles were transferred into a vial, dried at 50 °C in a vacuum oven overnight. Finally,

PS-capped AuNP was dissolved in chloroform to give a stock solution, which has been used for further experiments.

3.3.4 Synthesis of Ag@SiO₂ and Au@SiO₂ Yolk-Shell Nanostructures

Enclosing Metal Nanoparticle within the Core of Block Copolymer Micelles: For enclosing AgNP or AuNP in micellar cores of PS-*b*-P4VP micelles, 10 mg of PS-*b*-P4VP was first dissolved in 50 mL chloroform and mixed with a measured amount of PS-capped AgNP or AuNP stock solution in chloroform. For the preparation of Ag@SiO₂ yolk-shells, the weight percentage of AgNPs was kept 40% with respect to the BCP content whereas for the Au@SiO₂ yolk-shells AuNP weight percentage was kept 20% with respect to the BCP content. After mixing both components, the volume of the whole mixture was adjusted to ca. 100 mL by adding chloroform. Next, an equal amount of methanol (ca. 100 mL) was added. Both the solvents were then slowly evaporated on a rotary evaporator to induce micellization. After complete removal of solvents, the weighed residue was dispersed in 100 g methanol and made up to a BCP concentration of 0.1 mg g⁻¹. The thus prepared dispersion was refluxed for 24 hours. After reflux, a mixture of AgNP (or AuNP) and PS-*b*-P4VP in methanol formed a long-term stable micellar solution containing PS-stabilized nanoparticles enclosed within PS cores of PS-*b*-P4VP micelles was formed.

Preparation of Silica Sol: Silica sol was prepared by mixing tetraethyl orthosilicate (silica precursor) with ethanol, water, and catalyst. Sol-gel process can be carried out in the presence of an acid (HCl) or a base (NH₃), as a catalyst.²⁶³ Acid catalysed system results in a less cross-linked monolith structure whereas base catalysed system creates highly cross-linked colloidal particles. In the present work, acid catalysed sol-gel process was used by following a synthetic procedure discussed above (Section 3.3.1).

Synthesis of Ag@SiO₂ and Au@SiO₂ Yolk-Shell Nanostructures: For the preparation of Ag@SiO₂ and Au@SiO₂ yolk-shell nanostructures (nanoparticles) silica deposition was done by adding a measured volume of freshly prepared and filtered silica sol (2.4 mL, 4VP:TEOS 400mr) to 10 g of a micellar solution of Ag@PS-*b*-P4VP or Au@PS-*b*-P4VP and vigorously stirring for a certain period of time (from 2 hours to 24 hours) at room temperature. The reaction mixture was then centrifuged at 13,500 rpm for 10 minutes to collect the silica deposited particles. The unreacted reagents were washed out with ethanol by repeated centrifugation/redispersion procedure. The final product was collected and dried under vacuum at 50°C for 2 hours. The thus prepared silica deposited particles were powdered and subjected to a stepwise pyrolysis at 450°C for 4 hours in order to remove the BCP template which leaves behind hollow mesoporous silica shell with metal nanoparticle as the core. The pyrolyzed sample was then collected, powdered, and dispersed in Millipore water at the desired concentration prior to its use as a catalyst.

3.3.5 Synthesis of Porous Silica-supported Yolk-Shell Catalyst (Au@SiO₂@PSS)

For the synthesis of Au@SiO₂@PSS catalyst, Au@PS-*b*-P4VP@SiO₂ particles were prepared using a protocol as discussed in Section 3.3.4, followed by one additional synthetic step purposed to convert unreacted silica precursor into porous silica support (PSS). In particular, 2.4 mL of freshly prepared silica sol was added to the 10 g of the Au@PS-*b*-P4VP micellar solution in methanol and allowed to react for 2 hours. After 2 hours the mixture was exposed to ammonia vapour for 48 hours to complete the hydrolysis-condensation of TEOS. The unreacted reagents were washed out with methanol by repeated centrifugation/redispersion procedure (10 min at 13,500 rpm). The obtained Au@PS-*b*-P4VP@SiO₂@PSS was dried under vacuum at 80 °C for 2 hours to yield a fine pink powder. To remove the block copolymer template, the Au@PS-*b*-P4VP@SiO₂@PSS powder was first ground with a mortar and pestle and subjected to oxidative step-wise pyrolysis at 450°C for 4 hours. The obtained powder was again fine powdered using mortar and pestle and dispersed in water at 2.0 mg mL⁻¹ concentration and further used as a stock solution for the catalytic experiments.

3.3.6 Fabrication of Flow-Type Catalytic Reactors by Infiltration of Au@PS-*b*-P4VP@SiO₂ in Porous Glass Frit

In order to prepare flow-type catalytic reactors, Au@PS-*b*-P4VP particles were prepared as described in Section 3.3.4. The Au@PS-*b*-P4VP micellar dispersion ($c_{\text{BCP}} = 0.1 \text{ mg g}^{-1}$) was mineralized via a sol-gel procedure. The silica deposition was done by reacting the micellar dispersion with silica sol for 2 hours, by maintaining a molar ratio between TEOS and 4VP as 400 mr. The thus prepared Au@BCP@SiO₂ particles were collected and washed with ethanol to remove the unreacted precursor, unbound oligomers, water, and HCl. Finally, particles were dispersed in ethanol to give a stock solution of 0.1 mg g⁻¹ (BCP mass based) and used for infiltration. The collected and washed, Au@PS-*b*-P4VP@SiO₂ particles were then infiltrated into porous glass frits (sintered glass frit discs, biplane, series 16, with a frit diameter, $d_{\text{(frit)}} = 2.0 \text{ cm}$, procured from ROBU) using a water jet vacuum aspirator pump with an end vacuum of 16 mbar and a flow rate of 400 mL h⁻¹. Prior to infiltration, the frits were washed multiple times with methanol and ethanol using the water jet vacuum aspirator pump. Frits were prepared with three different Au@SiO₂ particle loadings, namely 0.5 mg, 1.0 mg, 2.0 mg (BCP mass based), respectively, by infiltration of an appropriate amount of Au@PS-*b*-P4VP@SiO₂ dispersion in ethanol. The frits were then subjected to a stepwise pyrolysis in the air at 300°C for 6 hours to remove the block copolymer template and other organic residues present if any. Collected filtrate was kept for further analysis.

3.4 IN-SITU MONITORING OF SILICA SHELL FORMATION

The whole procedure was carried out in disposable DLS cuvettes without stirring. 1 g of the PS-*b*-P4VP micellar stock solution was added to a cuvette. Next, 227 μL of silica sol was added and intensively mixed for 20 s. The cuvette was placed in Z-sizer and continuous DLS

measurements were started. The interval between successive measurements was 2 min, whereas the time interval between addition of silica sol and the first DLS record was approximately 3.5 min which is the time required for mixing of components and temperature equilibration. The refractive indices and viscosity were set as specified for methanol ($n = 1.326$, $\eta = 0.5476$ cP) and polystyrene latex ($n = 1.590$). For each measurement point, ten autocorrelation functions of 10 s data collection time per scan were averaged and evaluated by the Dispersion Technology Software (DTS) appendant to Zetasizer Nano S. DTS includes cumulant analysis and multi-modal size distribution algorithm NNLS, which have been used for the calculation of hydrodynamic particle size, PDI, and particle size distributions.

3.5 CATALYTIC STUDIES

3.5.1 Catalytic Reactions using Ag@SiO₂, Au@SiO₂ Yolk-Shell Nanoparticles, and Au@SiO₂@PSS Catalyst

Catalytic experiments were carried out in a quartz cuvette (1 cm path length) under mechanical stirring at 400 rpm. Stirring was required to obtain reproducible results on reaction kinetics. Ag@SiO₂ and Au@SiO₂ yolk-shell nanoparticles were powdered and dispersed in Millipore water with a catalyst concentration of 0.02 mg mL⁻¹. Au@SiO₂@PSS catalyst was dispersed in Millipore water using an ultrasonic bath to give the stock dispersion with the catalyst concentration of 2.0 mg mL⁻¹. A measured volume of catalyst dispersion (from 0.02 to 0.5 mL) was added to a mixture of freshly prepared aqueous solution of NaBH₄ (0.9 mL, 0.2 M), aqueous solution of 4-NP (0.3 mL, 0.2 mM) and Millipore water (from 0.5 to 0.98 mL), such that total volume of the reaction mixture in all experiments was kept constant (2.2 mL). Successive UV-Vis spectra were recorded every minute in the wavelength range 250-700 nm immediately after addition of the catalyst. For Ag@SiO₂, Au@SiO₂, and Au@SiO₂@PSS catalysts, evaluation of the reaction kinetics was done by monitoring the intensity change of nitrophenolate absorption peak ($\lambda_{\text{max}} = 400$ nm) with respect to the time. Experiments on the catalytic degradation of Congo Red using Au@SiO₂@PSS catalyst were carried out maintaining experimental conditions similar to those for 4-nitrophenol. Evaluation of reaction kinetics was done by monitoring the intensity change of absorption peak at 498 nm with respect to the time. Similar experimental conditions were maintained for studying the catalytic degradation of Methyl Orange and Methylene Blue and the evaluation of the reaction kinetics was done by monitoring the intensity change of absorption peak at 464 nm and 664 nm respectively.

3.5.2 Continuous Flow Catalytic Studies

Continuous flow catalytic experiments were carried out by connecting the as prepared frit to a peristaltic pump and to a flow-through cell (1cm path length). A peristaltic pump (Ismatec REGLO Digital 2/6 Variable Speed Pump with a flow rate range of 0.005 to 59 mL min⁻¹ operating at 115V/230V) was used to maintain a continuous flow through the frit and control the flow rate. The frit was placed into a self-designed holder and the cap of the holder with inlet

opening was tightened to the frit head with a silicone rubber gasket using screws. The feed solution was fed to the pump which in turn channelled to the frit followed by the cuvette and outlet. The feed solution of Congo Red (0.067 mM) was prepared by diluting 100 mL, 0.2 mM solution of Congo Red with 200 mL of Millipore water. The feed solution was passed through the frit to ensure proper wetting of the embedded catalyst. After measuring the absorption spectra of Congo Red for 10 min, NaBH₄ was added as a powder to the feed solution. The amount of NaBH₄ was calculated and weighed such that the molar ratio between Congo Red and NaBH₄ will always be 3000. Successive UV-Vis spectra were recorded every minute in the wavelength range of 250-700 nm. Evaluation of the reaction kinetics was done by monitoring the intensity change of the Congo Red dye at 499 nm with respect to time. Experiments on the catalytic degradation of Methyl Orange ($\lambda_{\text{max}} = 464 \text{ nm}$), and 4-nitrophenol ($\lambda_{\text{max}} = 400 \text{ nm}$) were carried out maintaining the experimental conditions similar to those for Congo Red.

4 RESULTS AND DISCUSSION

4.1 IN-SITU MONITORING OF SILICA SHELL FORMATION

4.1.1 Motivation

In the recent past, the synthesis of inorganic hybrid hollow nanostructures has gained a great interest in the field of chemistry and material science due to their low density, large specific area, temperature and mechanical stabilities, and surface permeability.⁸³ These hollow nanostructures have a wide variety of application in cosmetics, catalysis, coatings, composite materials, dyes, artificial cells, fillers, and in biomedical field to encapsulate drugs and imaging agents. Such hollow nanostructures can be synthesised via a multitude of techniques such as hard or soft templating, chemical etching, layer-by-layer (LbL) deposition, emulsion polymerization, etc.

Lately, much interest has been shed to using sacrificial templates for the synthesis of inorganic hollow nanostructures. Among the various templates, self-assembled block copolymer structures are often used for the synthesis of functional nanomaterials and possess many advantages.^{264–268} For instance, BCP has been used as templates for the fabrication of smart materials for drug delivery, controlled release materials, or porous catalysts.²⁶⁹ Self-assembled BCP structures can be stabilised by cross-linking one of the blocks and then disintegrated using an appropriately selected solvent to produce isolated hairy particles.^{270,271} Among the large variety of block copolymers available, those composed of reactive blocks, such as poly(2-vinyl pyridine) or poly(4-vinyl pyridine) attract much attention. Ease of complexation of reactive pyridine units with small molecules and metal precursors makes these BCPs promising candidate for the preparation of such functional nanostructures.^{272–275} The lone pair of electrons at the pyridine unit enables the coordination with other electron-deficient species or complexation with additives via hydrogen bonding.²⁷⁶ Moreover, in protonated or quaternized state 4VP units can electrostatically interact with charged molecules, particles, and substrates.²⁷⁷ The most widely used BCPs are PS-*b*-P2VP and PS-*b*-P4VP. Comparably high χ values for PS/P4VP pair allows the disassembly of the matrix forming components with selective solvent without affecting the shape of domains formed by the minority component.²⁷⁸

Wang et al. studied the formation of hollow silica microspheres via a sol-gel process by using PS-*b*-P4VP as a sacrificial template. Block copolymer micelles were created with a PS core and P4VP corona.²⁷⁹ The silica shell was deposited on the BCP micelles, which later removed by calcination. The reactive nature of the P4VP facilitates the hydrolysis-condensation reaction of the silica precursor (TEOS) on the outer shell of the micelle. The shell thickness can be changed by varying the TEOS: 4VP ratio.

Khanal et al. employed PS-*b*-P2VP-*b*-PEO triblock copolymer templates to create hollow silica nanospheres (Figure 4.1).⁸³ They first synthesised PS-*b*-P2VP-*b*-PEO micelles, which has a glassy PS core, an ionizable hydrophilic P2VP shell, and a hydrophilic PEO corona. Due to the repulsive forces among the protonated P2VP chains, the P2VP shell extends at low pH (< 5).⁶⁰ The addition of anionic species into these micelles nullifies the positive charge of

the P2VP unit, resulting in a morphological change in the P2VP shell from an extended to a shrunken form.^{83,280} The authors explored these properties of the micelles to selectively deposit the silica shell on the P2VP block of the micelles via a sol-gel technique. The protonated P2VP chains act as an acid catalyst site for the hydrolysis of the silica precursor (tetramethoxysilane) and the negative charge of the silica at pH 4 helps them to strongly bind to the protonated P2VP block. The block copolymer micellar template was later removed by calcination to obtain hollow silica nanospheres.

They have concluded that utilising the reactive nature of the block copolymer templates, inorganic nanospheres can be prepared by selectively depositing the inorganic material in the targeted micro-compartment of the triblock copolymer micelle. It was also stated that the void volume of the hollow particle can be controlled by the size of the micellar core. Moreover, the shell thickness of the nanospheres can be varied by changing the concentration of the silica precursor during the sol-gel reaction.

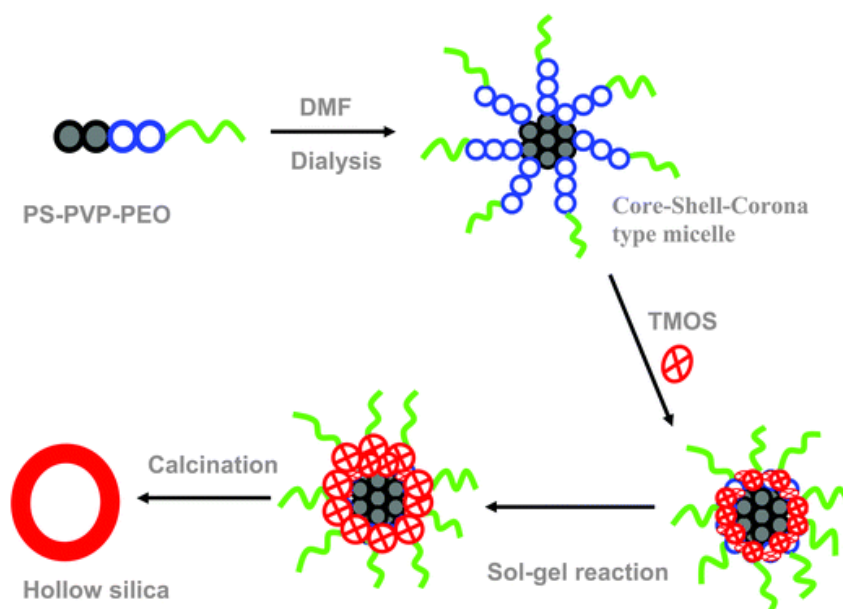
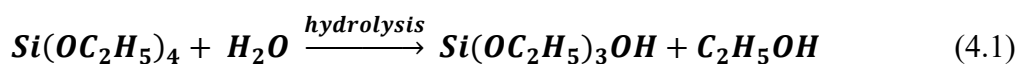
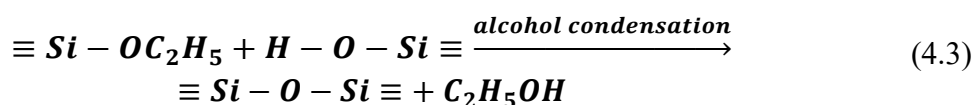
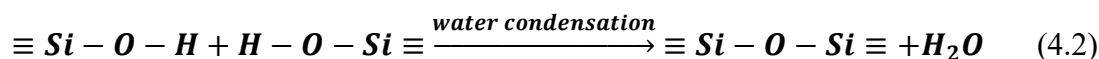


Figure 4.1 Fabrication of hollow silica nanosphere from PS-*b*-P2VP-*b*-PEO micelle template. Reproduced from Ref. 83.

Sol-Gel Process: It involves the hydrolysis and condensation of a silicon alkoxide (eg. Tetraethylorthosilicate) in presence of an acid or a base, as a catalyst.²⁶³ Acid catalysed system results in a less cross-linked monolith structure whereas base catalysed system creates highly cross-linked colloidal particles. The general process of hydrolysis and condensation of the silicon alkoxide leading to the formation of silica particles, taking tetraethylorthosilicate as an example, are as follows:





Hydrolysis of alkoxide groups results in the formation of silanol groups while the condensation or polymerization between silanol groups or between silanol groups and ethoxy groups results in siloxane (Si-O-Si) bridges. Condensation can be increased by applying temperature or by increasing the H^+ content whereas, an increase in water content results in reduced condensation.

The kinetics and mechanism of acid or base catalysed sol-gel reactions depend on the temperature, pH, type of catalyst, and composition of the reaction medium.^{281,282} The rate of condensation is very slow at pH closer to the isoelectric point whereas the gelation time is high and increases with an increase of precursor/solvent ratio. Thus, changes in pH and/or composition of reaction medium affect the kinetics and mechanism of the sol-gel process and subsequently alter the properties of the formed silica particles. Silica particles synthesised using different acid catalysts will also differ in size and morphology. In general, the pathways, stages, and mechanisms of sol-gel processes are well studied as for today. If the sol-gel reaction is carried out in the presence of templates, it might be much more complex, especially if such templates are “reactive” with respect to the sol-gel components. In the present work, PS-*b*-P4VP block copolymer micelles were used as templates for silica shell formation. The aim of this study was to understand the mechanism of silica shell formation and possible pathways of the sol-gel process taking place in the presence of reactive BCP micelles. In particular, the main focus was shed on monitoring the silica shell formation around the block copolymer micelles using acidic silica sol as a precursor and PS-*b*-P4VP micelles as the reactive template using DLS technique.

4.1.2 Synthesis of PS-*b*-P4VP@SiO₂ Particles

In order to prepare the block copolymer micelles, asymmetric PS-*b*-P4VP block copolymer with PS block as minority component with $M_n(\text{PS}) = 18,500 \text{ g mol}^{-1}$, $M_n(\text{P4VP}) = 40,500 \text{ g mol}^{-1}$, $\text{PDI} = 1.10$, $\phi(\text{PS}) = 0.3 \text{ vol. \%}$, $\phi(\text{P4VP}) = 0.7 \text{ vol. \%}$ was used. In P4VP selective solvents, such as methanol or ethanol, PS-*b*-P4VP forms micelles composed of collapsed PS core and swollen P4VP corona. Although PS-*b*-P4VP of this particular composition self-assembles into cylindrical morphology in bulk, the shape of BCP micelles in P4VP selective solvents might be altered from cylindrical to spherical by ageing or heating PS-*b*-P4VP micellar solution.

Figure 4.2 shows the steps involved in the synthesis of PS-*b*-P4VP@SiO₂ particles. PS-*b*-P4VP block copolymer with minor PS and major P4VP block acts as a structure directing component for deposition of silica shell. The PS-*b*-P4VP micelles were prepared via solvent

exchange method by adding methanol to the block copolymer solution in chloroform followed by the slow evaporation of solvents. Chloroform being more volatile evaporates faster. Thus, during slow evaporation of the solvent, the fraction of chloroform was gradually reduced, whereas the fraction of methanol gradually increased forming PS-*b*-P4VP micelles with collapsed PS core and extended P4VP corona. After the complete evaporation of solvents, the obtained residue was redispersed in methanol and refluxed to obtain stable spherical PS-*b*-P4VP micelles. Upon reaction with the silica sol, the extended P4VP corona gets protonated in the presence of acidic sol and acts as additional catalytic sites for hydrolysis-condensation reaction of silica precursor onto the PS-*b*-P4VP micelles. The procedure for the synthesis of PS-*b*-P4VP@SiO₂ particles is detailed in Section 3.3.1. The resultant sediment was then diluted to required concentration for microscopical as well as spectroscopical characterizations.

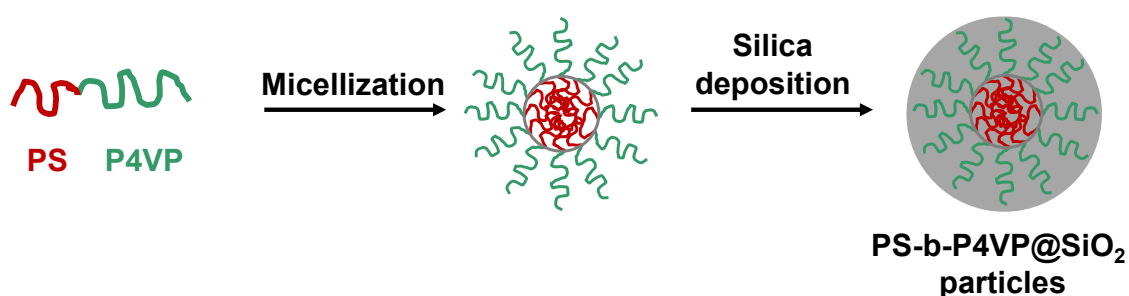


Figure 4.2 Schematic showing the synthesis of PS-*b*-P4VP@SiO₂ particles.

4.1.3 Effect of Processing Conditions on the Morphology of PS-*b*-P4VP@SiO₂

As mentioned earlier, the properties of the yolk-shell nanoparticles can be tuned by altering the shell properties. So it is very important to understand the effect of processing conditions on the morphology of PS-*b*-P4VP@SiO₂ particles. Effect of various processing conditions such as molar ratio of TEOS: 4VP, BCP concentration, and reaction time on the morphology and properties PS-*b*-P4VP@SiO₂ particles are discussed in the following section.

Effect of the Amount of Silica Precursor: In order to study the effect of varying the amount of silica sol on the morphology of PS-*b*-P4VP@SiO₂ particles, different amount of silica sol was added to the micellar solution whereas the BCP concentration (0.1 mg g⁻¹) and reaction time (24 hours) was kept constant. The silica sol content was estimated based on the molar ratio (mr) between silica sol precursor (TEOS) and 4VP units. The silica deposited nanospheres were then collected and washed several times with ethanol using a high-speed centrifuge at 13,500 rpm. The purified PS-*b*-P4VP@SiO₂ particles were re-dispersed in ethanol maintaining the initial concentration (0.1 mg g⁻¹). The particle dispersion was drop-casted on cleaned silica wafers and characterised using SEM without any additional coating.

Figure 4.3 shows the effect of the different amount of silica sol on the morphology of obtained PS-*b*-P4VP@SiO₂ particles. The particles formed at lower molar ratio shows an inhomogeneous particle distribution over the substrate surface where the particles appear aggregated and non-uniform in size (Figure 4.3 a, d). With the increase in molar ratio to 400 mr, more distinctly spherical particles with uniform size and shape with homogeneous particle distribution were observed. But with further increase in molar ratio, the particles were found to lose homogeneity by forming aggregates and networks though they still maintain their spherical shape (Figure 4.3 c, d and g, h). At higher amounts of silica sol, the excess silica precursor present in the acidic reaction medium might undergo further hydrolysis-condensation reaction leading to the formation of silica networks where PS-*b*-P4VP@SiO₂ are interlinked and enclosed within the networks. The formation of such aggregation can also be a partial contribution from the drying effect of solvent on the silica substrate, where the particles come closer upon solvent evaporation. However, it is unmistakable that the amount of silica sol plays an important role in controlling the homogeneity of the particles formed.

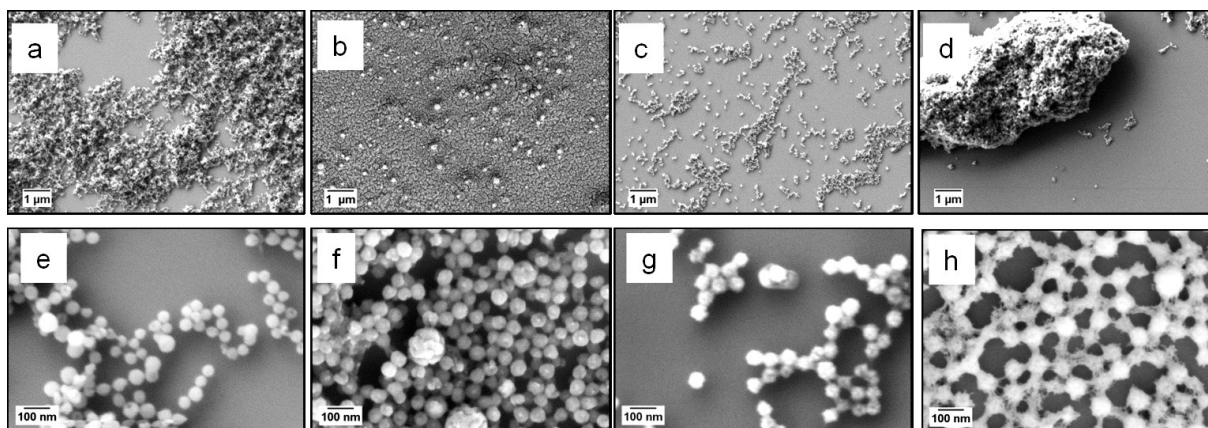


Figure 4.3 SEM micrographs showing the morphologies of PS-*b*-P4VP@SiO₂ particles obtained by sol-gel process in methanol at different TEOS: 4VP molar ratios: (a, e) 100mr; (b, f) 400mr; (c, g) 1000mr; (d, h) 4000mr. Scale bars are 1 μm (top) and 100 nm (bottom).

Effect of Block Copolymer Concentration: Another parameter that affects the morphology of PS-*b*-P4VP@SiO₂ particles is the block copolymer concentration. Micellar dispersion with three different PS-*b*-P4VP concentrations is used to study the effect of BCP concentration on the morphology of PS-*b*-P4VP@SiO₂. The TEOS: 4VP molar ratio was kept constant at 400 mr and the reaction time as 24 hours.

As can be seen from Figure 4.4, at a low BCP concentration of 0.1 mg g⁻¹, homogeneous particles of PS-*b*-P4VP@SiO₂ was obtained. With 0.5 mg g⁻¹ BCP concentration, the particles obtained seemed to be closely packed and slightly networked whereas at a high BCP concentration of 2 mg g⁻¹ a fully networked structure was obtained. Thus, by changing the PS-*b*-P4VP concentration, different morphologies varying from monodispersed homogeneous spheres to networks can be achieved.

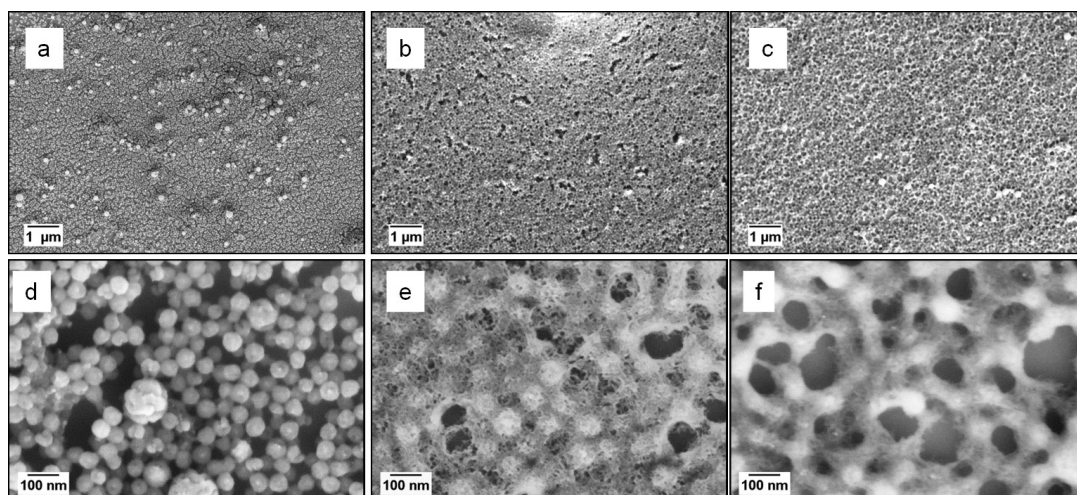


Figure 4.4 SEM micrographs showing the silica deposited PS-*b*-P4VP particle morphology in methanol at different block copolymer concentration: (a, d) 0.1 mg g⁻¹; (b, e) 0.5 mg g⁻¹; (c, f) 2 mg g⁻¹. Scale bars 1 μm (top) and 100 nm (bottom).

Effect of Reaction Time: The reaction time plays an important role in the silica shell growth around the block copolymer micelles. In order to study the effect of reaction time on the PS-*b*-P4VP@SiO₂ particles, the block copolymer concentration (0.1 mg g⁻¹) and the TEOS: 4VP molar ratio (400 m) was kept constant. The reaction time was varied from 6 hours, 24 hours, 48 hours, 72 hours, up to 192 hours as shown in Figure 4.5.

From the results obtained from the experiments done, it was observed that a BCP concentration of 0.1 mg g⁻¹ is optimum to obtain spherical particles without any aggregation and networking. But as shown in Figure 4.5, it is evident that longer reaction time with silica precursor plays a significant role in determining the particle morphology. At lower reaction time such as 6 hours, the particles formed appeared to be closely packed with localized aggregates (Figure 4.5 a, b). With the increase in reaction time more distinctly spherical particle with a uniform distribution was formed (Figure 4.5 c, d). But longer reaction time with silica precursor leads to the formation of a mixture of large and small particles, where the smaller particles have a coffee bean shape. The presence of such coffee bean shaped particles can be attributed to the additional nucleation and formation of silica particles without the polymer template.

Thus, from these experiments, it is very important to understand the effect of processing conditions on the formation of PS-*b*-P4VP@SiO₂ particles, as these parameters play a key role in determining the properties of the silica shell formed.

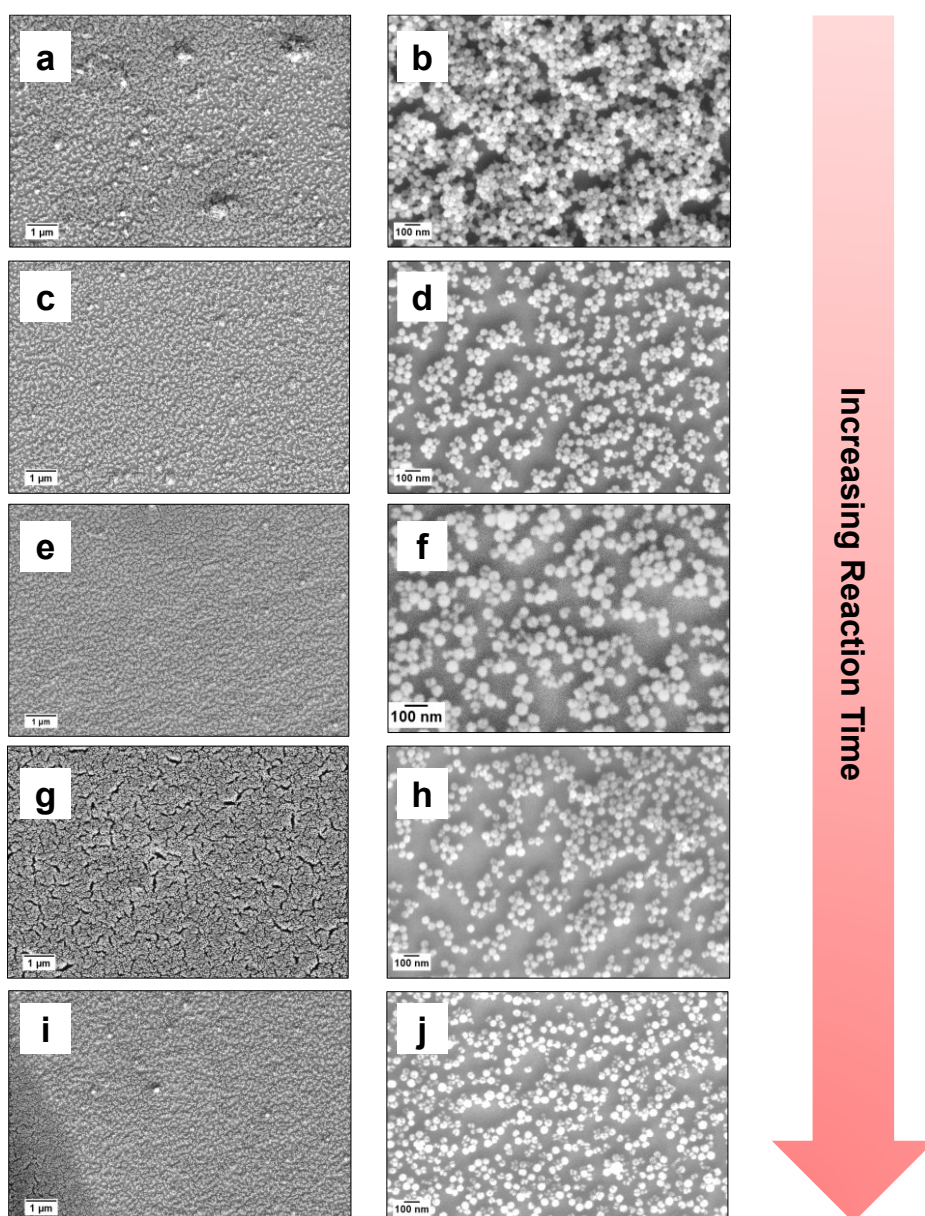


Figure 4.5 SEM micrographs showing the silica deposited PS-*b*-P4VP particle morphology in methanol at different reaction time: (a, b) 6 hours; (c, d) 24 hours; (e, f) 48 hours; (g, h) 72 hours; (i, j) 192 hours. Scale bars are 1 μm (left column) and 100 nm (right column).

4.1.4 Mechanism of Silica Shell Formation in the Presence of Reactive Block Copolymer Templates

The yolk-shell particles are prepared via the deposition of silica shell on a sacrificial block copolymer template. As described earlier, it is understandable that the properties of the yolk-shell nanoparticles depend on the characteristics of the shell such as thickness, morphology, its compactness and density. Thus, monitoring the shell formation during the reaction is very important in predicting and controlling the final properties of such particles. Therefore, a

thorough understanding of the sol-gel reaction taking place in the presence of such “reactive” templates is necessary for the synthesis of core-shell nanostructures with predefined characteristics and properties. Although the above-discussed results show that the processing conditions and different reaction parameters affect the formation of silica shell in presence of reactive template, the mechanism of silica shell formation over the BCP template is still unclear. Thus, in-situ dynamic light scattering (DLS) and transmission electron microscopy were combined to investigate the silica shell formation on top of PS-*b*-P4VP micelles and to understand the mechanism and pathways of the process.

Initial studies were conducted by coating the spherical PS-*b*-P4VP micelles, having a PS core and a P4VP corona, with silica shell forming PS-*b*-P4VP@SiO₂ particles. The thus prepared particles were separated from the reaction mixture at different time intervals during silica shell deposition. Then these particles were washed and re-dispersed in ethanol. Corresponding SEM, TEM, and AFM images and the height profile are represented in Figure 4.6 and Figure 4.7 respectively. The particle size was measured using DLS, as it is one of the most easily accessible and simple methods to study particle size.

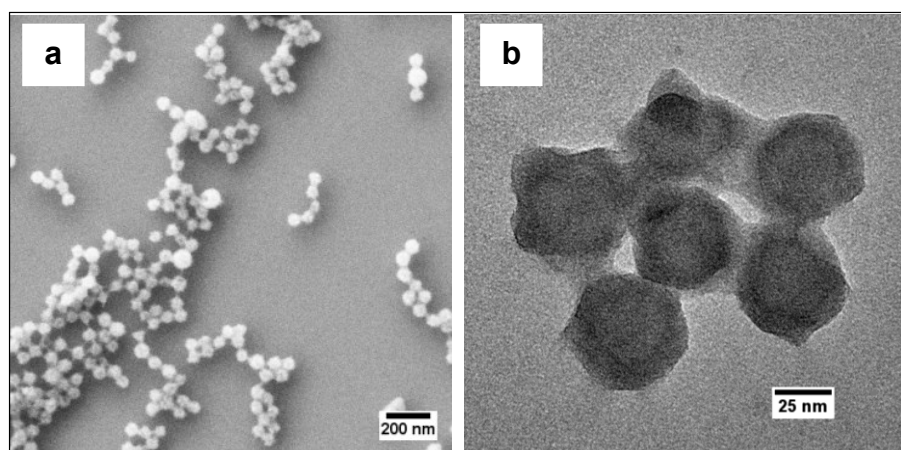


Figure 4.6 (a) Overview SEM; (b) Close view TEM images of PS-*b*-P4VP@SiO₂ particles isolated from the reaction mixture after 24 hours of shell formation. Scale bars on image (a) 200 nm; (b) 25 nm.

However, most of the DLS results obtained from isolated and re-dispersed particles were different from each other. When the PS-*b*-P4VP@SiO₂ particles were centrifuged and then re-dispersed, a considerable increase in the polydispersity index (PDI) and broadened size distribution were detected. This difference could be attributed to the presence of particle clusters and aggregates which are formed during the centrifugation step when particles are compactly packed. The SEM and TEM image (Figure 4.6 a, b) represents the PS-*b*-P4VP@SiO₂ particles which are isolated from the reaction mixture, centrifuged and re-dispersed. The isolated particles upon centrifugation settle down and form small aggregates which remain even after re-dispersion which is evident from Figure 4.6 (a, b). The AFM image (Figure 4.7 a) also shows the presence of aggregated particles. The height profile (Figure 4.7 b) reveals the polydispersity

of the system. These samples containing particle aggregates caused errors in the values obtained from DLS measurement which affected the quality of the results.

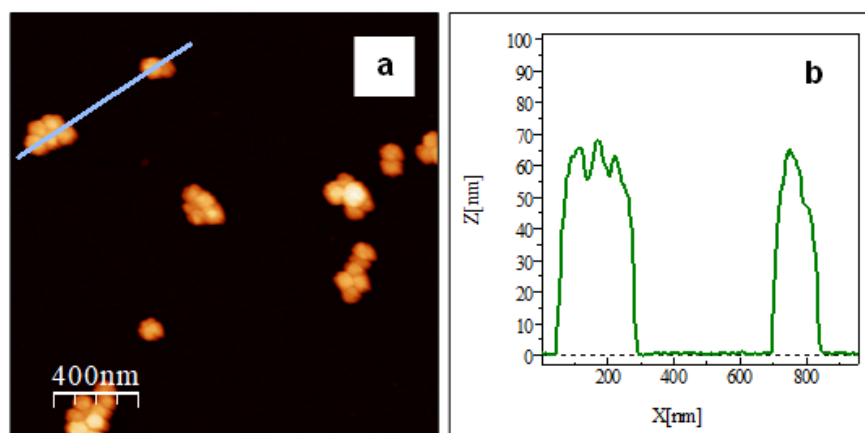


Figure 4.7 (a) Topography AFM images of PS-*b*-P4VP@SiO₂ particles isolated from the reaction mixture after 24 hours of shell formation; (b) Height profile of PS-*b*-P4VP@SiO₂ particles across the line on the AFM image (a).

In order to overcome the difficulties mentioned above, the DLS experiments were done in-situ to monitor the silica shell formation around the PS-*b*-P4VP micelles. Samples with respect to corresponding time were studied using TEM. Spherical PS-*b*-P4VP micelles were used as templates for monitoring the process with DLS. The PS-*b*-P4VP micelles were first measured and then a pre-determined amount of freshly prepared silica sol was added to the spherical micellar dispersion. The particle size evolution was monitored with DLS for a period of several days. However, due to the presence of several components (such as water, TEOS and products of hydrolysis and condensation) in the reaction mixture the particle size obtained from DLS experiments should be considered as apparently measured size (d_{app}), which differs from the actual hydrodynamic particle diameter (except for those referred for PS-*b*-P4VP micelles).

Figure 4.8 (a) shows the apparent size, d_{app} (cubes), and PDI (triangles) of the PS-*b*-P4VP micelle and PS-*b*-P4VP@SiO₂ particles as a function of time before (red) and after addition of acidic silica sol (black). The initial size of micelles was 126.7 ± 1.7 nm and PDI of 0.083 ± 0.017 . Immediately after the addition of acidic sol, d_{app} steeply increased up to 155 nm and then gradually decreased, reaching a plateau at ca. 15 hours after addition of sol. The particle size evolution was further monitored for a period of several days as shown in Figure 4.8 (b). After a gradual decrease until the plateau is established, the apparent particle size increased, but with a considerably slower rate as compared to the previous stage. Remarkably, the PDI remained unchanged within the same range (between 0.05 and 0.10) before and after silica sol addition, as well as after prolonged reaction time indicating that no clustering or particle aggregation occurs (Figure 4.8). From Figure 4.9, it is clear that the particle size distribution remains unchanged before and after addition of silica sol up to a few days indicating that there is no clustering or particle aggregation occurs.

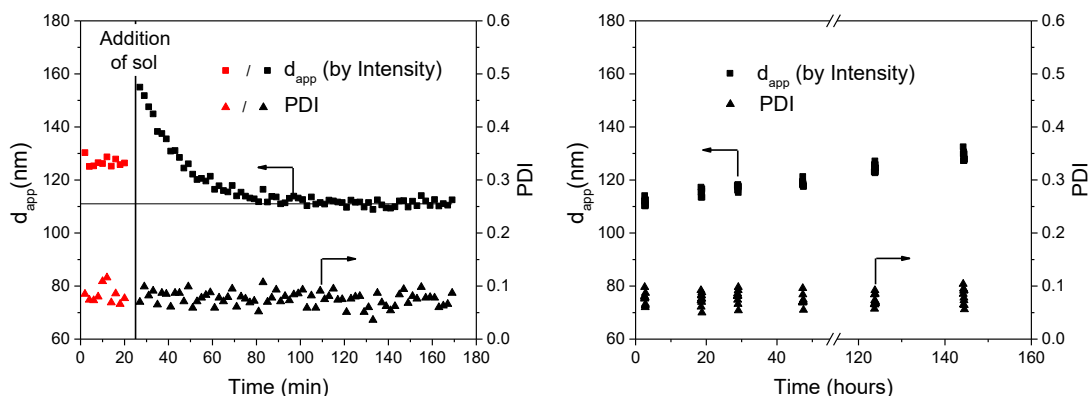


Figure 4.8 (a) Apparent particle size, d_{app} , (rectangles) and PDI (triangles) of PS-*b*-P4VP micelles in methanol (red symbols) and PS-*b*-P4VP@SiO₂ particles (black symbols) measured by intensity and PDI (triangles) as a function of time. The results were obtained by in-situ DLS during the initial period of silica shell formation; (b) Long-time behaviour of d_{app} (rectangles) and PDI (triangles) for PS-*b*-P4VP@SiO₂ particles obtained by DLS during the continuous sol-gel process.

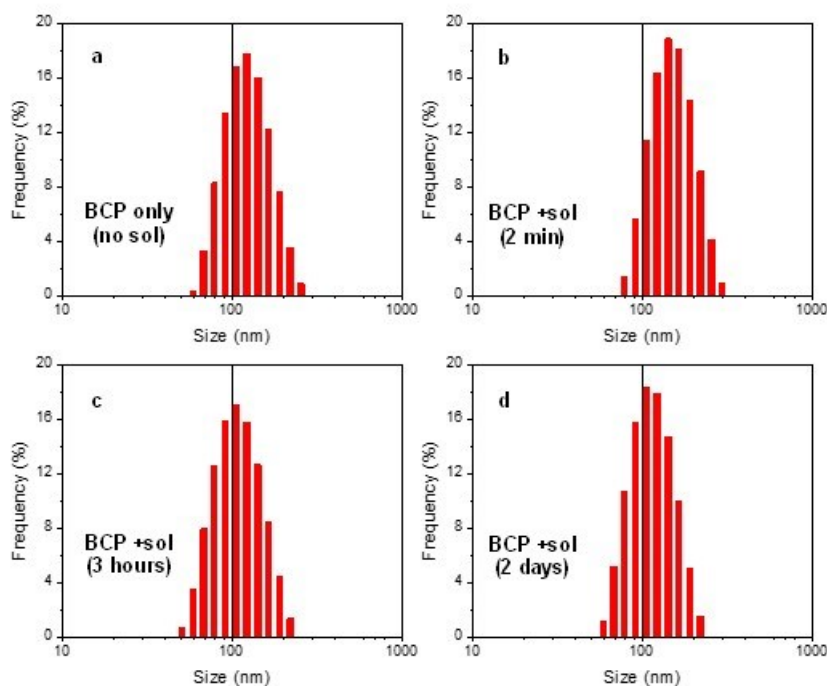


Figure 4.9 Intensity-average apparent particle size distributions (a) Before; (b-c) After addition of silica sol: (b) After 2 min; (c) After 3h (at a plateau); (d) After 2 days of silica shell formation.

The evolution of apparent particle size with time suggests that several simultaneous processes occur in the system. There are several reasons which may induce the initial step increase of the apparent particle size upon addition of acidic sol. First of all, due to the protonation of pyridine units and electrostatic repulsion, the neighbouring P4VP chains of the micellar corona are expected to stretch as compared to the initial state in methanol. In their protonated

form, P4VP chains become more hydrophilic. The protonated P4VP chains cause additional solvation of micellar corona, particularly with water present in the reaction mixture.^{283,284} Additional solvation and possible enrichment with water subsequently lead to an increased apparent particle size.

To obtain more details about the initial stage of silica shell formation, elemental analysis of PS-*b*-P4VP@SiO₂ particles immediately after addition of silica sol was performed. Figure 4.10 shows the TEM (a) and EFTEM (b-d) elemental maps of silicon, carbon and nitrogen of PS-*b*-P4VP@SiO₂ particles deposited from the reaction mixture immediately after addition of silica sol. As can be seen, at the early stage of shell formation, particles are surrounded by a silica-rich irregularly shaped corona. When particles are closely located with respect to each other, coronas merge suggesting their soft deformable nature.

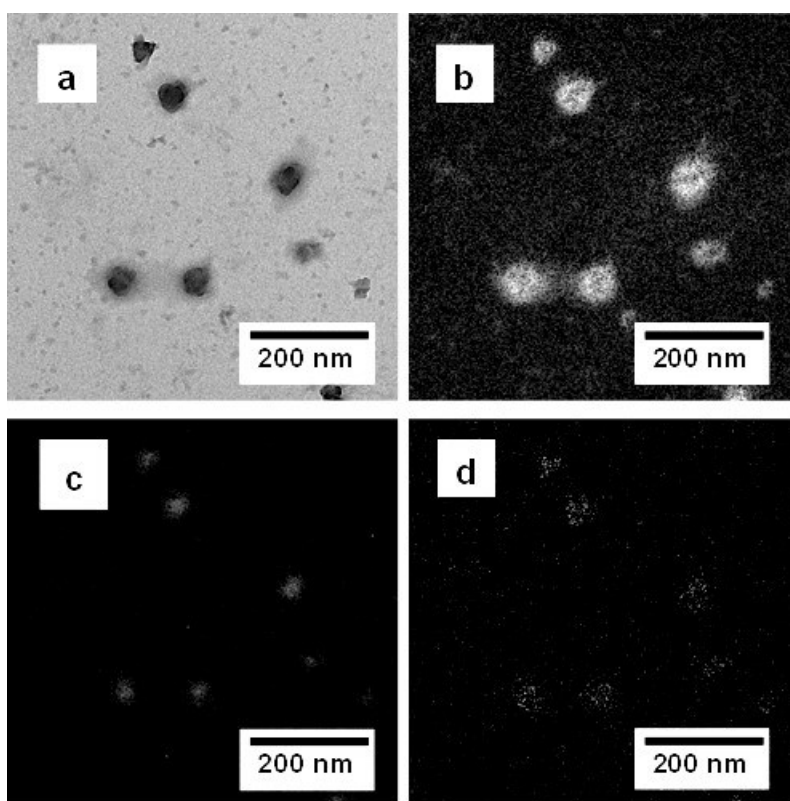


Figure 4.10 (a) Bright field TEM image; (b-d) Elemental maps of PS-*b*-P4VP@SiO₂ core-shell particles deposited from the reaction mixture on TEM grid immediately after addition of silica sol: (b) Si map; (c) Carbon map; (d) Nitrogen map. Scale bars are 200 nm.

The TEM and EFTEM results explain the initial steep increase of particle size after addition of silica sol as observed by DLS measurements. Upon mixing with PS-*b*-P4VP micelles, the silica sol accumulates immediately around protonated P4VP corona. Micelles surrounded by sol will diffuse slower as compared to BCP micelle, which subsequently leads to an increased apparent particle size. The presence of ions and the total ionic strength of the

medium are known factors affecting the particle diffusivity by changing the thickness of the double layer. Low ionic strength medium produces an extended double layer of ions around particles, reduces diffusion and results in a larger apparent hydrodynamic particle size. Higher ionic strength compresses the electrical double layer and hence, reduces the apparent hydrodynamic particle size. Finally, the presence of water, TEOS, and products of its hydrolysis and condensation affect the viscosity and refractive index of the reaction medium, which subsequently influences apparently measured particle size.

After the initial steep increase, the apparent particle size gradually decreases and then reaches a plateau. During this stage, template-directed hydrolysis-condensation of silica precursor determines the hydrodynamic behaviour of particles. Protonated and, plausibly, water-enriched P4VP coronas act as multiple catalytic sites for hydrolysis-condensation reaction. Under these conditions, condensation and subsequent networking of hydrolyzed precursor should be more probable. In other words, in the vicinity of PS-*b*-P4VP micelles, the sol-gel reaction occurs much faster as compared to the rest of solution.

The above-mentioned assumptions were further investigated by TEM images as shown in Figure 4.11. A substantial difference in particle morphology at the beginning of the shell formation (Figure 4.11 a, b) and after reaching the plateau (Figure 4.11 c, d) is clearly observed. A gradual decrease of the particle size observed by DLS can be explained as a result of locally accelerated condensation of sol and formation of a network like silica layer around PS-*b*-P4VP micelles. The latter, so far loose in nature, acts as a cross-linker and reduces the conformational entropy of P4VP chains. In addition, solvent molecules which initially occupy the P4VP corona are gradually replaced by condensing silica which is entropically favourable. Both effects increase the diffusion rate and subsequently reduce the apparently measured particle size.

Although the presence of the shell becomes quite well visible at the plateau, particles retain their irregular shape (Figure 4.11 d) indicating that at this stage the condensation process is still not complete. Expectedly, the increase of reaction time induces densification of the shell; in the following 15 hours, particles adopt well-defined core-shell morphology (Figure 4.11 e, f). Within this period, particles are slightly reduced in size. At this stage, the hydrodynamic behaviour of core-shell particles shows an opposite trend. After reaching the plateau, a continuous and slow increase of the apparent particle size was observed by DLS (Figure 4.11 b) which might be a result of the gradual change in properties of the reaction medium itself. When reaction time was increased further, the silica shell becomes smooth and more uniform (Figure 4.11 g and h). Moreover, during this time period, the shell continued to grow, as can be concluded from the appearance of an additional outer layer in Figure 4.11 (h).

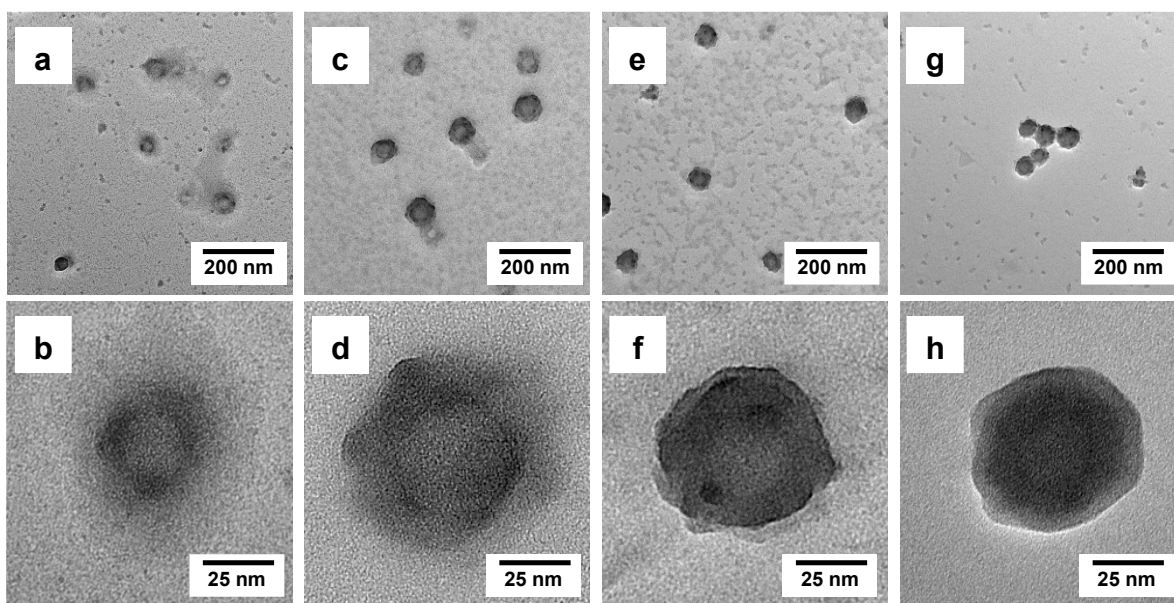


Figure 4.11 Overview (top) and high-magnification TEM images (bottom) of PS-*b*-P4VP@SiO₂ particles deposited from the reaction mixture on TEM grid: (a, b) Immediately after addition of silica sol; (c, d) After 3 hours; (e, f) After 18 hours; (g, h) After 2 days of silica shell formation. Scale bars are 200 nm (top) and 25 nm (bottom).

As can be seen, the changes of particle size monitored by DLS and observed by TEM show an opposite trend. According to TEM, particles adopt the largest size at the reaction stage which corresponds to the plateau region, i.e., when the PS-*b*-P4VP@SiO₂ particles have the smallest hydrodynamic size. In contrast to the results obtained from DLS, after reaching plateau particles appear visually smaller, while apparent hydrodynamic particle size increases. This contradiction can be explained as a result of two complementary effects: (1) an increased electron density of the SiO₂-rich but still loosely networked micellar corona leads to the visually larger particles (TEM); (2) networking and densification of the shell reduces the apparent hydrodynamic particle size (DLS). After reaching the plateau, the hydrodynamic particle size increases mainly due to the changes in the environment (changes in viscosity), whereas an actual increase of the particle size because of the shell growth is negligibly small.

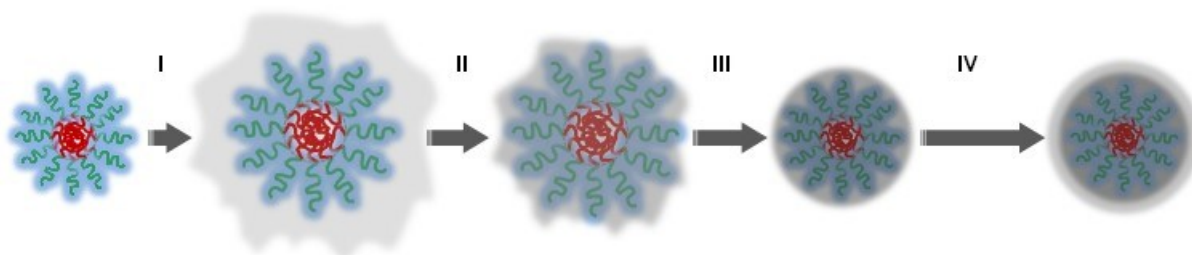


Figure 4.12 Schematics depicting four stages of silica shell formation using acidic sol-gel process and spherical PS-*b*-P4VP micelles as reactive templates. Reproduced from Ref. 322.

Based on the results discussed above, the whole process of silica shell formation and growth involves the following stages: (I) sol assembly around BCP micelles, (II) hydrolysis-condensation reaction accelerated by the protonated P4VP corona, (III) shell densification, and (IV) shell growth, as schematically shown in Figure 4.12.

4.1.5 Conclusion

The properties of the yolk-shell nanoparticles depend on the properties of the silica shell which is dependent on the processing conditions. Thus, it is really important to understand the formation of silica shell around the PS-*b*-P4VP micelles. The work conducted by Yang et al. demonstrated the synthesis of hollow silica particles through the sol-gel process of TEOS employing a quasi-hard template method using P4VP.²⁷⁹ The P4VP act as a reactive template to catalyse the sol-gel process which leads to the directed surface sol-gel process of TEOS on the template, thereby fabricating well-defined hollow silica spheres. The size of such spheres was studied using DLS and TEM. Similar works carried out by Wang et al. and Khanal et al. also shows the use of pyridine containing polymers such as PS-*b*-P4VP as a reactive template to fabricate hollow silica spheres.^{83,215} Although there were many works discussing the formation of silica shell through reactive templates, a thorough study on the mechanism of silica shell formation is yet to be conducted.

The present work mainly dealt with studying the effect of different processing conditions and the mechanism of silica shell formation through reactive templates. The whole process of silica shell formation on PS-*b*-P4VP reactive template was monitored in-situ using DLS. The results obtained revealed that the whole process of silica shell formation and growth involves 4 distinct stages starting from the sol assembly around the BCP template, followed by hydrolysis-condensation reaction accelerated by P4VP corona, shell densification, and finally shell growth.

Although the above-described results show the time evolution of the shell formation, they already provide distinctive and important information regarding the pathway, stages, and possible mechanism of the sol-gel process which takes place in the presence of reactive templates such as PS-*b*-P4VP micelles. Other parameters, such as pH, temperature, the amount and composition of added sol, the type of solvent are also expected to have an influence on the shell formation. The template method provides a direct way for the encapsulation of various “active” species, such as quantum dots or catalytically active nanoparticles, and fabrication of so-called yolk-shell particles. By quenching the reaction at a particular stage it should be possible to alter and tune the structure and properties of the shell, such as shell thickness and porosity, pore size distribution, shell permeability, and selectivity.

4.2 YOLK-SHELL NANOSTRUCTURES AS BIFUNCTIONAL CATALYSTS

4.2.1 Motivation

The importance of nanoparticles in the catalytic process has gained much interest in the recent times in order to design superior catalysts with improved efficiency and selectivity which could be used for minimising the use of fossil fuels, for energy harvesting, and pollution control. Noble metal nanoparticles, due to their totally different properties in the nano-regime, are the most widely studied system in catalysis. As the catalyst efficiency increase with an increase in surface area, nanoparticles are effective candidates due to their high surface area to volume ratio.²⁸⁵ Surface and strain drove lattice distortion, variation in electronic state density, and oxidation induced charge redistribution also add up to their use as an efficient catalyst.¹⁰ It was believed that gold nanoparticles were catalytically inactive until in 1997 Haruta and co-workers found the catalytic properties of gold nanoparticles and used them for oxidative reactions.²⁸⁶ The catalytic properties strongly depend on the surface properties, electronic structure, and particle size of the nanoparticle.²⁸⁷

Heterogeneous catalytic reactions occur on the surface of solid catalysts and involve elementary surface chemical processes such as adsorption of reactants from a reaction mixture, surface diffusion and reaction of adsorbed species, and desorption of reaction products (Appendix 8.1). The accelerated rate of surface-mediated reaction is due to the presence of highly reactive surface atoms which facilitates the bond breaking and rearrangement of adsorbed molecules.²⁸⁸ However, the major problem associated with virgin nanoparticles is their low dispersion stability and tendency to agglomerate which lowers the availability of accessible reaction sites, thereby lowering their efficiency. Agglomeration of nanoparticles can be minimised by modifying them with surfactants, low molecular weight ligands, polymers, dendrimers, or charged molecules. However, ligand-stabilized nanoparticles become catalytically less active or even inactive, again due to reduced accessibility of catalytically active sites for the reactants.

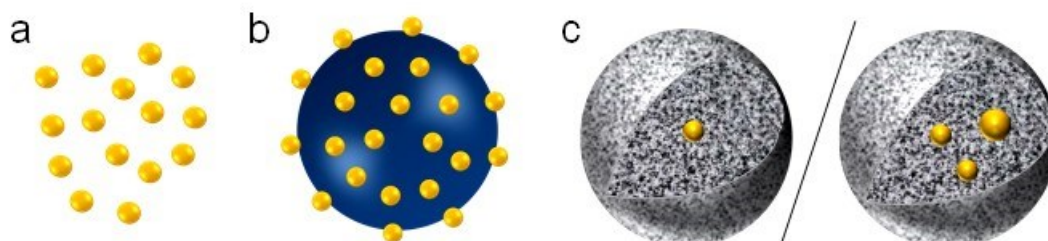


Figure 4.13 Schematic showing (a) Unsupported nanoparticles in dispersion; (b) Nanoparticles attached on the surface of the support; (c) Nanorattles or yolk-shell nanostructures.

The problems associated with particle stability without affecting their activity can be solved by a great deal using nanoparticles incorporated into secondary supporting structures. In order to increase the stability of the nanoparticles, functionalized polymers,⁸⁷ polyelectrolyte brushes,²⁸⁹ dendrimers,²⁹⁰ membranes,²⁹¹ and porous metal oxides^{151,292} have been employed to

support them either by attaching the particles on the surface of such supports or by enclosing them inside (Figure 4.13 b and c). Among the various supports used, numerous metal oxides of different structure and morphologies are promising candidates. For instance, catalytically active nanoparticles such as Ag and Au can be coated with a reactant permeable shell with tunable shell porosity.^{22,203} Controllable integration of noble metals such as Au,²⁴ Ag,²⁹³ Pt,²¹⁹ and Pd,²⁸ and metal oxide supports such as TiO₂,^{10,219} SiO₂,^{10,151,294} CeO₂,^{27,295} Co₃O₄,²⁹² ZrO₂,¹⁷ into a single structure, became a hot topic as they combine both the functions of individual nanoparticles and the shell. This enhances the catalytic properties when compared to single component materials. Moreover, such metal oxide support help to solve the problems associated with particle leaching, recovery, and dispersion stability to an extent.

These structures can be synthesised via impregnation,^{296,297} co-precipitation,²⁹⁸ or deposition-precipitation.²⁹⁹ The performance improvement can be attained by adopting more refined procedures such as confinement of noble metal nanoparticles into mesoporous supports,^{300,301} modifying the support,³⁰² by using alloys of nanoparticle instead of using a single nanoparticle,^{303,304} or by encapsulating the metal nanoparticles into supports with a core-shell structure.^{149,150,305–307} Depending on the synthetic route, different supporting structures (Figure 4.13) can be obtained. This includes core-shell structures where a single nanoparticle core is uniformly surrounded by a metal oxide shell; yolk-shell or rattle-type structures with a fixed/movable nanoparticle core enclosed inside a hollow metal oxide shell, and sandwich structures constitute multiple nanoparticles as an interlayer embedded into a metal oxide shell. Among which the yolk-shell nanoparticles have gained much attention in the recent past owing to their ability to alter their properties. Due to the presence of a hollow interior these structures can act as nanoreactors in the field of nanocatalysis. They can also be considered as a bifunctional catalyst.

Bifunctional catalysts, which contain catalytically active metal nanoparticles and a high surface area support, are basic structures that exhibit high activity and efficiency for significant chemical reactions. Apart from stabilising the nanoparticle, the support can act as a relay to transport reactants onto the catalytic surface, control the diffusion rates of reactants and products, and provide electrons or protons to modify total reactivity.²⁰³ The reactants diffuse through the hollow porous shell and reaction take place at the surface of the catalytically active nanoparticle core, which is the rate determining step and the product then diffuses out through the porous shell (Figure 4.14). Hence the porosity of the shell plays a key role in the efficiency of the catalysis process as a whole.

Metal oxide-based yolk-shell nanoparticles have shown high resistance against temperature or reaction induced sintering of nanoparticles, thus preserving the catalyst active. Their fine tunability of physical and chemical properties, as well as the functionality in both core and hollow shell, renders them with advanced properties. Yolk-shell nanoparticles are superior when compared to the existing structures with particle on supports as the former has no or minimal shielding effect of the core due to hollow space present. Enclosing the nanoparticles in a shell also prevents the leaching out of particles. Recently more focus has been shed to yolk-

shell nanoparticles with Ag or Au core since they have great potential application in catalysis, battery, surface-enhanced Raman scattering, and biomedicine.

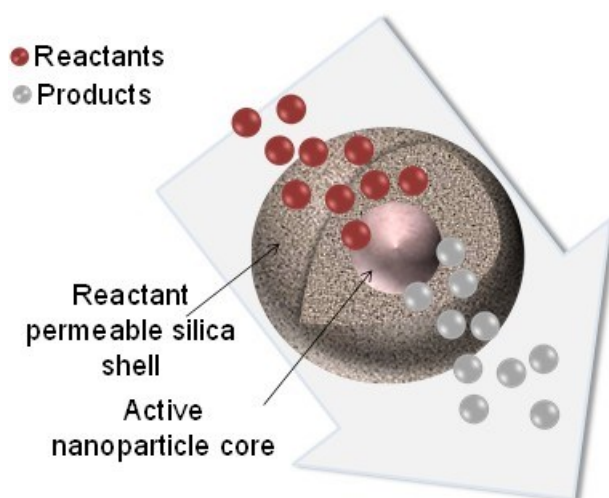


Figure 4.14 Yolk-shell nanostructure as a bifunctional heterogeneous catalyst.

4.2.2 Fabrication of Ag@SiO₂ and Au@SiO₂ Yolk-Shell Nanostructures

Here, the experimental work was focused mainly on the fabrication and application of Ag@SiO₂ and Au@SiO₂ yolk-shell type catalysts. Same procedures were done in order to synthesis both Ag@SiO₂ and Au@SiO₂ yolk-shell nanostructures. To obtain a yolk-shell nanostructure, for enclosing metal nanoparticles into porous silica shells, there are certain prerequisites: (1) metal nanoparticles (eg. AgNPs or AuNPs) should be completely covered by the silica shell i.e., metal nanoparticles should be large enough not to leak out through the silica shell pore, (2) silica hollow spheres should be homogeneously loaded with metal nanoparticle, (3) no bulky metal nanoparticle should be formed outside the nanocontainers, and (4) a void between the silica shell and AuNPs should be maintained.³⁰⁸ Figure 4.15 shows the general steps involved in the synthesis of Au@SiO₂ yolk-shells. Synthesis is accomplished in following steps: (1) synthesis and surface modification of nanoparticles (AgNP or AuNP); (2) entrapment of polymer-stabilized AuNP within the core of the block copolymer micelles; (3) deposition of silica shell to form Au@PS-*b*-P4VP@SiO₂ particles; (4) pyrolytic removal of the block copolymer template to attain silica enclosed metal nanoparticle yolk shells.

PS-*b*-P4VP block copolymer with minor PS and major P4VP block acts as a structure directing component for both encapsulation of metal nanoparticle and deposition of silica shell. As mentioned above, in P4VP-selective solvents PS-*b*-P4VP forms micelles with collapsed PS cores and swollen P4VP coronas. In order to encapsulate nanoparticles within the PS core of the PS-*b*-P4VP micelles, the nanoparticles were modified with SH functionalized PS ligands. The selective localization of nanoparticles to the PS core of the PS-*b*-P4VP micelles was done via a solvent exchange method. The PS-stabilized nanoparticle and the block copolymer were

first dissolved in chloroform, a common solvent for both components. Micellisation was induced by adding an equal amount of methanol which is a favourable solvent for the P4VP block. Upon removal of the solvents, chloroform being more volatile evaporates faster which results in an increased fraction of methanol in the system. This results in the formation of PS-*b*-P4VP micelles with a collapsed PS core and a swollen P4VP corona with nanoparticles selectively located in the PS core. The appearance of a slight turbidity during evaporation confirmed the initiation of micellization. To ensure that no chloroform remains, both solvents were completely removed and the solid residue was redispersed in methanol maintaining a block copolymer concentration of 0.1 mg g⁻¹. The Ag/PS-*b*-P4VP or Au/PS-*b*-P4VP mixture in methanol was refluxed for 24 hours to obtain stable spherical micelles of Ag@PS-*b*-P4VP or Au@PS-*b*-P4VP.

The stable micelles were deposited with silica shell from an acidic silica sol via an acid catalysed sol-gel process using TEOS as the precursor. The molar ratio between TEOS and 4VP was kept as 400:1. After the completion of the reaction (24 hours), the particles were collected by centrifugation and purified from unreacted silica sol by repeated washing with ethanol. The pyrolytic removal of the polymeric template led to the formation of Ag@SiO₂ and Au@SiO₂ yolk-shell nanoparticles. It is stated in the literature that pyridine rings in P4VP shells get protonated in the acidic sol medium and act as binding sites for negatively charged silica particles by forming cationic pyridine units.^{83,309} The protonated pyridine groups also act as a catalyst for the hydrolysis of TEOS favouring the further growth of silica structures. The silica shell was assumed to grow over and out of the P4VP corona leaving the polymer chains partially or completely merged into the silica matrix which contributed to additional shell porosity upon the pyrolytic removal of the BCP template. For characterization purposes, Ag@PS-*b*-P4VP@SiO₂ and Au@PS-*b*-P4VP@SiO₂ particles were collected by centrifugation and purified from the rest of the unreacted sol. A detailed synthetic procedure is discussed in Section 3.3.4.

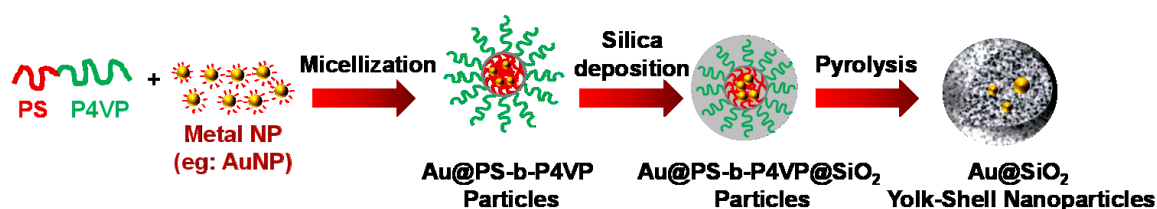


Figure 4.15 Schematic showing the synthesis of Ag@SiO₂ and Au@SiO₂ yolk-shell nanostructures.

4.2.3 Ag@SiO₂ Yolk-Shell Nanostructures

As an initial study Ag@PS-*b*-P4VP@SiO₂ particles were prepared. Silver nanoparticles (AgNP) were synthesized using protocol reported by Hiramatsu with some modification as described in Section 3.3.2.²⁶¹ As it was mentioned before, OAm acts both as a reducing agent and as a capping agent for stabilizing the particles. Commonly used capping agents to stabilize gold and silver are citrates, quaternary ammonium salts, mercaptans, or polymers. Using polymeric

ligands stable dispersions of nanoparticles can be obtained.³¹⁰ Moreover, by modifying the nanoparticles using polymers with suitable end group or side chain functionalities, metal nanoparticles can be incorporated into hydrophobic polymer domains.³¹¹ In the present work, the nanoparticles are to be selectively localised in the PS core of the PS-*b*-P4VP micelles (discussed below). Hence the particles are modified with thiol-terminated polystyrene. Because of the high affinity of thiols to metal nanoparticles, a strong bond between the particles and the thiol group is formed.³¹¹

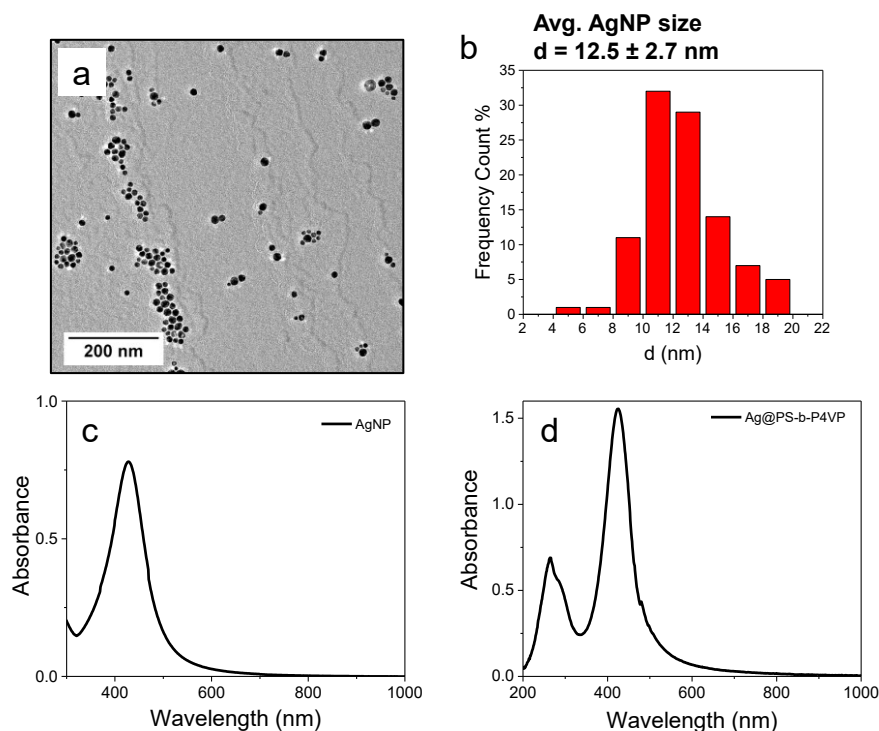


Figure 4.16 (a) TEM image; (b) Size distribution of as synthesised AgNPs; (c) UV-Vis spectrum of as synthesised AgNPs in xylene; (d) UV-Vis absorbance spectrum of Ag@PS-*b*-P4VP particles with AgNP of size 12.5 ± 2.7 nm in methanol.

TEM investigation of the obtained particles revealed the formation of uniform spherical shaped AgNPs with the size of 12.5 ± 2.7 nm and narrow size distribution (Figure 4.16 a, b). The AgNPs were then coated with polystyrene ligand in order to selectively encapsulate into PS cores of PS-*b*-P4VP micelles. The thus obtained Ag@PS-*b*-P4VP micelles in methanol were used as templates for the synthesis of Ag@PS-*b*-P4VP@SiO₂ particles. Ag@PS-*b*-P4VP@SiO₂ particles were prepared by the sol-gel method according to the modified protocol described in Section 3.3.4. Figure 4.16 c and d show the absorbance spectra of as synthesised AgNPs in xylene and Ag@PS-*b*-P4VP in methanol respectively.

The electron microscopy results (Figure 4.17) revealed the morphology of Ag@PS-*b*-P4VP@SiO₂. The bright spots in SEM image (b) (ESB detector) indicate an existence of inclusions inside of the micelles, which are attributed to the presence of silver nanoparticles inside silica coated BCP micelles. This was further confirmed by TEM imaging (Figure 4.17 c).

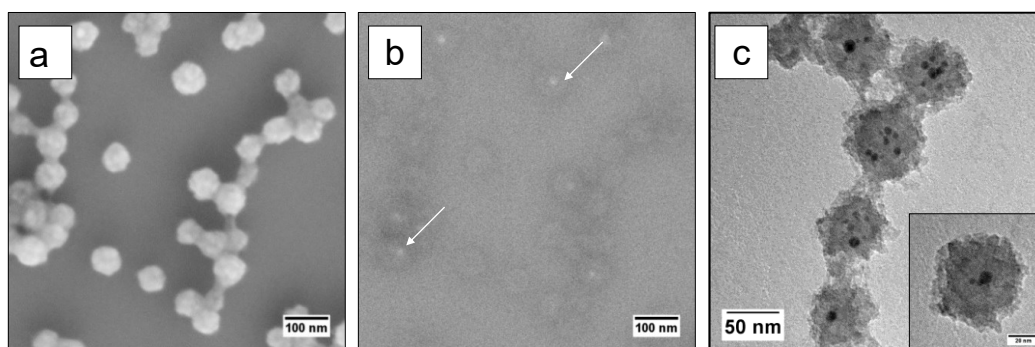


Figure 4.17 (a, b) SEM; (c) TEM micrographs of $\text{Ag@PS-}b\text{-P4VP@SiO}_2$ particles. The bright spots (indicated by white arrows) in the ESB (b) image and the black spots in the TEM (c) image shows the presence of AgNP inside the silica deposited block copolymer micelles. Scale bars on image (a, b) 100 nm; (c) 50 nm.

Thus prepared $\text{Ag@PS-}b\text{-P4VP@SiO}_2$ particles were then pyrolyzed in the air at $450\text{ }^\circ\text{C}$ for 4 hours to remove the PS-*b*-P4VP template. After pyrolysis, Ag@SiO_2 yolk-shell nanoparticles are formed having Ag cores enclosed inside hollow silica shell. These Ag@SiO_2 yolk-shells were then powdered, weighed, and dispersed in water. Next, Ag@SiO_2 yolk-shells were tested as a catalyst for borohydride reduction of 4-nitrophenol (4-NP), a model reaction commonly used to study various (nano)catalytic systems.³¹² Figure 4.18 shows successive UV-Vis spectra taken every minute for catalytic reduction of 4-NP in the presence of different amount of Ag@SiO_2 yolk-shell catalyst. As can be seen, the time required to achieve complete reduction of 4-NP progressively decreases upon increasing of Ag@SiO_2 content, as was expected.

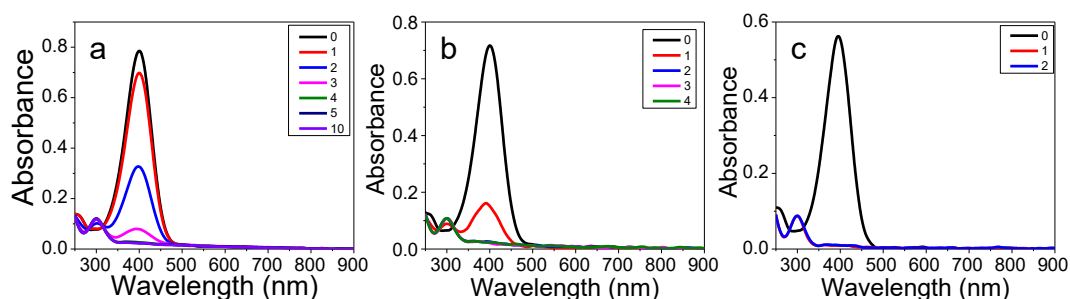


Figure 4.18 Successive spectra taken after every minute during borohydride assisted reduction of 4-NP after the addition of Ag@SiO_2 yolk shells showing the decrease in peak intensity of 4-NP with respect to increase in time. All experiments were carried out with initial concentrations $[4\text{-NP}]_0 = 0.027\text{ mmol L}^{-1}$ and $[\text{NaBH}_4]_0 = 0.081\text{ mol L}^{-1}$. Amount of Ag@SiO_2 in reaction mixture was: (a) $1.6 \times 10^{-3}\text{ mg}$; (b) $3 \times 10^{-3}\text{ mg}$; (c) $4 \times 10^{-3}\text{ mg}$. The total volume of reaction mixture in the cuvette was 2.2 mL.

However, based on TEM image analysis it was found that the size of AgNPs in $\text{Ag@PS-}b\text{-P4VP@SiO}_2$ sample (Figure 4.19) was reduced as compared to initially synthesized AgNPs (compare with Figure 4.16).

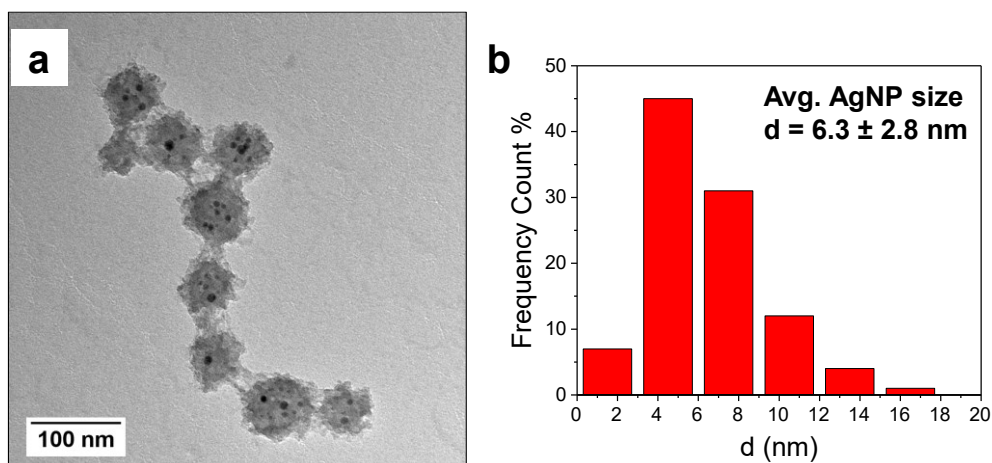


Figure 4.19 (a) TEM image of $\text{Ag@PS-}b\text{-P4VP@SiO}_2$; (b) Size distribution histogram of AgNPs obtained after 24 hours of silica shell deposition reaction time.

The reasons for such changes in particle size are discussed in the following section. From the literature, it is well-known that silver nanoparticles are prone to dissolution under specific conditions. Dissolution of AgNP occurs through the oxidation of metallic AgNPs to Ag^+ into the solution.¹⁸⁵ The release of silver ions depends on the intrinsic physicochemical properties of AgNP and properties of the solution as well. The parameters that influence the rate of AgNP dissolution include ionic strength, pH, dissolved oxygen concentration, temperature, dissolved complexing ligands (organic matter, sulphur, and chlorine), AgNP surface coating, shape, and size.^{313–317}

Figure 4.20 shows (a) UV-Vis spectra of $\text{Ag@PS-}b\text{-P4VP@SiO}_2$ particles collected from the reaction mixture after different periods of the reaction time and (b) relative intensity, A_t/A_0 , of silver plasmon peak at 420 nm versus time obtained upon silica shell deposition. The UV-Vis spectra were taken immediately after the addition of silica sol and during the initial stage of silica shell formation. The progress of the reaction was monitored further. The measurements were done by taking aliquots from the reaction mixture at a respective time and the measurements were done in quartz cuvette under constant stirring to avoid settling down of the $\text{Ag@PS-}b\text{-P4VP@SiO}_2$. As the reaction time was increased, a substantial decrease in AgNP plasmon peak intensity was observed which is attributed to the dissolution of silver nanoparticles. However, upon prolongation of the reaction up to 4 weeks, the plasmon peak intensity was reduced to ca. 40 % with respect to the initial peak values. The UV-Vis studies support previously discussed TEM results showing a decrease of AgNP size ca. 12 nm to ca. 6 nm after prolonged reaction with the silica sol (Figure 4.16 a, b, and Figure 4.19).

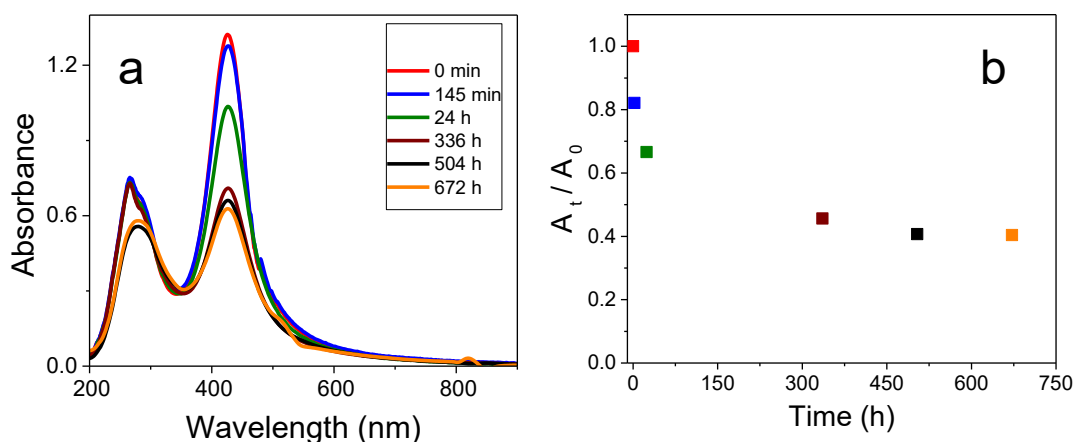
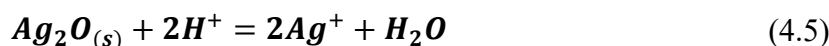


Figure 4.20 (a) UV-Vis spectra of Ag@PS-b-P4VP@SiO₂ particles in reaction mixture taken at different time periods after addition of acidic silica sol to the Ag@PS-b-P4VP micellar solution; (b) Relative intensity, A_t/A_0 , of silver plasmon peak at 420 nm versus time obtained upon silica shell deposition.

Tai et al. studied the dissolution and stability of AgNPs in solution at a pH ranging from highly acidic to neutral environment.³¹⁵ They observed that at highly acidic pH (~2.3) the particles started to dissolve and form larger and irregularly shaped aggregates. They also noticed that the dissolution of surface AgNPs and the particle aggregation decreased with an increase in pH (pH approaching neutral values). They modified AgNPs with bovine serum albumin (BSA) which protected the surface atoms of AgNPs from dissolution and increased solution stability. Similar studies were conducted by Molleman to understand oxidative dissolution of AgNPs depending on the time, pH, and size.³¹⁶ Tanya et al. studied the effect of pH, capping agents, and nanoparticle size on the rate of dissolution of the AgNPs.³¹⁷ Upon studying the dissolution of silver nanoparticles of various sizes in aqueous medium, they observed that the silver nanoparticles which are smaller in size (6 nm > 9 nm > 13 nm > 70 nm) dissolves faster than that are larger in size. No dissolution was observed in the case of particles with 70 nm. A similar effect was observed in an acidic medium of pH 3. The rate of dissolution was higher in the acidic medium than in the case of the aqueous medium. It was also found out that the particle shape remained constant while the particle size distribution became broader than initial ones after dissolution. Thus, the proposed mechanism of dissolution of silver nanoparticles is the oxidative dissolution through reaction of metallic Ag with dissolved oxygen and protons, which is explained by the following reaction.^{316,317}



The dissolved oxygen initiates dissolution by the oxidation of metallic silver on the surface of AgNPs which eventually leads to the formation of a thick layer of silver (I) oxide (Ag₂O). The Ag₂O layer dissolves releasing Ag⁺ into the solution until the Ag₂O is completely

dissolved. This leads to the further oxidation of metallic silver to Ag_2O and the reaction continues further. The increased dissolution of silver nanoparticles in presence of an increased pH supports the formation of Ag_2O . In presence of an aqueous medium, the surface of the Ag_2O layer is covered with surface hydroxyl groups (Ag-OH) that undergo protonation at acidic pH (Ag-OH_2^+).³¹⁸ In the presence of protonated environment, for example in presence of acidic silica sol which contains both water and acid, the oxidative dissolution occurs faster. This arises due to the fact that the protonation tends to weaken and break the Ag-O bonds easily resulting in the increased release of Ag^+ into the solution.³¹⁷ Moreover, the thermodynamic calculations reveal that AgNPs are not stable at pH ranging from 4 to 12 and will dissolve completely.³¹⁹ In the case of $\text{Ag}@PS-b-P4VP$ the pH of added silica sol is highly acidic (between pH 0 and 1). As previously described, at this high acidic pH AgNPs can undergo oxidative dissolution by forming an Ag_2O layer and release Ag^+ and therefore the decrease in plasmon peak of AgNP with extended reaction time with silica sol. Interestingly, in the case of $\text{Ag}@PS-b-P4VP@SiO_2$ particles, a complete dissolution of silver nanoparticles was not observed even upon prolonged reaction time up to several weeks. The reasons for such results are not clear yet. One possible explanation might be that at later stages of the sol-gel reaction, the AgNP surface became somehow passivated against dissolution. This could be due to the presence of a polymer layer and/or the deposited silica shell which acts as a protective shield that allows the dissolved silver ions to re-adsorb onto the AgNPs, and limited diffusivity of oxygen and protons to the reaction sites. Therefore, further experiments are needed to clarify these results.

In order to use $\text{Ag}@SiO_2$ yolk-shell nanoparticles for catalytic application, the stability of nanoparticles to the reactant molecules is important. Besides stability, the size of the nanoparticle also plays a major role in its catalytic activity. Due to the partial dissolution of silver nanoparticles upon silica shell formation, it is not practical to obtain an efficient catalytic system with small-sized particles for the system discussed above and the like. Considering above mentioned, gold nanoparticles (AuNPs) have been chosen for our further work which is discussed in the following sections. Subsequently, similar experiments were done with $\text{Au}@PS-b-P4VP$ and $\text{Au}@PS-b-P4VP@SiO_2$ systems which have been proved more stable to dissolution in an acidic environment when compared to silver nanoparticles.

4.2.4 $\text{Au}@SiO_2$ Yolk-Shell Nanostructures

For the synthesis of $\text{Au}@SiO_2$ yolk-shell nanostructures, citrate-stabilized gold nanoparticles were synthesized using a similar procedure described by Brown et al.²⁶² In order to selectively localise the AuNPs to the core of the $PS-b-P4VP$ micelles they were surface modified using thiol terminated PS. A detailed synthetic procedure is given in Section 3.3.3. The PS stabilised AuNPs were entrapped into the PS core of the $PS-b-P4VP$ micelles via a solvent exchange step as discussed before.

The TEM image of the obtained particles revealed the formation of uniform spherical shaped AuNPs (Figure 4.21 a). Figure 4.21 (b, c) shows the UV-Vis absorbance spectrum of the as-prepared AuNPs in water ($\lambda = 540$ nm) and the Au@PS-*b*-P4VP in methanol.

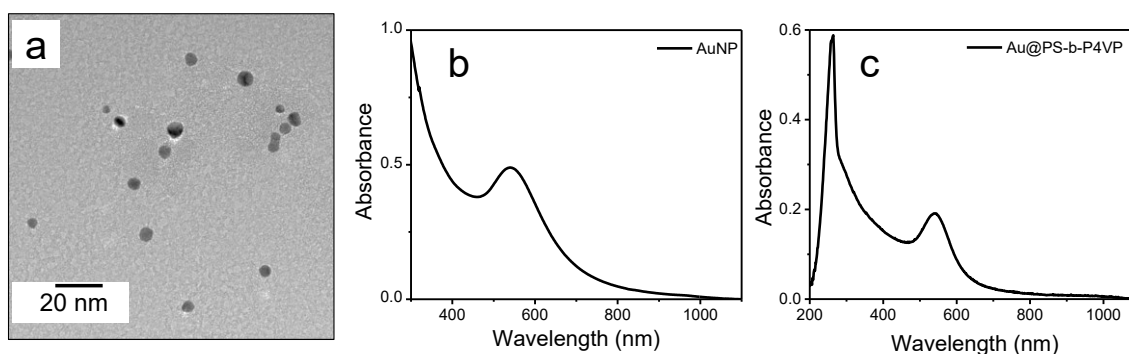


Figure 4.21 (a) TEM image of AuNP; (b) UV-Vis spectrum of as synthesised AuNP in H_2O ; (c) UV-Vis spectrum of Au@PS-*b*-P4VP in methanol. The scale bar on the image (a) is 20 nm.

The thus prepared Au@PS-*b*-P4VP micelles were deposited with silica sol maintaining a molar ratio between TEOS and 4VP as 1: 400. Au@SiO₂ yolk-shell nanostructures were synthesised using the procedure as explained by Figure 4.15 and a detailed experimental procedure is given in Section 3.3.4. Figure 4.22 shows the TEM image and size distribution histogram of Au@PS-*b*-P4VP@SiO₂ particles separated from the reaction mixture after the deposition of silica shell. The black spots in the TEM image (Figure 4.22 a) reveal the presence of multiple AuNPs within the Au@PS-*b*-P4VP@SiO₂ particles.

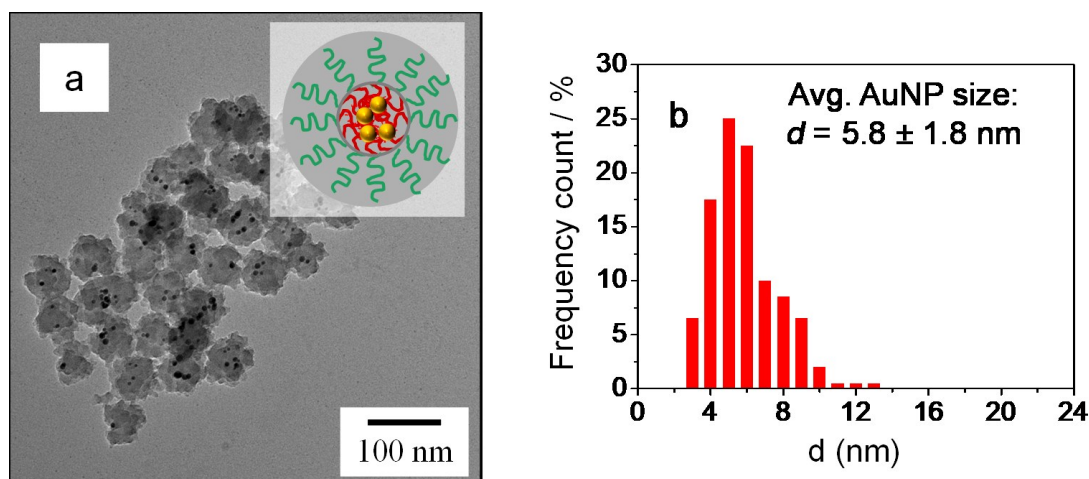


Figure 4.22 (a) TEM image of Au@PS-*b*-P4VP@SiO₂; (b) Size distribution histogram of AuNPs inside the Au@PS-*b*-P4VP@SiO₂. The scale bar on the image (a) is 100 nm.

In order to study the effect of silica sol on the particle size of AuNPs, experiments similar to that done with AgNPs were conducted. Figure 4.23 shows the UV-Vis spectra of the reaction mixture taken at different time intervals after addition of silica sol and relative AuNP

plasmon peak intensity, A_t/A_0 , versus reaction time. The UV-Vis absorbance spectra were taken immediately after the addition of silica sol and during the reaction course of silica shell formation. The measurements were done by taking aliquots from the reaction mixture at respective time. The spectra were measured in quartz cuvette under constant stirring to avoid settling down of the $\text{Au}@PS\text{-}b\text{-}P4VP@SiO_2$ particles. Unlike the results obtained from AgNPs, no decrease of plasmon peak intensity was observed with AuNPs even after several days (Figure 4.23 b). A slight increase in plasmon peak intensity (ca. 5 %) as compared to initial spectrum was observed in case of AuNP which can be associated with the change in reaction environment after the addition of silica sol.

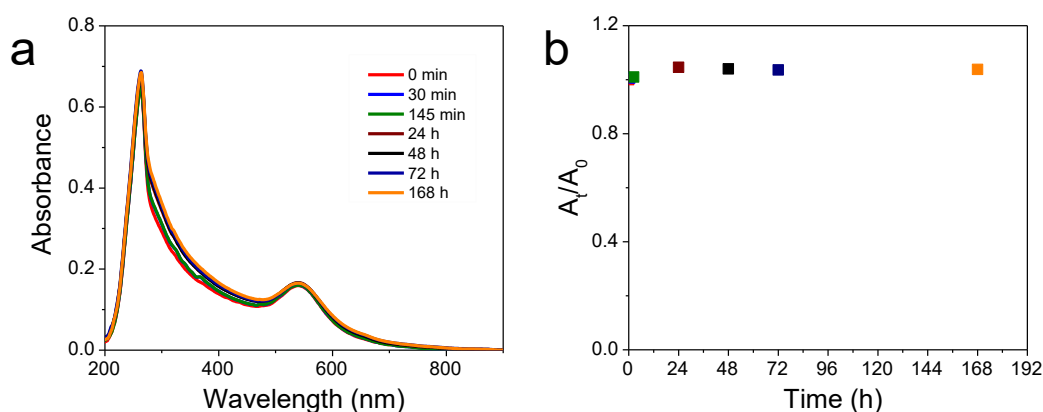


Figure 4.23 (a) UV-Vis spectra $\text{Au}@PS\text{-}b\text{-}P4VP@SiO_2$ taken at different time periods after addition of acidic silica sol to the $\text{Au}@PS\text{-}b\text{-}P4VP$ micellar solution; (b) Relative intensity, A_t/A_0 , of gold plasmon peak at 540 nm versus time obtained upon silica shell deposition.

In the next step, $\text{Au}@PS\text{-}b\text{-}P4VP@SiO_2$ particles were pyrolyzed in the air in order to remove the BCP template. During pyrolysis, the temperature was increased slowly up to 450 °C and then kept constant for 4 hours. The mass loss measured by TGA, by analysing powdered $\text{Au}@BCP@SiO_2$ sample prepared from a micellar solution of 0.1 mg g⁻¹ BCP concentration, also provides an insight to the removal of the BCP template at this temperature. Figure 4.24 shows the TGA curve depicting the mass loss (weight %) of $\text{Au}@BCP@SiO_2$ sample when heated up to 800 °C in the N₂ atmosphere. The dry powdered samples were prepared from a micellar solution of BCP concentration 0.1 mg mL⁻¹.

The TGA experiments were done in an inert (N₂) atmosphere where the complete removal of the BCP template was around 600 °C whereas the pyrolysis of $\text{Au}@PS\text{-}b\text{-}P4VP$ was done in the air which accelerates the oxidation of the BCP template at a lower temperature. Moreover, it is known that pyrolytic treatments in the presence of a nitrogen atmosphere result in deposition of carbon compounds while the pyrolysis in presence of oxygen the polymer oxidises to form gaseous carbon compounds without leaving behind any residues. Hence it is clear such pyrolytic treatment allows the complete removal of the polymeric template without the deposition of any carbonaceous compounds and prevents crumbling of silica shell.³²⁰

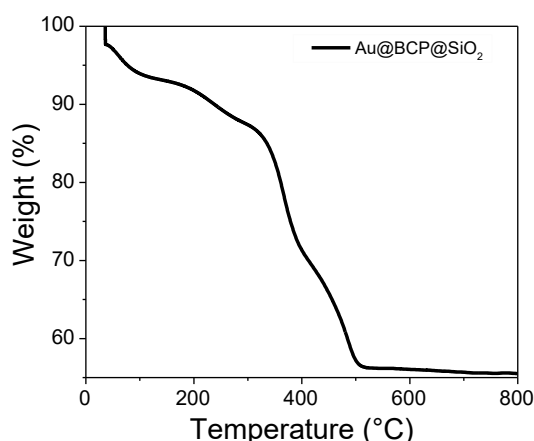


Figure 4.24 TGA curve showing the weight loss of Au@BCP@SiO₂ measured by heating up to 800 °C in the N₂ atmosphere.

Figure 4.25 shows the corresponding TEM images of Au@SiO₂ yolk-shell nanoparticles obtained after pyrolysis of Au@PS-*b*-P4VP@SiO₂ particles. The initial size obtained for the as-synthesized Au@PS-*b*-P4VP@SiO₂ was estimated as ca. 60 nm, which after pyrolysis decreased to 50 nm due to the removal of the PS-*b*-P4VP template. As expected, after pyrolysis (Figure 4.25 a, b) the gold nanoparticles appeared enclosed inside the hollow silica shell, with a distinct interface between the shell and the hollow interior. Notably, an increase in the size of the enclosed AuNPs was also observed after pyrolysis.

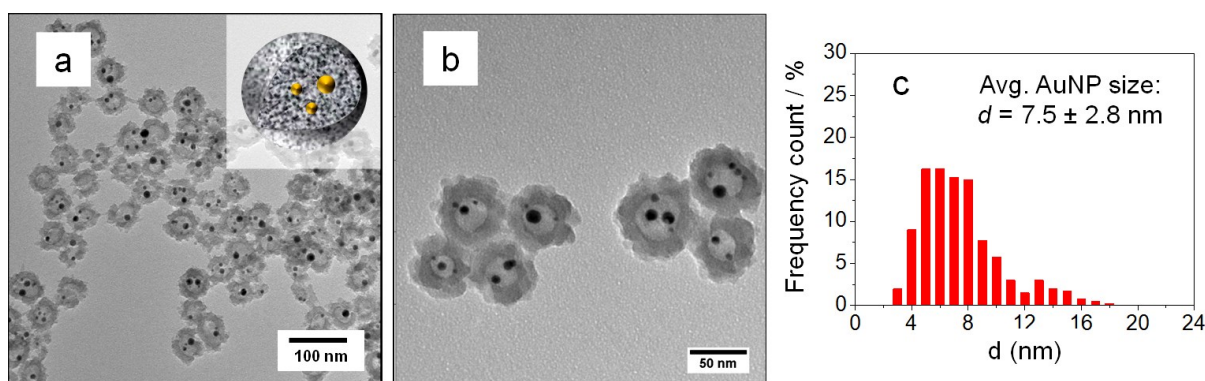


Figure 4.25 (a, b) TEM images of Au@SiO₂ yolk-shell nanoparticles; (c) Size distribution histogram of AuNPs inside Au@SiO₂ yolk-shell nanoparticles. Scale bars on image (a) 100 nm; (b) 50 nm.

Based on TEM image analysis the number-average size (d_{av}) of AuNP before and after pyrolysis were 5.8 ± 1.8 nm and 7.5 ± 2.8 nm, respectively (Figure 4.22 and Figure 4.25). The presence of multiple AuNPs inside the silica shell can lead to the melting and fusion of nanoparticle upon pyrolysis. Therefore, after pyrolysis, the nanoparticle size distribution was broadened as compared to that before pyrolysis.

It should be pointed that after pyrolysis the Au@SiO₂ particles appeared fused together and formed large aggregates as shown in Figure 4.26. This fusion is a drawback since access of reactants to the catalytic sites located inside of such aggregates will be hindered, leading, thus, to a reduced activity of the catalyst. In Section 4.3 it will be shown how to prevent formation of such aggregates by embedding Au@SiO₂ yolk-shell into a porous support.

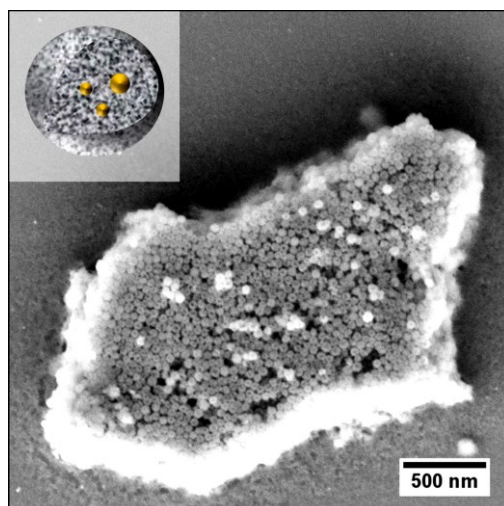


Figure 4.26 SEM micrograph showing Au@SiO₂ yolk-shell nanoparticles fused into large aggregates after pyrolysis. Scale bar is 500 nm.

As mentioned earlier, mesoporous yolk-shell nanostructures have good catalyst loading properties for confined cooperative catalysis and for such system the reactants and products should have access to the catalyst surface. The presence of a porous shell equips the catalyst surface freely accessible to the reactants and products.^{185,321} For efficient catalysis the nanoparticle surface must be accessible by the reactants. Such accessibility is provided by the porous nature of the shell. In order to analyse the porosity of Au@PS-*b*-P4VP@SiO₂ and Au@SiO₂ yolk-shell nanoparticles, N₂ adsorption experiments were performed. Figure 4.27 shows the adsorption-desorption isotherms of unpyrolyzed Au@PS-*b*-P4VP@SiO₂ (red circles) and pyrolyzed Au@SiO₂ particles (blue circles).

From Figure 4.27 (a) it is evident that both the samples exhibit type IV adsorption-desorption isotherms with characteristic hysteresis loops, which is a characteristic feature for highly porous systems, in 0.4-0.9 P/P₀ region. The surface area (BET) of unpyrolysed and pyrolysed samples differ significantly. Before pyrolysis the BET surface area of Au@PS-*b*-P4VP@SiO₂ particles was 150 m² g⁻¹, it increased after pyrolysis up to 430 m² g⁻¹. After pyrolysis, the size of mesopores was reduced from 10 to 8 nm (Figure 4.27 b). As mentioned earlier, the Au@SiO₂ yolk-shell nanoparticles fuse together and form large aggregates and arrange themselves in a closely packed manner. Moreover, the formation of such aggregates was also observed in the case of unpyrolysed Au@PS-*b*-P4VP@SiO₂ particles after centrifugation and drying.

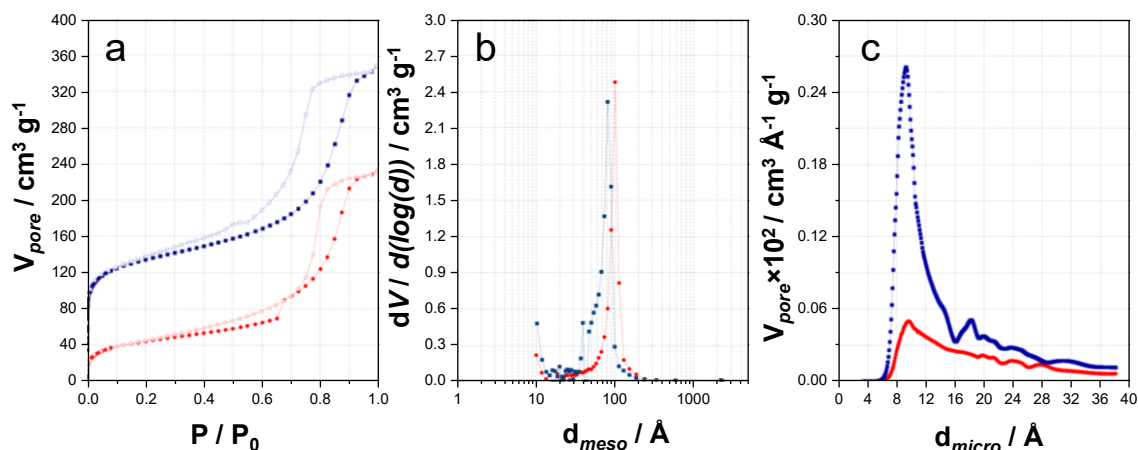


Figure 4.27 (a) N_2 adsorption-desorption isotherms of unpyrolysed $Au@PS-b-P4VP@SiO_2$ (red circles) and pyrolysed $Au@SiO_2$ yolk-shell nanoparticles (blue circles); corresponding size distributions of (b) Mesopores; (c) Micropores. Filled and unfilled symbols correspond to adsorption and desorption processes respectively.

During pyrolysis remaining non-hydrolysed ethyl substitutes of TEOS are removed causing shrinkage of interparticle voids. The decrease in particle size after pyrolysis and shrinkage of interparticle voids might result in the collapse of mesopores. The size of voids between closely packed hard spheres depends on the particle size and type of packing. In the case of tetrahedral packing, the size of tetrahedral void relative to the sphere diameter is 0.225. Thus, for closely packed hard spheres with a diameter of 50 nm and 60 nm, the calculated size of the interparticle void will be 11.25 nm and 13.5 nm, respectively. Though these values are larger than those obtained from gas sorption experiment, their ratio, $d_{60}/d_{50} \approx 0.83$ (or void shrinkage) matches very well with experimentally obtained mesopore size ratio after and before pyrolysis ($d_{pyr}/d_{unpyr} \approx 0.80$). Considering that $Au@PS-b-P4VP@SiO_2$ particles are not perfectly spherical and entirely hard (Figure 4.25 b), the interparticle voids should be smaller as compared to those calculated for the uniform hard spheres.¹³⁹ The significant increase in BET surface area and micropore volume fraction after pyrolysis (Figure 4.27 a and c) are specifically attributed to the pyrolytic removal of the PS-*b*-P4VP template. As described in the previous section (Section 4.1) the addition of silica sol leads to a sudden increase in the size of PS-*b*-P4VP micelle due to the stretching of protonated P4VP chains and additional solvation of P4VP corona.³²²

In view of the above facts, highly stretched P4VP chains interpenetrate into the surrounding silica shell which should act as an effective porogen and make the silica shell highly porous. The results obtained are in agreement with the studies reported by Ruthstein et al. who used Pluronic® block copolymers as a template for synthesis of structured mesoporous silicates and experimentally proved the source of the microporosity are the PEO chains trapped within the silica matrix.³²³

4.2.5 Catalysis Studies using Au@SiO₂ Yolk-Shell Nanoparticles

Catalysis using metal nanoparticles gained much importance in recent years. A major problem associated with this field of study is the quantification of the catalytic activity of nanoparticles. In order to analyse and quantify the kinetics and thereby co-relate the size and shape of the particles to its catalytic activity, a well-defined model reaction is essential.³²⁴ Such a model reaction should have the following characteristics.^{289,325}

1. The chemical reaction should be well-controlled which reacts from A to B only in the presence of metal nanoparticle without any side reactions or by-products.
2. A full kinetic analysis of the reaction rate should be possible as a function of time, leading to a detailed understanding of the reaction mechanism.
3. The reaction should proceed at room temperature and in mild solvents such as water and there should be no degradation, coagulation, or transformation of nanoparticles during the reaction.
4. A change of temperature should not lead to a change in the mechanism or to undesired side reactions.

Since most of the catalytic reactions occur on the surface of the particles, the surface area of the nanoparticles should be calculated with utmost accuracy.

4.2.6 Reduction of 4-Nitrophenol using Au@SiO₂ Yolk-Shell Nanoparticles

Catalytic reduction of 4-nitrophenol by sodium borohydride in presence of a metal catalyst has been widely used as a model reaction to evaluate the catalyst kinetics of noble metal nanoparticles.^{324,326,327} Pradhan et al. showed the reduction of 4-nitrophenol (4-NP) to 4-aminophenol (4-AP) by sodium borohydride (NaBH₄) in the presence of silver nanoparticles as an efficient model reaction to evaluate the catalyst kinetics.³²⁸ This reaction can be catalysed by free or immobilised metal nanoparticles. Moreover, it can be easily monitored via UV-Vis spectroscopy by the decrease of the strong absorption peak of 4-nitrophenolate ions at $\lambda = 400$ nm which leads directly to the calculation of rate constant. Although the reaction is thermodynamically feasible, it is kinetically restricted in the absence of a catalyst because of the kinetic barrier between the mutually repelling negative ions, 4-NP and BH₄⁻, is very high. The reduction pathway can be explained using Langmuir-Hinshelwood mechanism (Appendix 8.1.3).³²⁹

As depicted in Figure 4.28, borohydride ions that are adsorbed onto the nanoparticle surface and transfer surface hydrogen species to it. At the same time, 4-nitrophenol molecules are also adsorbed onto the surface of nanoparticles. Through the adsorption of active species on the surface, an electron transfer takes place from BH₄⁻ to 4-NP. Metallic nanoparticles relay electrons to complete the redox reaction. The adsorption of reactant species onto the particle surface contributes to overcoming the kinetic barrier of the reaction.

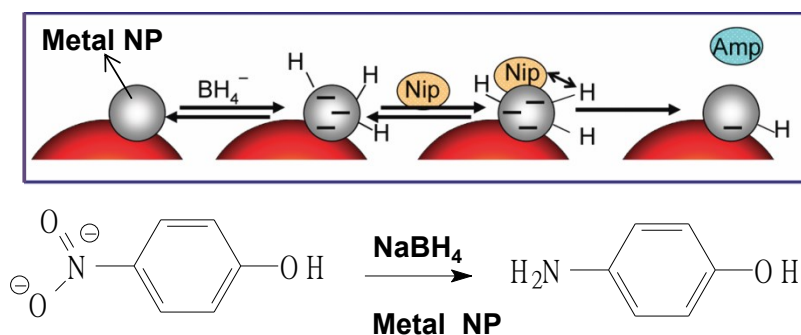


Figure 4.28 Mechanism of reduction of 4-nitrophenol by borohydride on the surface of metallic nanoparticles. Reproduced from Ref. 324.

Assuming that the diffusion of the reactants to the nanoparticle surface, as well as the adsorption-desorption steps are fast, the reduction of 4-NP adsorbed on the surface by the surface hydrogen species become the rate-determining step. Since, desorption of the product (4-AP), the last step in the catalytic cycle, is so fast that it does not enter into the kinetic equations.^{7,324} Typically, the reaction is carried out in the presence of an excess of borohydride such that it can be considered as a pseudo-first-order reaction and the rate of the reaction is solely dependent on the concentration of 4-nitrophenol in the reaction mixture. This can be expressed by the following equation:

$$\frac{dc_{NP}}{dt} = -k_{app} \cdot c_{4-NP} \cdot c_{BH_4} = -k_{app} \cdot c_{4-NP} \quad (4.6)$$

where c_{4-NP} is the concentration of 4-nitrophenol, c_{BH_4} is the concentration of borohydride, and k_{app} is the apparent rate constant.

In order to study the catalytic activity of Au@SiO₂ yolk-shell nanoparticles, the reduction of 4-nitrophenol with sodium borohydride was chosen as a model reaction. It has been verified to produce only 4-aminophenol without any side products.³³⁰ Therefore, the reaction can be monitored by the changes in UV-Vis absorption spectra of 4-nitrophenolate ($\lambda_{max} = 400$ nm) versus time. Catalytic experiments were carried out in a quartz cuvette (1 cm path length) under mechanical stirring at 400 rpm. Stirring was required to obtain reproducible results on reaction kinetics. Au@SiO₂ catalyst was dispersed in Millipore water using an ultrasonic bath to give the stock dispersion with the catalyst concentration of 0.02 mg mL⁻¹. A measured volume of catalyst dispersion (from 0.02 to 0.5 mL) was added to a mixture of freshly prepared aqueous solution of NaBH₄ (0.9 mL, 0.2 M), aqueous solution of 4-NP (0.3 mL, 0.2 mM) and Millipore water (from 0.5 to 0.98 mL), such that total volume of the reaction mixture in all experiments was kept constant (2.2 mL). Successive UV-Vis spectra were recorded every minute in the wavelength range 250 – 700 nm immediately after addition of the catalyst. Evaluation of the reaction kinetics was done by monitoring the intensity change of nitrophenolate absorption peak ($\lambda_{max} = 400$ nm) with respect to the time.

Figure 4.29 (a-c) shows the time-resolved change in UV-Vis spectra during the borohydride reduction of 4-NP in the presence of different amounts of Au@SiO₂ catalyst added. After the addition of a catalyst, the intensity of nitrophenolate peak gradually decreased with a simultaneous increase in the peak of 4-aminophenol ($\lambda_{\max} = 300\text{nm}$). The degree of 4-NP conversion (C_t/C_0) can be directly deduced from the UV-Vis spectra by monitoring the decrease in the absorption peak at 400 nm with time. As seen from Figure 4.29 the reaction proceeds with a very small amount of Au@SiO₂. When a low amount of catalyst, 0.4×10^{-3} mg, was added the reaction completed in 50 cycles. But with an increase in the amount of added catalyst, there was a considerable decrease in reaction time to less than 15 minutes (Figure 4.29 b, c). For a catalyst amount of 1.0×10^{-3} mg, the conversion (ca.98%) of 4-NP to 4-AP occurred in 5 minutes. At a higher amount of added catalyst, the reaction completed in less than 2 minutes after the addition of the catalyst and was beyond the possibility to be monitored.

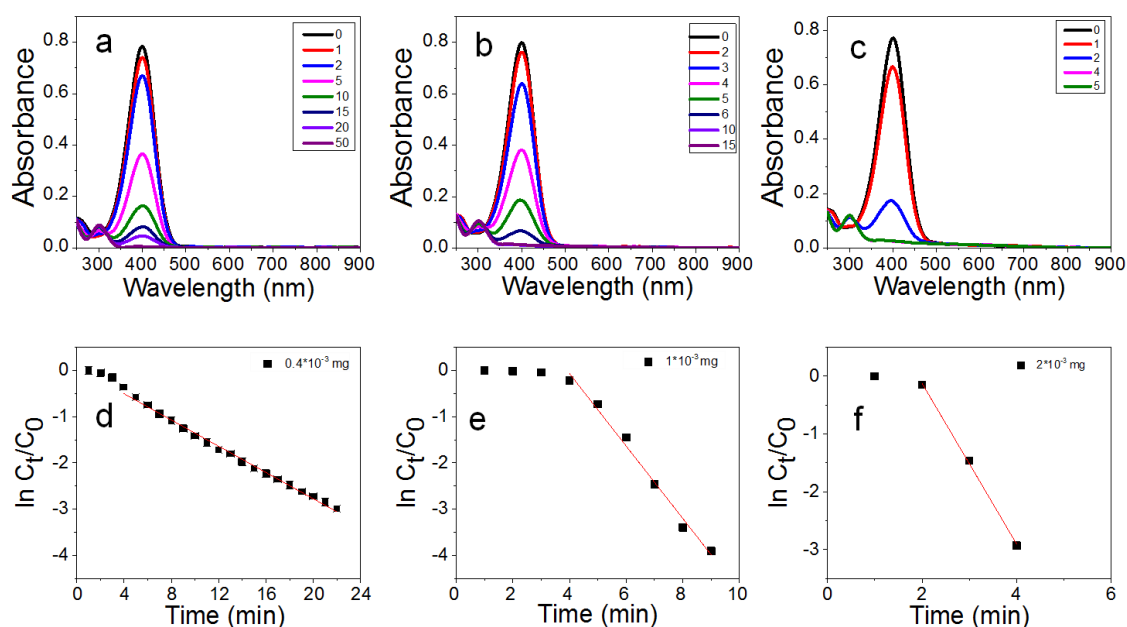


Figure 4.29 (a, b, c) Successive spectra taken after every minute during borohydride assisted the reduction of 4NP after the addition of Au@SiO₂ yolk shells showing the decrease in peak intensity of 4-NP with respect to increase in time; (d, e, f) Shows plots of $\ln(C_t/C_0) \sim \ln(A_t/A_0)$ versus time at different concentrations of Au@SiO₂ catalyst. All experiments were carried out with initial concentrations $[4\text{-NP}]_0 = 0.027 \text{ mmol L}^{-1}$ and $[\text{NaBH}_4]_0 = 0.081 \text{ mol L}^{-1}$. Amount of Au@SiO₂ catalyst in reaction mixture was: (a, d) 0.4×10^{-3} mg; (b, e) 1.0×10^{-3} mg; (c, f) 2.0×10^{-3} mg. Apparent rate constants determined from the slopes of linear fit are: (d) 0.124 min^{-1} ; (e) 0.808 min^{-1} ; (f) 1.391 min^{-1} .

When the reaction is carried out with an excess of NaBH₄, it follows pseudo 1st order kinetics.³¹² Thus, apparent rate constant (k_{app}) can be determined from the slope of the linear plot of $\ln(C_t/C_0)$ versus time. Figure 4.29 (d-f) shows the $\ln(C_t/C_0)$ plot versus time obtained after addition of a different amount of Au@SiO₂ catalyst to the 4-NP/NaBH₄ mixture with corresponding linear fits. At a lower amount of catalyst, an initiation time was observed which

could be attributed to the presence of agglomerated Au@SiO₂ particles. This can, in turn, create a high diffusion barrier which the reactants must overcome to reach the catalyst core located inside the aggregates as shown in Figure 4.26. At higher amounts of catalyst, the reaction is still within the measurable limits but the k_{app} values might not be accurate.

The efficiency of the catalyst after recovery was studied by collecting the added catalyst from the reaction mixture by high-speed centrifugation at 13,500 rpm followed by several washing cycles with Millipore water. After washing, the catalyst was dispersed in Millipore water and was then added to the freshly prepared new reaction mixture. The reaction was monitored for 10 minutes using UV-Vis spectroscopy for each cycle. This procedure was repeated and the catalyst activity was recorded up to 10 recovery cycles. Figure 4.30 (a) shows the time-resolved absorbance spectra during the borohydride reduction of 4-NP to 4-AP in the presence of Au@SiO₂ catalyst after recovery. The reaction was completed in less than 5 minutes with ca. 95-98 % conversion of 4-NP to 4-AP in the presence of the recovered catalyst. Figure 4.30 (b) shows the conversion of 4-NP to 4-AP for the recovered catalyst for 10 cycles. Despite the possible loss of some amount of catalyst during recovery, ca. 95 % conversion was achieved for all the 10 cycles, proving the recycling efficiency of Au@SiO₂ catalyst. Slight variations in the reduction efficiency were observed which, however, are at the limit of experimental method accuracy.

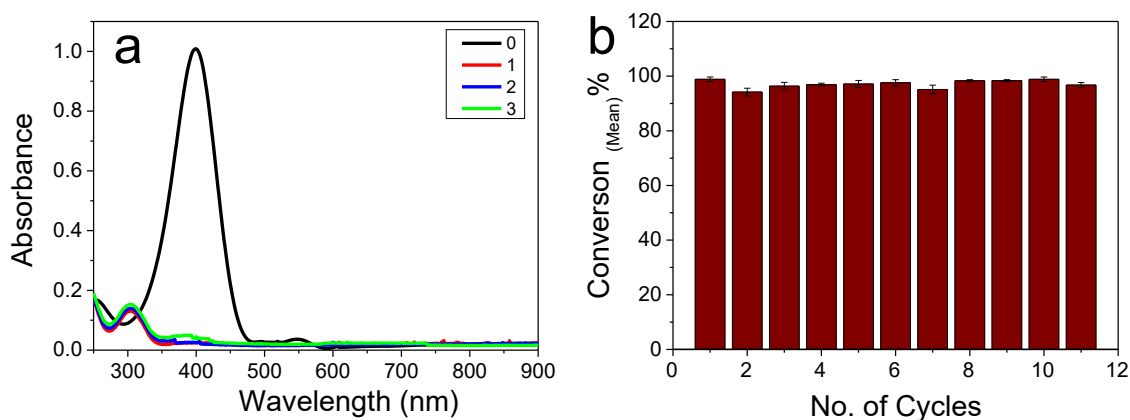


Figure 4.30 Plot showing (a) the absorbance spectra of 4-NP + NaBH₄ after addition of recycled catalyst; (b) Conversion of 4-NP to 4-AP in presence of Au@SiO₂ yolk-shell catalyst for 10 recovery cycles.

Although Au@SiO₂ yolk-shell nanoparticles exhibited prominent catalytic activity and good recyclability, there was an aggregation of Au@SiO₂ particles upon removal of the PS-*b*-P4VP template. Due to these aggregates, the reactants have different access to the catalyst core located inside the yolk-shell nanoparticles. This, in turn, caused non-reproducible rate constants and irregularities in the experiment. Hence, the reaction parameters were modified to eliminate the above-mentioned problems. During optimising the reaction conditions on silica deposition, the reaction parameters such as the concentration of the components, 4VP: TEOS ratio, HCl

concentration in the reaction mixture has been systematically varied. It was found that all the parameters influenced the rate of silica shell formation as expected as discussed in Section 4.1.3 and 4.1.4. Exceptionally, it was observed that the Au@PS-*b*-P4VP@SiO₂ particle size only marginally depends on the amount of added silica sol or with the extension of the reaction time. Also, it was found that the mass yield of Au@PS-*b*-P4VP@SiO₂ particles and the amount of AuNP@SiO₂ remained equally low in a broad range of varied reaction condition. Therefore, by introducing an additional step to the synthetic procedure, a new structure has been designed.

4.2.7 Conclusion

Yolk-shell nanostructures due to their multitude properties have been widely studied for their application as a catalyst. They can be synthesized using different methods such as hard and soft templating. Hard template method uses selective etching of the core or the shell where the obtained particles can be irregularly shaped thereby negatively affecting the catalyst efficiency.¹⁸⁴ Soft templating, on the other hand, uses usually a polymer template which can later be removed via pyrolysis.¹³⁵ In the present work, a simple and robust synthetic procedure has been adopted to prepare yolk-shell nanostructures with a hollow mesoporous silica shell and a catalytically active noble metal nanoparticle core having high catalytic efficiency and recyclability when compared to similar methods reported in the literature. The procedure discussed here used a reactive PS-*b*-P4VP template for enclosing the catalytic core and for the deposition of the silica shell, which later on removed to obtain yolk-shell nanoparticles. The initial studies conducted on Ag@SiO₂ showed the considerable dissolution of silver nanoparticle in presence of acidic silica sol when compared to the gold enclosed yolk-shell nanoparticles. Hence, Au@SiO₂ nanoparticles were used for further experiments. The P4VP chains of PS-*b*-P4VP block copolymer being interpenetrated into the silica shell plausibly were responsible for the substantial increase of shell porosity during pyrolytic removal of the BCP template. This facilitated the reactants to reach the catalyst core faster, which resulted in an improved catalyst activity. Complete recovery of the catalyst from the reaction medium with a stable catalyst activity is feasible because of the increased size of the yolk-shell nanoparticles when compared to the naked nanoparticles. Though they exhibited high catalytic efficiency, aggregation of these particles upon pyrolysis adversely affected the reaction kinetics in terms of reproducibility and rate of the reaction. Consequently, the evaluation of the catalytic activity of Au@SiO₂ nanoparticles was also difficult.

4.3 SILICA ENCAPSULATED GOLD NANOPARTICLE YOLK-SHELLS EMBEDDED IN POROUS SILICA STRUCTURE (Au@SiO₂@PSS)

4.3.1 Motivation

In order to overcome the drawbacks associated with aggregation and fusion of Au@SiO₂ yolk-shell nanoparticles, an alternative synthetic procedure was formulated by varying the experimental conditions which would allow preparation of catalyst with high yield and reproducible catalytic performance. From our previous experiments (see Section 4.1.4), it was found that within the range of applied experimental conditions only a minor part of silica precursor is reacting with protonated P4VP to form silica shell, whereas the major part of silica precursor remains non-hydrolysed and/or in the form of siloxane oligomers in the reaction mixture. The hydrolysis-condensation of TEOS in the vicinity of protonated P4VP chains of BCP micelles occur much faster as compared to that occurring in bulk solution. Taking these facts into account and in order to overcome the drawbacks associated with aggregation and fusion of Au@SiO₂ yolk-shell structures, an additional step has been introduced to the previously established synthetic procedure, where the yolk-shells are embedded in a porous silica structure.

4.3.2 Synthesis of Au@SiO₂@PSS Catalyst

Procedure for the preparation of Au@SiO₂@PSS catalyst is schematically illustrated in Figure 4.31. Synthesis is accomplished in following steps: (1) entrapment of polymer-stabilized gold nanoparticle within the core of the block copolymer micelles; (2) deposition of silica shell to form Au@PS-*b*-P4VP@SiO₂ particles; (3) formation of porous silica support (PSS); (4) pyrolytic removal of polymeric components to form Au@SiO₂@PSS catalyst.

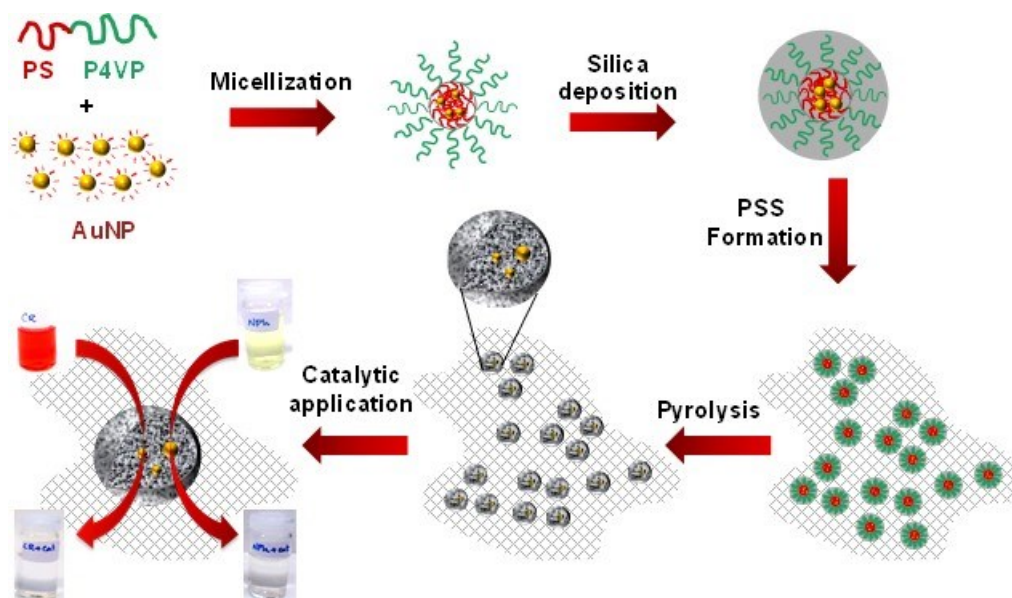


Figure 4.31 Schematics showing the preparation of Au@SiO₂@PSS catalyst via block copolymer template approach.

Au@PS-*b*-P4VP@SiO₂ particles were prepared by employing a similar procedure described in Section 3.3.4 and 4.2.2 with some minor modifications. An amount of silica sol equivalent to 400 mr between TEOS and 4VP was added to the Au@PS-*b*-P4VP particles and reacted for 2 hours. After 2 hours of reaction (silica shell formation), the reaction mixture was exposed to NH₃ vapours for 48 hours resulting in the gelation of the unreacted silica precursor in the reaction mixture and formation of Au@PS-*b*-P4VP@SiO₂@PSS (in the form of a jelly-like product). In order to remove unreacted components, the product was collected and washed with ethanol several times using a high-speed centrifuge. The washed Au@PS-*b*-P4VP@SiO₂@PSS was then dried under vacuum at 80 °C for 3 hours. Then the dried mass was manually powdered using a mortar and pestle. It was then subjected to step-wise pyrolysis at 450°C for 4 hours to remove the BCP template. This resulted in the formation of Au@SiO₂@PSS catalyst. Similar to the previous experiments, the temperature was raised step-wise to prevent crumbling of silica shell upon template removal. The catalyst was then powdered and dispersed in Millipore water at required concentration. Thus prepared dispersion was later on used for morphological characterization and for catalytic studies.

4.3.3 Characterization of Au@SiO₂@PSS Catalyst

Figure 4.32 (a-c) shows SEM and TEM images of a) Au@PS-*b*-P4VP@SiO₂@PSS and (b,c) Au@SiO₂@PSS, respectively. Both SEM and TEM images show the presence of PSS-embedded Au@SiO₂ particles with Au nanocatalyst encapsulated inside. For SEM and TEM imaging samples were dispersed in ethanol. A drop of the dispersion was placed on a silicon wafer or TEM grid and solvent was allowed to evaporate at ambient conditions.

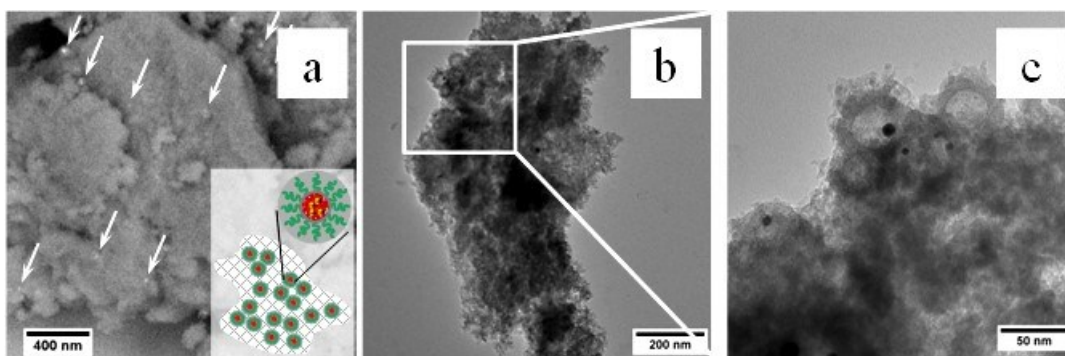


Figure 4.32 (a) SEM image (ESB detector) of Au@PS-*b*-P4VP@SiO₂@PSS sample before pyrolysis: Bright dots pointed with arrows correspond to Au@PS-*b*-P4VP@SiO₂ particles embedded in porous silica support; (b, c) TEM images of Au@SiO₂@PSS catalyst obtained after pyrolysis. Inset on images (a) and (b) show the schematic of corresponding structures. Scale bars on image (a) 400nm; (b) 200 nm; (c) 50 nm.

Figure 4.33 (a-c) shows the adsorption-desorption isotherms of Au@PS-*b*-P4VP@SiO₂@PSS and Au@SiO₂@PSS samples and corresponding pore size distributions in mesopore and micropore regions. Both samples exhibit characteristic type IV isotherms with almost similar N₂ uptake at relatively low pressure, as well as continuous uptake in the range

of 0.1-0.8 P/P_0 , indicating the presence of both mesopores (Figure 4.33 b) and micropores (Figure 4.33 c). After pyrolysis, the BET surface area decreased from $870 \text{ m}^2 \text{ g}^{-1}$ to $690 \text{ m}^2 \text{ g}^{-1}$. The size of the mesopores increased after pyrolysis from 5 nm to 6 nm whereas the content of the micropores has been slightly reduced.

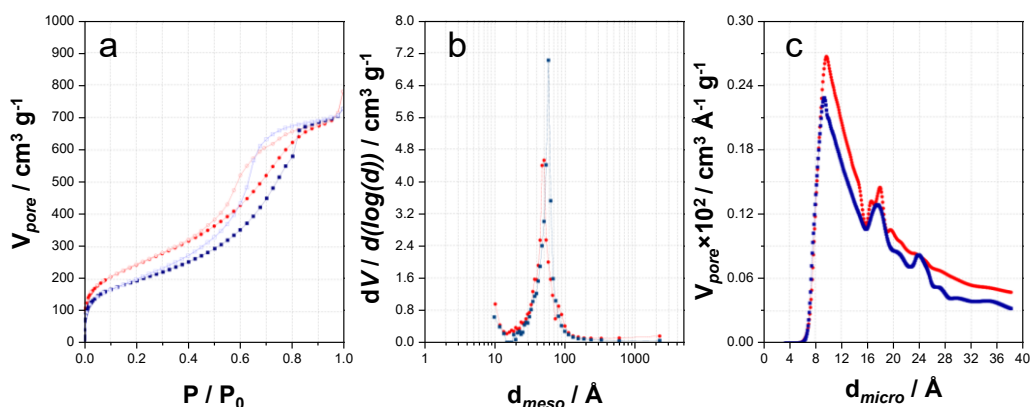


Figure 4.33 (a) N_2 adsorption-desorption isotherms of unpyrolyzed ($\text{Au@PS-}b\text{-P4VP@SiO}_2\text{@PSS}$, red circles) and pyrolyzed ($\text{Au@SiO}_2\text{@PSS}$, blue squares) samples; corresponding size distributions of (b) Mesopores; (c) Micropores. Filled and unfilled symbols correspond to adsorption and desorption processes, respectively.

The results shown in Figure 4.33 (a-c) is noticeably different as compared to $\text{Au@PS-}b\text{-P4VP@SiO}_2/\text{Au@SiO}_2$ discussed in Figure 4.27. Moreover, the changes in microporosity and mesoporosity after pyrolysis show an opposite trend. Taking into account that $\text{Au@PS-}b\text{-P4VP@SiO}_2$ and $\text{Au@PS-}b\text{-P4VP@SiO}_2\text{@PSS}$ samples are prepared under different conditions, such differences were expected and can be explained as follows. In the case of $\text{Au@PS-}b\text{-P4VP@SiO}_2$, silica shell deposition was carried out under acidic conditions while the formation of the porous silica structure was done via the two-step acid-base catalysed sol-gel process. The reaction was continued by the gradual change of pH from acidic to basic upon continuous exposure to ammonia vapours. This method ensures that hydrolysis and condensation reactions are separated and carried out at different pH.³³¹ This approach has been used to synthesise highly porous xerogels.³³² It is a well-known fact that the two-step acid-base catalysed sol-gel process produces silica network with a higher degree of cross-linking, reduced microporosity, but with a larger and broader distribution of mesopores.³³³ Upon pyrolysis of $\text{Au@PS-}b\text{-P4VP@SiO}_2\text{@PSS}$, along with the removal of block copolymer template, a reduction of the overall pore volume, surface area, and micropore fraction takes place. Pyrolytic treatment induces additional condensation of the neighbouring hydroxyl and alkoxy groups on the pore surface. Due to this reason, an increase in the mesopore size and partial closure of micropores occur.³³⁴ This results in a more compacted structure with a decreased micropore volume and surface area but an increased average mesopore size. Since the contribution of $\text{Au@PS-}b\text{-P4VP@SiO}_2$ particles in $\text{Au@PS-}b\text{-P4VP@SiO}_2\text{@PSS}$ being negligibly small, N_2 sorption results shown in Figure 4.33 (a-c) attributes mostly to the PSS support.

From the experimental results obtained for both silica shell and the silica support, it could be concluded that they are porous in nature. It is also evident that PS-*b*-P4VP has been removed upon pyrolytic treatment, leaving hollow silica particles with the gold nanocatalyst encapsulated inside. In addition, embedding of particles in porous silica matrix largely prevents Au@SiO₂ particles from aggregation and/or fusion. These features provide reactants with an easy access to the surface of encapsulated gold nanocatalyst.

4.3.4 Reduction of 4-Nitrophenol using Au@SiO₂@PSS catalyst

In order to investigate the catalytic activity of Au@SiO₂@PSS catalyst, reduction of 4-nitrophenol (4-NP) with sodium borohydride was chosen as the model reaction.^{312,324,335} The powdered Au@SiO₂@PSS catalyst was dispersed in Millipore water using an ultrasonic bath to give the stock dispersion with the catalyst concentration of 2.0 mg mL⁻¹. The rest of the conditions for catalytic experiments were kept similar to Au@SiO₂ catalysis (Section 4.2.6).

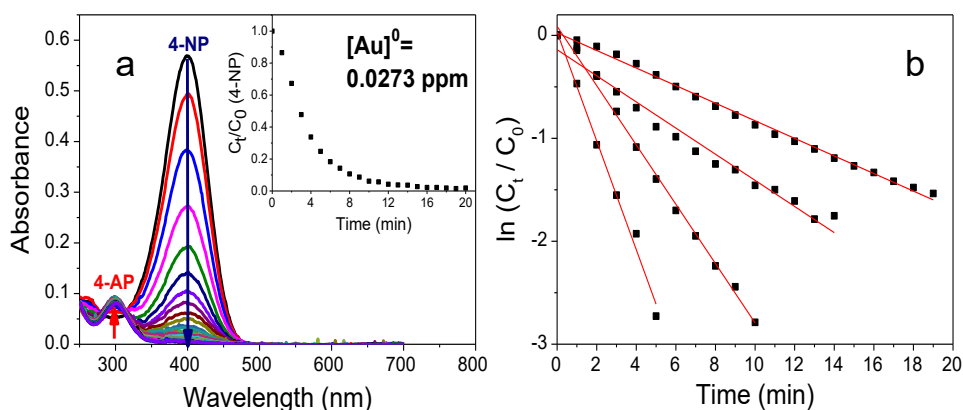


Figure 4.34 (a) Successive UV-Vis spectra taken every minute during borohydride reduction of 4-NP after addition of Au@SiO₂@PSS catalyst and 4-NP conversion plot ($A_t/A_0 \sim C_t/C_0$) versus time (inset); (b) Plots of $\ln(C_t/C_0) \sim \ln(A_t/A_0)$ versus time at different concentrations of Au@SiO₂@PSS catalyst. All experiments were carried out with initial concentrations $[4\text{-NP}]_0 = 0.027 \text{ mmol L}^{-1}$ and $[\text{NaBH}_4]_0 = 0.081 \text{ mol L}^{-1}$. $[\text{Au}^0]$ in reaction mixture was: (1) 0.0136 ppm; (2) 0.0273 ppm; (3) 0.0545 ppm; (4) 0.1091 ppm. Apparent rate constants determined from the slopes of linear fit are: (1) 0.0854 min⁻¹; (2) 0.1297 min⁻¹; (3) 0.2881 min⁻¹; and (4) 0.5286 min⁻¹.

Figure 4.34 (a) shows the time-resolved change in the UV-Vis spectra during borohydride reduction of 4-NP in the presence of Au@SiO₂@PSS catalyst. After addition of the catalyst, the intensity of nitrophenolate peak gradually decreased, whereas the peak of 4-aminophenol ($\lambda_{\text{max}} = 300 \text{ nm}$) increased as the reaction proceeded. The degree of 4-NP conversion (C_t/C_0) can be directly deduced from the UV-Vis spectra by monitoring the decrease in the absorption peak at 400 nm with time (Figure 4.34 a - inset). When the reaction is carried out with an excess of NaBH₄, it follows pseudo 1st order kinetics.³¹² Thus, apparent rate constant (k_{app}) can be determined from the slope of the linear plot of $\ln(C_t/C_0)$ versus time. Figure 4.34 (b) shows the $\ln(C_t/C_0)$ plots versus time obtained after addition of different amounts of Au@SiO₂@PSS catalyst to the 4-NP/NaBH₄ mixture with corresponding linear fits.

As can be seen, the concentration of gold in the reaction mixture (0.1091 ppm) was sufficient to achieve ca. 95% conversion of the 4-NP in 5 minutes. At $[Au^0] = 0.136$ ppm complete reduction of 4-nitrophenol took place in only 2 cycles after addition of catalyst (less than 2 minutes). It was also observed that the reaction began immediately after the addition of catalyst pointing out that the induction time, t_0 , required for the surface restructuring of the nanocatalyst and/or for passing reagents through the porous shell is well below 1 minute.^{324,336} These features direct to the following points: (1) despite the presence of surrounding silica shell, encapsulated gold nanocatalyst remains easily accessible for the reactants; (2) both reagents and products undergo adsorption/desorption on gold surface and pass through the shell very quickly.

Although the apparent rate constants provide information about the efficiency of the nanocatalyst, they cannot be directly compared with k_{app} values for other analogues reported elsewhere. To normalise the apparent rate constants, some authors use catalyst weight or the number of moles. Alternatively, surface-normalized rate constants are often used to characterise and compare the efficiency of catalytic systems having nanocatalysts of different size.³³⁷ In the present work, the rate constants were normalised by the gold content (K_m) and nanocatalyst surface area (K_s).

The gold content in Au@SiO₂@PSS catalyst was estimated as 0.060 ± 0.002 wt. % or 3.0×10^{-6} mmol mg⁻¹ with respect to the total silica content by ICP-OES analysis. In order to do this, four portions of catalyst sample (ca. 10 mg each) were accurately (± 0.0001 mg) weighed and individually digested in 2 mL boiling aqua regia for 1 h. Each solution was adjusted to a total volume of 25 mL Millipore water and further used for determination of gold content. A detailed analytical procedure is discussed in Section 3.1.6. Specific surface area of gold per unit mass of Au@SiO₂@PSS catalyst was determined to be 1.92×10^{-5} m² mg⁻¹. The normalised rate constants for this reaction are $K_m = (1.75 \pm 0.40) \times 10^4$ s⁻¹ mol⁻¹ L and $K_s = 2.52 \pm 0.60$ s⁻¹ m⁻² L, respectively. (Calculations done in order to estimate the AuNP content and the specific surface area of AuNP in the catalyst is given in Section 8.3).

In the present work, the obtained results on 4-NP reduction were compared with other analogous yolk-shell type systems reported in literature up to date.^{160,184,231,338-342} In Figure 4.35, the reaction rate constants normalised by the nanocatalyst surface area (K_s) and the gold content (K_m , in moles) are plotted against the specific surface area.

It is evident that K_s value obtained for Au@SiO₂@PSS catalyst is almost 4 times higher as compared to that reported by Shaik and co-workers and up to 3 orders of magnitude higher as compared to other analogous systems.³³⁸ The difference in catalytic activity becomes even more pronounced if K_m values are compared (Figure 4.35 a, b). K_m value for Au@SiO₂@PSS catalyst is one to three orders of magnitude higher as compared to those reported for other analogues. An additional interesting fact is the dependency of K_m or K_s values on the nanocatalyst surface area or nanocatalyst size. For smaller AuNPs the catalytic efficiency increases at first but decreases considerably with further decrease in AuNP size. These observations can be directly related to the size-dependent catalytic activity of AuNP based yolk-shell nanoparticles. The studies did by Fenger et al. on the size-dependent catalytic activity of CTAB-stabilized

AuNP can be taken into account in this case.³⁴³ However, a thorough investigation is needed in this aspect before coming to any conclusion as the catalytic efficiency of the yolk-shell nanoparticles depends on the synthetic methods, the size of the core and the shell, distinct void volume, shell porosity etc. Besides, other parameters such as catalyst concentration, the concentration ratio of the reactants also need to be considered, since they also affect the reaction kinetics.

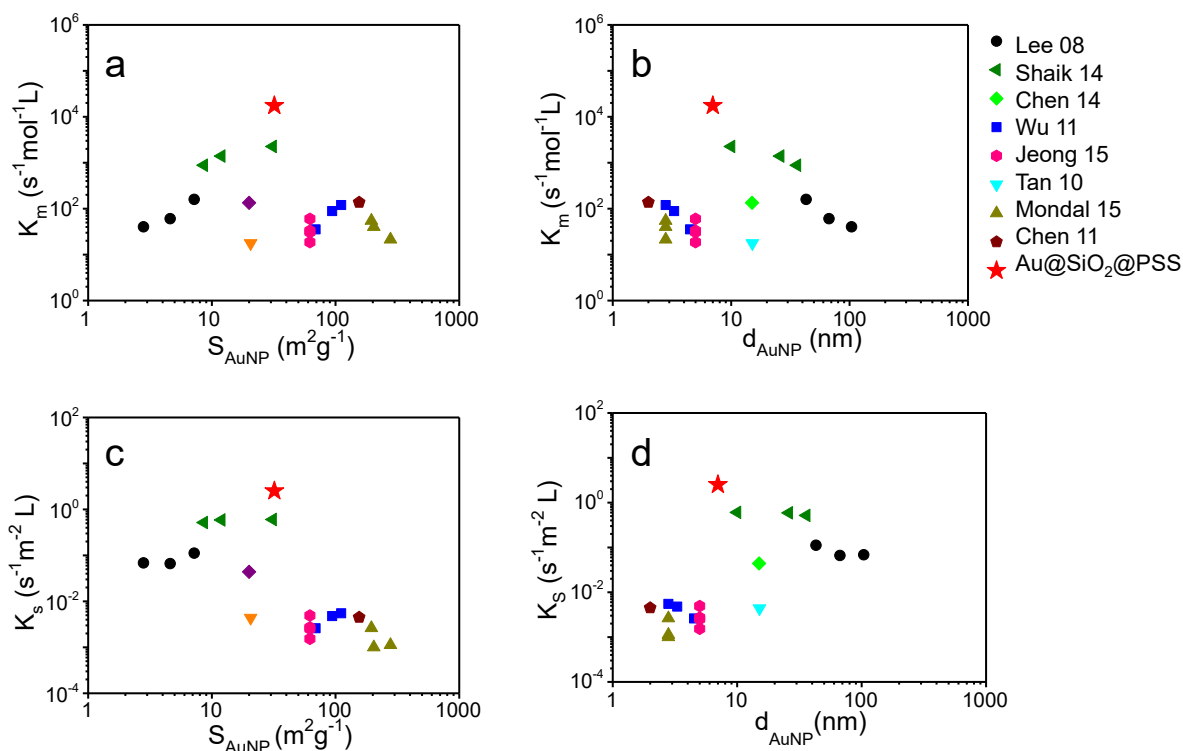


Figure 4.35 The comparison of normalised reaction rate constants (a,b) K_m and (c,d) K_s determined for $\text{Au@SiO}_2\text{@PSS}$ catalyst (red star) with values reported in the literature for analogous catalytic systems: black circles – Lee08¹⁸⁴ green triangles (left) – Shaik14³³⁸ green diamond – Chen14,³⁴² blue rectangles – Wu11¹⁶⁰ pink hexagons – Jeong15⁴³ cyan triangles (down) – Tan10²³¹ dark yellow triangles (up) – Mondal15³³⁹ brown pentagons – Chen11.³⁴¹

Table 4.1 summarises apparent rate constants (k_{app}) and rate constants normalised with respect to the molar catalyst concentration in the reaction mixture (K_m) and catalyst surface area (K_s). In all cases, the nanoparticles are considered as spherical particles for simplicity. Numerical values, which are reported in corresponding publications, are shown as it is. Other values were re-calculated based on experimental data provided for each particular system.

Table 4.1 Summary of the reaction rate constants for catalytic reduction of 4-NP reported in the literature for various Au@SiO_2 yolk-shell catalysts and some analogues.

Sample name	d_{AuNP} nm	S^*_{AuNP} $\text{m}^2 \text{g}^{-1}$	$\omega_{\text{Au/cat}}$ wt. %	k_{app} s^{-1}	K_{m} $\text{s}^{-1} \text{mol}^{-1} \text{L}$	K_{s} $\text{s}^{-1} \text{m}^{-2} \text{L}$	Ref. ^{a)}
Au(43)@SiO ₂	43	7.2	4.6	3.9×10^{-3}	1.6×10^2	1.1×10^{-1}	184
Au(67)@SiO ₂	67	4.6	17.4	5.6×10^{-3}	6.0×10^1	6.6×10^{-2}	
Au(104)@SiO ₂	104	3.0	65.0	1.4×10^{-2}	4.0×10^1	6.9×10^{-2}	
Au@SiO ₂ -10	10	31.1	n/a	5.3×10^{-4}	2.3×10^3	6.0×10^{-1}	338
Au@SiO ₂ -26	26	11.9		3.5×10^{-3}	1.4×10^3	5.9×10^{-1}	
Au@SiO ₂ -36	36	8.6		5.9×10^{-3}	8.8×10^2	5.2×10^{-1}	
Au@meso-SiO ₂	15 ^{b)}	20 ^{b)}	37.1	1.3×10^{-3}	1.4×10^2	3.3×10^{-2}	342
0.5-Au@HSNs	2.8	111.9	1.2	6.5×10^{-4}	1.2×10^2	5.5×10^{-3}	160
1.0-Au@HSNs	3.3	94.1	2.5	1.0×10^{-3}	8.9×10^1	4.8×10^{-3}	
2.0-Au@HSNs	4.5	69.0	4.9	7.8×10^{-4}	3.5×10^1	2.6×10^{-3}	
SiO ₂ -Au@SiO ₂	5 ^{b)}	62.1	n/s	4.0×10^{-3}	1.9×10^1	1.5×10^{-3}	340
SiO ₂ -Au@SiO ₂ -H ₂ O				6.6×10^{-3}	3.1×10^1	2.5×10^{-3}	
SiO ₂ -Au@SiO ₂ -cal				7.1×10^{-3}	3.3×10^1	2.7×10^{-3}	
SiO ₂ -Au@SiO ₂ -NH ₃				1.3×10^{-2}	6.0×10^1	4.9×10^{-3}	
Au@SiO ₂ @SiO ₂	15.1	20.6	3.76	1.7×10^{-3}	1.8×10^1	4.4×10^{-3}	231
Ag@SiO ₂	2.8 ^{b)}	204.3	n/a	4.2×10^{-4}	4.0×10^1	1.2×10^{-3}	339
Pd@SiO ₂	2.8 ^{b)}	178.3		5.8×10^{-4}	2.1×10^1	1.1×10^{-3}	
AgPd@SiO ₂	2.8 ^{b)}	191.3		8.0×10^{-4}	5.5×10^1	2.7×10^{-3}	
GMS ^{c)}	2.0 ^{b)}	155.3	n/s	3.5×10^{-3}	1.4×10^2	4.5×10^{-3}	341
Au@SiO ₂ @PSS (present work)	7.0 ^{d)}	32.0	0.060	n/a ^{e)}	1.75×10^4	2.52	139

^{a)} References are given in the reference section with same numbers as mentioned in the table;

^{b)} Approximate size / particles with broad size distribution / no data on particle size distribution;

^{c)} AuNP intercalated in mesoporous silica (GMS);

^{d)} Median AuNP size determined from descriptive analysis of TEM images;

^{e)} k_{app} varied depending on the amount of added Au@SiO₂@PSS catalyst.

4.3.5 Reduction of Organic Dyes – Congo Red, Methyl Orange, and Methylene Blue

Various dyes such as Congo Red (CR), Methyl Orange (MO) (anionic), Methylene Blue (MB) (cationic), and others are extensively used in textile, leather, paper, rubber, and plastic industry. When discharged without proper treatment they cause serious ecological damage to the environment. Due to this, the need for an efficient yet simple method for the degradation of dyes has gained greater significance. In recent years, metal nanoparticles, owing to their large surface to volume ratio, became a promising candidate for the catalytic degradation of organic dyes.

Mechanism of Degradation of Azo Dyes: A plausible mechanism of azo dye degradation in presence of metal nanoparticles such as AuNPs can be explained as shown in Figure 4.36. This reaction proceeds with the adsorption of reactive species onto the nanoparticle surface. The borohydride ions act as a hydrogen source and deliver surface hydrogen species which are adsorbed onto the nanoparticles. Metal nanoparticles activate the azo nitrogen and can also bind with sulphur and oxygen atoms of the dyes, which results in the weakening of azo double bond via conjugation.³⁴⁴ This eventually results in azo bond cleavage and in the formation of lower aromatic by-products. Moreover, the metal nanoparticles act as an electron relay and electron transfer takes place via the metal nanoparticles from the BH_4^- donor to azo dye (CR, MO) acceptor.³⁴⁵

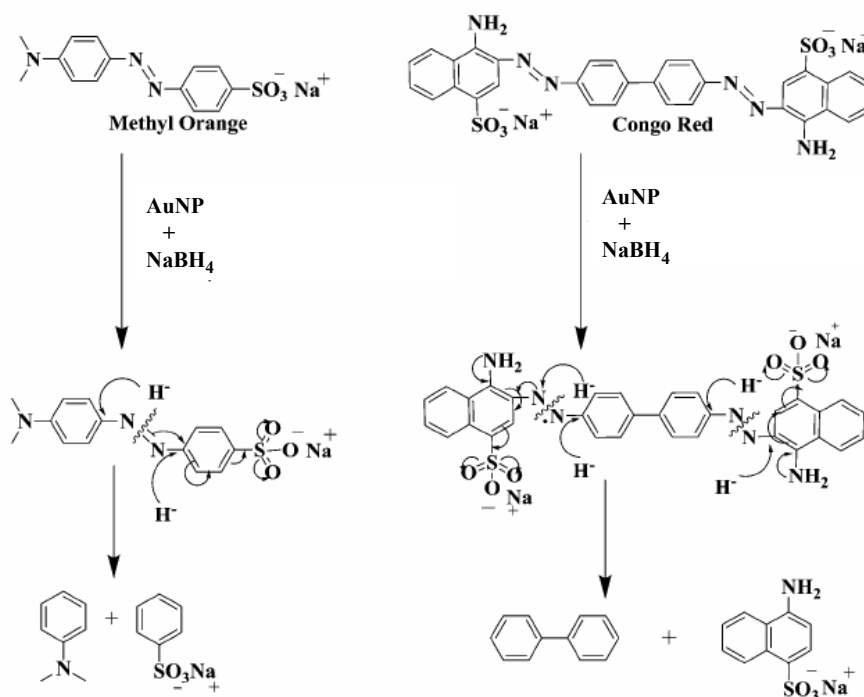


Figure 4.36 Plausible reduction mechanism for Congo Red and Methyl Orange. Reproduced from Ref. 344.

Reduction Mechanism for Methylene Blue: Methylene blue is a water-soluble cationic dye used as a redox indicator. It is also a major water pollutant. In aqueous media, MB absorbs light around 664 and it decreases and become colourless in presence of excess of NaBH_4 resulting in the formation of Leuco Methylene Blue (LMB). Studies conducted by B. Reddy explains a possible mechanism for the catalytic degradation of Methylene Blue to Leuco Methylene Blue using gold nanoparticles in the presence of sodium borohydride (Figure 4.37).³⁴⁵

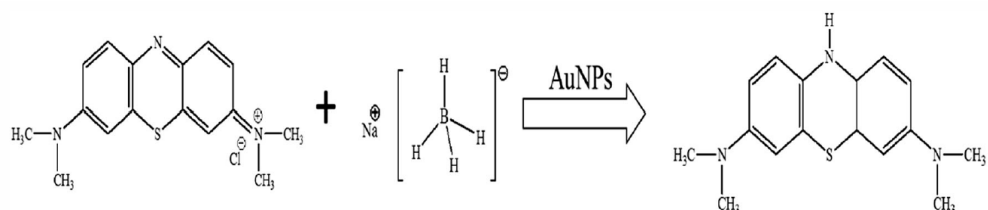


Figure 4.37 Plausible degradation mechanism of Methylene Blue to Leuco-Methylene Blue. Reproduced from Ref. 345.

The reduction of Methylene Blue by AuNP in presence of NaBH_4 can be explained by Langmuir-Hinshelwood mechanism (see Section 8.1.3) where the initially adsorbed BH_4^- ions act as a donor and donate electrons to the AuNPs which leads to the formation of a negatively charged layer around them.²¹⁸ Successively, AuNPs transfer these electrons to MB molecules which facilitate the reduction reaction at the surface of AuNPs. Works did by Azad et al., and Khan et al. showed a similar tendency of BH_4^- ions to form a negatively charged layer around AuNPs in an aqueous environment.^{346,347} This facilitated the strong attraction of the cationic MB onto the surface of AuNPs through electrostatic interaction, which results in a fast electron transfer between BH_4^- ions and MB ions.³⁴⁶ The reaction kinetics could be easily monitored by measuring the decrease in absorption peak intensity of methylene blue at 664 nm and 614 nm.

Reduction of Congo Red (CR): Rajesh et al. studied the catalytic degradation of Congo Red using Ag and Au nanoparticles in the presence of sodium borohydride.³⁴⁴ This reaction can be carried out at room temperature and the degradation happens only in the presence of a catalyst (Figure 8.9). Additionally, this reaction can be easily monitored using UV-visible spectrometer by measuring the decrease in absorption intensity of two absorption peaks at 495 nm ($\pi \rightarrow \pi^*$) and 350 nm ($n \rightarrow \pi^*$) respectively. Since these reactions are carried out in the presence of an excess of sodium borohydride they can be considered as pseudo-first order reaction.

Figure 4.38 (a) shows the successive UV-Vis spectra of degradation of Congo Red ($\lambda = 498$ nm) taken every minute after addition of $\text{Au}@SiO_2@PSS$ catalyst and (b) shows the linear plot of C_t/C_0 versus time obtained for different amounts of added catalyst. Similar to the 4-NP case, this reaction also follows pseudo-first order kinetics in the presence of an excess of NaBH_4 , and the apparent reaction rate constants can be estimated from the slopes of $\ln(C_t/C_0)$ linear plots versus time. In contrast to the reduction of 4-nitrophenol, the induction time increased to about 2 minutes for more bulky CR molecule.

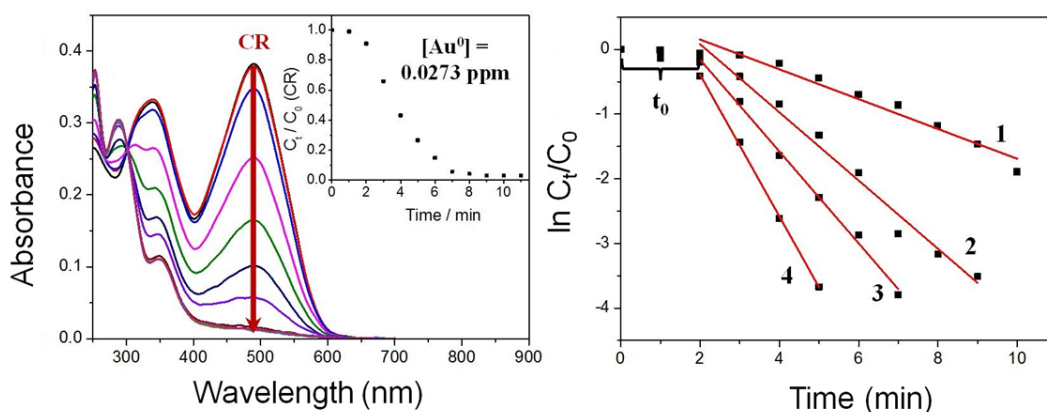


Figure 4.38 (a) Successive UV-Vis spectra were taken every minute during borohydride degradation of Congo Red after addition of Au@SiO₂@PSS catalyst and corresponding conversion plot versus time (inset); (b) Plots of $\ln(C_t/C_0)$ versus time obtained at different concentrations of Au@SiO₂@PSS catalyst. All experiments were carried out with initial concentrations $[CR]_0 = 0.027 \text{ mmol L}^{-1}$ and $[NaBH_4]_0 = 0.081 \text{ mol L}^{-1}$. $[Au^0]$ in reaction mixture was: (1) 0.0136 ppm; (2) 0.0273 ppm; (3) 0.0409 ppm; (4) 0.0545 ppm. Apparent rate constants determined from the slopes of linear fit are: (1) 0.230 min^{-1} ; (2) 0.527 min^{-1} ; (3) 0.710 min^{-1} ; and (4) 1.10 min^{-1} .

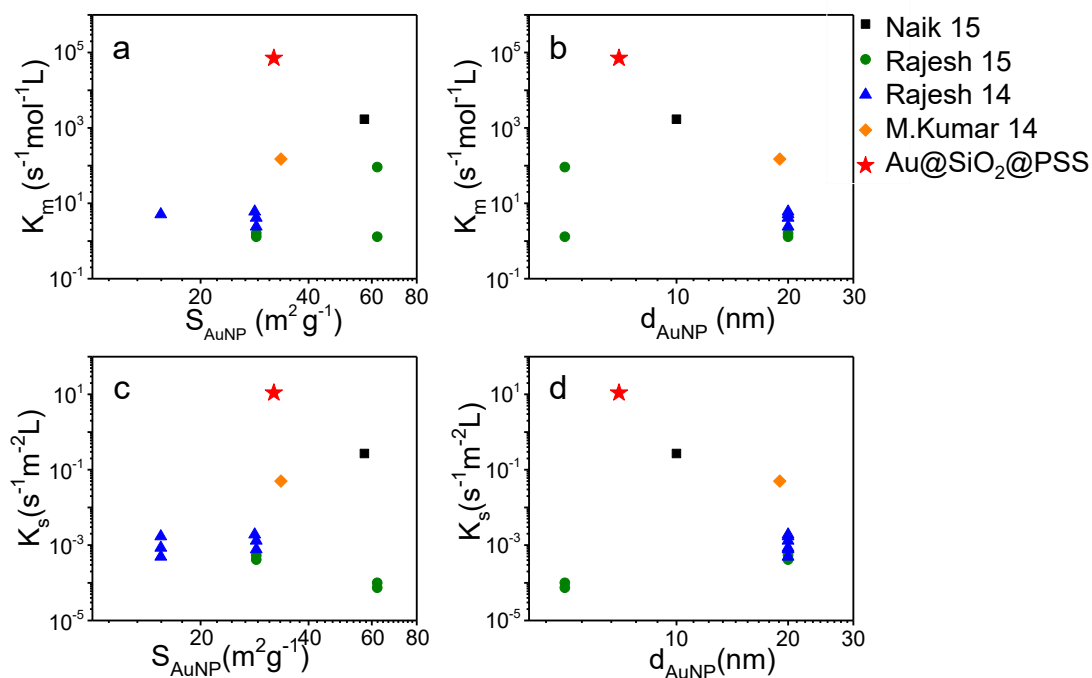


Figure 4.39 The comparison of normalised reaction rate constant, (a, b) K_m ; (c, d) K_s , determined for Au@SiO₂@PSS catalyst (red star) with values reported in the literature for analogous catalytic systems: black cubes - Naik15,³⁴⁸ green circles - R.Rajesh15³⁴⁹ blue triangles (up) - R.Rajesh14³⁴⁴ orange diamonds - M.Kumar14.³⁵⁰

Surprisingly, normalised rate constants determined for this reaction exceed those for 4-NP more than 4 times: $K_m = (7.1 \pm 1.3) \times 10^4 \text{ s}^{-1} \text{ mol}^{-1} \text{ L}$ and $K_s = 10.9 \pm 2.0 \text{ s}^{-1} \text{ m}^{-2} \text{ L}$, respectively. Figure 4.39 shows the comparison between K_m and K_s values obtained for the reduction of CR using other analogous yolk-shell type catalysts reported in literature up to date.^{344,348–350} The acquired results revealed that the obtained K_m and K_s values for CR were found up to 4 orders of magnitude higher as compared to other catalysts recently reported in the literature. This study was of particular interest for water purification.

Table 4.2 summarises apparent rate constants (k_{app}) and rate constants normalised with respect to the molar catalyst concentration in the reaction mixture (K_m) and catalyst surface area (K_s). In all cases, the nanoparticles are considered as spherical particles for simplicity. Numerical values, which are reported in corresponding publications, are presented as obtained values. Other values were re-calculated based on experimental data provided for each particular system.

Table 4.2 Summary of the reaction rate constants for catalytic reduction of Congo Red and Methyl Orange azo-dyes reported in the literature for various Au and Ag supported catalyst.

Sample name	d_{AuNP} nm	S^*_{AuNP} $\text{m}^2 \text{ g}^{-1}$	$\omega_{Au/cat}$ wt. %	k_{app} s^{-1}	K_m $\text{s}^{-1} \text{ mol}^{-1} \text{ L}$	K_s $\text{s}^{-1} \text{ m}^{-2} \text{ L}$	Ref. ^{a)}
Ag@CoFe ₂ O ₄	10	57.2	10.0	1.07×10^{-2}	1.7×10^3	2.7×10^{-1}	348
Ag/GO–Chit	20	28.6	17.7 ^{c)}	3.4×10^{-3}	1.3×10^0	4.1×10^{-4}	349
Au/GO–Chit	5	62.1	28.3 ^{c)}	2.1×10^{-3}	9.1×10^1	7.4×10^{-5}	
Ag/GO–Chit (MO) ^{b)}	20	28.6	17.7	4.4×10^{-3}	1.6×10^0	5.3×10^{-4}	
Au/GO–Chit (MO) ^{b)}	5	62.1	28.3	3.0×10^{-3}	1.3×10^0	1.0×10^{-4}	
Ag/GO-G3PAMAM	20	28.6	17.7 ^{c)}	1.6×10^{-2}	6.0×10^0	1.9×10^{-3}	344
Ag/GO-G3PAMAM	20	28.6	17.7	1.1×10^{-2}	4.1×10^0	1.3×10^{-3}	
Ag/GO-G3PAMAM	20	28.6	17.7	4.8×10^{-3}	2.4×10^0	7.7×10^{-4}	
Au/GO-G3PAMAM	20	15.5	28.3 ^{c)}	1.2×10^{-2}	5.1×10^0	1.7×10^{-3}	
Au/GO-G3PAMAM	20	15.5	28.3	6.1×10^{-3}	5.1×10^0	8.5×10^{-4}	
Au/GO-G3PAMAM	20	15.5	28.3	3.5×10^{-3}	5.1×10^0	4.9×10^{-4}	
Ag _{0.6} Ni _{0.4} NPs (MO) ^{b)}	19 ^{c)}	33.5	n/s	1.2×10^{-1}	1.5×10^2	5.0×10^{-2}	350
Au@SiO ₂ @PSS (present work)	7.0 ^{d)}	32.0	0.060	n/a ^{e)}	7.1×10^4	1.1×10^1	139

^{a)} References are given in the reference section with numbers same as mentioned in the table;

^{b)} MO: Methyl Orange;

^{c)} Content of Au(Ag) not specified, loading (wt.%) was determined based on experimental conditions;

^{d)} Median AuNP size determined from descriptive analysis of TEM images;

^{e)} k_{app} varied depending on the amount of added Au@SiO₂@PSS catalyst.

Reduction of Methyl Orange (MO): As mentioned above, the Au@SiO₂@PSS catalyst was used to study the degradation of methyl orange in the presence of sodium borohydride. The experiment was carried out by measuring the reduction of absorbance of Methyl Orange ($\lambda = 464$ nm) at different amount of added catalyst. The reaction was monitored using UV-Vis spectroscopy. Figure 4.40 (a) shows the successive UV-Vis spectra of degradation of Methyl Orange taken every 2 minutes after addition of Au@SiO₂@PSS catalyst and (b) shows the plot of $\ln(C_t/C_0)$ versus time obtained for different amounts of added catalyst.

From the absorbance spectra, it is evident that at a low amount of AuNPs (0.273 ppm) a complete degradation of Methyl Orange is reached. Despite the fact that this reaction is carried out in the presence of an excess of NaBH₄ maintaining similar experimental conditions as followed in the previous cases when compared to the catalytic reduction of 4-NP and CR this reaction deviates slightly from the first order kinetics due to unknown reasons. Hence it was not possible to estimate the rate constants for this reaction. Nevertheless, from the Figure 4.40 (b), it is evident that even at a low amount of AuNP (0.0545 ppm) the reaction was completed in less than 5 minutes showing the high activity of the Au@SiO₂@PSS catalyst.

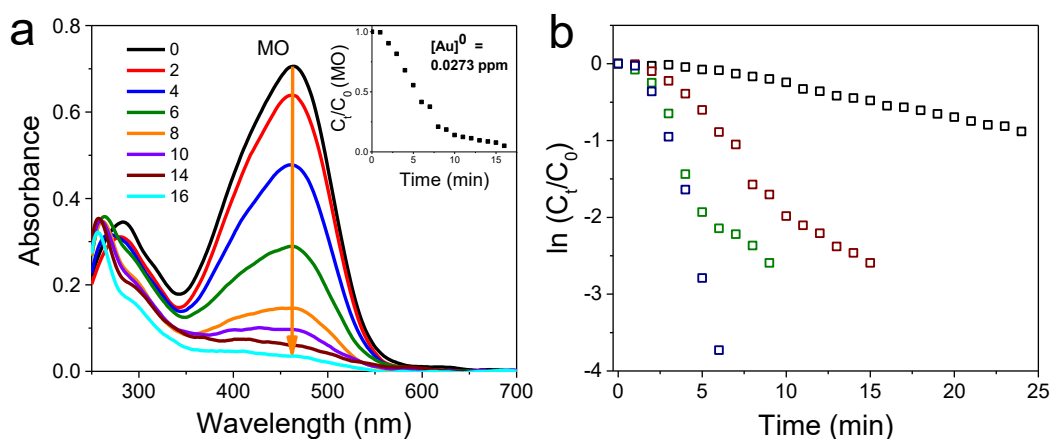


Figure 4.40 (a) Successive UV-Vis spectra were taken every minute during borohydride degradation of Methyl Orange in the presence of sodium borohydride after addition of Au@SiO₂@PSS catalyst and corresponding conversion plot versus time (inset); (b) Plots of $\ln(C_t/C_0)$ versus time obtained at different concentrations of Au@SiO₂@PSS catalyst. All experiments were carried out with initial concentrations $[MO]_0 = 0.027$ mmol L⁻¹ and $[NaBH_4]_0 = 0.081$ mol L⁻¹. Amount of catalyst in the reaction mixture was: black squares - 0.0136 ppm; brown squares - 0.0273 ppm; green squares - 0.0409 ppm; and blue squares - 0.0545 ppm.

Reduction of Methylene Blue (MB): The reduction of Methylene Blue follows a pathway which is similar to that of azo dye (Figure 4.37). In this case, the nanoparticle acts as an electron relay between the nucleophilic BH₄⁻ ions and electrophilic MB ions. Figure 4.41 (a) shows the successive UV-Vis spectra of degradation of Methylene Blue taken every minute after addition of Au@SiO₂@PSS catalyst and (b) shows the logarithmic plot of $\ln(C_t/C_0)$ versus time obtained

for different amounts of added catalyst. The reaction was monitored by measuring the decrease in absorbance intensity at $\lambda = 664 \text{ nm}$.^{345,351} Similar to Methyl Orange degradation, this reaction also deviates from the first order kinetics, although a complete degradation of Methylene Blue was observed in less than 10 minutes at a lower amount of added catalyst (0.0273 ppm).

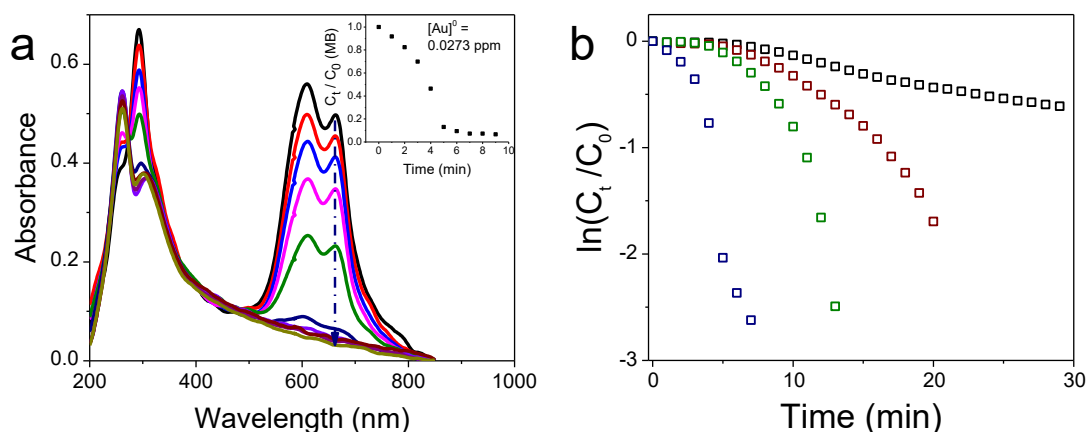


Figure 4.41 Successive UV-Vis spectra taken every minute during borohydride degradation of Methylene Blue after addition of $\text{Au@SiO}_2\text{@PSS}$ catalyst and corresponding conversion plot versus time (inset); (b) Plots of $\ln(C_t/C_0)$ versus time obtained at different concentrations of $\text{Au@SiO}_2\text{@PSS}$ catalyst. All experiments were carried out with initial concentrations $[\text{MB}]_0 = 0.027 \text{ mmol L}^{-1}$ and $[\text{NaBH}_4]_0 = 0.081 \text{ mol L}^{-1}$. Amount of catalyst in the reaction mixture was: black squares - 0.00544 ppm; brown squares - 0.00816 ppm; green squares - 0.0136 ppm; and blue squares - 0.0273 ppm.

4.3.6 Conclusion

The $\text{Au@SiO}_2\text{@PSS}$ catalyst was prepared using PS-*b*-P4VP block copolymer as a sacrificial template and pre-synthesized AuNPs via sequential formation of silica shell and porous silica support, followed by pyrolytic removal of organic and polymeric components. PS-*b*-P4VP micelles were used as a dual template for encapsulating the gold nanocatalyst and deposition of silica shell, enabling an easy, robust, and scalable synthesis of $\text{Au@PS-}b\text{-P4VP@SiO}_2$ particles. The embedding of Au@SiO_2 particles into porous silica support not only prevented Au@SiO_2 particles from aggregation and fusion but also ensured an easy access to the nanocatalyst surface for reactants during catalytic process. In addition, gold nanocatalyst enclosed inside porous silica shell is free of any capping agents after pyrolysis. The $\text{Au@SiO}_2\text{@PSS}$ catalyst was used to study the catalytic reduction of 4-NP and degradation of CR, MO and MB. The results obtained from the reduction of 4-NP and degradation of CR were compared to similar yolk-shell structures reported in the literature. The catalytic activity of $\text{Au@SiO}_2\text{@PSS}$ catalyst was found superior as compared to other analogous catalytic systems reported in literature till date, which is presumably attributed to above-mentioned factors.

4.4 CONTINUOUS CATALYSIS

4.4.1 Motivation

In the recent past, flow-type catalytic microreactors which utilise the advantages of both nanocatalysis and flow chemistry has gained a lot of interest.^{352–360} The comparison of catalysed Suzuki-Miyaura reactions in batch and flow microreactor system conducted by Phan et al. had shown that the miniaturisation of the interaction area between the catalyst and the reactants enables improved heat and mass transfers and an intimate contact between reagents and catalysts leading to a higher activity than that in batch.³⁵⁶ Frost et al. demonstrated that anchoring heterogeneous catalysts inside a continuous-flow reactor or in a microreactor can overcome many drawbacks associated with their activity and interaction between reactants.³⁵⁷ Besides, microreactors enhance the possibility of catalyst screening and highly efficient catalytic reactions providing the opportunity to perform safe and efficient chemical reactions. The flow catalysis approach enables a directed reactant flux through an immobilised catalyst facilitating an increased mass transfer. It exploits and enhances the advantages of both nanocatalysis and flow chemistry. It is based on the efficient immobilisation and stabilisation of nanocatalysts inside the microreactor thereby supporting nanoparticles that are uniform in size and have good accessibility to their active sites by the reagents.

Lately, metal nanoparticles with supported structures have gained a lot of interest in the field of nanocatalysis. In one such study, Park et al. have employed Ni@SiO₂ yolk-shell structures as a model catalyst in the steam reforming of methane.³⁶¹ The catalyst studies were conducted in a fixed bed continuous flow reactor containing the yolk-shell catalyst. At a high Ni loading with respect to the silica (ca. 89 wt. %) the catalyst exhibited above 90 % efficiency for methane conversion and the catalyst was regenerated by a heat treatment. A similar work did by Guo et al. dealt with the use of Ru@C yolk-shell nanostructures in a fixed bed reactor to study the hydrogenation of toluene.³⁶² Recently, Gao et al. developed a continuous flow reactor using a slurry of copper hydroxysulfates@metal organic framework (CHS@MOF) yolk-shell structure type catalyst in the form of a tubular reactor and passing the reactants through the slurry at a flow rate of 0.05 mL min⁻¹ for the acetalization of aldehydes with ethanol.³⁶³

From the results and high performance obtained for the already discussed system, a continuous catalytic reactor to effectively remove azo dyes from contaminated water was devised. The catalytic system discussed here comprises above-discussed Au@SiO₂ yolk-shells infiltrated into a porous glass substrate.

4.4.2 Fabrication

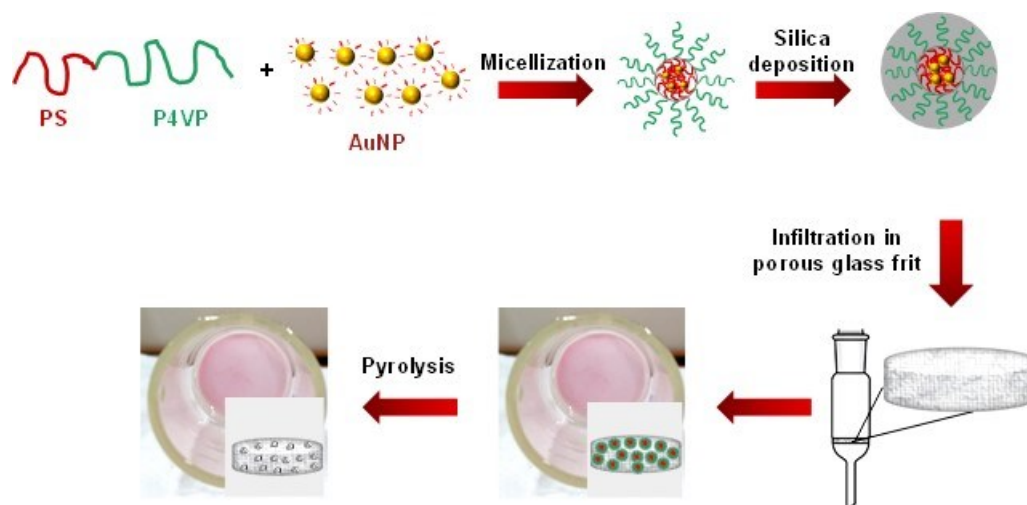


Figure 4.42 Schematic showing the preparation of flow-type catalytic system by infiltration of Au@SiO₂ yolk-shells in a porous glass frit.

As shown in Figure 4.42, the preparation of continuous flow catalytic system (reactor) based on yolk-shell particles involves 4 steps as follows: (1) Enclosing the metal nanocatalyst (eg. AuNPs) in the PS core of PS-*b*-P4VP BCP micelles via solvent exchange; (2) Deposition of silica shell onto the block copolymer micelles; (3) Infiltration of Au@PS-*b*-P4VP@SiO₂ in a porous glass frit; (4) Removal of the block copolymer template via pyrolysis leaving Au@SiO₂ yolk-shells sintered to the glass frit.

Three frits, P5-0.5, P5-1.0, and P5-2.0, were prepared with different Au@PS-*b*-P4VP@SiO₂ loading with respect to the mass of BCP ($m_{\text{BCP}} = 0.5 \text{ mg}, 1.0 \text{ mg}, 2.0 \text{ mg}$). Au@PS-*b*-P4VP@SiO₂ particles were prepared as discussed in Section 3.3.4. A pre-weighed amount of Au@PS-*b*-P4VP micellar dispersion was reacted with silica sol for 2 hours. After 2 hours, the reaction mixture was collected and Au@PS-*b*-P4VP@SiO₂ particles were purified by multiple washing cycles with ethanol to remove the unreacted precursor and other organic residues which are plausibly present after the reaction. Washed Au@PS-*b*-P4VP@SiO₂ particles were redispersed in ethanol maintaining an initial concentration of 0.1 mg g^{-1} . As support for the infiltration of pre-synthesized Au@PS-*b*-P4VP@SiO₂ particles commercially available porous glass frits (sintered glass frit discs, biplane, Series 16, diameter of the frit, $d_{\text{frit}} = 2.0 \text{ cm}$, procured from ROBU) were used. Two frits with a pore size of 10-16 μm (P4) and 1.0-1.6 μm (P5) were tested. Prior to infiltration, the frit was washed several times with ethanol using a water jet vacuum aspirator pump with an end vacuum of 16 mbar and a flow rate of 400 mL h^{-1} . The as-prepared Au@PS-*b*-P4VP@SiO₂ particles were infiltrated through the frit using the water jet vacuum aspirator pump. The frit was then subjected to pyrolysis at $300 \text{ }^\circ\text{C}$ for 6 hours to remove the block copolymer template and other organic residues present if any. The frit loaded with $m_{\text{BCP}} = 1.0 \text{ mg}$ was used for catalyst studies.

The parent dispersion of Au@PS-*b*-P4VP@SiO₂ particles, the frits, and the filtrate collected after infiltration was studied and characterized using several different methods (SEM, EDX, ICP-OES) in order to analyse infiltration efficiency.

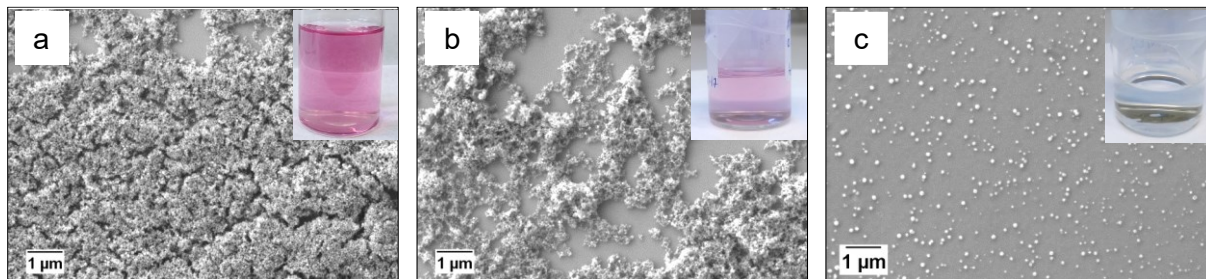


Figure 4.43 SEM images of the (a) As prepared Au@PS-*b*-P4VP@SiO₂ particles deposited from ethanol; (b) Filtrate collected after infiltration through P4 frit; (c) Filtrate collected after infiltration through the P5 frit. Inset show optical images of (a) As prepared dispersion; (b) Filtrate after infiltration of the feed through P4 frit; (c) Filtrate after infiltration of the feed through the P5 frit.

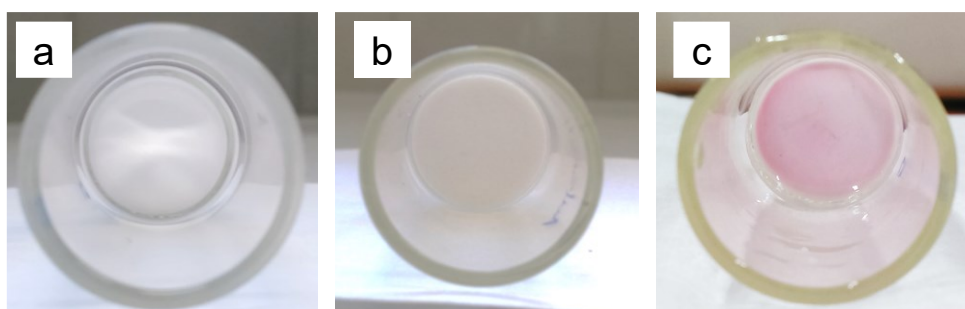


Figure 4.44 Optical images of (a) Empty P5 frit; (b) P4 frit, (c) P5 frit loaded with Au@SiO₂ yolk-shell nanoparticles.

Figure 4.43 (a) shows the SEM images of the as-prepared Au@PS-*b*-P4VP@SiO₂ nanoparticles deposited onto silica wafer from ethanol, whereas images (b) and (c) show the corresponding SEM images of the collected filtrate after infiltration through the frits P4 (10-16 μm pore size) and P5 (1.0-1.6 μm pore size), respectively. Figure 4.44 shows the optical image of an empty P5 frit and P4 and P5 frits after infiltration of the Au@PS-*b*-P4VP@SiO₂ particles. The sample collected after infiltration through the P4 frit shows the presence of considerable amount of Au@PS-*b*-P4VP@SiO₂ particles similar to the as-prepared feed solution. The pink colour of the filtrate (inset of Figure 4.43 b) and the optical image of the frit (Figure 4.44 b) also suggests that major amount of Au@PS-*b*-P4VP@SiO₂ particles passed through the P4 frit with 10-16 μm pore size. In contrast, the filtrate collected after passing Au@PS-*b*-P4VP@SiO₂ particles through the frit P5 with a pore size of 1.0-1.6 μm shows a relatively small amount of Au@PS-*b*-P4VP@SiO₂ particles present in the filtrate (Figure 4.43 c) as compared to the as-prepared sample and the filtrate from P4. The pink colour of P5 frit after infiltration (Figure

4.44 c) also proves that infiltration efficiency in the P5 case was much better as compared to P4.

These findings were further confirmed by UV-Vis spectroscopy. From the UV-Vis spectra (Figure 4.45 a) it can be clearly seen that after infiltration the absorption intensity of AuNP plasmon peak ($\lambda_{\max} = 540$ nm) decreased slightly after passing through P4 frit pointing to the entrapment of some of the Au@PS-*b*-P4VP@SiO₂ particles in the frit pores. But in the case of filtrate from P5 frit, the absorption intensity was considerably reduced when compared to the as-prepared sample and with filtrate from the P4 frit. Notably, in P5 filtrate the intensity of AuNPs' plasmon peak in the filtrate was beyond the detection limit of the instrument, suggesting efficient entrapment of Au@PS-*b*-P4VP@SiO₂ particles in the frit pores. Thus all further experiments were carried out with P5 frits with a pore size of 1.0 - 1.6 μm . After infiltration of Au@PS-*b*-P4VP@SiO₂ particles, the P5 frit was pyrolyzed in the air at 300 $^{\circ}\text{C}$ for 6 hours. Pyrolysis was done in order to remove the block copolymer template to obtain Au@SiO₂ yolk-shell nanoparticles. It was also expected that during pyrolysis the Au@SiO₂ particles will be sintered onto the grains surfaces comprising frit which facilitates the particles to attach firmly to the frit pore walls.

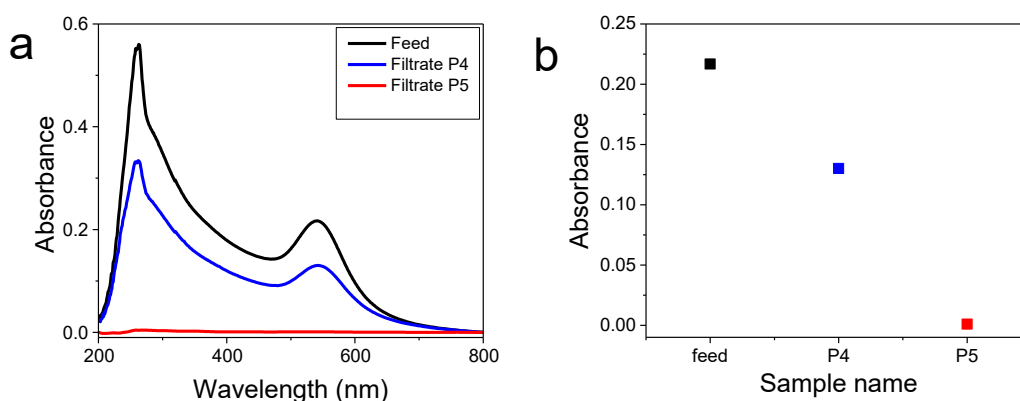


Figure 4.45 (a) The UV-Vis absorbance spectra of as-prepared Au@PS-*b*-P4VP@SiO₂ feed solution (black), and filtrates collected after infiltration of feed solution into P4 (blue) and P5 (red), respectively; (b) The intensities of plasmon peak of AuNP at 540 nm in feed solution and filtrate collected after infiltration of particles into P4 and P5 filter frits.

Figure 4.46 shows the top-view optical image of P5 frit and Figure 4.47 shows top view SEM images of P5 frit after loading with Au@SiO₂ yolk-shell nanoparticles taken at different magnifications using (a) Secondary electron (SE2) detector, (b, c) InLens detector and (d) Backscattered electron detector (ESB). Au@SiO₂ yolk-shell nanoparticles deposited on the surface of the frit grains can be clearly seen on high magnification SEM images. The uniformity of Au@SiO₂ yolk-shell nanoparticle distribution over the frit surface can be revealed from the low magnification SEM and optical images.



Figure 4.46 Top view optical image of P5 frit after loading of with Au@SiO₂ yolk-shell nanoparticles.

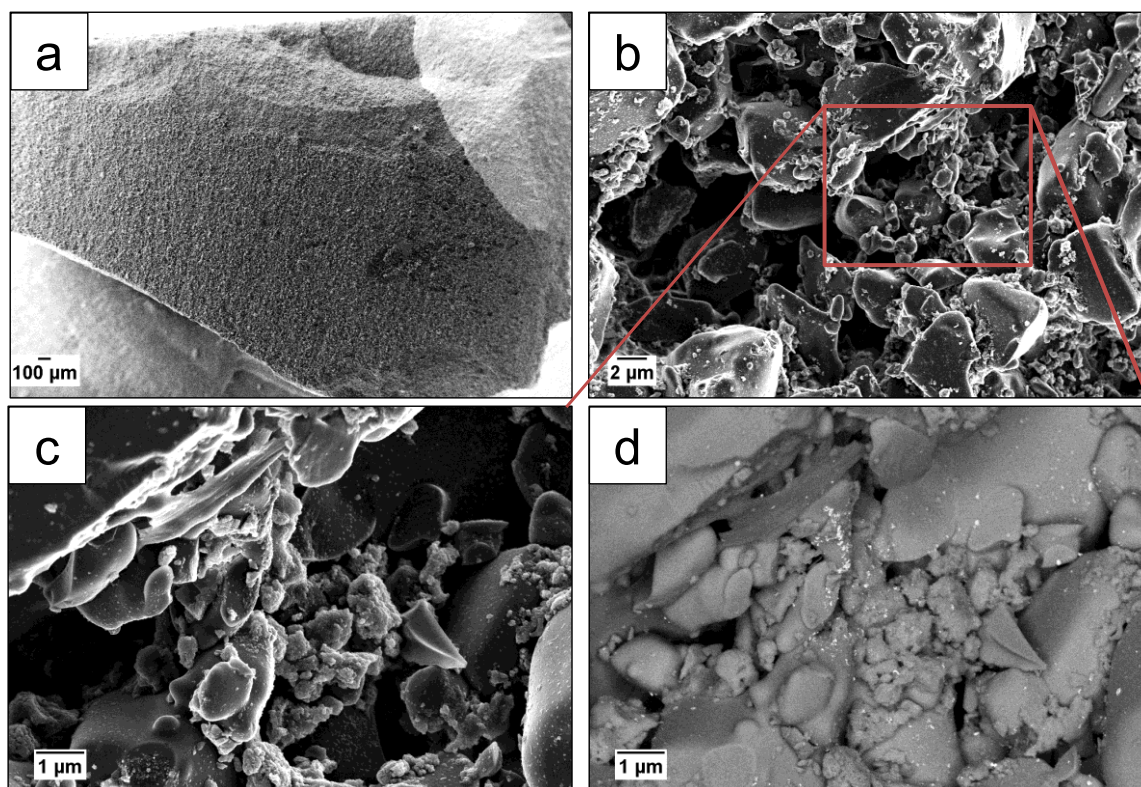


Figure 4.47 Top view SEM images of P5 frit after loading with Au@SiO₂ yolk-shell nanoparticles taken at different magnifications using (a) SE2 detector; (b, c) InLens detector; and (d) ESB detector; (c,d) shows the magnified view of the rectangular region in the image (b). Scale bars on image (a) 100 μm ; (b) 2 μm ; (c, d) 1 μm .

To study the distribution of Au@SiO₂ yolk-shell particles through the frit, it was broken into pieces using a blade. Figure 4.48 and Figure 4.49 shows optical and SEM cross-sectional images of the same frit. From the comparison of the top view and cross-sectional images shown in Figure 4.47 and Figure 4.49, it can be concluded that distribution of Au@SiO₂ yolk-shells

located in the upper part of the frit is relatively uniform. The pink colour originating from the infiltrated Au@SiO₂ yolk-shells penetrates ca. 20-30 % of the frit thickness, as can be concluded from the cross-sectional optical image (Figure 4.48). The penetration thickness is a bit shallower at one side of the frit and deeper at the opposite side. Furthermore, from the cross-sectional optical image, it is obvious that there exists a distinct borderline between frit parts with and without Au@SiO₂ yolk-shells.



Figure 4.48 Cross-sectional optical image of P5 frit. The upper pink part shows the loaded Au@SiO₂ particles and the lower white part show the empty frit.

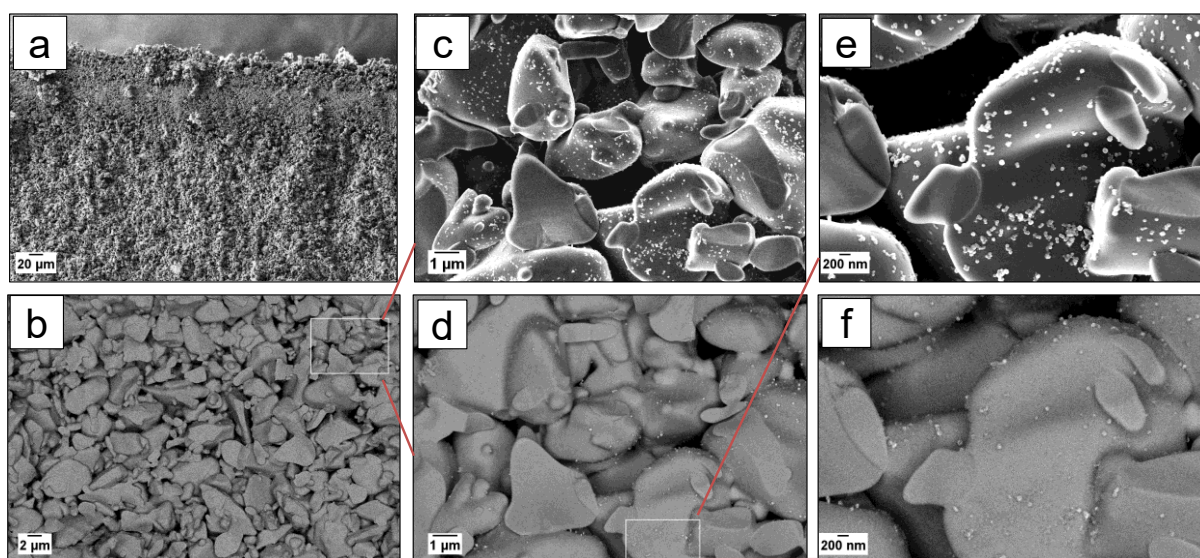


Figure 4.49 Cross-sectional SEM images of P5 frit after loading with Au@SiO₂ yolk-shell nanoparticles taken at different magnifications using InLens (top line) and ESB (bottom line) detectors. Image (c, d) shows the magnified image of the rectangular region in the image (b). Image (e, f) shows the magnified image of the rectangular region in image (d). Scale bars on image (a) 20 μm; (b) 2 μm; (c, d) 1 μm; and (e, f) 200 nm.

The presence of AuNP in the frit was further confirmed by EDX analysis. Figure 4.50 (a-d) shows SEM images and corresponding EDX gold maps taken from the upper pink part (top line) of the frit (loaded with Au@SiO₂ yolk-shell nanoparticles). Figure 4.50 e shows EXD spectra of three boxed areas shown on the corresponding SEM image (Figure 4.50 b), which confirms that Au signal in EDX spectrum indeed originates from small dot-like objects visible on SEM image, i.e., from the infiltrated Au@SiO₂ yolk-shells.

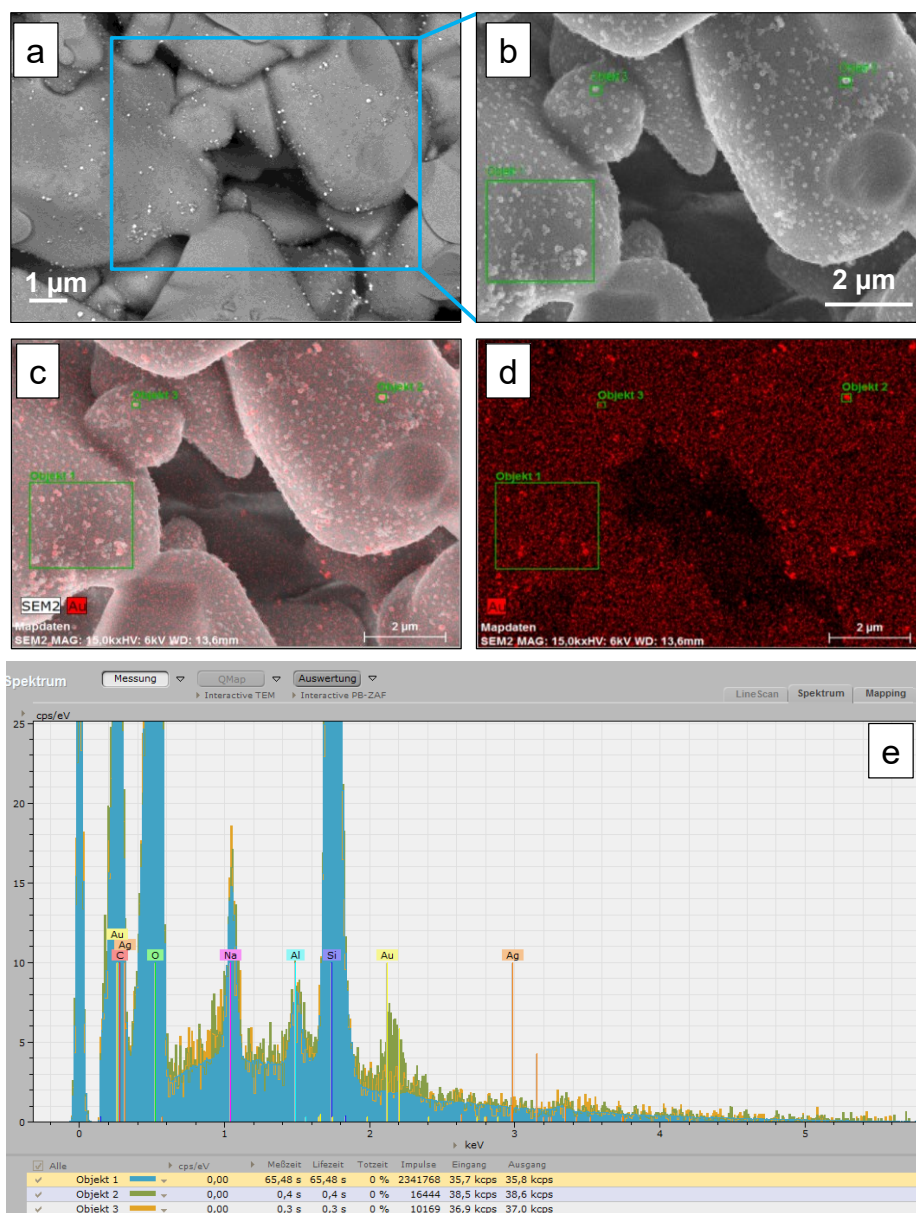


Figure 4.50 (a, b) Cross-sectional SEM images and (c, d) EDX gold map of the Au@SiO₂ yolk-shell nanoparticles infiltrated P5 frit indicating the presence of AuNP; (e) EDX spectra taken from the three boxed areas shown on the corresponding SEM image (b).

It is obvious that for most efficient flow catalytic system it is essential to have Au@SiO₂ particles uniformly distributed through the thickness of porous support, i.e., frit. In the following experiment, trials were made to increase the loading of yolk-shells into the frit by increasing the amount of infiltrated Au@PS-*b*-P4VP@SiO₂. However, this trial experiment was not successful since a substantial amount of yolk-shell nanoparticles were found on the surface of the frit and formed a closely-packed layer on top of the frit, which is discussed below in detail.

P5 frits loaded with three different amounts of Au@PS-*b*-P4VP@SiO₂ particles based on the mass of BCP ($m(\text{BCP}) = 0.5 \text{ mg}, 1.0 \text{ mg}, \text{ and } 2.0 \text{ mg}$) have been prepared which are further denoted as P5-0.5, P5-1.0 and P5-2.0, respectively. Figure 4.47 and Figure 4.49 shows the top-view and cross-sectional SEM images of P5-1.0 frit and results were discussed in previous part of this section. Figure 4.51 and Figure 4.52 shows the top-view and cross-sectional optical and SEM images of P5-0.5 and P5-2.0 frits, respectively. The scratch on the frit surface in Figure 4.51 (d) was caused by the glass cutter during sample preparation for SEM imaging.

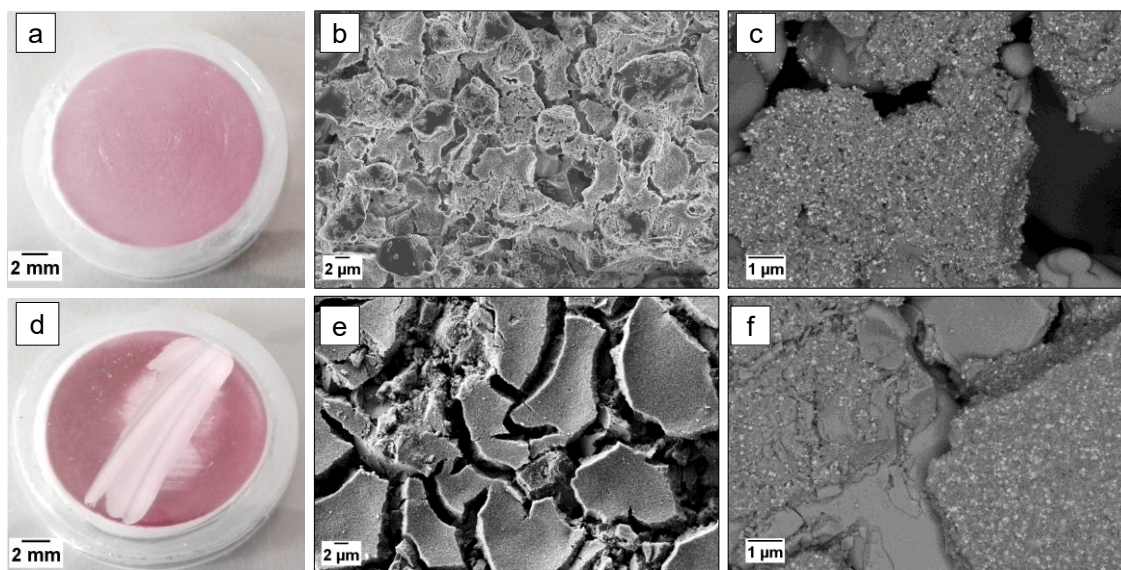


Figure 4.51 Top view optical images (a, d) and SEM images of (b, c) P5-0.5; (e, f) P5-2.0 frits after loading with Au@PS-*b*-P4VP@SiO₂ particles respectively; (b, e) InLens detector; (c, f) ESB detector. Scale bars on image (a,d) 2 mm; (b, e) 2 μm; (c, f) 1 μm.

Surprisingly, for both P5-0.5 and P5-2.0 frits, i.e. those infiltrated with the lowest and highest amount of Au@PS-*b*-P4VP@SiO₂ particles, a large fraction of the infiltrated particles were found on the surface of the frit as big assemblies when compared to P5-1.0 frit (Figure 4.47). In the case of P5-0.5 frit, the absence of Au@SiO₂ yolk-shells inside the cross-section of the frit points out to the fact that maybe the amount of particles infiltrated were not adequate to achieve a deep penetration (Figure 4.52 a-c). At the same time, in the case of P5-2.0 frit, it seems, that upon infiltration a certain fraction of particles might have been deposited inside the frit pores, whereas the other portion remained on the top surface which later might have blocked the pores of the frit. This resulted in the deposition of the following portions of the particles on the frit surface and, eventually, led to the formation of big assemblies of particles on the frit surface (Figure 4.51 e) and limited penetration of particles inside the frit cross-section. The reasons for such difference in particle penetration behaviour and their aggregation on the frit surface are not clear yet. Nevertheless, it is assumed that better infiltration efficiency, i.e. deeper penetration and homogeneous particle distribution within the frit pores, still might be achieved by further optimisation of infiltration condition, for example infiltrating higher amount of

Au@PS-*b*-P4VP@SiO₂ particles from both sides of the frit. Further experiments are currently in progress in this direction. Considering these results, the rest of the experiments were done with P5-1.0 frit.

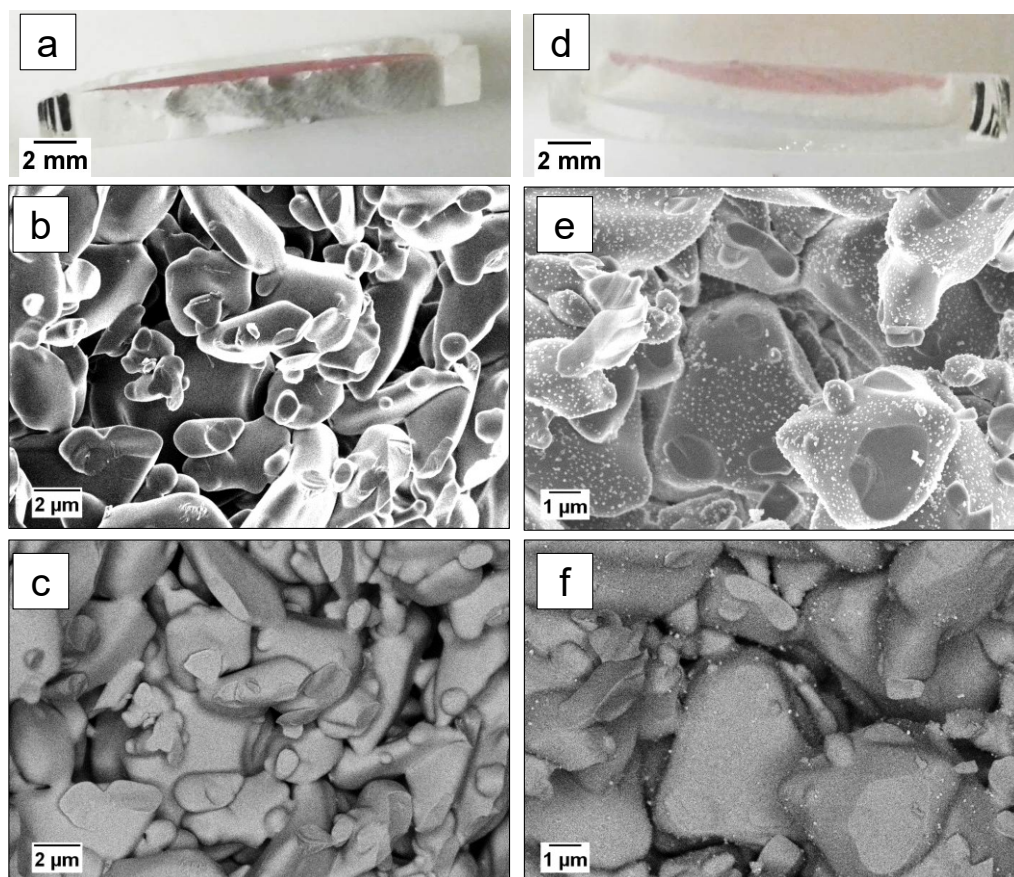


Figure 4.52 Cross-sectional optical (a, d) and SEM images of (b, c) P5-0.5; (e, f) P5-2.0 frits after loading with Au@PS-*b*-P4VP@SiO₂ particles; (b, e) InLens detector; (c, f) ESB detector. Scale bars on image (a, d) 2 mm; (b, c) 2 μm; (e, f) 1 μm.

To estimate the content of gold in the frit, Au@PS-*b*-P4VP micellar solution, Au@PS-*b*-P4VP@SiO₂ feed solution, as well as filtrate solution collected after the infiltration into P5 frit was analysed. For this purpose, 1.0 g of each solution was placed into a glass vial and solvents were evaporated on a rotary evaporator. The solid residues were then digested in aqua regia and analysed using inductively coupled plasma optical emission spectroscopy (ICP-OES). The results of the ICP-OES analysis are summarized in Table 4.3. As can be seen, the concentration and, subsequently, the amount of gold in parent Au@PS-*b*-P4VP micellar solution and Au@PS-*b*-P4VP@SiO₂ feed solution are almost same. Small differences are due to a minor loss of sample during silica shell formation and subsequent sample purification. In contrast, the content of gold in the collected filtrate is much lower, but still, comprises ca. 10 % of gold as compared to feed solution. Considering that during the infiltration step 10.0 g of feed solution of Au@PS-*b*-P4VP@SiO₂ particles was used as a standard, the content of gold being infiltrated into the frit can be estimated as the difference between the content of gold in feed solution and

in the collected filtrate. Based on ICP-OES results, the content of gold in frit was estimated as 72.2 μg . This information is essential for the further analysis of stability of Au@SiO₂ yolk-shell particles against leaching during continuous flow catalysis experiments.

Table 4.3 Results of ICP-OES analysis of Au@PS-*b*-P4VP micellar solution, Au@PS-*b*-P4VP@SiO₂ feed solution, and the filtrate.

Sample name	Solvent	m g	V ^a mL	[Au] ^b $\mu\text{g/g}$	m(Au) ^c μg
Au@PS- <i>b</i> -P4VP micellar solution	Methanol	10.0	12.63	8.14	81.4
Au@PS- <i>b</i> -P4VP@SiO ₂ particles, feed solution	Ethanol	10.0	12.67	8.12	81.2
Au@PS- <i>b</i> -P4VP@SiO ₂ particles, filtrate after P5 infiltration	Ethanol	8.94 ^d	11.33	0.10	9.0

^a – calculated based on solvent density, the content of solid counterpart was neglected;

^b – gold concentration was determined in $\mu\text{g/mL}$ and then converted into $\mu\text{g/g}$;

^c – total mass of gold determined for each sample;

^d – amount of filtrate collected after infiltration of 10.0 g of feed solution.

4.4.3 Flux Experiments on Frits Infiltrated with Au@SiO₂ Yolk-Shell Nanoparticles

For a catalyst to be used in continuous flow catalysis, the system should possess good stability throughout the reaction. Flow experiments were done in order to determine the range of flow rate at which continuous flow catalytic experiments can be conducted and calculate the flux at corresponding flow rates. This was done by passing water or reaction mixture (Congo Red and sodium borohydride) through the frit at different flow rates varying from 0.524 mL min⁻¹ to 3.007 mL min⁻¹. A peristaltic pump (Ismatec REGLO Digital 2/6 Variable Speed Pump with a flow rate range of 0.005 to 59 mL min⁻¹ operating at 115V/230V) was used to maintain a continuous flow through the frit and control the flow rate. The frit was placed into a self-designed holder and the cap of the holder with inlet opening was tightened to the frit head with a silicone rubber gasket using screws (see also Figure 4.55). The flow experiment was continued for 10 minutes at each flow rate and the corresponding filtrate was weighed with 2 minute time interval. The mass of collected solution was converted into the volume. The content of CR and sodium borohydride in solution was negligibly small (0.76 wt. %) with respect to the total weight of the solution. Therefore, the water density (1.0 g mL⁻¹) was used for all experiments. The flux was determined by dividing the volume of the filtrate collected per hour by the area of the frit ($d_{\text{frit}} = 2 \text{ cm}$, $S_{\text{frit}} = 3.14 \times 10^{-4} \text{ m}^2$).

Figure 4.53 shows the results on volumetric flux (J) corresponding to different volumetric flow rates (Q) for water passing through the empty P5 frit (black squares), water passing through the P5 frit infiltrated with Au@SiO₂ yolk-shell nanoparticles (blue triangles), and CR + BH₄ solution passing through the P5 frit infiltrated with Au@SiO₂ yolk-shell nanoparticles (red circles).

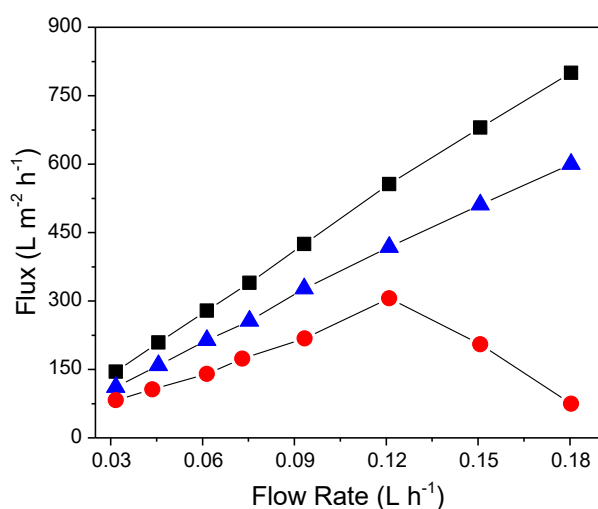


Figure 4.53 Comparison plot showing the variation in volumetric flux (J) as a function of volumetric flow rates (Q) for: black squares - water passing through empty P5 frit; blue triangles - water passing through P5 frit loaded with Au@SiO₂ yolk-shell particles; red circles - an aqueous solution containing Congo Red (0.067 mM) and sodium borohydride (0.2 M) passing through P5 frit loaded with Au@SiO₂ yolk-shell particles.

Water was passed through empty and loaded frit at varying flow rates, Q , and the flow were monitored for a definite period of time. The weight of the filtrate has been measured at each flow rate and the flux, J , has been calculated. The flux increases linearly with increase in the flow rate for both the empty and loaded frits. As can be seen, after infiltration of Au@SiO₂ yolk-shell nanoparticles the flux was slightly reduced as compared to the flux values obtained for the empty frit. The reduced flux values in the case of loaded frit can be due to the resistance offered by the Au@SiO₂ particle aggregates to the water flow. These aggregates may result in the partial closing of the frit pores. This can slow down the water flowing through these pores causing a reduction in flux when compared to the empty frit where water is allowed to flow freely without any additional hindrances. On the contrary, when the frit loaded with Au@SiO₂ yolk-shell nanoparticles was subjected under a feed of aqueous solution of Congo Red and sodium borohydride a further reduction of flux was detected as compared to the water feed alone. The flux values showed a linear behaviour with respect to the flow rate until 2.016 mL min⁻¹. At flow rates above 2.016 mL min⁻¹, feed started to accumulate at the frit head accompanied by a sudden decline in the flux values. It should be noted that sodium borohydride decomposes very quickly when dissolved in water and produces hydrogen gas. The presence of hydrogen might have caused an increase in the internal pressure, especially at higher flow rates,

which hindered the flow and thereby reduced the flux of the system at flow rates above $2.016 \text{ mL min}^{-1}$. It was also observed that after the continuous passing of Congo Red solution through the P5 frit for a longer period of time the frit surface became more red, suggesting that some part of dye might be deposited on the frit (Figure 4.54). But considering that CR molecule is very small as compared to the frit pores, it is rather less probable that frit pores have been blocked by dye molecules. Exact reasons for this variation in flux are not understood yet and require more studies. Nevertheless, taking into account of the results shown in Figure 4.53 and those discussed above, the experimental conditions for further catalytic experiments were limited to the flow rates ranging from 0.5 to 2.0 mL min^{-1} where no accumulation of feed in the frit head was visually observed.

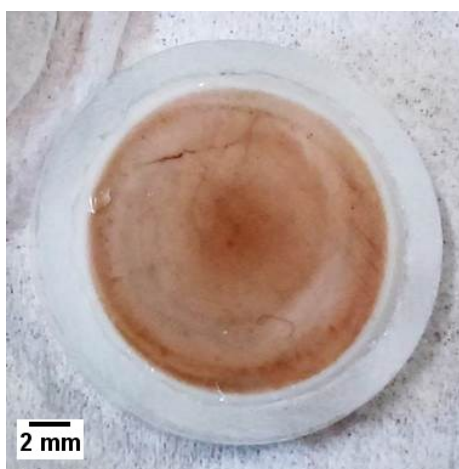


Figure 4.54 P5 frit after the continuous passing of CR + NaBH_4 solution for ca. 45 hours.

4.4.4 Continuous Flow Catalysis

Experimental Set Up: The efficiency of a continuous flow catalyst is described in terms of its ability to withstand the feed flow and its stability throughout the reaction. The as-prepared frit infiltrated with $\text{Au}@\text{SiO}_2$ yolk-shell nanoparticles was used as a flow-type catalyst for several catalytic processes. Its catalytic activity was investigated using the model reaction of borohydride reduction of 4-nitrophenol and catalytic degradation of various azo dyes.

The experimental setup employed to study continuous flow catalysis is depicted in Figure 4.55. The reaction mixture (feed) is passed to the frit head (inlet) with the aid of a peristaltic pump. The flux through the frit was regulated by varying the flow rate using the pump. The filtrate coming out of the frit was passed through the outlet tube to the flow-through UV-Vis cuvette which was placed inside the UV-Vis spectrometer. The absorbance of the filtrate inside the cuvette is measured continuously for certain period of time and recorded every minute during the continuous flow catalysis experiment. After each continuous flow experiment, the frit was intensively washed by pumping Millipore water through the frit for at least 20 minutes followed by passing nitrogen gas through the frit to remove residual water from the pores. Any

kind of heat and vacuum treatment of the frit was omitted in order to avoid possible temperature-induced changes in the catalytic activity.

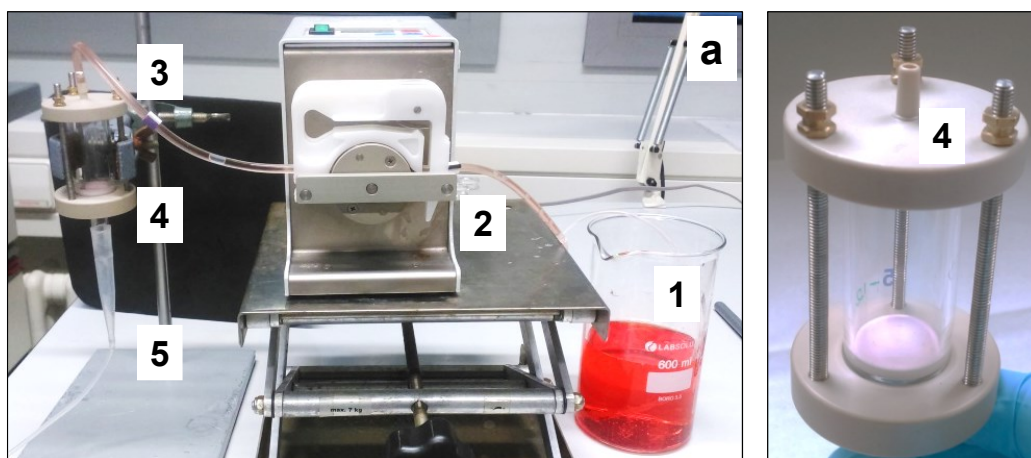


Figure 4.55 (a) Experimental setup for continuous flow catalysis; (b) Image of the frit holder. The parts are explained as 1 – Feed; 2 – Peristaltic Pump; 3 – Feed Inlet; 4 – Frit Holder; 5 – Outlet.

Stability of The Catalyst against Leaching under Continuous Flow: In order to study the stability of the AuNPs infiltrated inside the frit, the frit was subjected under a flow of water, Congo Red, and a mixture of Congo Red and sodium borohydride. The filtrate after the reaction was collected from the frit and used directly for measurements using inductively coupled plasma optical emission spectroscopy (ICP-OES). Water was passed through the frit at a low flow rate for an extended time and then at different flow rates. In Figure 4.56 (a), the red stars (in the blue rectangle) show the elution of AuNPs from the frit with respect to different flow rates of water. It can be seen that during each flow time some amount of AuNP is lost from the frit. But when the flow rate was increased (black squares bordered by blue circles) there was no considerable increase/change in the amount of AuNP eluded i.e., independent of the flow rate. On the other hand in Figure 4.56 (b), the red triangles corresponding to the concentration of AuNPs in the filtrate (blue rectangle) shows a higher concentration of ca. $1.5 \mu\text{g L}^{-1}$ of AuNPs present in the initial filtrate. This is in contrast to the mass of AuNPs eluted which is a very negligible amount of ca. $0.05 \mu\text{g}$ (Figure 4.56 a - red stars in blue square). When the flow time was increased the AuNP concentration decreased whereas the mass came to stable values. Upon further increase in flow, there was no change in the concentration and mass of AuNPs in the filtrate with respect to the second filtrate values, i.e., in both the cases (Figure 4.56 a, b) the AuNP elution was independent of the flow time and flow rate. This loss of particles can be explained based on the plausible reasons mentioned below. During infiltration, it is possible that some of the yolk-shells containing AuNPs loosely adhere to the frit pore. They can also be loosely bound to the surface of the frit (not in the pore). In this case, when fluid is passed through the frit, due to the pressure exerted by the liquid these loosely bound particles can leach out to the filtrate.

A slight increase in the concentration of AuNPs in the filtrate was detected by ICP-OES upon passing an aqueous solution of Congo Red through the frit (Figure 4.56 b - red triangles

bordered by a brown circle). A sudden increase in both the mass of AuNP (ca. $0.63 \mu\text{g}$, Figure 4.56 a – red star bordered by brown circle) and in the concentration of AuNP in the filtrate ($157 \mu\text{g L}^{-1}$, Figure 4.56 b – red triangle bordered by a brown circle) was observed upon passing a mixture of aqueous solution of Congo Red and sodium borohydride. It is assumable that the addition of borohydride ions might have caused some instabilities, such as change of pH from neutral to alkaline, in the system which resulted in a sudden increase in the washing out of AuNPs. It is known from the literature that sodium borohydride is used to dissolve solid silica particles to form hollow silica particles.³⁶⁴ Similar effects can be expected in this case also. It is plausible that upon passing the sodium borohydride through the frit, there is a sudden change of environment inside the frit and the sodium borohydride can partially dissolve/etch the silica shell of the loosely bound yolk-shell particles located inside or on the surface of the frit. This dissolution can cause either an increase in the pore size of the shell or in the partial degradation of the shell causing the nanoparticles to wash out from inside of the yolk-shell or in the washing out of the yolk-shell particle as a whole. With further extension of flow time at a single flow rate, the mass of AuNPs seemed to be stable whereas the concentration of AuNPs in the filtrate was decreased and came to a lower value ($< 0.1 \mu\text{g L}^{-1}$) which was beyond the detection limit of the instrument. Thus, after 6 hours of extended flow time under water, Congo Red, and an aqueous mixture of Congo Red and sodium borohydride, the total mass of AuNP lost was ca. $0.7 \mu\text{g}$.

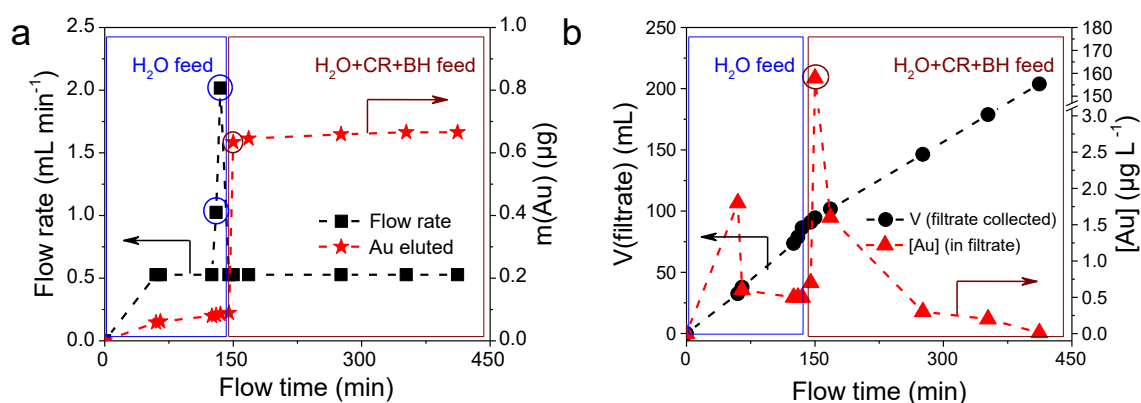


Figure 4.56 (a) Flow rate vs Flow time (black squares) and mass of AuNPs leached out from the frit (red stars) during continuous flow experiment under a feed of water (blue boxed area) and CR + NaBH₄ reaction mixture (brown boxed area); (b) Volume of the filtrate as function of flow time (black circles) and concentration AuNPs present in the filtrate with respect to corresponding flow time (red triangles) under a feed of water (blue boxed area) and CR + NaBH₄ reaction mixture (brown boxed area).

Reduction of Congo Red (CR): Initial continuous flow catalytic experiments were carried out on the catalytic degradation of Congo Red (CR) using sodium borohydride. The feed solution was prepared by diluting 0.2 mM, 100 mL solution of Congo Red with 200 mL of Millipore water followed by the addition of sodium borohydride (NaBH₄) equivalent to 0.2 M as a powder. The working concentration of CR and NaBH₄ was 0.067 mM and 0.2 M, respectively (CR:NaBH₄ = 1:3000 mol / mol) and the flow rate was kept constant at $0.528 \text{ mL min}^{-1}$. Figure

4.57 shows photographs of the frit mounted inside the holder, aqueous solutions of CR and CR + NaBH₄ collected before and after passing through the frit. The efficiency of CR degradation using given flow catalyst system can be clearly seen already from the optical images.

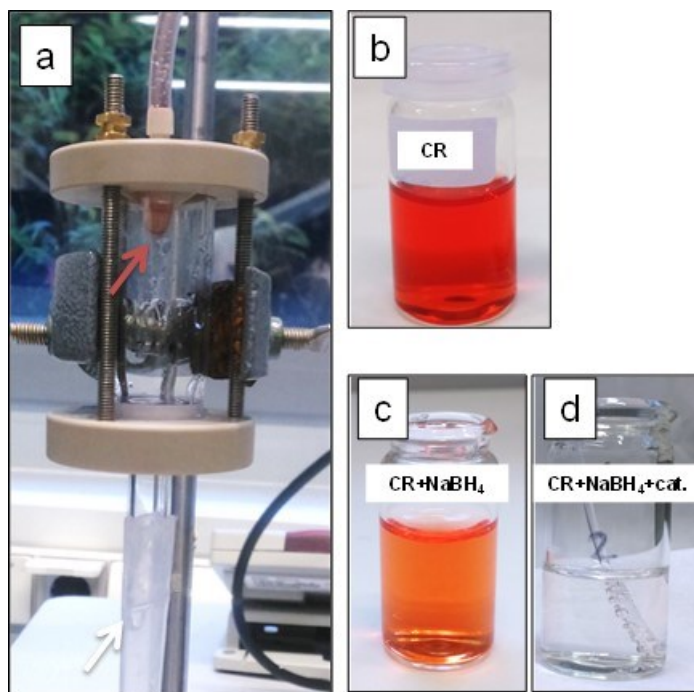


Figure 4.57 Optical images showing (a) Frit inside the holder; (b) Aqueous solution of CR; aqueous solution CR + NaBH₄ reaction mixture: (c) before passing; (d) after passing through the frit infiltrated with the Au@SiO₂ yolk-shell catalyst. The arrows on the image (a) point out the crimson coloured CR + NaBH₄ feed drop at the inlet and the colourless reaction mixture coming out of the frit loaded with Au@SiO₂ catalyst.

To investigate the efficiency of the catalytic system under the given reaction conditions, the course of the degradation of Congo Red was extended to ca. 5 hours. The reaction was monitored by UV-Vis in the wavelength range of 250 – 800 nm and the reduction in the absorbance peak of Congo Red at 499 nm versus time was measured. Figure 4.58 (a) shows selected UV-Vis spectra of CR (black) and CR+NaBH₄ aqueous solution after passing through the frit loaded with the Au@SiO₂ yolk-shell catalyst taken at particular times. Figure 4.58 (b) shows the plot of A_t / A_0 at 499 nm versus time during the continuous flow experiment, where A_0 and A_t are the absorbance of the initial spectrum and spectra were taken after t minutes of flow experiment, respectively. Initially, a feed of an aqueous solution of CR (0.067 mM) was fed through the frit and the absorbance was measured at $\lambda = 499$ nm with a time interval of 1 minute between the cycles. Next, a weighed amount of sodium borohydride equivalent to 0.2 M concentration (CR: NaBH₄ = 3000) was added to the feed as a powder and completely solubilized within ca. 1 minute. The CR + NaBH₄ reaction mixture (feed) was continuously passed through the frit for a period of ca. 5 hours at the flow rate of 0.528 mL min⁻¹ and the spectra were continuously recorded. The first 14 points in Figure 4.58 (b) correspond to CR only (black squares), whereas red points correspond to CR + NaBH₄ mixture. As can be seen from Figure

4.58 (b), a slight decrease in the absorbance intensity observed upon the passing of CR solution through the frit might be due to the deposition of CR in the frit pores. After addition of NaBH_4 , the absorbance intensity of CR remained on the same level for following several minutes, but then rapidly decreased within 2-3 minutes, indicating almost complete degradation of CR upon passing the reaction mixture through the frit loaded with $\text{Au}@/\text{SiO}_2$ yolk-shell catalyst. The time delay of ca. 5 minutes, i.e. from the time point when NaBH_4 was added until complete degradation of CR observed, was due to the presence of a residual solution of pure CR in connection tubes, which subsequently was replaced by CR/ NaBH_4 reaction mixture. As soon as CR/ NaBH_4 reaction mixture got in contact with $\text{Au}@/\text{SiO}_2$ particles located in the frit, complete degradation of CR was achieved being catalysed by the yolk-shell catalyst.

As can be seen from the plot shown in Figure 4.58 (b), after reaching its minima the absorbance values remained unchanged for the whole course of continuous flow catalysis experiment. The efficiency of CR degradation was maintained at 94 – 97 % for the whole flow catalysis experiment. These results clearly demonstrate the stability of given catalytic system under the continuous flow conditions and also shows that catalyst remained active throughout the reaction without any decline in its activity for the degradation of Congo Red dye.

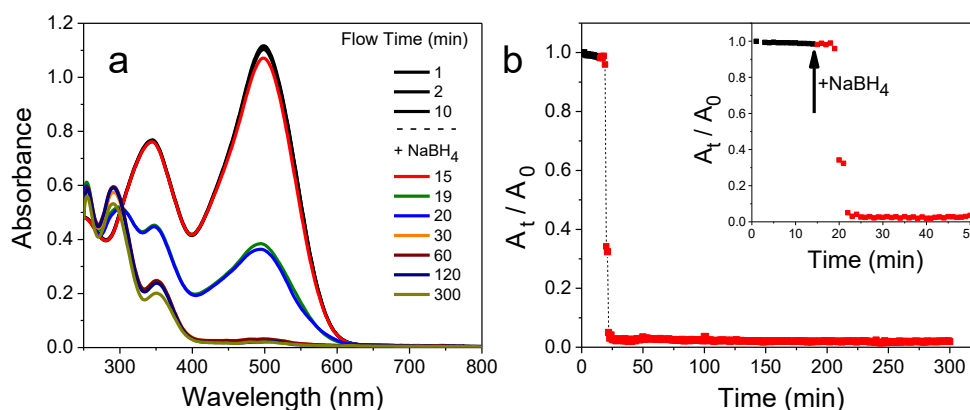


Figure 4.58 (a) Representative UV-Vis spectra of Congo Red (black) and Congo Red + NaBH_4 reaction mixture after passing through the frit loaded with $\text{Au}@/\text{SiO}_2$ yolk-shells taken at selected time points; (b) Plot of A_t/A_0 ($\lambda = 499$ nm) versus time obtained during the continuous flow catalysis experiment on degradation of Congo Red. Inset on (b) shows magnified part of initial 50 minutes of continuous flow catalysis experiment.

Reduction of Methyl Orange (MO): In order to investigate the catalytic efficiency of the same $\text{Au}@/\text{SiO}_2$ loaded frit, catalytic degradation of methyl orange (MO) was studied in addition to the degradation of Congo Red. After being used for CR degradation, frit was intensively washed with Millipore water, dried with the N_2 flow and then used for MO degradation. The experimental set-up and other experimental conditions were similar to those used for CR degradation (as described above). At first, a feed of aqueous solution of MO (0.067 mM) was fed through the frit and spectra were recorded to obtain initial absorbance intensity at $\lambda_{\text{max}} = 464$ nm. After

15 cycles, sodium borohydride was added as a powder to the aqueous solution of MO and solubilized to maintain the NaBH_4 concentration of 0.2 M. After addition of NaBH_4 , spectra were recorded for the next 5 hours and time dependency of peak intensity was monitored.

Figure 4.59 (a) shows the selected UV-Vis spectra of MO (black) and MO + NaBH_4 mixture after passing through the $\text{Au}@SiO_2$ loaded frit at time points of continuous flow catalysis experiment and (b) plot of A_t/A_0 measured at $\lambda = 464$ nm versus time. As can be seen, the time-dependent behaviour of MO + NaBH_4 mixture after passing through the frit is quite different as compared to previously discussed Congo Red experiment. Initially, after addition of sodium borohydride the A_t/A_0 values dropped from 1.0 to ca. 0.12 within 7 minutes, reaching maximum degradation efficiency of ca. 88%. Then, within next 25 minutes A_t/A_0 values gradually increased back, such that after ca. 50 minutes of continuous flow experiment degradation of MO was at ca. 40.% level (see Figure 4.59 b, inset). However, upon further period of time A_t/A_0 values started to decrease slowly again and after ca. 5 hours reached the level of ca. 0.3, that is ~70 % degradation of MO was achieved.

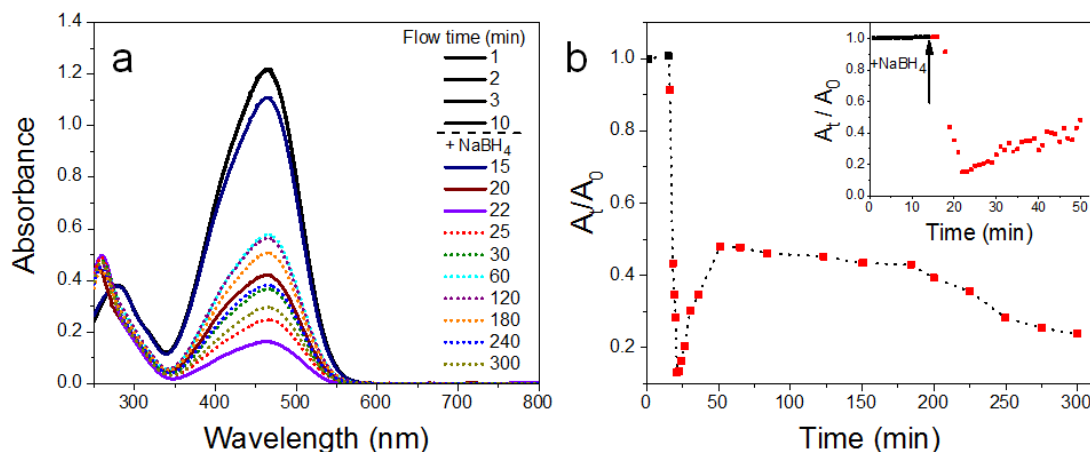


Figure 4.59 (a) Representative UV-Vis spectra of Methyl Orange (black) and Methyl Orange + NaBH_4 reaction mixture after passing through the frit loaded with $\text{Au}@SiO_2$ yolk-shells taken at selected time points; (b) Plot of A_t/A_0 ($\lambda_{max} = 464$ nm) versus time obtained during the continuous flow catalysis experiment on degradation of Methyl Orange. Inset on (b) shows magnified part of initial 50 minutes of continuous flow catalysis experiment. Spectra shown as dotted lines on the image (a) correspond to the time period when an increased A_t/A_0 values were observed as compared to its minima, that is starting from 25 minutes of continuous flow experiment.

Such non-monotonic behaviour is not completely understood yet. One possible explanation might be that upon addition of fresh sodium borohydride next portion of $\text{Au}@SiO_2$ particles was leached out from the frit. The effect of NaBH_4 on $\text{Au}@SiO_2$ stability was already discussed in the previous section. On the other hand, the prolonged continuous passing of NaBH_4 solution through the frit may lead to partial etching of silica shell of $\text{Au}@SiO_2$ particles, making thus silica shell more porous and more easily accessible for the reactants. Another possible reason for this non-monotonic behaviour shown in Figure 4.59 is the reverse reaction of product recombination which subsequently leads to the regeneration of MO. For instance,

Zheng et al. studied degradation of MO in presence of NaBH_4 using AgNPs as a catalyst.³⁶⁵ Authors found that the degradation products of MO could undergo reverse catalysis to regenerate MO again. When MO molecules are adsorbed onto the surface of the dispersed AgNPs, the surface atoms become polarised and activated. This accelerates the electron transfer between MO and NaBH_4 thereby reducing the activation energy. Thus the dispersed AgNPs catalyse the reduction of MO to N, N-dimethyl 1,4-phenylenediamine and sodium sulfanilate in the presence of NaBH_4 and then diffused to the solution. However, upon addition of CTAB to the reaction medium the AgNPs agglomerate resulting in the recombination of degradation products of MO to regenerate Methyl Orange. Therefore the authors proposed the following mechanism to explain the reverse catalysis of MO in presence of AgNP upon the addition of CTAB. The addition of cetrimonium bromide (CTAB) into the solution caused the nanoparticles to aggregate due to hydrophobic effect. This lead to the products of the reaction between MO and NaBH_4 to be wrapped in the hydrophobic layer and their diffusion to the solution was restricted resulting in the recombination of degradation products to form MO. Thus, reversibility of the reaction can be also considered as a plausible reason for the increase in the intensity of MO after passing through the frit. To clarify this question, additional and more systematic experiments are required.

Reduction of Nitrophenol (4-NP): As a next continuous flow experiment, catalytic degradation of 4-nitrophenol (4-NP) was studied using the same Au@SiO₂ loaded frit. After being used for MO degradation, the frit was intensively washed with Millipore water, dried with the N₂ flow and then used for 4-NP degradation. The experimental set-up and reagent concentration were similar to those used for CR and MO degradation (as described above). However, in contrast to CR and MO experiments, UV-Vis spectrum of pure 4-NP cannot be used as a reference to determine A_0 and monitor reaction through the time.

The UV-Vis spectra of 4-NP and nitrophenolate formed after addition of sodium borohydride are different in terms of peak position and peak intensities, as shown in Figure 4.60. Thus, for the determination of A_0 and, subsequently, for the analysis of 4-nitrophenol conversion to aminophenol, UV-Vis spectrum of the reaction mixture passing through the frit and having the highest peak intensity ($\lambda_{\text{max}} = 400 \text{ nm}$) was taken as a reference (A_0).

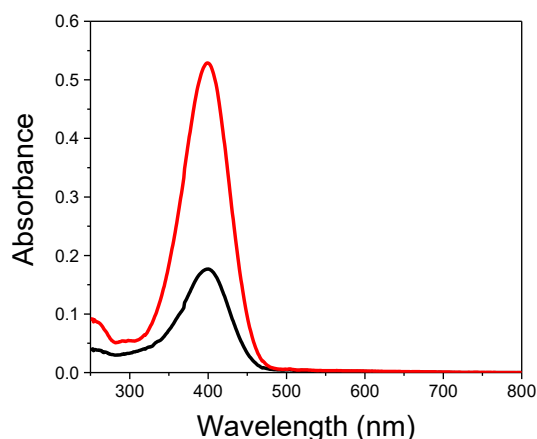


Figure 4.60 UV-Vis spectra of 4-Nitrophenol (black) and Nitrophenolate (red). The concentration of 4-NP was 0.067 mM whereas the 4-NP: NaBH₄ ratio was 1: 3000.

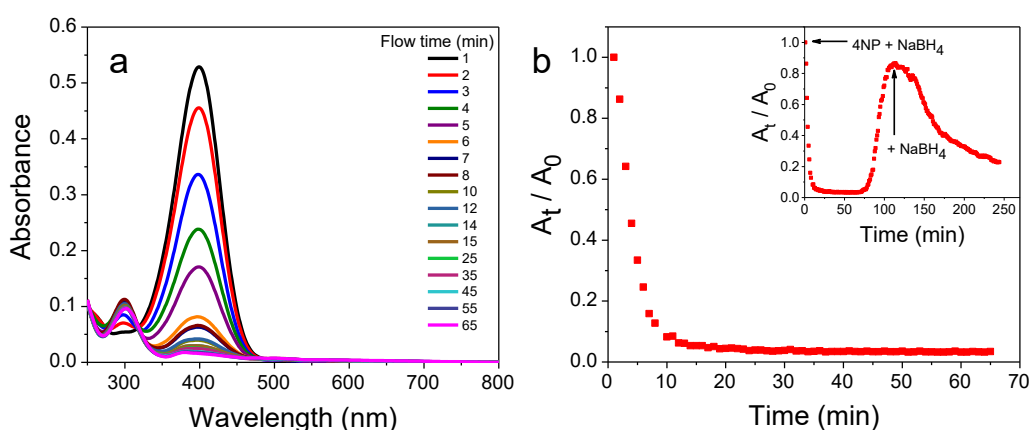


Figure 4.61 (a) Representative UV-Vis spectra of 4NP + NaBH₄ reaction mixture after passing through the frit loaded with Au@SiO₂ yolk-shells taken at selected time points; (b) Plot of A_t/A_0 ($\lambda_{max} = 400$ nm) versus time obtained during the continuous flow catalysis experiment on degradation of 4-NP during the first 65 minutes of continuous flow catalysis experiment. Inset on (b) shows A_t/A_0 time dependency obtained upon prolonged continuous flow experiment.

Figure 4.61 shows (a) selected UV-Vis spectra of 4NP + NaBH₄ mixture after passing through the Au@SiO₂ loaded frit at time points of continuous flow catalysis experiment and (b) plot of A_t/A_0 at $\lambda_{max} = 400$ nm versus time for the first 65 minutes of flow experiment. As can be seen, after a gradual decrease of peak intensity, the 4-NP reduction reaches ca. 97 % level. However, during the next 60 minutes of continuous flow experiment A_t/A_0 values increased from ~ 0.03 to ~ 0.8 level, thus indicating the substantial loss of catalytic efficiency of the system (Figure 4.61 b, inset). From the literature, it is known that for catalytic reduction of a 4-NP solution, sodium borohydride should be freshly prepared.^{324,326} To check the effect of sodium borohydride decomposition with time, an additional portion of NaBH₄ powder was added to the reaction mixture and reaction course was monitored further. As can be seen, after

addition of fresh NaBH_4 A_t/A_0 values started to decrease again, however with a lower rate as initially. Within next two hours, complete reduction of 4-NP was still not reached. At this point, the experiment was terminated due to technical reasons.

Considering also results from CR and MO degradation experiments discussed above, it might be assumed that such drastic decrease of catalytic efficiency of present system in case on 4-NP reduction might be the result of several simultaneous effects: (1) NaBH_4 decomposition, which has no such drastic effects in case of CR and MO, so far; (2) additional leaching of Au@SiO_2 yolks-shells from the frit under a basic pH in presence of NaBH_4 ; (3) it is also possible that surface of AuNP was passivated or contaminated during long-time and repeated continuous flow experiment. To clarify the situation more systematic studies are necessary.

4.4.5 Conclusion

The application of Au@SiO_2 yolk-shell nanoparticles in continuous flow catalysis was discussed here. $\text{Au@PS-}b\text{-P4VP@SiO}_2$ particles were prepared and infiltrated in a porous glass substrate (a glass frit) of pore size 1.0-1.6 μm . Infiltration of Au@BCP@SiO_2 particles in the frit pores followed by pyrolytic treatment of the frit resulted in the formation of Au@SiO_2 yolk-shell nanoparticles that are strongly attached to the frit pore, giving them a good capacity to withstand the flow of reactants. The microscopical studies gave insight to the distribution of Au@SiO_2 yolk-shell nanoparticles inside the frit pores. The penetration depth and distribution of Au@SiO_2 yolk-shells were found to be dependent on the amount of yolk-shell particles infiltrated. The stability of the particles inside the frit was studied by passing water and the reaction mixture through the frit and measuring the corresponding filtrate solution to determine the amount of AuNPs present in the filtrate. Thus the prepared frit was used for catalytic reduction of azo dyes and nitrophenol in presence of sodium borohydride. The results obtained showed a high catalytic activity of the frit in the degradation of Congo Red (ca. 97%). The catalyst also maintained stability throughout the continuous flow catalytic process for the time period of 5 hours. The same frit was further used for the reduction of Methyl Orange and 4-nitrophenol, which, however, gave a decreased efficiency when compared to the degradation of Congo Red. A reason for the decreased conversion rate for Methyl Orange might be due to its regeneration from the degradation products in the absence of a catalyst. Nevertheless, the decreased conversion rate for 4-NP, upon prolongation of the reaction is unknown until now. However, we observed that the catalyst maintained the same efficiency for the degradation of Congo Red even after its repeated use for other reactions (MO and 4-NP).

The studies conducted by Gao et al. showed that the repeated exposure of the catalyst to the reactant mixture decreased the conversion efficiency of the ascribed flow system.³⁶³ In the case of Au@SiO_2 continuous flow catalyst system, the basic environment of the reaction mixtures and comparatively long continuous flow process (up to 45 hours in total) are assumed to be as main reasons for the slight decrease in catalytic efficiency mainly in the case of 4-NP reduction. Nevertheless, for the yolk-shell systems reported in literature additional supports were needed to use them as a fixed bed reactor for the continuous catalysis reactions and the

catalyst recovery was done by heat treatment.^{361–363} Moreover, the fabrication of such yolk-shells involved tedious and complex procedures and only at a high catalyst loading, they attained high efficiency. On the other hand, the ascribed Au@SiO₂ yolk-shell based flow-type catalytic system has a simple and easily reproducible synthetic strategy. Moreover, the catalyst-loaded frits were readily used without any additional modification. Also, it shows good stability and long-term catalytic efficiency at a very low catalyst loading compared to that reported in the literature. Although there have been many flow type catalyst systems mentioned in the literature, to the best of our knowledge, the flow type catalytic system based on Au@SiO₂ yolk-shell type nanocatalyst (discussed here) is exceptional of its kind and has rarely been reported in the literature so far.

5 SUMMARY

The present thesis embraces the topic of catalytically active yolk-shell nanoparticles, their design, characterization and studying the catalytic activity. Four different aspects of the topic which deals with the mechanism of shell formation over the BCP template, design of the yolk-shell catalyst system having a mesoporous silica shell and a nanocatalyst core (AgNP or AuNP), their synthetic modification and characterization, their catalyst activity and devising a continuous flow catalyst reactor using the AuNP based yolk-shell nanoparticles were discussed.

Initial studies were conducted to study the effect of different processing conditions, as well as the stages involved in the formation of silica shell over a reactive polymer template, has been done. The growth of silica shell over reactive PS-*b*-P4VP spherical micelles was studied using *in-situ* DLS method and TEM. The results obtained shed more insights into the mechanism of silica shell formation over reactive BCP micelles. The first stage involves the accumulation of sol around the micellar corona which is accompanied by a steep increase in the hydrodynamic particle size. The protonated P4VP chains increase the hydrolysis-condensation of silica precursor around the PS-*b*-P4VP micelles resulting in the formation of loose silica network. At the same time, the condensation and densification of the silica network progressed to result in the formation of distinct PS-*b*-P4VP@SiO₂ particles. With the extension of reaction time, the silica shell grows further. The whole process of silica shell formation could be monitored using DLS by continuously measuring the change in particle size (Figure 5.1). TEM studies are needed to visually image the changes occurring at different stages of silica shell formation and growth.

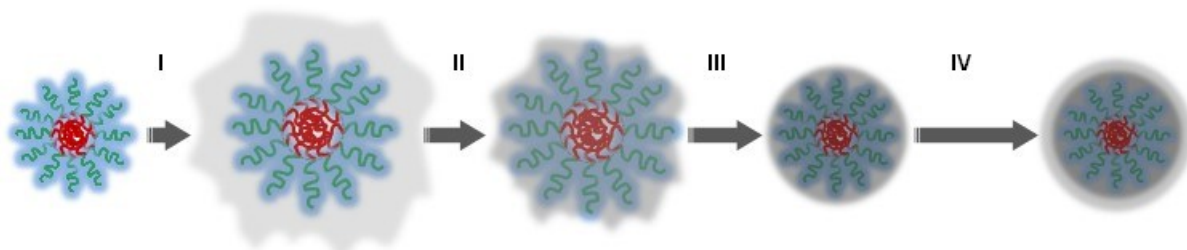


Figure 5.1 Schematic showing the mechanism of silica shell formation around the PS-*b*-P4VP micellar templates.

A deep and thorough understanding of the mechanism of silica shell formation over reactive BCP template helps in the synthesis of yolk-shell, core-shell, and hollow nanostructures. It enables one to alternate the properties of such structures by varying the reaction parameters during silica deposition and shell growth. By quenching the reaction at a particular stage it should be possible to alter and tune the structure and properties of the shell, such as shell thickness and porosity, pore size distribution, shell permeability and selectivity. Other parameters, such as pH, temperature, the amount and composition of added sol, the type of solvent are also expected to have an influence on the shell formation. The template method also provides a direct way for the encapsulation of various “active” species, such as quantum dots or catalytically active nanoparticles, and fabrication of so-called yolk-shell nanostructures. The

reactive template method might be also valuable for other hybrid structures prepared by the sol-gel process, especially when the control over the particle size and shape is challenging. We believe that obtained results will be important for producing core-shell and hollow particles with predetermined properties.

The main focus of this thesis was on the synthesis of Ag@SiO_2 and Au@SiO_2 yolk-shell nanoparticles and their application as a catalyst for the reduction of 4-nitrophenol. PS-*b*-P4VP micelles were used as a dual template for both encapsulation of nanocatalyst and deposition of silica shell, enabling a simple, robust and scalable synthesis of $\text{Ag@PS-}b\text{-P4VP@SiO}_2$ and $\text{Au@PS-}b\text{-P4VP@SiO}_2$ particles. For the preparation of such structures, initial studies were conducted based on AgNPs. However, it was found that in presence of acidic silica sol AgNP underwent depletion in their size even when they were enclosed in PS-*b*-P4VP micelles ($\text{Ag@PS-}b\text{-P4VP}$). On the other hand, AuNPs ($\text{Au@PS-}b\text{-P4VP}$) were found stable against dissolution. Hence AuNPs were chosen as the catalytic core materials for further studies.

The pyrolytic removal of BCP template and other organic components from $\text{Au@PS-}b\text{-P4VP@SiO}_2$ particles lead to the formation of yolk-shell nanostructures composed of an AuNP core and hollow mesoporous silica shell (Au@SiO_2). The P4VP chains of PS-*b*-P4VP block copolymer being interpenetrated into the silica shell plausibly were responsible for the substantial increase of shell porosity during pyrolytic removal of the BCP template. The pyrolytic removal of the BCP template resulted in the aggregation of Au@SiO_2 yolk-shell nanoparticles. Although the catalyst exhibited good catalytic efficiency and recyclability, the agglomeration of particles created inhomogeneities in the catalyst dispersion and limited accessibility of nanocatalyst surface for the reagents (Figure 5.2). These, in turn, caused difficulties in studying the catalyst efficiency and affected the reproducibility of kinetic studies. Besides the low yield of the catalyst, the inhomogeneities in the catalyst dispersion proved that the above-mentioned system needs synthetic modifications.

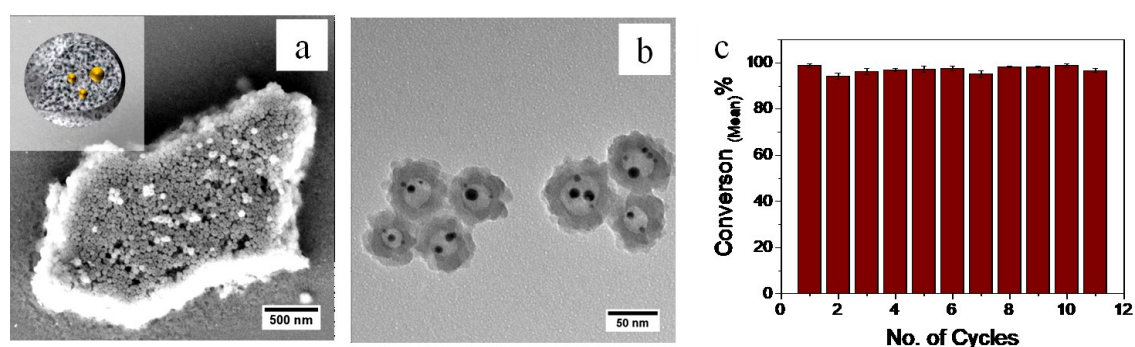


Figure 5.2 (a, b) SEM images showing agglomerated Au@SiO_2 yolk-shell nanoparticles; (c) Bar graph showing the recyclability of Au@SiO_2 yolk-shell nanocatalyst.

The above experiments revealed the need for modifications in the synthetic procedures for Au@SiO₂ nanocatalyst to overcome the agglomeration during drying and pyrolysis. Hence additional steps were introduced in the synthetic procedures resulting in the formation of a catalytic system composed of Au@SiO₂ particles embedded in a porous silica support (PSS) (Figure 5.3).

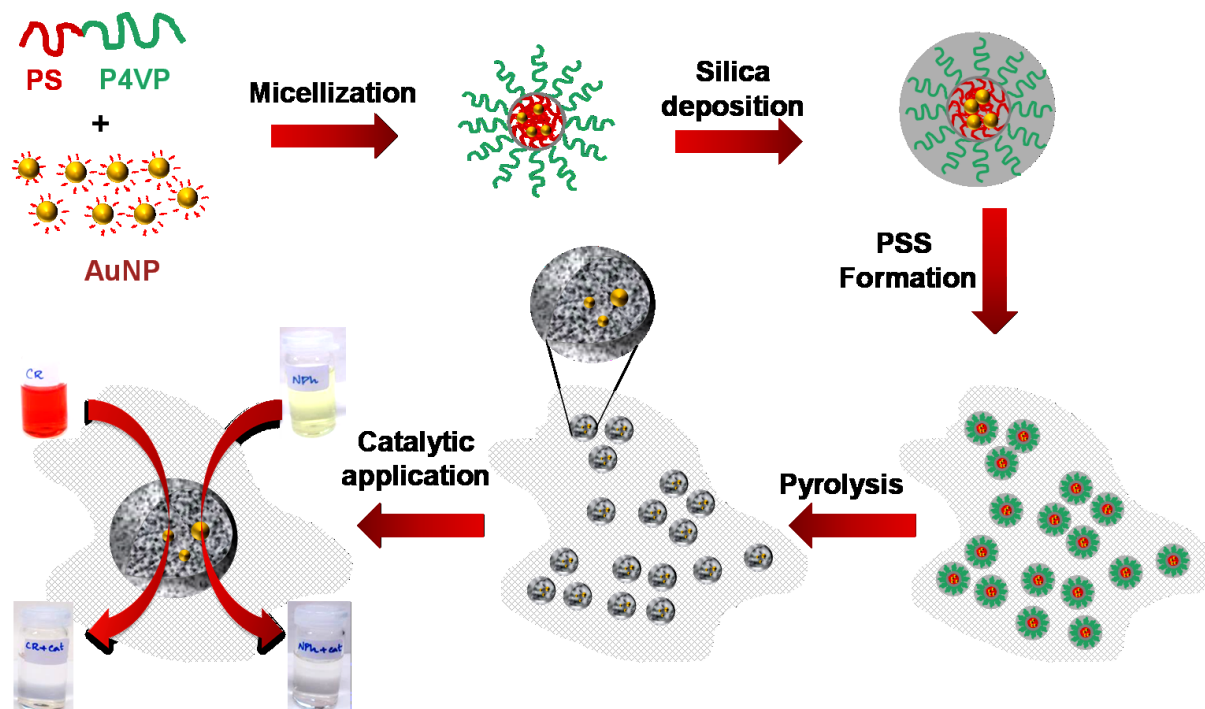


Figure 5.3 Fabrication and catalytic activity of Au@SiO₂@PSS catalyst.

The Au@SiO₂@PSS catalyst was prepared from PS-*b*-P4VP block copolymer as a sacrificial template and pre-synthesized Au nanoparticles via sequential formation of silica shell and porous silica support, followed by pyrolytic removal of organic and polymeric components. The embedding of Au@SiO₂ particles into porous silica support prevents Au@SiO₂ particles from aggregation and fusion and ensures an easy access to the nanocatalyst surface for reactants during catalytic process. In addition, nanocatalyst enclosed inside porous silica shell is free of any capping agents after pyrolysis. Most importantly, the catalytic activity of Au@SiO₂@PSS catalyst was found superior as compared to other analogous catalytic systems reported in literature till date, which is presumably attributed to above-mentioned factors.

Catalytic performance of Au@SiO₂@PSS can be optimised and improved further, for instance, by adjusting the size of encapsulated nanocatalyst. Additionally, the content of Au@SiO₂ particles in PSS matrix can be tuned by changing PS-*b*-P4VP/Si precursor ratio such that different loadings of Au (or other metal nanocatalysts) per unit mass of catalyst can be achieved. Finally, Au@SiO₂ particles in PSS matrix might be distributed more homogeneously by adopting an appropriate synthetic condition. The yolk-shell nature of the nanocatalyst and high porosity of silica support should enable Au@SiO₂@PSS or analogues to be used in continuous flow catalytic reactors.

Additionally and more importantly, the catalytic studies on the degradation of various organic dyes show the prospective use of Au@SiO₂@PSS catalyst in the field of water purification (Figure 5.4).

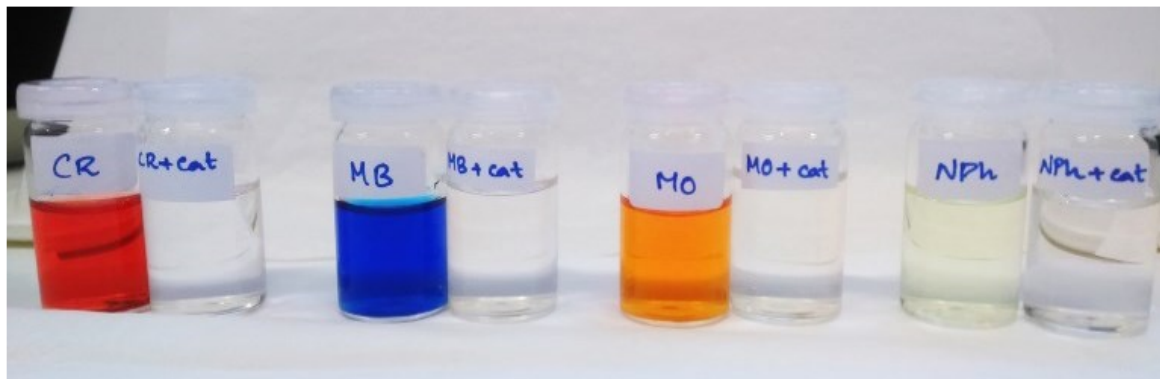


Figure 5.4 Image showing the results on catalytic degradation/reduction of Congo Red (CR), Methylene Blue (MB), Methyl Orange (MO), and 4-Nitrophenol (4-NP) using Au@SiO₂@PSS catalyst.

The good catalytic activity and efficient recyclability of the aforementioned Au@SiO₂ yolk-shell nanocatalyst lead the way to further use of their catalytic properties in continuous flow catalytic reactors. Hence the such a continuous flow catalytic system composed of Au@SiO₂ yolk-shell nanoparticles was devised for the effective reduction of organic dyes which could be later scaled up for wastewater treatment. A summary of such a continuous flow catalytic system is shown in Figure 5.5.

The continuous flow catalytic system was prepared by the deposition of silica shell over the Au@PS-*b*-P4VP micelles followed by the infiltration of Au@PS-*b*-P4VP@SiO₂ particles into the pores of porous glass supports (frits). The PS-*b*-P4VP template was then removed by the pyrolysis of the frit infiltrated with Au@PS-*b*-P4VP@SiO₂, resulting in the formation of Au@SiO₂ yolk-shell nanoparticles sintered inside the frit pores. The Au@SiO₂ loaded frit was used for several types of catalytic reactions. The results obtained show that the catalytic efficiency might be as high as 98-99% of reagent conversion in flow regime and the frit was stable for a long time under the flow. The fast interaction of reactant molecules with the entrapped Au@SiO₂ yolk-shell nanoparticles in the frit pores resulted in the high efficiency of the catalyst. Although there have been many studies on continuous catalysis and microreactors, continuous flow catalytic reactors based on yolk-shell nanostructures are seldom reported in the literature. Hence we believe that this system is exceptional of its kind.

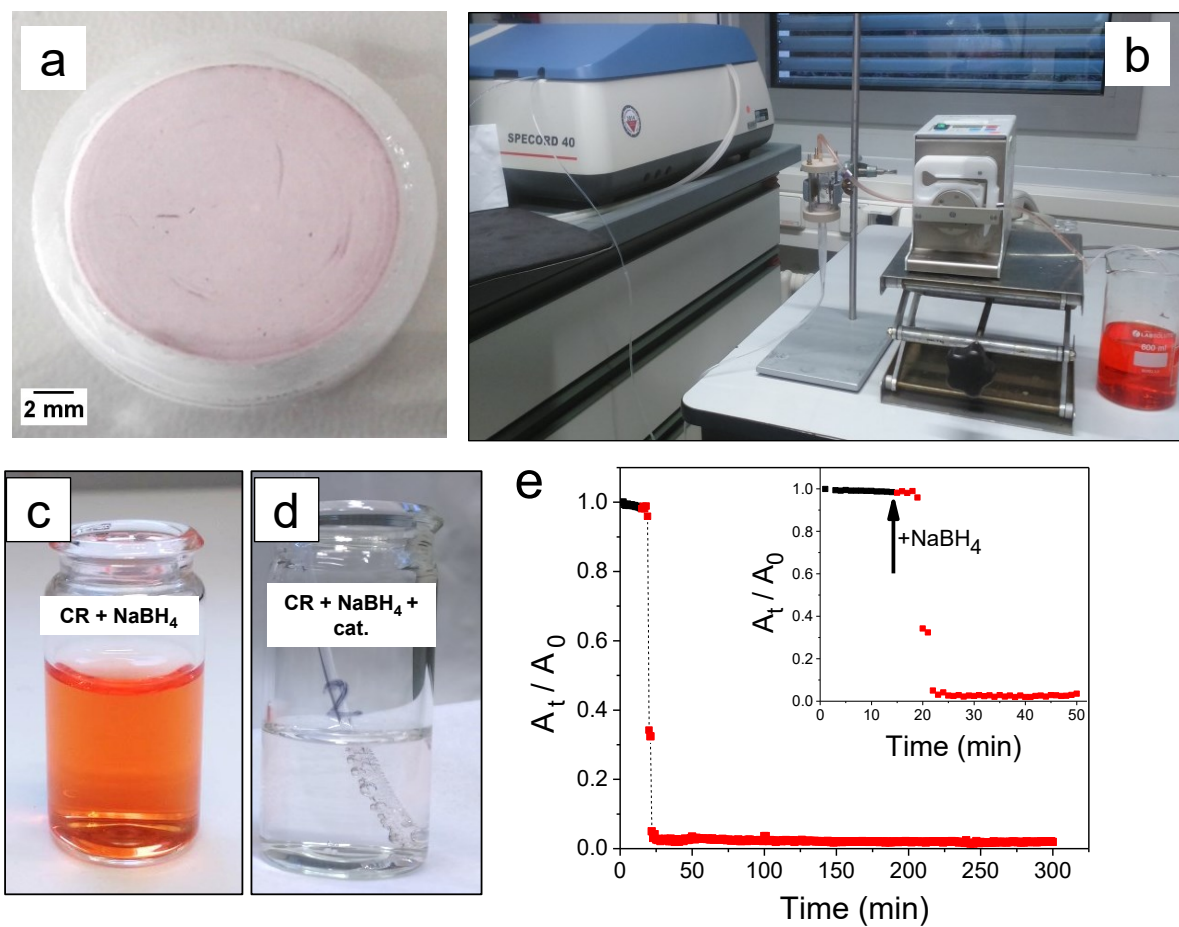


Figure 5.5 Summary showing the continuous flow catalytic system.

6 FUTURE OUTLOOK

The recent research interests gained in the field of yolk-shell nanoparticles indicate the importance of investigating such structures and their efficiency in fulfilling the requirement of multifunctionality in the field of material science. With different synthetic approaches to produce yolk-shell nanoparticles, it is possible to attain controlled functionalities and material compositions at a reasonable time and cost-effective. Nevertheless, the synthesis of yolk-shell nanoparticles on a large scale and their application on an industrial scale is still a huge challenge. To obtain the desired functionalities and structure, it is important to understand the mechanism of yolk-shell nanoparticle formation, which varies with respect to the materials and the synthetic procedures used. One way to attain spherical yolk-shell nanoparticles with less number of synthetic steps and minimal effort is to employ the soft templating approach. In this method, a soft template material such as a polymer is used as a substrate material to encapsulate the core and deposit the shell followed by the removal of the polymer to obtain yolk-shell nanoparticles. The experiments done in the first part of the work shed an insight into the mechanism of shell formation around the polymer template. This understanding is important for producing yolk-shell nanoparticles with predetermined properties. By quenching the reaction at a particular stage it should be possible to alter and tune the structure and properties of the shell, such as shell thickness and porosity, pore size distribution, shell permeability and selectivity.

In terms of application, it is very beneficial to employ the unique properties of yolk-shell nanoparticles in the field of multifunctional smart materials, catalysis, batteries, drug delivery vehicles etc. We studied the use of yolk-shell nanoparticles as an effective catalyst for the degradation of different dyes. The next step in this area would be to test the catalysis reaction using different model reactions, synthesising yolk-shell nanoparticles with different material composition and studying their application in various fields.

We took a step further in using the yolk-shell nanoparticles in flow system as an effectual method for continuous catalysis. This employed the degradation of various azo dyes which can be further applied for water purification. The next step in this direction will be to attain frits loaded with yolk-shell nanoparticles throughout its whole cross-sectional area and to study the activity of the yolk-shell nanoparticles immobilised in different substrates to develop a potential continuous flow reactor for water purification.

In conclusion, the current work has provided a substantial contribution in the particular field of noble metal@silica yolk-shell nanostructures, their synthesis, process optimization, and catalytic applications, suggesting different approaches to improve the various aspects in these fields. Although different solutions have been put forth, an area for improvement still lies in the above-mentioned topics. Considering the potential of noble metal@silica yolk-shell nanoparticles, further extensive investigations on this topic are of great importance in various disciplines, such as material science, energy storage, and biomedicine (drug delivery and photothermal therapy).

7 REFERENCE

1. Talapin, D. V., Lee, J. S., Kovalenko, M. V. & Shevchenko, E. V. Prospects of colloidal nanocrystals for electronic and optoelectronic applications. *Chem. Rev.* **110**, 389–458 (2010).
2. Pradeep, T. & Anshup. Noble metal nanoparticles for water purification: A critical review. *Thin Solid Films* **517**, 6441–6478 (2009).
3. Park, J. C., Lee, H. J., Kim, J. Y., Park, K. H. & Song, H. Catalytic hydrogen transfer of ketones over Ni@SiO₂ Yolk-shell nanocatalysts with tiny metal cores. *J. Phys. Chem. C* **114**, 6381–6388 (2010).
4. Lee, K. S. & El-Sayed, M. A. Gold and silver nanoparticles in sensing and imaging: Sensitivity of plasmon response to size, shape, and metal composition. *J. Phys. Chem. B* **110**, 19220–19225 (2006).
5. Li, S. *et al.* High-rate aluminium yolk-shell nanoparticle anode for Li-ion battery with long cycle life and ultrahigh capacity. *Nat. Commun.* **6**, 7872 (2015).
6. Jain, P. K., Huang, X., El-Sayed, I. H. & El-Sayed, M. A. Noble metals on the nanoscale: Optical and photothermal properties and some applications in imaging, sensing, biology, and medicine. *Acc. Chem. Res.* **41**, 1578–1586 (2008).
7. Hervés, P. *et al.* Catalysis by metallic nanoparticles in aqueous solution: model reactions. *Chem. Soc. Rev.* **41**, 5577 (2012).
8. Li, G. L., Tai, C. A., Neoh, K. G., Kang, E. T. & Yang, X. Hybrid nanorattles of metal core and stimuli-responsive polymer shell for confined catalytic reactions. *Polym. Chem.* **2**, 1368 (2011).
9. Mei, Y. *et al.* High catalytic activity of platinum nanoparticles immobilized on spherical polyelectrolyte brushes. *Langmuir* **21**, 12229–12234 (2005).
10. Li, G. & Tang, Z. Noble metal nanoparticle@metal oxide core/yolk-shell nanostructures as catalysts: recent progress and perspective. *Nanoscale* **6**, 3995–4011 (2014).
11. Kamata, K., Lu, Y. & Xia, Y. Synthesis and characterization of monodispersed core-shell spherical colloids with movable cores. *J. Am. Chem. Soc.* **125**, 2384–2385 (2003).
12. Kim, M., Sohn, K., Na, H. Bin & Hyeon, T. Synthesis of Nanorattles Composed of Gold Nanoparticles Encapsulated in Mesoporous Carbon and Polymer Shells. *Nano Lett.* **2**, 1383–1387 (2002).
13. Priebe, M. & Fromm, K. M. Nanorattles or Yolk – Shell Nanoparticles — What Are They , How Are They Made , and What Are They Good For? *Chem. Eur.J.* **21**, 3854–3874 (2015).
14. Park, J. C., Kim, J. Y., Heo, E., Park, K. H. & Song, H. Platinum-centered yolk-shell nanostructure formation by sacrificial nickel spacers. *Langmuir* **26**, 16469–16473 (2010).
15. Hu, S. H. & Gao, X. Nanocomposites with spatially separated functionalities for combined imaging and magnetolytic therapy. *J. Am. Chem. Soc.* **132**, 7234–7237 (2010).
16. Lin, Y.-S. *et al.* Synthesis of hollow silica nanospheres with a microemulsion as the template. *Chem. Commun. (Camb)*. 3542–3544 (2009). doi:10.1039/b902681a

17. Arnal, P. M., Comotti, M. & Schüth, F. High-temperature-stable catalysts by hollow sphere encapsulation. *Angew. Chemie - Int. Ed.* **45**, 8224–8227 (2006).
18. Pérez-Lorenzo, M., Vaz, B., Salgueiriño, V. & Correa-Duarte, M. A. Hollow-shelled nanoreactors endowed with high catalytic activity. *Chem. - A Eur. J.* **19**, 12196–12211 (2013).
19. Dahlberg, K. a & Schwank, J. W. Kevin A. Dahlberg and Johannes W. Schwank*. *Chem. Mater.* **24**, 2635–2644 (2012).
20. Hong, Y. J., Son, M. Y. & Kang, Y. C. One-pot facile synthesis of double-shelled SnO₂ yolk-shell-structured powders by continuous process as anode materials for li-ion batteries. *Adv. Mater.* **25**, 2279–2283 (2013).
21. Hong, Y. J., Son, M. Y., Park, B. K. & Kang, Y. C. One-pot synthesis of yolk-shell materials with single, binary, ternary, quaternary, and quinary systems. *Small* **9**, 2224–2227 (2013).
22. Lee, J., Park, J. C., Bang, J. U. & Song, H. Precise Tuning of Porosity and Surface Functionality in Au@SiO₂ Nanoreactors for High Catalytic Efficiency. *Chem. Mater.* **20**, 5839–5844 (2008).
23. Wu, H. *et al.* Biocompatibility, MR imaging and targeted drug delivery of a rattle-type magnetic mesoporous silica nanosphere system conjugated with PEG and cancer-cell-specific ligands. *J. Mater. Chem.* **21**, 3037 (2011).
24. Zhang, K. *et al.* A facile in situ hydrophobic layer protected selective etching strategy for the synchronous synthesis/modification of hollow or rattle-type silica nanoconstructs. *J. Mater. Chem.* **22**, 12553 (2012).
25. Shmakov, S. N. & Pinkhassik, E. Simultaneous templating of polymer nanocapsules and entrapped silver nanoparticles. *Chem. Commun.* **46**, 7346–7348 (2010).
26. Hah, H. J., Um, J. I., Han, S. H. & Koo, S. M. New synthetic route for preparing rattle-type silica particles with metal cores. *Chem. Commun.* 1012–1013 (2004). doi:10.1039/b401387e
27. Zhang, N., Fu, X. & Xu, Y.-J. A facile and green approach to synthesize Pt@CeO₂ nanocomposite with tunable core-shell and yolk-shell structure and its application as a visible light photocatalyst. *J. Mater. Chem.* **21**, 8152 (2011).
28. Chen, C., Fang, X., Wu, B., Huang, L. & Zheng, N. A Multi-Yolk-Shell Structured Nanocatalyst Containing Sub-10nm Pd Nanoparticles in Porous CeO₂. *ChemCatChem* **4**, 1578–1586 (2012).
29. Liu, N. *et al.* A yolk-shell design for stabilized and scalable Li-ion battery alloy anodes. *Nano Lett.* **12**, 3315–3321 (2012).
30. Chen, D., Li, N., Tang, F. & Qi, S. Facile and scalable synthesis of tailored silica ‘nanorattle’ structures. *Adv. Mater.* **21**, 3804–3807 (2009).
31. Liu, B. *et al.* A general method for the synthesis of various rattle-type microspheres and their diverse applications. *RSC Adv.* **3**, 18506–18518 (2013).
32. Yan, N. *et al.* High catalytic activity for CO oxidation of Co₃O₄ nanoparticles in SiO₂ nanocapsules. *J. Mater. Chem. A* **1**, 637–643 (2013).

33. Kang, X. *et al.* Design and synthesis of multifunctional drug carriers based on luminescent rattle-type mesoporous silica microspheres with a thermosensitive hydrogel as a controlled switch. *Adv. Funct. Mater.* **22**, 1470–1481 (2012).
34. Qin, Z. *et al.* Synthesis of metal sulfide nanoboxes based on Kirkendall effect and Pearson hardness. *CrystEngComm* **15**, 897–902 (2013).
35. Kuai, L., Wang, S. & Geng, B. Gold-platinum yolk-shell structure: A facile galvanic displacement synthesis and highly active electrocatalytic properties for methanol oxidation with super CO-tolerance. *Chem. Commun.* **47**, 6093–6095 (2011).
36. Dong, K., Liu, Z. & Ren, J. A general and eco-friendly self-etching route to prepare highly active and stable Au@metal silicate yolk-shell nanoreactors for catalytic reduction of 4-nitrophenol. *CrystEngComm* **15**, 6329 (2013).
37. Dong, K., Liu, Z. & Ren, J. A general and eco-friendly self-etching route to prepare highly active and stable Au@metal silicate yolk-shell nanoreactors for catalytic reduction of 4-nitrophenol. *CrystEngComm* **15**, 6329 (2013).
38. Dong, W. *et al.* A performance study of enhanced visible-light-driven photocatalysis and magnetical protein separation of multifunctional yolk-shell nanostructures. *J. Mater. Chem. A* **1**, 10030 (2013).
39. Dong, W. *et al.* A performance study of enhanced visible-light-driven photocatalysis and magnetical protein separation of multifunctional yolk-shell nanostructures. *J. Mater. Chem. A* **1**, 10030 (2013).
40. Wei, Z. *et al.* Multifunctional Ag@Fe₂O₃ yolk-shell nanoparticles for simultaneous capture, kill, and removal of pathogen. *J. Mater. Chem.* **21**, 16344 (2011).
41. Shi, B., Ren, J., Liu, X., Lu, G. & Wang, Y. Fabrication of well-defined superparamagnetic rattle-type Fe₃O₄@polyaniline hollow microspheres with large cavity. *Synth. Met.* **162**, 1443–1450 (2012).
42. Zeng, T. *et al.* A functional rattle-type microsphere with a magnetic-carbon double-layered shell for enhanced extraction of organic targets. *Chem. Commun.* **49**, 6039–6041 (2013).
43. Purbia, R. & Paria, S. Yolk/shell nanoparticles: classifications, synthesis, properties, and applications. *Nanoscale* **7**, 19789–19873 (2015).
44. Zhang, T. *et al.* Formation of Hollow Silica Colloids through a Spontaneous Dissolution–Regrowth Process. *Angew. Chemie Int. Ed.* **47**, 5806–5811 (2008).
45. Nagarajan, R. & Ganesh, K. Block copolymer self-assembly in selective solvents: Spherical micelles with segregated cores. *J. Chem. Phys.* **90**, 5843 (1989).
46. Lee, D.-E., Je, N. J., Yoo, S. Il & LEE, D. H. Directed Self-Assembly of Block Copolymer Micelles onto Topographically Patterned Surface. *Langmuir* [acs.langmuir.5b03419](https://doi.org/10.1021/acs.langmuir.5b03419) (2015). doi:10.1021/acs.langmuir.5b03419
47. Braunecker, W. A. & Matyjaszewski, K. Controlled/living radical polymerization: Features, developments, and perspectives. *Prog. Polym. Sci.* **32**, 93–146 (2007).
48. Hadjichristidis, N., Pitsikalis, M. & Iatrou, H. Synthesis of block copolymers. *Adv. Polym. Sci.* **189**, 1–124 (2005).

49. Riess, G. Micellization of block copolymers. *Prog. Polym. Sci.* **28**, 1107–1170 (2003).
50. Bates, F. S. & Fredrickson, G. H. Block Copolymers—Designer Soft Materials. *Phys. Today* **52**, 32 (1999).
51. Mai, Y. & Eisenberg, A. Self-assembly of block copolymers. *Chem. Soc. Rev.* **41**, 5969 (2012).
52. Miller, A. C. *et al.* Block copolymer micelles as nanocontainers for controlled release of proteins from biocompatible oil phases. *Biomacromolecules* **10**, 732–741 (2009).
53. Hamley, I. W. *The Physics of Block Copolymers*. (Oxford University Press, 1998).
54. Mai, Y. & Eisenberg, A. Selective localization of preformed nanoparticles in morphologically controllable block copolymer aggregates in solution. *Acc. Chem. Res.* **45**, 1657–1666 (2012).
55. Förster, S. & Plantenberg, T. From self-organizing polymers to nanohybrid and biomaterials. *Angew. Chem. Int. Ed. Engl.* **41**, 689–714 (2002).
56. Kim, J. K., Yang, S. Y., Lee, Y. & Kim, Y. Functional nanomaterials based on block copolymer self-assembly. *Prog. Polym. Sci.* **35**, 1325–1349 (2010).
57. Orilall, M. C. & Wiesner, U. Block copolymer based composition and morphology control in nanostructured hybrid materials for energy conversion and storage: solar cells, batteries, and fuel cells. *Chem. Soc. Rev.* **40**, 520–535 (2011).
58. Matsen, M. W.; Bates, F. S. Unifying Weak- and Strong-Segregation Block Copolymer Theories. *Macromolecules* **29**, 1091–1098 (1996).
59. Riess, G. Micellization of block copolymers. *Prog. Polym. Sci.* **28**, 1107–1170 (2003).
60. Gohy, J. Block copolymer micelles. *Adv. Polym. Sci.* **190**, 65–136 (2005).
61. Forster, S. *et al.* Polyelectrolyte Block Copolymer Micelles. *Adv. Polym. Sci.* **166**, 173–210 (2004).
62. Zhang, L. F. . & Eisenberg, A. Formation of crew-cut aggregates of various morphologies from amphiphilic block copolymers in solution. *Polym. Adv. Technol.* **9**, 677–699 (1998).
63. Zhang, L. & Eisenberg, A. Multiple Morphologies of ‘ Crew-Cut ’ Aggregates of Polystyrene-b-poly (acrylic acid) Block Copolymers. *Science (80-.)*. **268**, 1728–1731 (1995).
64. Hamley, I. *Block Copolymers in Solution: Fundamentals and Applications*. (John Wiley & Sons, Ltd., 2005). doi:10.1002/9780470016985
65. Tsunashima, Y., Hirata, M. & Kawamata, Y. Diffusion motions and microphase separation of styrene-butadiene diblock copolymer in solution. 1. Extremely dilute solution region. *Macromolecules* **23**, 1089–1096 (1990).
66. Moffitt, M., Khougaz, K. & Eisenberg, a. Micellization of ionic block copolymers. *Acc. Chem. Res.* **29**, 95–102 (1996).
67. Gaucher, G. *et al.* Block copolymer micelles: preparation, characterization and application in drug delivery. *J. Control. Release* **109**, 169–188 (2005).

68. Nishiyama, N. *et al.* Novel Cisplatin-Incorporated Polymeric Micelles Can Eradicate Solid Tumors in Mice. *Cancer Res.* **63**, 8977–8983 (2003).
69. Nishiyama, N., Kato, Y., Sugiyama, Y. & Kataoka, K. Cisplatin-loaded polymer-metal complex micelle with time-modulated decaying property as a novel drug delivery system. *Pharm. Res.* **18**, 1035–1041 (2001).
70. Williams, R. J., Dove, A. P. & O'Reilly, R. K. Self-assembly of cyclic polymers. *Polym. Chem.* **6**, 2998–3008 (2015).
71. Yang, Y.-W., Yang, Z., Zhou, Z.-K., Attwood, D. & Booth, C. Association of Triblock Copolymers of Ethylene Oxide and Butylene Oxide in Aqueous Solution. A Study of Bn Em Bn Copolymers. *Macromolecules* **29**, 670–680 (1996).
72. Yang, Z. *et al.* Effect of Block Structure on the Micellization and Gelation of Aqueous Solutions of Copolymers of Ethylene Oxide and Butylene Oxide. *Macromolecules* **27**, 2371–2379 (1994).
73. Minatti, E. *et al.* Effect of cyclization of polystyrene/polyisoprene block copolymers on their micellar morphology. *Macromol. Rapid Commun.* **23**, 978–982 (2002).
74. Borsali, R. *et al.* From 'Sunflower-like' assemblies toward giant wormlike micelles. *Langmuir* **19**, 6–9 (2003).
75. Munk, P. in *Solvents and Self-Organization of Polymers* (ed. Webber, S. E. *et al.*) 367–381 (Kluwer Academic Publishers, 1996).
76. Stepanek, P. & Lodge, T. P. Dynamic Light Scattering from Block Copolymer Melts near the Order–Disorder Transition. *Macromolecules* **29**, 1244–1251 (1996).
77. Mortensen, K. Structural properties of self-assembled polymeric aggregates in aqueous solutions. *Polym. Adv. Technol.* **12**, 2–22 (2001).
78. Mortensen, K. Structural studies of aqueous solutions of PEO - PPO - PEO triblock copolymers, their micellar aggregates and mesophases; a small-angle neutron scattering study. *J. Phys. Condens. Matter* **8**, A103–A124 (1999).
79. Alexandridis, P. & Yang, L. SANS Investigation of Polyether Block Copolymer Micelle Structure in Mixed Solvents of Water and Formamide, Ethanol, or Glycerol. *Macromolecules* **33**, 5574–5587 (2000).
80. Seib, J. & Gallot, Y. Comportement de copolymères greffés en milieu solvant sélectif des greffons: Cas des copolymères poly (styrène-g-bromure de vinyl-4 N-éthylpyridinium). *Makromol. Chem.* **182**, 1775–1786 (1981).
81. Booth, C., Naylor, T. D., Price, C., Rajab, N. S. & Stubbersfield, R. B. Investigation of the size distribution of nonionic micelles formed from a polystyrene-polyisoprene block copolymer in N,N-dimethylacetamide. *J. Chem. Soc. Faraday Trans. 1 Phys. Chem. Condens. Phases* **74**, 2352–2362 (1978).
82. Khanal, A. & Nakashima, K. Incorporation and release of cloxacillin sodium in micelles of poly(styrene-b-2-vinyl pyridine-b-ethylene oxide). *J. Control. Release* **108**, 150–160 (2005).
83. Khanal, A., Inoue, Y., Yada, M. & Nakashima, K. Synthesis of Silica Hollow Nanoparticles Templated by Polymeric Micelle with Core - Shell - Corona Structure. *J.*

- Am. Chem. Soc.* **129**, 1534–1535 (2007).
84. Alemdaroglu, F. E., Alemdaroglu, N. C., Langguth, P. & Herrmann, A. DNA block copolymer micelles - A combinatorial tool for cancer nanotechnology. *Adv. Mater.* **20**, 899–902 (2008).
 85. Glass, R., Möller, M. & Spatz, J. P. Block copolymer micelle nanolithography. *Nanotechnology* **14**, 1153–1160 (2003).
 86. Auriemma, F. & de Rosa, C. Nanotechnological applications of block copolymers in biomedicine. *Trop. J. Pharm. Res.* **10**, 1–2 (2011).
 87. Tsunoyama, H., Sakurai, H., Negishi, Y. & Tsukuda, T. Size-specific catalytic activity of polymer-stabilized gold nanoclusters for aerobic alcohol oxidation in water. *J. Am. Chem. Soc.* **127**, 9374–9375 (2005).
 88. Guet, A. *et al.* Hydrophobic Nanoreactor Soft-Templating: A Supramolecular Approach to Yolk@Shell Materials. *Adv. Funct. Mater.* **25**, 6228–6240 (2015).
 89. Zarka, M. T., Nuyken, O. & Weberskirch, R. Amphiphilic polymer supports for the asymmetric hydrogenation of amino acid precursors in water. *Chem. - A Eur. J.* **9**, 3228–3234 (2003).
 90. Gall, B., Bortenschlager, M., Nuyken, O. & Weberskirch, R. Cascade reactions in polymeric nanoreactors: Mono (Rh)- and bimetallic (Rh/Ir) micellar catalysis in the hydroaminomethylation of 1-Octene. *Macromol. Chem. Phys.* **209**, 1152–1159 (2008).
 91. Lee, M., Jang, C. J. & Ryu, J. H. Supramolecular reactor from self-assembly of rod-coil molecule in aqueous environment. *J. Am. Chem. Soc.* **126**, 8082–8083 (2004).
 92. Ryu, J., Jang, C., Yoo, Y., Lim, S. & Lee, M. Supramolecular Reactor in an Aqueous Environment: Aromatic Cross Suzuki Coupling Reaction at Room Temperature. *J. Org. Chem.* **70**, 8956–8962 (2005).
 93. Liang, J., Wang, L., He, L. & Sun, S. Pyridine-containing block copolymer/silica core-shell nanoparticles for one-step preparation of superhydrophobic surfaces. *Phys. Chem. Chem. Phys.* **15**, 10921–9 (2013).
 94. Cho, H. *et al.* Development of various PS-b-P4VP micellar morphologies: Fabrication of inorganic nanostructures from micellar templates. *J. Colloid Interface Sci.* **356**, 1–7 (2011).
 95. Hashimoto, T., Harada, M. & Sakamoto, N. Incorporation of Metal Nanoparticles into Block Copolymer Nanodomains via in-Situ Reduction of Metal Ions in Microdomain Space. *Macromolecules* **32**, 6867–6870 (1999).
 96. Kim, B. J., Chiu, J. J., Yi, G. R., Pine, D. J. & Kramer, E. J. Nanoparticle-induced phase transitions in diblock-copolymer films. *Adv. Mater.* **17**, 2618–2622 (2005).
 97. Luo, Q., Hickey, R. J. & Park, S. J. Controlling the location of nanoparticles in colloidal assemblies of amphiphilic polymers by tuning nanoparticle surface chemistry. *ACS Macro Lett.* **2**, 107–111 (2013).
 98. Gai, Y., Lin, Y., Song, D. P., Yavitt, B. M. & Watkins, J. J. Strong Ligand-Block Copolymer Interactions for Incorporation of Relatively Large Nanoparticles in Ordered Composites. *Macromolecules* **49**, 3352–3360 (2016).

99. Jang, S. G., Kramer, E. J. & Hawker, C. J. Controlled Supramolecular Assembly of Micelle-Like Gold Nanoparticles in PS-*b*-P2VP Diblock Copolymers via Hydrogen Bonding. *J. Am. Chem. Soc.* **133**, 16986–16996 (2011).
100. Chiu, J. J., Kim, B. J., Kramer, E. J. & Pine, D. J. Control of nanoparticle location in block copolymers. *J. Am. Chem. Soc.* **127**, 5036–5037 (2005).
101. Chiu, J. J. *et al.* Distribution of nanoparticles in lamellar domains of block copolymers. *Macromolecules* **40**, 3361–3365 (2007).
102. Kim, B. J., Fredrickson, G. H., Hawker, C. J. & Kramer, E. J. Nanoparticle surfactants as a route to bicontinuous block copolymer morphologies. *Langmuir* **23**, 7804–7809 (2007).
103. Kim, B. J., Fredrickson, G. H. & Kramer, E. J. Effect of polymer ligand molecular weight on polymer-coated nanoparticle location in block copolymers. *Macromolecules* **41**, 436–447 (2008).
104. Jang, S. G. *et al.* Synthesis of thermally stable Au-core/Pt-shell nanoparticles and their segregation behavior in diblock copolymer mixtures. *Soft Matter* **7**, 6255 (2011).
105. Kim, B. J., Fredrickson, G. H., Bang, J., Hawker, C. J. & Kramer, E. J. Tailoring core - Shell polymer-coated nanoparticles as block copolymer surfactants. *Macromolecules* **42**, 6193–6201 (2009).
106. Yoo, M. *et al.* Controlling the orientation of block copolymer thin films using thermally-stable gold nanoparticles with tuned surface chemistry. *Macromolecules* **44**, 9356–9365 (2011).
107. Lee, J. Y., Shou, Z. & Balazs, A. C. Predicting the Morphologies of Confined Copolymer / Nanoparticle Mixtures. *Macromolecules* **36**, 7730–7739 (2003).
108. Thompson, R. B., Ginzburg, V. V., Matsen, M. W. & Balazs, A. C. Predicting the mesophases of copolymer-nanoparticle composites. *Science* **292**, 2469–2472 (2001).
109. Pieranski, P. Two-dimensional interfacial colloidal crystals. *Phys. Rev. Lett.* **45**, 569–572 (1980).
110. Wang, J., Li, W. & Zhu, J. Encapsulation of inorganic nanoparticles into block copolymer micellar aggregates: Strategies and precise localization of nanoparticles. *Polym. (United Kingdom)* **55**, 1079–1096 (2014).
111. Kassam, A., Bremner, G., Clark, B., Ulibarri, G. & Lennox, R. B. Place Exchange Reactions of Alkyl Thiols on Gold Nanoparticles. *J. Am. Chem. Soc.* 3476–3477 (2006).
112. Shibasaki, Y. *et al.* Crosslinked, glassy styrenic surfactants stabilize quantum dots against environmental extremes. *J. Mater. Chem.* **19**, 6324 (2009).
113. Dubertret, B. *et al.* In Vivo Imaging of Quantum Dots Encapsulated in Phospholipid Micelles. *Science (80-.)*. **298**, 1759–1763 (2002).
114. Huff, T. B. *et al.* Controlling the Cellular Uptake of Gold Nanorods. *Langmuir* **23**, 1596–1599 (2007).
115. Kim, B. S. & Taton, T. A. Multicomponent nanoparticles via self-assembly with cross-linked block copolymer surfactants. *Langmuir* **23**, 2198–2202 (2007).

116. Boyer, C., Whittaker, M. R., Nouvel, C. & Davis, T. P. Synthesis of hollow polymer nanocapsules exploiting gold nanoparticles as sacrificial templates. *Macromolecules* **43**, 1792–1799 (2010).
117. Chen, T., Yang, M., Wang, X., Li, H. T. & Chen, H. Controlled assembly of eccentrically encapsulated gold nanoparticles. *J. Am. Chem. Soc.* **130**, 11858–11859 (2008).
118. Mai, Y. & Eisenberg, A. Controlled incorporation of particles into the central portion of block copolymer rods and micelles. *Macromolecules* **44**, 3179–3183 (2011).
119. Kang, Y. & Taton, T. A. Core/shell gold nanoparticles by self-assembly and crosslinking of micellar, block-copolymer shells. *Angew. Chemie - Int. Ed.* **44**, 409–412 (2005).
120. Azzam, T. & Eisenberg, A. Monolayer-protected gold nanoparticles by the self-assembly of micellar poly(ethylene oxide)-b-poly(ε-caprolactone) block copolymer. *Langmuir* **23**, 2126–2132 (2007).
121. Ribeiro, T., Prazeres, T. J. V, Moffitt, M. G., Paulo, J. & Farinha, S. Enhanced Photoluminescence from Micellar Assemblies of Cadmium Sulfide Quantum Dots and Gold Nanoparticles Enhanced Photoluminescence from Micellar Assemblies of Cadmium Sulfide Quantum Dots and Gold Nanoparticles. (2013). doi:10.1021/jp311200r
122. Kim, B. S., Qiu, J. M., Wang, J. P. & Taton, T. A. Magnetomicelles: Composite nanostructures from magnetic nanoparticles and cross-linked amphiphilic block copolymers. *Nano Lett.* **5**, 1987–1991 (2005).
123. Hickey, R. J., Haynes, A. S., Kikkawa, J. M. & Park, S. Controlling the Self-Assembly Structure of Magnetic Nanoparticles and Amphiphilic Block-Copolymers: From Micelles to Vesicles. *J. Am. Chem. Soc.* **133**, 1517–1525 (2011).
124. Zhu, J. & Hayward, R. C. Spontaneous generation of amphiphilic block copolymer micelles with multiple morphologies through interfacial instabilities. *J. Am. Chem. Soc.* **130**, 7496–7502 (2008).
125. Chen, H. Y. *et al.* Encapsulation of single small gold nanoparticles by diblock copolymers. *ChemPhysChem* **9**, 388–392 (2008).
126. Tan, L.H.; Xing, S.; Chen, T.; Chen, G.; Huang, X.; Yhang, H.; Chen, H. Fabrication of Polymer Nanocavities with Tailored Openings. *ACS Nano* **3**, 3469–3474 (2009).
127. Chen, G. *et al.* Measuring ensemble-averaged surface-enhanced Raman scattering in the hotspots of colloidal nanoparticle dimers and trimers. *J. Am. Chem. Soc.* **132**, 3644–3645 (2010).
128. Kang, Y. & Taton, T. A. Controlling shell thickness in core-shell gold nanoparticles via surface-templated adsorption of block copolymer surfactants. *Macromolecules* **38**, 6115–6121 (2005).
129. Glotzer, S. C. & Solomon, M. J. Anisotropy of building blocks and their assembly into complex structures. *Nat. Mater.* **6**, 557–562 (2007).
130. Liu, K., Zhao, N. & Kumacheva, E. Self-assembly of inorganic nanorods. *Chem. Soc. Rev.* **40**, 656–671 (2011).
131. Li, W. *et al.* Ordering of gold nanorods in confined spaces by directed assembly.

- Macromolecules* **46**, 2241–2248 (2013).
132. Wang, M., Zhang, M., Siegers, C., Scholes, G. D. & Winnik, M. A. Polymer vesicles as robust scaffolds for the directed assembly of highly crystalline nanocrystals. *Langmuir* **25**, 13703–13711 (2009).
 133. Xu, J. *et al.* Mechanical nanosprings: Induced coiling and uncoiling of ultrathin Au nanowires. *J. Am. Chem. Soc.* **132**, 11920–11922 (2010).
 134. Grzelczak, M. *et al.* Steric hindrance induces crosslike self-assembly of gold nanodumbbells. *Nano Lett.* **12**, 4380–4384 (2012).
 135. Wang, J., Li, W. & Zhu, J. Encapsulation of inorganic nanoparticles into block copolymer micellar aggregates: Strategies and precise localization of nanoparticles. *Polymer (Guildf)*. **55**, 1079–1096 (2014).
 136. Gao, X., Cui, Y., Levenson, R. M., Chung, L. W. K. & Nie, S. In vivo cancer targeting and imaging with semiconductor quantum dots. *Nat. Biotechnol.* **22**, 969–976 (2004).
 137. Michalet, X. Quantum Dots for Live Cells , in Vivo Imaging, and Diagnostics. *Science (80-.)*. **37**, 538–545 (2005).
 138. Wang, Y. *et al.* Synthesis of gold nanoparticles stabilized with poly(N-isopropylacrylamide)-co-poly(4-vinyl pyridine) colloid and their application in responsive catalysis. *J. Mol. Catal. A Chem.* **280**, 1–6 (2008).
 139. Shajkumar, A. *et al.* Silica-supported Au@hollow-SiO₂ particles with outstanding catalytic activity prepared via block copolymer template approach. *J. Colloid Interface Sci.* **491**, 246–254 (2017).
 140. Peng, X. Mechanisms for the shape-control and shape-evolution of colloidal semiconductor nanocrystals. *Adv. Mater.* **15**, 459–463 (2003).
 141. Burda, C., Chen, X., Narayanan, R. & El-Sayed, M. A. *Chemistry and properties of nanocrystals of different shapes. Chemical Reviews* **105**, (2005).
 142. Li, Y. & Shi, J. Hollow-structured mesoporous materials: Chemical synthesis, functionalization and applications. *Adv. Mater.* **26**, 3176–3205 (2014).
 143. Lou, X. W. (David), Archer, L. A. & Yang, Z. Hollow Micro-/Nanostructures: Synthesis and Applications. *Adv. Mater.* **20**, 3987–4019 (2008).
 144. Zhao, Y. & Jiang, L. Hollow micro/nanomaterials with multilevel interior structures. *Adv. Mater.* **21**, 3621–3638 (2009).
 145. Kalele, S., Gosavi, S. W., Urban, J. & Kulkarni, S. K. Nanoshell particles : synthesis , properties and applications. *Curr. Sci.* **91**, 1038–1052 (2006).
 146. Mahmoud, M. A., O’Neil, D. & El-Sayed, M. A. Hollow and solid metallic nanoparticles in sensing and in nanocatalysis. *Chem. Mater.* **26**, 44–58 (2014).
 147. Zhang, Q., Wang, W., Goebel, J. & Yin, Y. Self-templated synthesis of hollow nanostructures. *Nano Today* **4**, 494–507 (2009).
 148. Reiss, P., Protière, M. & Li, L. Core/shell semiconductor nanocrystals. *Small* **5**, 154–168 (2009).

149. Zhang, Q., Lee, I., Joo, J. I. B. & Zaera, F. Core À Shell Nanostructured Catalysts. *Acc. Chem. Res.* **46**, 1816–1824 (2013).
150. Chaudhuri, R. G. & Paria, S. Core / Shell Nanoparticles : Classes , Properties , Synthesis Mechanisms , Characterization , and Applications. *Chem.Rev.* **112**, 2373–2433 (2012).
151. Liu, J. *et al.* Yolk/shell nanoparticles: new platforms for nanoreactors, drug delivery and lithium-ion batteries. *Chem. Commun.* **47**, 12578 (2011).
152. Wu, S.-H. *et al.* Catalytic nano-rattle of Au@hollow silica: towards a poison-resistant nanocatalyst. *J. Mater. Chem.* **21**, 789–794 (2011).
153. Lattuada, M. & Hatton, T. A. Synthesis, properties and applications of Janus nanoparticles. *Nano Today* **6**, 286–308 (2011).
154. Walther, A. & Müller, A. H. E. Janus particles: Synthesis, self-assembly, physical properties, and applications. *Chem. Rev.* **113**, 5194–5261 (2013).
155. Wei, S. *et al.* Multifunctional composite core–shell nanoparticles. *Nanoscale* **3**, 4474 (2011).
156. Bryan, J. D. & Gamelin, D. R. Doped Semiconductor Nanocrystals : Synthesis , Characterization , Physical Properties , and Applications. *Prog. Inorg. Chem.* **54**, 47–126 (2005).
157. Liu, S. & Su, X. The synthesis and application of doped semiconductor nanocrystals. *Anal. Methods* **5**, 4541 (2013).
158. Erwin, S. C. *et al.* Doping semiconductor nanocrystals. *Nature* **436**, 91–94 (2005).
159. Liu, J. *et al.* Double-Shelled Yolk – Shell Microspheres with Fe₃O₄ Cores and SnO₂ Double Shells as High-Performance Microwave Absorbers. *J. Phy Chem C* **117**, 489–495 (2013).
160. Wu, S.-H. *et al.* Catalytic nano-rattle of Au@hollow silica: towards a poison-resistant nanocatalyst. *J. Mater. Chem.* **21**, 789–794 (2011).
161. Yin, Y., Erdonmez, C., Aloni, S. & Alivisatos, A. P. Faceting of nanocrystals during chemical transformation: From solid silver spheres to hollow gold octahedra. *J. Am. Chem. Soc.* **128**, 12671–12673 (2006).
162. Walther, A. & Müller, A. H. E. Janus particles. *Soft Matter* **4**, 663 (2008).
163. Gao, J. *et al.* FePt@CoS₂ yolk-shell nanocrystals as a potent agent to kill HeLa cells. *J. Am. Chem. Soc.* **129**, 1428–1433 (2007).
164. Yin, Y. D. *et al.* Formation of Hollow Nanocrystals through the Nanoscale Kirkendall Effect. *Science (80-.)*. **304**, 711–714 (2004).
165. Yang, Y. *et al.* A yolk-shell nanoreactor with a basic core and an acidic shell for cascade reactions. *Angew. Chemie - Int. Ed.* **51**, 9164–9168 (2012).
166. Liang, X. *et al.* Diffusion through the shells of yolk-shell and core-shell nanostructures in the liquid phase. *Angew. Chemie - Int. Ed.* **51**, 8034–8036 (2012).
167. Zhou, X. *et al.* Nanoparticles With Tunable Shell Thickness and As Core Templates. *Dalt. Trans.* 11834–11842 (2014). doi:10.1039/c4dt01138d

168. Hu, Y. *et al.* Silica-based complex nanorattles as multifunctional carrier for anticancer drug. *J. Mater. Chem.* **21**, 8052–8056 (2011).
169. Li, L. In Vivo Delivery of Silica Nanorattle Encapsulated Docetaxel for Hepatocellular Carcinoma Therapy with Low Toxicity and High Efficacy. *ACS Nano* **4**, 6874 (2010).
170. Xie, Q., Li, J., Tian, Q. & Shi, R. Template-free synthesis of zinc citrate yolk–shell microspheres and their transformation to ZnO yolk–shell nanospheres. *J. Mater. Chem.* **22**, 13541 (2012).
171. Zhang, Q. *et al.* Rattle-type silica colloidal particles prepared by a surface-protected etching process. *Nano Res.* **2**, 583–591 (2009).
172. Fan, C.-M. *et al.* Novel CeO₂ yolk–shell structures loaded with tiny Au nanoparticles for superior catalytic reduction of p-nitrophenol. *Nanoscale* **4**, 6835 (2012).
173. Fang, W. Q. *et al.* Yolk@shell anatase TiO₂ hierarchical microspheres with exposed {001} facets for high-performance dye sensitized solar cells. *J. Mater. Chem.* **22**, 22082 (2012).
174. Hao, M. C. *et al.* Fabrication of nanorattles with passive shell. *J. Phys. Chem. B* **110**, 19162–19167 (2006).
175. Cui, Y., Zhang, H. & Wong, C. C. Facile hydrothermal synthesis of novel Cu₂O core-shell nanospheres via a template-free route. *Mater. Lett.* **86**, 104–107 (2012).
176. Zhong, J., Cao, C., Liu, H., Ding, Y. & Yang, J. Fabrication of Hollow and Yolk – Shell Structured η - Fe₂O₃ Nanoparticles with Versatile Configurations. *Ind.Eng.Chem.Res.* **52**, 1303–1308 (2013).
177. Liu, B. & Zeng, H. C. Symmetric and asymmetric ostwald ripening in the fabrication of homogeneous core-shell semiconductors. *Small* **1**, 566–571 (2005).
178. Pang, H. *et al.* Template-free bottom-up synthesis of yolk-shell vanadium oxide as high performance cathode for lithium ion batteries. *Chem. Commun.* **49**, 1536–1538 (2013).
179. Huang, X., Guo, C., Zuo, J., Zheng, N. & Stucky, G. D. An assembly route to inorganic catalytic nanoreactors containing sub-10-nm gold nanoparticles with anti-aggregation properties. *Small* **5**, 361–365 (2009).
180. Pandey, A. D., Güttel, R., Leoni, M., Schüth, F. & Weidenthaler, C. Influence of the Microstructure of Gold - Zirconia Yolk - Shell Catalysts on the CO Oxidation Activity. *J. Phy Chem C* **114**, 19386–19394 (2010).
181. Galeano, C. *et al.* Yolk-shell gold nanoparticles as model materials for support-effect studies in heterogeneous catalysis: Au, @C and Au, @ZrO₂ for CO oxidation as an example. *Chem. - A Eur. J.* **17**, 8434–8439 (2011).
182. Güttel, R., Paul, M. & Schüth, F. Ex-post size control of high-temperature-stable yolk–shell Au, @ZrO₂ catalysts. *Chem. Commun.* **46**, 895–897 (2010).
183. Li, J. & Zeng, H. C. Size tuning, functionalization, and reactivation of Au in TiO₂nanoreactors. *Angew. Chemie - Int. Ed.* **44**, 4342–4345 (2005).
184. Lee, J., Park, J. C. & Song, H. A Nanoreactor framework of a Au@SiO₂ yolk/shell structure for catalytic reduction of p-nitrophenol. *Adv. Mater.* **20**, 1523–1528 (2008).

185. Liu, J., Qiao, S. Z., Hartono, S. B. & Lu, G. Q. Monodisperse yolk-shell nanoparticles with a hierarchical porous structure for delivery vehicles and nanoreactors. *Angew. Chemie - Int. Ed.* **49**, 4981–4985 (2010).
186. Guo, J., Yang, W., Deng, Y., Wang, C. & Fu, S. Organic-dye-coupled magnetic nanoparticles encaged inside thermoresponsive PNIPAM microcapsules. *Small* **1**, 737–741 (2005).
187. Liu, J. *et al.* A facile vesicle template route to multi-shelled mesoporous silica hollow nanospheres. *J. Mater. Chem.* **20**, 4595 (2010).
188. Huang, C. C., Huang, W. & Yeh, C. S. Shell-by-shell synthesis of multi-shelled mesoporous silica nanospheres for optical imaging and drug delivery. *Biomaterials* **32**, 556–564 (2011).
189. Chen, Z., Geng, Z., Zhang, Z., Liu, Z. & Wang, Z. Template-free synthesis of single-crystalline SmF₃ rattle-structured sub-micropumpkins. *CrystEngComm* **12**, 2841 (2010).
190. Mahmoud, M. A. Plasmon resonance hybridization of gold nanospheres and palladium nanoshells combined in a rattle structure. *J. Phys. Chem. Lett.* **5**, 2594–2600 (2014).
191. Liu, S. *et al.* Novel sea urchin-like hollow core-shell SnO₂ superstructures: Facile synthesis and excellent ethanol sensing performance. *Sensors Actuators, B Chem.* **151**, 229–235 (2010).
192. Liu, N. *et al.* A pomegranate-inspired nanoscale design for large-volume-change lithium battery anodes. *Nat. Nanotechnol.* **9**, 187–192 (2014).
193. Zhou, X. Y., Tang, J. J., Yang, J., Xie, J. & Ma, L. L. Silicon@carbon hollow core-shell heterostructures novel anode materials for lithium ion batteries. *Electrochim. Acta* **87**, 663–668 (2013).
194. Wei Seh, Z. *et al.* Sulphur–TiO₂ yolk–shell nanoarchitecture with internal void space for long-cycle lithium–sulphur batteries. *Nat. Commun.* **4**, 1331 (2013).
195. Chen, S. *et al.* Silicon core–hollow carbon shell nanocomposites with tunable buffer voids for high capacity anodes of lithium-ion batteries. *Phys. Chem. Chem. Phys.* **14**, 12741 (2012).
196. Wu, B. X. & Xu, D. Soft Template Synthesis of Yolk / Silica Shell particles. *Adv. Mater.* **22**, 1516–1520 (2010).
197. Hu, Y. *et al.* Silica-based complex nanorattles as multifunctional carrier for anticancer drug. *J. Mater. Chem.* **21**, 8052 (2011).
198. Tang, F., Li, L. & Chen, D. Mesoporous silica nanoparticles: Synthesis, biocompatibility and drug delivery. *Adv. Mater.* **24**, 1504–1534 (2012).
199. Roca, M. & Haes, A. J. Silica - Void - Gold Nanoparticles : Temporally Stable Surface-Enhanced Raman Scattering Substrates Silica-Void-Gold Nanoparticles : Temporally Stable Surface-Enhanced Raman Scattering Substrates. *J. Am. Chem. Soc.* **130**, 14273–14279 (2008).
200. Wang, J., Shah, Z. H., Zhang, S. & Lu, R. Silica-based nanocomposites via reverse microemulsions: classifications, preparations, and applications. *Nanoscale* **6**, 4418 (2014).

201. Tauster, S. J., Fung, S. C., Baker, R. T. K. & Horsley, J. A. Strong Interactions in Supported-Metal Catalysts. *Science (80-.)*. **211**, 1121–1125 (1981).
202. Zhang, Q., Lee, I., Ge, J., Zaera, F. & Yin, Y. Surface-protected etching of mesoporous oxide shells for the stabilization of metal nanocatalysts. *Adv. Funct. Mater.* **20**, 2201–2214 (2010).
203. Park, J. C. & Song, H. Metal@Silica yolk-shell nanostructures as versatile bifunctional nanocatalysts. *Nano Res.* **4**, 33–49 (2011).
204. Somorjai, G. a., Frei, H. & Park, J. Y. Advancing the frontiers in nanocatalysis, biointerfaces, and renewable energy conversion by innovations of surface techniques. *J. Am. Chem. Soc.* **131**, 16589–16605 (2009).
205. Park, J. C. *et al.* Gram-Scale Synthesis of Magnetically Separable and Recyclable Co@SiO₂ Yolk-Shell Nanocatalysts for Phenoxycarbonylation Reactions. *ChemCatChem* **3**, 755–760 (2011).
206. Okada, A., Nagao, D., Ueno, T., Ishii, H. & Konno, M. Colloidal polarization of yolk/shell particles by reconfiguration of inner cores responsive to an external magnetic field. *Langmuir* **29**, 9004–9009 (2013).
207. Liu, J. *et al.* Synthesis and microwave absorption properties of yolk-shell microspheres with magnetic iron oxide cores and hierarchical copper silicate shells. *ACS Appl. Mater. Interfaces* **5**, 2503–2509 (2013).
208. Hache, F., Ricard, D., Flytzanis, C. & Kreibig, U. The Optical Kerr Effect in Small Metal Particles and Metal Colloids: the Case of Gold. *Appl. Phys. A Mater. Sci. Process.* **47**, 347–357 (1988).
209. Willets, K. A. & Van Duyne, R. P. Localized Surface Plasmon Resonance Spectroscopy and Sensing. *Annu. Rev. Phys. Chem.* **58**, 267–297 (2007).
210. Kelly, K. L., Coronado, E., Zhao, L. L. & Schatz, G. C. The Optical Properties of Metal Nanoparticles: The Influence of Size, Shape, and Dielectric Environment. *J. Phys. Chem. B* **107**, 668–677 (2003).
211. Liz-Marzán, L. M. Tailoring surface plasmons through the morphology and assembly of metal nanoparticles. *Langmuir* **22**, 32–41 (2006).
212. Lu, X., Rycenga, M., Skrabalak, S. E., Wiley, B. & Xia, Y. Chemical Synthesis of Novel Plasmonic Nanoparticles. *Annu. Rev. Phys. Chem.* **60**, 167–192 (2009).
213. Fleischmann, M.; Hendra, P.J.; McQuillan, A. J. Raman spectra of pyridine adsorbed a silver electrode. *Chemical Physics Letters* **26**, 163–166 (1974).
214. Neouze, M.-A. & Schubert, U. Surface Modification and Functionalization of Metal and Metal Oxide Nanoparticles by Organic Ligands. *Monatshefte für Chemie - Chem. Mon.* **139**, 183–195 (2008).
215. Wang, S., Zhang, M. & Zhang, W. Yolk - Shell Catalyst of Single Au Nanoparticle Encapsulated within Hollow Mesoporous Silica Microspheres. *ACS Catal.* **1**, 207–211 (2011).
216. Priebe, M. & Fromm, K. M. One-Pot Synthesis and Catalytic Properties of Encapsulated Silver Nanoparticles in Silica Nanocontainers. *Part.Part.Sys.Character.* 1–7 (2014).

- doi:10.1002/ppsc.201300304
217. Park, J. C. & Song, H. Metal@Silica yolk-shell nanostructures as versatile bifunctional nanocatalysts. *Nano Res.* **4**, 33–49 (2011).
 218. Jiang, Z.-J., Liu, C.-Y. & Sun, L.-W. Catalytic properties of silver nanoparticles supported on silica spheres. *J. Phys. Chem. B* **109**, 1730–1735 (2005).
 219. Zhang, N., Liu, S., Fu, X. & Xu, Y. J. Synthesis of M@TiO₂ (M = Au, Pd, Pt) core-shell nanocomposites with tunable photoreactivity. *J. Phys. Chem. C* **115**, 9136–9145 (2011).
 220. Li, X., Fu, X. & Yang, H. Preparation and photocatalytic activity of eccentric Au-titania core-shell nanoparticles by block copolymer templates. *Phys. Chem. Chem. Phys.* **13**, 2809–2814 (2011).
 221. Cho, E. C., Camargo, P. H. C. & Xia, Y. Synthesis and characterization of noble-metal nanostructures containing gold nanorods in the center. *Adv. Mater.* **22**, 744–748 (2010).
 222. Sun, Y., Wiley, B., Li, Z. Y. & Xia, Y. Synthesis and optical properties of nanorattles and multiple-walled nanoshells/nanotubes made of metal alloys. *J. Am. Chem. Soc.* **126**, 9399–9406 (2004).
 223. Gong, X., Yang, Y. & Huang, S. A novel side-selective galvanic reaction and synthesis of hollow nanoparticles with an alloy core. *J. Phys. Chem. C* **114**, 18073–18080 (2010).
 224. Imhof, A. Preparation and Characterization of Titania-Coated Polystyrene Spheres and Hollow Titania Shells. *Langmuir* **17**, 3579–3585 (2001).
 225. Valdés-Solís, T., Valle-Vigón, P., Sevilla, M. & Fuertes, A. B. Encapsulation of nanosized catalysts in the hollow core of a mesoporous carbon capsule. *J. Catal.* **251**, 239–243 (2007).
 226. Li, G., Kang, E. T., Neoh, K. G. & Yang, X. Concentric hollow nanospheres of mesoporous silica shell-titania core from combined inorganic and polymer syntheses. *Langmuir* **25**, 4361–4364 (2009).
 227. Linley, S., Leshuk, T. & Gu, F. X. Synthesis of magnetic rattle-type nanostructures for use in water treatment. *ACS Appl. Mater. Interfaces* **5**, 2540–2548 (2013).
 228. Xiong, W., Lou, C., Yuan, C., Zhang, Q. & Archer, L. A. Platinum-functionalized octahedral silica nanocages: Synthesis and characterization. *Angew. Chemie - Int. Ed.* **45**, 3825–3829 (2006).
 229. Guo, L. *et al.* Hollow mesoporous carbon spheres with magnetic cores and their performance as separable bilirubin adsorbents. *Chem. - An Asian J.* **4**, 1480–1485 (2009).
 230. Low, X. W., Yuan, C., Rhoades, E., Zhang, Q. & Archer, L. A. Encapsulation and Ostwald ripening of Au and Au-Cl complex nanostructures in silica shells. *Adv. Funct. Mater.* **16**, 1679–1684 (2006).
 231. Tan, L., Chen, D., Liu, H. & Tang, F. A silica nanorattle with a mesoporous shell: An ideal nanoreactor for the preparation of tunable gold cores. *Adv. Mater.* **22**, 4885–4889 (2010).
 232. Song, G. *et al.* A simple transformation from silica core-shell-shell to yolk-shell nanostructures: a useful platform for effective cell imaging and drug delivery. *J. Mater.*

- Chem.* **22**, 17011 (2012).
233. Yang, Y., Liu, J., Li, X., Liu, X. & Yang, Q. Organosilane-assisted transformation from core-shell to yolk-shell nanocomposites. *Chem. Mater.* **23**, 3676–3684 (2011).
234. Li, L., Zhang, Y., Hao, N., Chen, D. & Tang, F. Fabrication of PLGA coated silica nanorattle for controlling the drug release behavior. *Chinese Sci. Bull.* **57**, 3631–3638 (2012).
235. Liu, T. *et al.* Silica nanorattle with enhanced protein loading: A potential vaccine adjuvant. *J. Colloid Interface Sci.* **400**, 168–174 (2013).
236. Gedde, U. W. *Polymer Physics*. (Chapman & Hall, 1995).
237. Li, Y. & Somorjai, G. A. Nanoscale Advances in Catalysis and Energy Applications. *Nano Lett.* **10**, 2289–2295 (2010).
238. Zhao, B. W. *et al.* Uniform Rattle-type Hollow Magnetic Mesoporous Spheres as Drug Delivery Carriers and their Sustained-Release Property**. *Adv.Funct.Mater.* **18**, 2780–2788 (2008).
239. Ni, W. *et al.* Integration of Sn/C yolk–shell nanostructures into free-standing conductive networks as hierarchical composite 3D electrodes and the Li-ion insertion/extraction properties in a gel-type lithium-ion battery thereof. *J. Mater. Chem. A* **2**, 19122–19130 (2014).
240. Zhu, Y., Ikoma, T., Hanagata, N. & Kaskel, S. Rattle-type Fe₃O₄@SiO₂ hollow mesoporous spheres as carriers for drug delivery. *Small* **6**, 471–478 (2010).
241. Zhu, Y., Fang, Y. & Kaskel, S. Folate-Conjugated Fe₃O₄@SiO₂ Hollow Mesoporous Spheres for Targeted Anticancer Drug Delivery. *J. Phys. Chem. C* **114**, 16382–16388 (2010).
242. Zhu, Y. F., Kockrick, E., Ikoma, T., Hanagata, N. & Kaskel, S. An Efficient Route to Rattle-Type Fe₃O₄@SiO₂ Hollow Mesoporous Spheres Using Colloidal Carbon Spheres Templates. *Chem. Mater.* **21**, 2547–2553 (2009).
243. Wu, S. *et al.* Thermosensitive Au-PNIPA yolk-shell nanoparticles with tunable selectivity for catalysis. *Angew. Chemie - Int. Ed.* **51**, 2229–2233 (2012).
244. Wu, S., Kaiser, J., Drechsler, M., Ballauff, M. & Lu, Y. Thermosensitive Au-PNIPA yolk-shell particles as ‘ nanoreactors ’ with tunable optical properties. *Colloid Polym. Sci.* **291**, 231–237 (2013).
245. McMullan, D. Scanning electron microscopy 1928–1965. *Scanning* **17**, 175–185 (1995).
246. Bradbury, S.; Joy, C.D.;Ford, J. B. Transmission Electron Microscope. *Encyclopedia Britannica Inc.* (2017). Available at: <https://www.britannica.com/print/article/602949>.
247. Pavia, D. L., Lampman, G. M. & Kriz, G. S. *Introduction to Spectroscopy*. (Thomson Learning, Inc., 2001).
248. Theoretical principles. *Sheffield Hallam University* 4–7 (2010). Available at: <https://teaching.shu.ac.uk/hwb/chemistry/tutorials/molspec/uvvisab1.htm>.
249. Thakur, A. Principle , working and applications of UV spectroscopy Introduction to UV spectroscopy Concept of Chromophore and Auxochrome in the UV spectroscopy. *India*

- Study Channel* 1–5 (2014). Available at: <http://www.indiastudychannel.com/resources/146681-Principle-working-and-applications-of-UV-spectroscopy.aspx>.
250. Arzenšek, D., Podgornik, R. & Kuzman, D. Dynamic light scattering and application to proteins in solutions. *Semin. Dep. Physics, Univ. Ljubljana* 1–18 (2010).
251. Miao, X. M., Xiong, C., Wang, W. W., Ling, L. S. & Shuai, X. T. Dynamic-light-scattering-based sequence-specific recognition of double-stranded DNA with oligonucleotide-functionalized gold nanoparticles. *Chem. - A Eur. J.* **17**, 11230–11236 (2011).
252. Malvern Instruments. Dynamic Light Scattering: An Introduction in 30 Minutes. <Http://Www.Malvern.Com/En/Products/Technology/Dynamic-Light-Scattering/> 1–8 (2014).
253. Dąbrowski, A. Adsorption - From theory to practice. *Adv. Colloid Interface Sci.* **93**, 135–224 (2001).
254. Bolis, V. in *Calorimetry and Thermal Methods in Catalysis* (ed. Auroux.A) (Springer, 2013). doi:10.1007/978-3-642-11954-5
255. Inductively Coupled Plasma Optical Emission Spectroscopy (ICP - OES Analysis) Typical Industries using ICP - OES. *Lucideon Ltd.* (2017). Available at: <https://www.lucideon.com/testing-characterization/techniques/inductively-coupled-plasma-optical-emission-spectroscopy-icp-oes>.
256. Binnig, G. & Quate, C. F. Atomic Force Microscope. *Phys. Rev. Lett.* **56**, 930–933 (1986).
257. Meyer, E. *Atomic force microscopy*. Oxford University Press (2010). doi:10.1007/0-387-25919-8
258. PerkinElmer Inc. Thermogravimetric Analysis - A Beginner ' s Guide. (2013).
259. Anderson Materials Evaluation Inc. Thermogravimetry (TG) or Thermogravimetric Analysis (TGA) or Thermal Gravimetric Analysis. 1–5 (2017). Available at: <http://www.andersonmaterials.com/tga.html>.
260. Chen, D., Park, S., Chen, J., Redston, E. & Russell, T. P. A Simple Route for the Preparation of Mesoporous Nanostructures Using Block Copolymers. *ACS Nano* **3**, 2827–2833 (2009).
261. Hiramatsu, H. & Osterloh, F. E. A simple large-scale synthesis of nearly monodisperse gold and silver nanoparticles with adjustable sizes and with exchangeable surfactants. *Chem. Mater.* **16**, 2509–2511 (2004).
262. Brown, K. R., Walter, D. G. & Natan, M. J. Seeding of colloidal Au nanoparticle solutions. 2. Improved control of particle size and shape. *Chem. Mater.* **12**, 306–313 (2000).
263. Rahman, I. A. & Padavettan, V. Synthesis of Silica Nanoparticles by Sol-Gel: Size-Dependent Properties, Surface Modification, and Applications in Silica-Polymer Nanocomposites—A Review. *J. Nanomater.* **2012**, 1–15 (2012).
264. Park, S., Wang, J. Y., Kim, B. & Russell, T. P. From nanorings to nanodots by patterning

- with block copolymers. *Nano Lett.* **8**, 1667–1672 (2008).
265. Vignolini, S. *et al.* A 3D optical metamaterial made by self-assembly. *Adv. Mater.* **24**, 23–27 (2012).
266. Sarkar, B. & Alexandridis, P. Block copolymer-nanoparticle composites: Structure, functional properties, and processing. *Prog. Polym. Sci.* **40**, 33–62 (2014).
267. Bigall, N. C., Nandan, B., Gowd, E. B., Horechyy, A. & Eychmüller, A. High-Resolution Metal Nanopatterning by Means of Switchable Block Copolymer Templates. *ACS Appl. Mater. Interfaces* **7**, 12559–12569 (2015).
268. Cowman, C. D. *et al.* Multicomponent Nanomaterials with Complex Networked Architectures from Orthogonal Degradation and Binary Metal Backfilling in ABC Triblock Terpolymers. *J. Am. Chem. Soc.* **137**, 6026–6033 (2015).
269. Rijn, P. Van *et al.* Challenges and advances in the field of self-assembled membranes. *Chem. Soc. Rev.* **42**, (2013).
270. Park, S. & Park, M. The Preparation and Characterization of the Cross-Linked Spherical, Cylindrical, and Vesicular Micelles of Poly (styrene- b -isoprene) Diblock Copolymers. *Langmuir* **23**, 6788–6795 (2007).
271. Zhang, K., Gao, L. & Chen, Y. Organic - Inorganic Hybrid Materials by Self-Gelation of Block Copolymer Assembly and Nanoobjects with Controlled Shapes Thereof. *Macromolecules* **40**, 5916–5922 (2007).
272. Aizawa, M. *et al.* Block Copolymer Templated Chemistry for the Formation of Metallic Nanoparticle Arrays on Semiconductor Surfaces. *Chem. Mater.* **19**, 5090–5101 (2007).
273. Mistark, P. A. *et al.* Block-Copolymer-Based Plasmonic Nanostructures. *ACS Nano* **3**, 3987–3992 (2009).
274. Zoelen, W. Van *et al.* Ordered Arrays of Ferroelectric Nanoparticles by Pulsed Laser Deposition on PS- b -P4VP (PDP) Supramolecule-Based Templates. *Chem. Mater.* **21**, 4719–4723 (2009).
275. Horechyy, A. *et al.* Highly ordered arrays of magnetic nanoparticles prepared via block copolymer assembly. *J. Mater. Chem.* **20**, 7734–7741 (2010).
276. Belfiore, L. A. & Mccurdie, M. P. A. T. Reactive Blending via Metal-Ligand Coordination. *J. Polym. Sci. Part B Polym. Phys.* **33**, 105–124 (1995).
277. Malynych, S., Luzinov, I. & Chumanov, G. Poly (Vinyl Pyridine) as a Universal Surface Modifier for Immobilization of Nanoparticles. *J. Phys. Chem. B* **106**, 1280–1285 (2002).
278. Clarke, C. J. & Eisenberg, A. Measurements of the Flory - Huggins Interaction Parameter for Polystyrene - Poly (4-vinylpyridine) Blends. *Macromolecules* **30**, 4184–4188 (1997).
279. Su, Y. *et al.* Synthesis of hierarchical hollow silica microspheres containing surface nanoparticles employing the quasi-hard template of poly(4-vinylpyridine) microspheres. *Langmuir* **27**, 8983–8989 (2011).
280. Khanal, A. & Nakashima, K. Incorporation and release of cloxacillin sodium in micelles of poly(styrene-b-2-vinyl pyridine-b-ethylene oxide). *J. Control. Release* **108**, 150–160

- (2005).
281. Brinker, C. J. . S. G. . *Sol-Gel Science: The Physics and Chemistry of Sol-Gel Processing*. (Academic Press, INC., 1990).
 282. Karmakar, B., De, G. & Ganguli, D. Dense silica microspheres from organic and inorganic acid hydrolysis of TEOS. *J. Non. Cryst. Solids* **272**, 119–126 (2000).
 283. Cheng, F., Yang, X., Peng, H., Chen, D. & Jiang, M. Well-Controlled Formation of Polymeric Micelles with a Nanosized Aqueous Core and Their Applications as Nanoreactors. *Macromolecules*. **40**, 8007–8014 (2007).
 284. Li, D., He, Q., Yang, Y., Mo, H. & Li, J. Two-Stage pH Response of Poly (4-vinylpyridine) Grafted Gold Nanoparticles. *Macromolecules* **41**, 7254–7256 (2008).
 285. Chaturvedi, S., Dave, P. N. & Shah, N. K. Applications of nano-catalyst in new era. *J. Saudi Chem. Soc.* **16**, 307–325 (2012).
 286. Haruta, M. Size- and support-dependency in the catalysis of gold. *Catal. Today* **36**, 153–166 (1997).
 287. Kinetics of Chemical Reactions. 5–32
 288. Somorjai, G. A. & Li, Y. Impact of surface chemistry. *Proc. Natl. Acad. Sci.* **108**, 917–924 (2011).
 289. Wunder, S., Lu, Y., Albrecht, M. & Ballauff, M. Catalytic activity of faceted gold nanoparticles studied by a model reaction: Evidence for substrate-induced surface restructuring. *ACS Catal.* **1**, 908–916 (2011).
 290. Pozun, Z. D. *et al.* A systematic investigation of p -nitrophenol reduction by bimetallic dendrimer encapsulated nanoparticles. *J. Phys. Chem. C* **117**, 7598–7604 (2013).
 291. Tripathi, B. P., Dubey, N. C., Choudhury, S., Formanek, P. & Stamm, M. Ultrathin and Switchable Nanoporous Catalytic Membranes of Polystyrene- b -poly-4-Vinyl Pyridine Block Copolymer Spherical Micelles. *Adv. Mater. Interfaces* **2**, (2015).
 292. Haruta, M. Catalysis of gold nanoparticles deposited on metal oxides. *Cattech* **6**, 102–115 (2002).
 293. Shmakov, S. N. & Pinkhassik, E. Simultaneous templating of polymer nanocapsules and entrapped silver nanoparticles. *Chem. Commun.* **46**, 7346–7348 (2010).
 294. Piao, L., Jianwei, J. & Kim, S.-H. The facile synthesis of Cu@SiO₂ yolk-shell nanoparticles via the disproportionation reaction of silica-encapsulated Cu₂O nanoparticle aggregates. *Nanoscale* **7**, 8299–8303 (2015).
 295. Zhang, N. & Xu, Y. Aggregation- and Leaching-Resistant, Reusable, and Multifunctional Pd@CeO₂ as a Robust Nanocatalyst Achieved by a Hollow Core-Shell Strategy. *Chem. Mater.* **25**, 1979–1988 (2013).
 296. Oh, S. H. & Hoflund, G. B. Chemical state study of palladium powder and ceria-supported palladium during low-temperature CO oxidation. *J. Phys. Chem. A* **110**, 7609–7613 (2006).
 297. Zorn, K. *et al.* CO Oxidation on Technological Pd - Al₂O₃ Catalysts : Oxidation State and Activity. *J. Phys. Chem. C* **115**, 1103–1111 (2011).

298. Guzman, J. *et al.* CO oxidation catalyzed by supported gold: Cooperation between gold and nanocrystalline rare-earth supports forms reactive surface superoxide and peroxide species. *Angew. Chemie - Int. Ed.* **44**, 4778–4781 (2005).
299. Wang, Y., Van de Vyver, S., Sharma, K. K. & Román-Leshkov, Y. Insights into the stability of gold nanoparticles supported on metal oxides for the base-free oxidation of glucose to gluconic acid. *Green Chem.* **16**, 719–726 (2014).
300. Chen, C. *et al.* Mesoporous multicomponent nanocomposite colloidal spheres: Ideal high-temperature stable model catalysts. *Angew. Chemie - Int. Ed.* **50**, 3725–3729 (2011).
301. Ma, C. Y. *et al.* Mesoporous Co₃O₄ and Au/Co₃O₄ Catalysts for Low-Temperature Oxidation of Trace Ethylene. *J. Am. Chem. Soc.* **132**, 2608–2613 (2010).
302. Zhao, K., Qiao, B., Wang, J., Zhang, Y. & Zhang, T. A highly active and sintering-resistant Au/FeO_x-hydroxyapatite catalyst for CO oxidation. *Chem. Commun.* **47**, 1779–1781 (2011).
303. Liu, X., Wang, A., Wang, X., Mou, C.-Y. & Zhang, T. Au–Cu Alloy nanoparticles confined in SBA-15 as a highly efficient catalyst for CO oxidation. *Chem. Commun.* 3187 (2008). doi:10.1039/b804362k
304. Feng, J. *et al.* Au–Pd nanoalloys supported on Mg–Al mixed metal oxides as a multifunctional catalyst for solvent-free oxidation of benzyl alcohol. *Dalt. Trans.* **42**, 14498 (2013).
305. Qi, J. *et al.* Facile synthesis of core–shell Au@CeO₂ nanocomposites with remarkably enhanced catalytic activity for CO oxidation. *Energy Environ. Sci.* **5**, 8937 (2012).
306. Zeng, H. C. Integrated nanocatalysts. *Acc. Chem. Res.* **46**, 226–235 (2013).
307. Liu, S., Bai, S. Q., Zheng, Y., Shah, K. W. & Han, M. Y. Composite Metal-Oxide Nanocatalysts. *ChemCatChem* **4**, 1462–1484 (2012).
308. Priebe, M. & Fromm, K. M. Nanorattles or yolk-shell nanoparticles-what are they, how are they made, and what are they good for? *Chem. Eur. J.* **21**, 3854–3874 (2015).
309. Sanwaria, S. *et al.* Synthesis of hollow silica nanostructures using functional hairy polymer nanofibers as templates. *RSC Adv.* **3**, 24009 (2013).
310. Pletsch, H. *et al.* Ultrasound-Mediated Synthesis of High-Molecular Weight Polystyrene-Grafted Silver Nanoparticles by Facile Ligand Exchange Reactions in Suspension. *Small* **10**, 201–208 (2014).
311. Ehlert, S., Taheri, S. M., Pirner, D., Drechsler, M. & Schmidt, H. Polymer Ligand Exchange to Control Stabilization and Compatibilization of Nanocrystals. *ACS Nano* 6114–6122 (2014).
312. Aditya, T., Pal, A. & Pal, T. Nitroarene reduction: a trusted model reaction to test nanoparticle catalysts. *Chem. Commun.* **51**, 9410–9431 (2015).
313. Hotze, E. M. *et al.* Environmental Transformations of Silver Nanoparticles : Impact on Stability and Toxicity Cle m. *Environ. Sci. Technol.* **46**, 6900–6914 (2012).
314. Misra, S. K., Dybowska, A., Berhanu, D., Luoma, S. N. & Valsami-Jones, E. The

- complexity of nanoparticle dissolution and its importance in nanotoxicological studies. *Sci. Total Environ.* **438**, 225–232 (2012).
315. Tai, J. T. *et al.* Protein-silver nanoparticle interactions to colloidal stability in acidic environments. *Langmuir* **30**, 12755–12764 (2014).
316. Molleman, B. & Hiemstra, T. Time, pH, and size dependency of silver nanoparticle dissolution: The road to equilibrium. *Environ. Sci. Nano* (2017). doi:10.1039/C6EN00564K
317. Peretyazhko, T. S., Zhang, Q. & Colvin, V. L. Size-Controlled Dissolution of Silver Nanoparticles at Neutral and acidic pH condition kinetic and size changes. *Environ. Sci. Technol.* **48**, 11954–11961 (2014).
318. [Werner_Stumm,_James_J._Morgan]_Aquatic_Chemistry(BookSee.org).pdf.
319. Liu, J. Y. & Hurt, R. H. Ion release kinetics and particle persistence in aqueous nano-silver colloids. *Environ. Sci. Technol.* **44**, 2169–2175 (2010).
320. Sanwaria, S. *et al.* Synthesis of hollow silica nanostructures using functional hairy polymer nanofibers as templates. *RSC Adv.* **3**, 24009 (2013).
321. Joo, S. H. *et al.* Thermally stable Pt/mesoporous silica core-shell nanocatalysts for high-temperature reactions. *Nat. Mater.* **8**, 126–131 (2009).
322. Horechyy, A. *et al.* In-situ monitoring of silica shell growth on PS-b-P4VP micelles as templates using DLS. *Polymer (Guildf)*. **107**, 485–491 (2016).
323. Ruthstein, S., Frydman, V., Kababya, S., Landau, M. & Goldfarb, D. Study of the formation of the mesoporous material SBA-15 by EPR spectroscopy. *J. Phys. Chem. B* **107**, 1739–1748 (2003).
324. Wunder, S., Polzer, F., Lu, Y., Mei, Y. & Ballauff, M. Kinetic Analysis of Catalytic Reduction of 4-Nitrophenol by Metallic Nanoparticles Immobilized in Spherical Polyelectrolyte Brushes. *J. Phys. Chem. C* **114**, 8814–8820 (2010).
325. Susana, C. R., Jorge, P. J., Pablo, H., Luis, M. L. M. & Paul, M. Colloidal gold-catalyzed reduction of ferrocyanate (III) by borohydride ions: A model system for redox catalysis. *Langmuir* **26**, 1271–1277 (2010).
326. Aditya, T., Pal, A. & Pal, T. Nitroarene reduction: a trusted model reaction to test nanoparticle catalysts. *Chem. Commun.* **51**, 9410–9431 (2015).
327. Zhao, P., Feng, X., Huang, D., Yang, G. & Astruc, D. Basic concepts and recent advances in nitrophenol reduction by gold- and other transition metal nanoparticles. *Coord. Chem. Rev.* **287**, 114–136 (2015).
328. Pradhan, N., Pal, A. & Pal, T. Silver nanoparticle catalyzed reduction of aromatic nitro compounds. *Colloids Surfaces A Physicochem. Eng. Asp.* **196**, 247–257 (2002).
329. Rowland, S. CHEM-UA 652 : Thermodynamics and Kinetics Notes for Lecture 23. *New York University* 1–5 (1995). Available at: http://www.nyu.edu/classes/tuckerman/pchem/lectures/lecture_23.pdf.
330. Wunder, S. Synthesis, characterization and catalytic activity of immobilized metallic nanoparticles. (2013).

331. Fidalgo, A., Emi, M. & Ilharco, L. M. Chemical Control of Highly Porous Silica Xerogels : Physical Properties and Morphology. *Chem. Mater.* **15**, 2186–2192 (2003).
332. Ciriminna, R. *et al.* The sol-gel route to advanced silica-based materials and recent applications. *Chem. Rev.* **113**, 6592–6620 (2013).
333. Soleimani Dorcheh, A. & Abbasi, M. H. Silica aerogel; synthesis, properties and characterization. *J. Mater. Process. Technol.* **199**, 10–26 (2008).
334. Izutsu, H., Mizukami, F., Nair, P. K., Kiyozumi, Y. & Maeda, K. Preparation and characterization of porous silica spheres by the sol-gel method in the presence of tartaric acid. *J. Mater. Chem.* **7**, 767–771 (1997).
335. Zhao, P., Feng, X., Huang, D., Yang, G. & Astruc, D. Basic concepts and recent advances in nitrophenol reduction by gold- and other transition metal nanoparticles. *Coord. Chem. Rev.* **287**, 114–136 (2015).
336. Lu, Y., Mei, Y., Drechsler, M. & Ballauff, M. Thermosensitive core-shell particles as carriers for Ag nanoparticles: Modulating the catalytic activity by a phase transition in networks. *Angew. Chemie - Int. Ed.* **45**, 813–816 (2006).
337. Panigrahi, S. Synthesis and size-selective catalysis by supported gold nanoparticles: Study on heterogeneous and homogeneous catalytic process. *J. Phys. Chem. C* **111**, 4596–4605 (2007).
338. Shaik, F., Zhang, W., Niu, W. & Lu, X. Volume-confined synthesis of ligand-free gold nanoparticles with tailored sizes for enhanced catalytic activity. *Chem. Phys. Lett.* **613**, 95–99 (2014).
339. Mondal, S., Samanta, A., Dhar, B. B. & Devi, R. N. Encapsulation of ultra small metal clusters in silica: Evolution of the concept of nanoreactors and the case of Ag-Pd@SiO₂ alloy catalyst. *Catal. Today* **251**, 114–120 (2015).
340. Jeong, U., Joo, J. B. & Kim, Y. Au nanoparticle-embedded SiO₂-Au@SiO₂ catalysts with improved catalytic activity, enhanced stability to metal sintering and excellent recyclability. *RSC Adv.* **5**, 55608–55618 (2015).
341. Chen, L., Hu, J., Qi, Z., Fang, Y. & Richards, R. Gold nanoparticles intercalated into the walls of mesoporous silica as a versatile redox catalyst. *Ind. Eng. Chem. Res.* **50**, 13642–13649 (2011).
342. Chen, J., Xue, Z., Feng, S., Tu, B. & Zhao, D. Synthesis of mesoporous silica hollow nanospheres with multiple gold cores and catalytic activity. *J. Colloid Interface Sci.* **429**, 62–67 (2014).
343. Fenger, R., Fertitta, E., Kirmse, H., Thünemann, a. F. & Rademann, K. Size dependent catalysis with CTAB-stabilized gold nanoparticles. *Phys. Chem. Chem. Phys.* **14**, 9343 (2012).
344. Rajesh, R., Kumar, S. S. & Venkatesan, R. Efficient degradation of azo dyes using Ag and Au nanoparticles stabilized on graphene oxide functionalized with PAMAM dendrimers. *New J. Chem.* **38**, 1551–1558 (2014).
345. Ganapuram, B. R. *et al.* Catalytic reduction of methylene blue and Congo red dyes using green synthesized gold nanoparticles capped by salmalia malabarica gum. *Int. Nano Lett.*

- 5, 215–222 (2015).
346. Khan, M. M., Lee, J. & Cho, M. H. Au@TiO₂ nanocomposites for the catalytic degradation of methyl orange and methylene blue: An electron relay effect. *J. Ind. Eng. Chem.* **20**, 1584–1590 (2014).
347. Azad, U. P., Ganesan, V. & Pal, M. Catalytic reduction of organic dyes at gold nanoparticles impregnated silica materials: Influence of functional groups and surfactants. *J. Nanoparticle Res.* **13**, 3951–3959 (2011).
348. Naik, B. *et al.* Preparation of a magnetically separable CoFe₂O₄ supported Ag nanocatalyst and its catalytic reaction towards the decolorization of a variety of dyes. *RSC Adv.* **5**, 40193–40198 (2015).
349. Rajesh, R., Sujanthi, E., Senthil Kumar, S. & Venkatesan, R. Designing versatile heterogeneous catalysts based on Ag and Au nanoparticles decorated on chitosan functionalized graphene oxide. *Phys. Chem. Chem. Phys.* **17**, 11329–11340 (2015).
350. Kumar, M. & Deka, S. Multiply Twinned AgNi Alloy Nanoparticles as Highly Active Catalyst for Multiple Reduction and Degradation Reactions. *ACS Appl. Mater. Interfaces* **6**, 16071–16081 (2014).
351. Narayanan, K. B. & Park, H. H. Homogeneous catalytic activity of gold nanoparticles synthesized using turnip (*Brassica rapa* L.) leaf extract in the reductive degradation of cationic azo dye. *Korean J. Chem. Eng.* **32**, 1273–1277 (2015).
352. McNeff, C. V. *et al.* A continuous catalytic system for biodiesel production. *Appl. Catal. A Gen.* **343**, 39–48 (2008).
353. Ricciardi, R., Huskens, J. & Verboom, W. Nanocatalysis in Flow. *ChemSusChem* (2015). doi:10.1002/cssc.201500514
354. Ricciardi, R. Catalysis in flow microreactors with coatings of acidic polymer brushes and dendrimer encapsulated nanoparticles. (University of Twente, 2015).
355. Ricciardi, R., Huskens, J. & Verboom, W. Dendrimer-encapsulated Pd nanoparticles as catalysts for C-C cross-couplings in flow microreactors. *Org. Biomol. Chem.* **13**, 4953–9 (2015).
356. Phan, N. T. S., Khan, J. & Styring, P. Polymer-supported palladium catalysed Suzuki-Miyaura reactions in batch and a mini-continuous flow reactor system. *Tetrahedron* **61**, 12065–12073 (2005).
357. Frost, C. G. & Mutton, L. Heterogeneous catalytic synthesis using microreactor technology. *Green Chem.* **12**, 1687 (2010).
358. Bermudez, J. M. *et al.* Continuous flow nanocatalysis: reaction pathways in the conversion of levulinic acid to valuable chemicals. *Green Chem.* **15**, 2786 (2013).
359. Kirschning, A., Solodenko, W. & Mennecke, K. Combining enabling techniques in organic synthesis: Continuous flow processes with heterogenized catalysts. *Chem. - A Eur. J.* **12**, 5972–5990 (2006).
360. Obermayer, D. *et al.* Nanocatalysis in continuous flow: supported iron oxide nanoparticles for the heterogeneous aerobic oxidation of benzyl alcohol. *Green Chem.* **15**, 1530–1537 (2013).

361. Park, J. C., Bang, J. U., Lee, J., Ko, C. H. & Song, H. Ni@SiO₂ yolk-shell nanoreactor catalysts: High temperature stability and recyclability. *J. Mater. Chem.* **20**, 1239–1246 (2010).
362. Guo, M. *et al.* Enhancing the catalytic activity of Ru NPs deposited with carbon species in yolk-shell nanostructures. *J. Mater. Chem. A* **4**, 10956–10963 (2016).
363. Gao, H. *et al.* A Facile in Situ Self-Assembly Strategy for Large-Scale Fabrication of CHS @ MOF Yolk / Shell Structure and Its Catalytic Application in a Flow System. *ACS Appl. Mater. Interfaces* **7**, 4667–4674 (2015).
364. Zhang, T. *et al.* A Self-Templated Route to Hollow Silica Microspheres. *J. Phys. Chem. C* **113**, 3168–3175 (2009).
365. Zheng, L.-Q., Yu, X.-D., Xu, J.-J. & Chen, H.-Y. Reversible catalysis for the reaction between methyl orange and NaBH₄ by silver nanoparticles. *Chem. Commun.* **51**, 1050–1053 (2015).
366. Astruc, D. in *Nanoparticles and Catalysis* (ed. Astruc, D.) 1–48 (Wiley-VCH Verlag GmbH & Co. KGaA, Weinheim, Germany, 2008). doi:10.1002/9783527621323.ch1
367. Davis, M. E. & Davis, R. J. Heterogeneous Catalysis. *Fundam. Chem. React. Eng.* **4**, 133–183 (2012).
368. M. Albert Vannice. *Kinetics of Catalytic reactions. Technique of organic chemistry, v. 2* (Springer New York, 2005).
369. Sips, R. On the Structure of a Catalyst Surface. II. *J. Chem. Phys.* **18**, 1024 (1950).
370. Jeppu, G. P. & Clement, T. P. A modified Langmuir-Freundlich isotherm model for simulating pH-dependent adsorption effects. *J. Contam. Hydrol.* **129–130**, 46–53 (2012).
371. Jaroniec, M., Deryło, A. & Marczewski, A. The Langmuir-Freundlich equation in adsorption from dilute solutions on solids. *Monatshefte für Chemie Chem. Mon.* **114**, 393–397 (1983).
372. Bettuzzi, S. Introduction. *Adv. Cancer Res.* **104**, 1–8 (2009).
373. Shelby, C. Diagram courtesy of Iowa State University References : *Purdue University* 1–3 (2015). Available at: <http://www.purdue.edu/rem/rs/sem.htm>.
374. Zhou, W. *Scanning Microscopy for Nanotechnology: Techniques and Applications. Scanning Microscopy for Nanotechnology: Techniques and Applications* (Springer New York LLC, 2006). doi:10.1007/978-0-387-39620-0
375. Otto, T. N. & Habicht, W. in *Scanning Electron Microscopy* (ed. Viacheslav, K.) (Intechopen books, 2012).
376. Cheney, B. in *Introduction to scanning electron microscopy.* **29**, 29–36 (2007).
377. R.Ubic. MSE 421/521 Introduction to Electron Microscopy. (1933).
378. Fraunhofer, J. & Kirchhoff, G. Fundamentals of Spectroscopy 5.1. *Microwaves* 79–88 (2002). doi:10.1002/0471733555.ch1
379. Eustis, S. & el-Sayed, M. a. Why gold nanoparticles are more precious than pretty gold: noble metal surface plasmon resonance and its enhancement of the radiative and

- nonradiative properties of nanocrystals of different shapes. *Chem. Soc. Rev.* **35**, 209–217 (2006).
380. Linic, S., Christopher, P. & Ingram, D. B. Plasmonic-metal nanostructures for efficient conversion of solar to chemical energy. *Nat. Mater.* **10**, 911–921 (2011).
381. Collier, A. Blue Sky. 1–6 (2007).
382. Shaw, R. Dynamic Light Scattering Training Achieving reliable nano particle sizing. *Malvern -Zetasizer-LS* Available from: <http://149.171.168.221/partcat/wp-content/uploads/Malvern-Zetasizer-LS.pdf>. (2014).
383. Lucideon. Brunauer-Emmett-Teller (BET) Surface Area Analysis and Barrett-Joyner-Halenda (BJH) Pore Size and Volume Analysis. (2015). Available at: <http://www.ceram.com/testing-analysis/techniques/brunauer-emmett-teller-surface-area-analysis-barrett-joyner-halenda-pore-size-and-volume-analysis/>.
384. Micromeritics Instrument Corporation. Gas Adsorption Theory. http://www.micromeritics.com/Repository/Files/Gas_Adsorption_Theory_poster.pdf 1 (1AD).
385. Balbuenat, P. B. & Gubbins, K. E. Theoretical Interpretation of Adsorption Behavior of Simple Fluids in Slit Pores. *Langmuir* **9**, 1801–1814 (1993).
386. Mai, W. Fundamental Theory of Atomic Force Microscopy. *Nanoscience GATech* (2010). Available at: <http://www.nanoscience.gatech.edu/zlwang/research/afm.html>.

8 APPENDIX

8.1 HETEROGENEOUS CATALYST

The general classification of catalysts includes homogeneous catalyst and heterogeneous catalyst. Homogeneous catalysts are those which occupy the same phase as that of the reaction mixture which allows greater interaction with the reaction mixture. Acid catalysis, organometallic catalysis, and enzymatic catalysis are typical examples of homogeneous catalysis. Though the same phase facilitates greater interaction with the reaction mixture, homogeneous catalysts are irrecoverable from the reaction mixture.

The heterogeneous catalysts, in contrast to homogeneous catalysts, are in a different phase in the reaction mixture, for example, a solid catalyst and fluid or gaseous reaction mixture. It facilitates easy recovery of catalyst on completion of the reaction and can withstand high temperatures.³⁶⁶ A heterogeneous catalytic reaction involves adsorption of reactants from a fluid phase onto a solid surface, the surface reaction of adsorbed species and desorption of products into the fluid phase. Adsorption processes can be described by adsorption isotherms as Langmuir, Freundlich or BET isotherms.

8.1.1 Adsorption Isotherms

Adsorption Process: The first step in a heterogeneous catalytic reaction involves activation of a reactant molecule by adsorption onto a catalyst surface. The activation step includes the formation of a strong chemical bond (chemisorption) or a weak physical bond (physisorption) with the catalyst surface.³⁶⁷ The rate of adsorption r_{ad} is proportional to the collision frequency F of the adsorbate with the surface and the probability of the adsorption, s :³⁶⁸

$$r_{ad} \propto F \cdot s \quad (8.1)$$

The collision rate F is proportional to c , the concentration of the molecules and v , their velocity. The mean velocity of the molecule is $(8 \cdot k_B \cdot T / \pi \cdot m)^{1/2}$ where k_B is the Boltzmann's constant, T the absolute temperature, and m the mass of the molecule. From the ideal gas law, the collision rate can be written as:³⁶⁸

$$F = \frac{P}{(2\pi m k_B T)^{1/2}} \quad (8.2)$$

In case of activated adsorption, the sticking probability s is dependent on the probability that a collision occurs with a free adsorption site $f(\theta)$, with θ being the fractional surface coverage, σ represents the probability that the molecule with sufficient energy E_{ad} , and colliding with a vacant site will adsorb.³⁶⁸

$$s = \sigma \cdot f(\theta) \cdot e^{\frac{-E_{ad}}{RT}} \quad (8.3)$$

Therefore the adsorption rate can be rewritten as³⁶⁸

$$r_{ad} = \frac{\sigma \cdot f(\theta) \cdot P}{(2\pi mkBT)^{1/2}} e^{-\frac{E_{ad}}{RT}} \quad (8.4)$$

Desorption Process: On the contrary to adsorption process, desorption has always activated the process. The rate of desorption r_{des} can be expressed as³⁶⁸

$$r_{des} = k_{des} f'(\theta) e^{-\frac{E_{des}}{RT}} \quad (8.5)$$

where k_{des} is the rate constant, $f'(\theta)$ is the fraction of covered sites available for desorption and $E_{des} = Q_{ad} + E_{ad}$, which is equal to the sum of the heat of adsorption, Q_{ad} and the activation energy of adsorption E_{ad} . On a uniform surface the rate constant, k_{des} and energy of desorption, E_{des} can vary with the surface coverage and in this case, the desorption rate can be expressed as³⁶⁸

$$r_{des} = k_{des}(\theta) f'(\theta) e^{-\frac{E_{des}(\theta)}{RT}} \quad (8.6)$$

Langmuir Isotherm: The Langmuir isotherm, which is one of the fundamental adsorption isotherms and is assumed here that adsorption and desorption are in equilibrium. The Langmuir isotherm on an ideal uniform surface is obtained based on the following assumptions:

- all adsorption sites are equal
- adsorption occurs only on vacant sites
- only one adsorbed species can exist per site, that is, saturation coverage is achieved at one monolayer
- the heat of adsorption is constant and independent of coverage, which assumes that no interaction occurs between adsorbed species.

At equilibrium, the rates of adsorption and desorption must be equal and by rearranging the equations of r_{ad} and r_{des} the following equation can be derived:

$$P = \frac{k_{des} (2\pi mkBT)^{1/2}}{\sigma} \cdot \frac{f'(\theta)}{f(\theta)} \cdot e^{-Q_{ad}/RT} = \frac{1}{K} \cdot \frac{f'(\theta)}{f(\theta)} \quad (8.7)$$

By assigning appropriate functions for $f(\theta)$ and $f'(\theta)$, different types of adsorption process can be described. The equation implies that the adsorption equilibrium constant, K , depends only on the temperature.

Competitive Adsorption: Adding additional adsorbates to the reaction mixture creates a competitive environment which can be readily accommodated by using the site balance. Assumably, when two adsorbates, A and B, adsorb simultaneously and compete for the same site, S,





which leads to,

$$1 = \theta_A + \theta_B + \theta_f \quad (8.10)$$

where, θ_A is the concentration of the sites covered with A, θ_B is the concentration sites covered with B on the surface and θ_f is the concentration of the free adsorption sites. And the adsorption rate constants K_A and K_B are as follows:

$$K_A = \frac{\theta_A}{P_A \cdot \theta_f} = \frac{\theta_A}{P_A(1 - \theta_A - \theta_B)} \quad (8.11)$$

$$K_B = \frac{\theta_B}{P_B \theta_f} = \frac{\theta_B}{P_B(1 - \theta_A - \theta_B)} \quad (8.12)$$

Freundlich Isotherm: Freundlich isotherm is an empirical expression which implies that at the higher coverage the adsorption will decrease leading to a partially or moderately covered surface. It is mainly applied on non-ideal surfaces where the Langmuir isotherm (ideal surfaces) does not fit. Freundlich isotherm will be similar to Langmuir isotherm in regions of moderate coverage.³⁶⁸

$$\theta = K_i P_i^{\frac{1}{m}} \quad (8.13)$$

where m is the Freundlich exponent.

Langmuir-Freundlich Isotherm or Sips Isotherm: The Langmuir-Freundlich isotherm or Sips isotherm, developed by Sips in 1948, is a versatile isotherm expression that combines the behaviour of both Langmuir and Freundlich isotherm.^{369,370} It describes the monolayer single – solute adsorption from dilute solutions on heterogeneous solid surfaces showing a quasi-Gaussian distribution of adsorption energies. The Langmuir-Freundlich equation is as follows:³⁷¹

$$\theta_i^0(c_i) = \frac{(K_i c_i)^{m_i}}{1 + (K_i c_i)^{m_i}} \quad (8.14)$$

where, θ_i^0 and c_i are the relative single-solute adsorption and concentration of the i^{th} solute respectively. K_i is the Langmuir-type constant determining position of the energy distribution and m_i is the heterogeneity parameter connected with the adsorbent. The equation is similar to the Langmuir isotherm when the Freundlich exponent, $m = 1$. At low concentrations it reduces to Freundlich isotherm.³⁷¹

8.1.2 Eley-Rideal Mechanism

Eley-Rideal mechanism explains when only one reactant, A, adsorbs onto the surface after which the other reactant, B, interacts with the adsorbed species directly to form product, C, which is the rate determining step (Figure 8.1 a).³⁷²

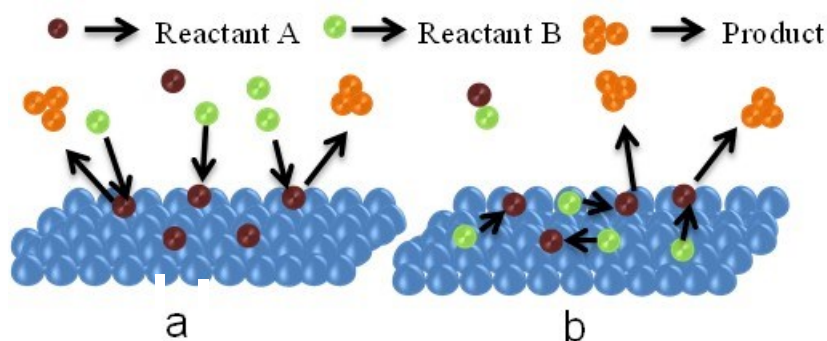
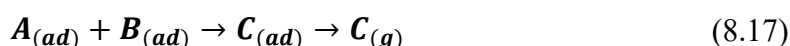


Figure 8.1 Schematic representation of (a) Eley-Rideal Mechanism; (b) Langmuir-Hinshelwood Mechanism. Adapted from Ref. 372.

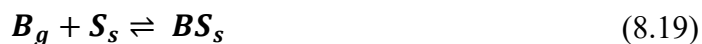
It is then followed by desorption of the reaction product, C, from the catalyst surface.³⁷² The reaction can be illustrated as:



The adsorption is modelled in terms of a Langmuir isotherm where the surface coverage of the components i is dependent on the adsorption constant and the concentration. The reaction rate is dependent on the surface coverage for molecule A, the partial pressure of gas-phase molecules B, is given by, $r = S \cdot k \cdot \theta_A \cdot P_B$, where S is the surface of nanoparticles and k is the adsorption constant.

8.1.3 Langmuir-Hinshelwood Mechanism (LH)

Similar to the Eley-Rideal mechanism, in Langmuir-Hinshelwood mechanism, both the reactants, A and B, pre-adsorb onto the catalyst surface, S, (Figure 8.1 b) and then the reaction takes place on the surface of the catalyst, which is facilitated by the surface diffusion. The reaction product formed, C then desorbs from the surface. The reaction mechanism is as follows:³²⁹



The surface supported reaction is the rate-determining step. Both reactants compete for the active site. Thus, the reactivity is highest when a stoichiometric amount of reactant is adsorbed on the surface and both reactants are fully dispersed over the surface and the reaction rate between reactants A and B is, $r = S \cdot k \cdot \theta_A \cdot \theta_B$. The rate is proportional to the intrinsic rate k , and the surface coverages of A and B. Considering the Langmuir isotherm; the rates can be rewritten as:

$$r = \frac{k \cdot S \cdot K_A \cdot [A] \cdot K_B \cdot [B]}{(1 + K_A \cdot [A] + K_B \cdot [B])^2} \quad (8.21)$$

If one reactant has more affinity towards the surface owing to its high concentration, leads to a decreased rate of reaction. On the other hand, a decrease in this concentration can lead to increased rates if the ratio of both reactants is not optimum (Figure 8.2).

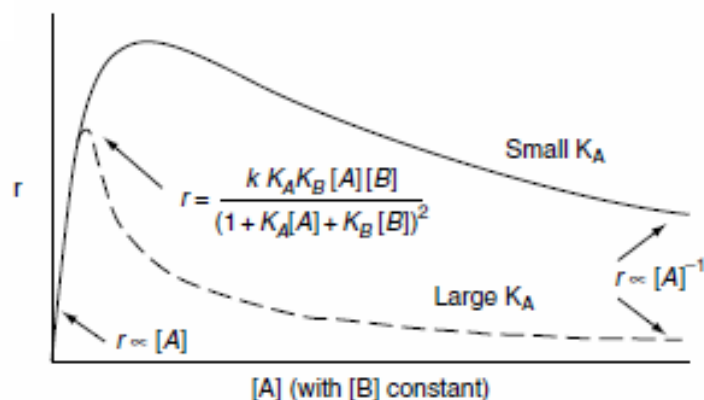


Figure 8.2 Variation of rate, r , with a concentration of $[A]$ for bimolecular process via LH mechanism. Reproduced from Ref. 368.

8.2 TECHNIQUES

8.2.1 Scanning Electron Microscopy (SEM)

The initial model of scanning electron microscope was first developed by Knoll in 1935 and was commercialised by Cambridge Instrument Company in 1965.²⁴⁵ It uses an electron beam in a raster scan pattern to image a sample. The electrons interact with the atoms that make up the sample, producing signals that contain information about the sample's surface topography, morphology and chemical composition. The possible magnification level in SEM is from less than 100X to 100KX. At the highest magnification, a resolution of 1 nm can be achieved for conducting surfaces.

A typical SEM consist of an electron source at the top (electron gun), electron beam manipulation system (condenser lenses and aperture), an area of beam-specimen interaction (specimen chamber), detection of scattered electrons and X-rays (scanning & detection system), signal processing and display and recording (Figure 8.3 a).³⁷³

The electron gun emits free electrons, generated by thermionic emission from a tungsten filament located inside a Wehnelt cylinder ($\sim 2700\text{K}$), which is directed towards the anode. The beam is then converged by the two condenser lenses. One of them eliminates high angle electrons, whereas the second one makes the electrons to a thin, tight, coherent beam, which is then directed towards the focal point. The condenser lenses are primarily responsible for determining the intensity of the electron beam when it strikes the specimen. The apertures reduce and exclude extraneous electrons in the lenses. The final lens aperture located below the scanning coils determines the diameter or spot size of the beam at the specimen. The spot size of the specimen will in part determine the resolution and depth of field electron stream. The scanning system scans the sample in a raster fashion using the deflection coils located inside the objective to obtain images. The specimen chamber is located at the lower portion of the column which comprises of the specimen stage and detectors. The electrons from the specimen are attracted to the detectors by a positive charge.

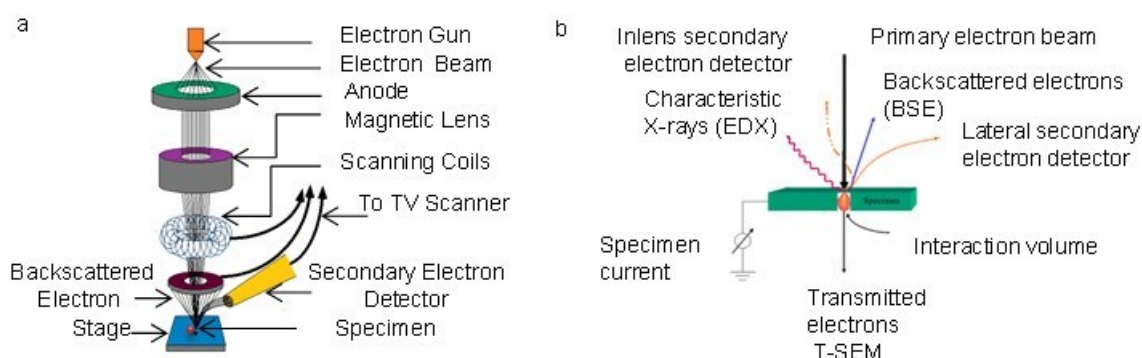


Figure 8.3 (a) Schematic diagram and working principle of SEM; (b) Types of electron-specimen interactions. Reproduced from Ref. 373, 375.

A vacuum system is necessary for the controlled electron beam generation of a normal SEM. The presence of air and dust particles inside the column can interfere and block the electrons before they reach the specimen in the sample chamber. Vacuum provides a clean and dust free environment which is essential for the performance of the column optics chamber. Moreover, a vacuum is necessary to prevent the oxidation and burning of the tungsten filament. A typical SEM operates generally at a vacuum pressure between 10^{-2} – 10^{-7} Torr.

When the primary electrons interact with the atoms of the specimen, a series of scattering events take place.³⁷⁴ While travelling through the tear-shaped interaction volume, the electrons lose the energy and change the direction with each atomic interaction. Scattering events can be divided into two general classes: (1) elastic scattering, in which the electron exchanges little or no energy, but changes direction; (2) inelastic scattering, in which the electron exchanges significant and definite amounts energy, but has its direction virtually unchanged. Both types of events determine the size and shape of the interaction volume. Inelastic scattering events are responsible for the wide variety of characteristics (i.e., element-specific) and non-specific information of the specimen. These include secondary electrons, Augér electrons, characteristic and continuum X-rays, long-wavelength radiation in the visible, IR and UV spectral range (cathodoluminescence), lattice vibrations or phonons, and electron oscillations or plasmons (Figure 8.3 b).³⁷⁵

In order to investigate the specimen surface, secondary and backscattered electrons are utilised, which is produced as a result of scattering of the primary electrons from the specimen. Secondary electrons are a result of the inelastic collisions and produced when the beam interacts with specimen electrons. They are characterised by energies < 50 eV and are used to reveal the surface structure of a material with a resolution of ~ 10 nm or better. Backscattered electrons are a result of elastic collisions and scattering of the beam with the nucleus of the specimen, which possess an energy that is > 50 eV. The X-rays are another signal that is commonly used to determine the elemental composition of the specimen.³⁷⁶ They are produced by recombination interactions between electrons and holes generated within the specimen. The size of the interaction volume depends on the atomic density, the topography of the specimen and acceleration potential of the primary electrons. The volume and depth of penetration increase with an increase of the beam energy and fall with the increasing specimen atomic number because specimens with higher atomic number have more particles to stop electron penetration.³⁷⁴ The signals produced as a result of such scattering events are then enhanced with the use of electronic amplifiers and sent to a TV scanner. The image is finally captured and displayed on a computer monitor.³⁷⁶

8.2.2 Transmission Electron Microscopy (TEM)

A transmission electron microscope has three basic components.³⁷⁷ On top, it has an electron gun which produces the electron beam, followed by a condenser lens which focuses the electron beam to an object. The objective lens, movable specimen stage, intermediate and projector lenses are collectively called as an image-producing system, which focuses the electrons passing through the specimen to form a real highly magnified image. The image-recording system converts the electron image into a virtual image that can be perceptible to the human eye. The image recording system consists of a fluorescent screen for viewing and focusing the image, and a digital camera for permanent records. Also, there is a vacuum system which maintains the necessary vacuum within the microscope.

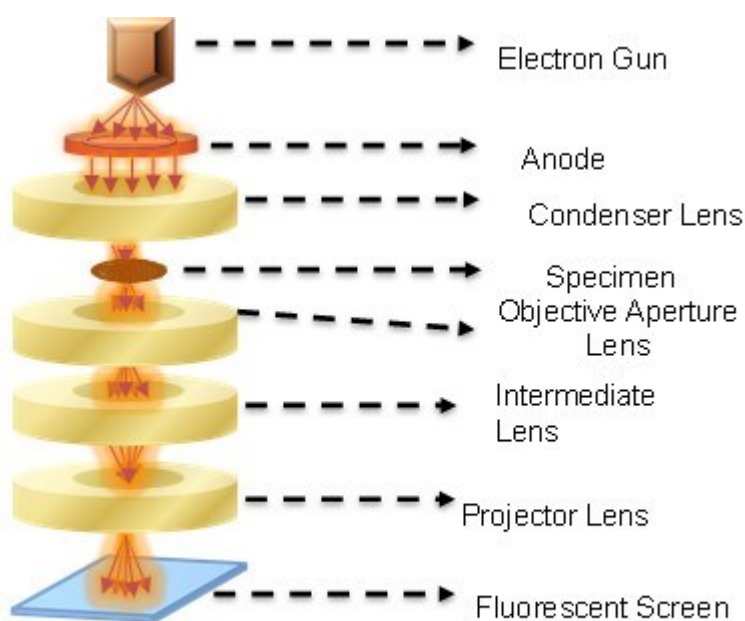


Figure 8.1 Schematic showing the working principle of TEM.

The electron gun consists of a cathode, which is the source of electrons, is a heated V-shaped tungsten filament or a sharply pointed rod of lanthanum hexaboride. Electrons which leave the cathode are accelerated towards the anode and then directed to the condenser lens. The condensed electron beam is then passed through the specimen grid which is carried in a small holder on a movable specimen stage. Depending on the density of the sample material, some of the electrons are scattered away from the beam. The unscattered electrons collected by an objective lens produce a real intermediate image which is further magnified by the projector lenses. By the use of interchangeable pole pieces in the projector a wide range of magnification can be obtained. The thus obtained electron image is made visible to the eye either by allowing the electrons to fall on a fluorescent screen fitted at the base of the microscope column or by capturing the image digitally for display on a computer monitor. The image obtained in a TEM can have a final magnification of 1,000-250,000X on the screen.²⁴⁶

8.2.3 UV-VIS Absorbance Spectroscopy

The absorbance of light is a phenomenon which involved the energy transfer from light to matter most in the form of thermal energy. Electromagnetic waves in the ultraviolet (200 -

400 nm) and visible range (400 - 800 nm) are able to induce electronic transitions in molecules.²⁴⁷ This is associated with excitation of electrons from their respective ground state to its higher energy levels.³⁷⁸ Among possible types of electronic transitions (π , σ , η) UV-vis spectroscopy measures mainly the $n \rightarrow \pi^*$ and $\pi \rightarrow \pi^*$ transitions. Most absorption spectroscopy of organic compounds is based on transitions of n or π electrons to the π^* excited state. This is because the absorption peaks for these transitions fall in an experimentally convenient region of the spectrum (200 – 700 nm).²⁴⁸

UV spectroscopy obeys the Beer-Lambert law which relates the absorbance of a solution to the concentration of the absorbing species by the following equation,

$$A = -\log \left(\frac{I_0}{I} \right) = \epsilon cl \quad (8.22)$$

where A is the absorbance, I_0 is the intensity of light incident upon sample cell, I is the intensity of the transmitted light after passing through the sample, ϵ is extinction coefficient, c is the concentration of the absorbing species in the solution, l is the path length of the light through the sample.²⁴⁹

Due to surface plasmon resonance, the noble metal nanoparticles show strong absorption bands in the UV-Vis region. Surface plasmon resonance (SPR) is the resonant, collective oscillation of valence electrons in a metal stimulated by incident light. The resonance condition is established when the frequency of light photons matches the natural frequency of surface electrons oscillating against the restoring force of positive nuclei.²¹⁰ The unique optical properties of noble metal nanoparticles are associated with their surface plasmon resonance. When confined to sub-wavelength dimensions, plasmons can be excited by visible light and their frequency effectively tuned by varying the size and the dielectric environment of the particles. In the presence of the oscillating electromagnetic field of the light, the free electrons of the metal nanoparticles undergo an oscillation with respect to the metal lattice. This process is resonant at a particular frequency of the light and is termed as the localised surface plasmon resonance (LSPR).²⁰⁹ After absorption, the surface plasmon decays radiatively resulting in light scattering or non-radiatively by converting the absorbed light into heat.

Gold and silver nanoparticles have size-shape-dependent optical properties due to their interaction with light.^{379,380} For AuNPs with particle size around 10 nm have a strong absorption maximum around 520 nm in aqueous solution due to their LSPR. Increasing particle size red shifts the SPR wavelength and also the intensity (Figure 8.4).^{379,380}

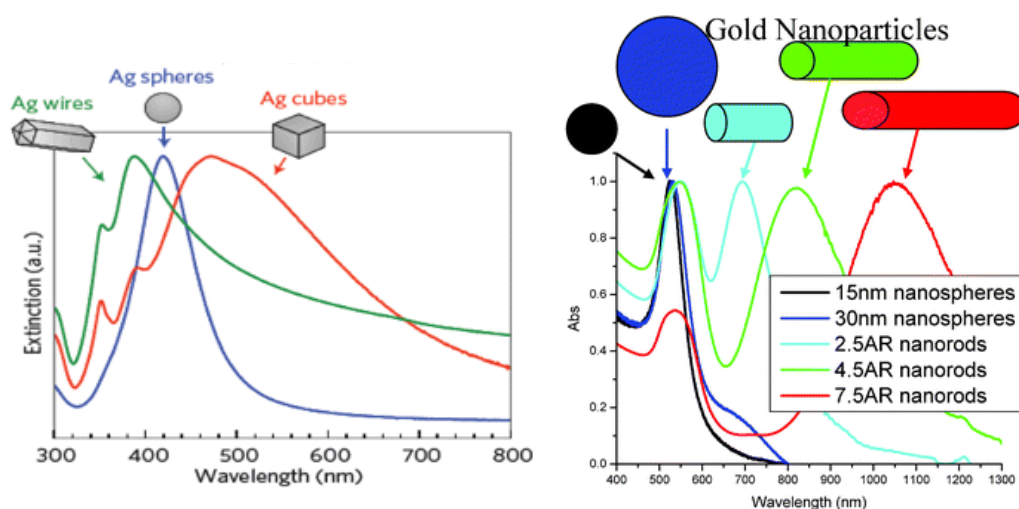


Figure 8.4 Absorption spectra of gold and silver nanoparticles of various shapes. Reproduced from Ref. 379, 380.

By interpreting the position, width, and symmetry of these absorption bands, information regarding the size distribution and interparticle distance of nanoparticles can be generated. This can be done by means of UV-Vis spectroscopy. It utilises light in the visible and near-UV and near-infrared ranges.

A typical UV-Vis spectrometer consists of a light source, excitation monochromator, sample and reference cells, a detector, an amplifier and recording devices. The light source consists of a tungsten filament and hydrogen-deuterium lamps which cover the whole UV-Vis region. Monochromators are composed of prisms and slits. A UV-Vis spectrophotometer can either be a double beam or single beam spectrophotometer. In double beam spectrophotometer, the radiation emitted from the primary source is dispersed with the help of rotating prisms and the various wavelengths of the light are then selected by the slits that are monochromatic. They are further divided into two beams with the help of another prism. One of the two divided beams is passed through the sample solution and the second beam is passed through the reference solution. On the other hand in a single beam spectrophotometer, a single beam of light passes through the sample cell. In a single beam UV-vis spectrophotometer, the instrument is standardised by placing a reference in a sample holder and the resulting value is subtracted from subsequent sample measurements to remove effects from the solvent and the cell. The light is modulated rapidly by means of a rotating chopper located between the light source and the sample cell. The signals from the sample are passed through a monochromator which is then led to the detector. Thus, single beam spectrophotometers have a high energy throughput due to non-splitting of source beam and hence possess a high sensitivity of detection. UV-visible spectroscopy is suitable for measurements in the wavelength range from 190 to 1100nm.

8.2.4 Dynamic Light Scattering (DLS)

Dynamic Light Scattering (DLS) or Photon Correlation Spectroscopy (PCS) is one of the most widely used techniques to study the properties of suspensions and solutions of colloids.^{250,251} Shining a monochromatic light beam on particles in Brownian motion results in Doppler shift as the light hit the moving particle. This, in turn, results in changing the wavelength of the incoming light. This change can be related to the size of the particle. The process is quasi-elastic as the photons are scattered by mobile particles, and the technique was initially named as quasi-elastic light scattering (QELS). QELS measurements yield information on the dynamics of the scatterer, which gives rise to the term dynamic light scattering, DLS.²⁵⁰

The light scattering can be explained on the basis of two light scattering theories: (1) Rayleigh Scattering Theory and (2) Mie Theory, and Brownian motion of colloidal particles.³⁸¹

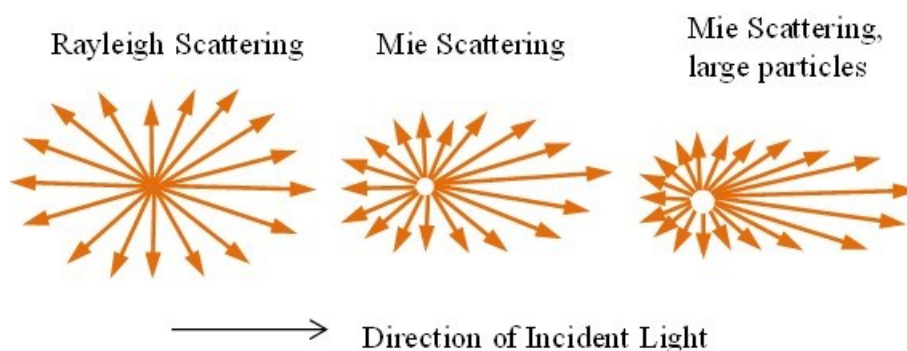


Figure 8.5 Schematics showing different scattering theories for spherical particles Reproduced from Ref. 381.

Rayleigh's scattering law (for smaller particles with diameter less than one-tenth of the wavelength of light) states that if the particles are small compared to the wavelength of the laser used, then the scattering from a particle illuminated by a vertically polarized laser will be essentially isotropic, i.e., the light will be scattered equally in all directions. Whereas Mie theory gives an exact description of how spherical particles of different sizes scatter the light. It states that when particles become larger than $\lambda/10$, the scattering changes from being isotropic to a distortion in the forward scattering direction, whereas when the size of the particles become equivalent to or greater than the wavelength of incident light, the scattering becomes a complex function with maxima and minima with respect to the angle of the incidence.³⁸²

DLS measures the speed at which particles are diffusing due to the Brownian motion: the larger the particle, the lesser the Brownian motion. The temperature needs to be stable, as the convection currents in the sample will cause non-random movements which can result in the wrong interpretation of size under varying temperatures. For a system under Brownian motion which scatters light, the intensity fluctuations are observed depending on the size of the

particles. The small particles cause more rapid intensity fluctuations than the large ones. These fluctuations can be effectively measured by a digital autocorrelator.

A correlator acts as a signal comparator which measures the degree of similarity between two signals or one signal with itself at varying time intervals. If the intensity of a signal is compared with itself at a particular point in time and a time much later, then for a randomly fluctuating signal, there will be no correlation between the two signals. On the other hand, if the intensity of the signal at time τ is compared to the intensity at a very small time later (i.e. $\tau+\Delta\tau$), there will be a strong correlation between the two signals. When the signal at τ is compared to a signal at $\tau+2\Delta\tau$, there will still be a correlation but not as good as that for τ and $\tau+\Delta\tau$ pair. Thus, the correlation will reduce with time. If the particles are large the signal will be changing slowly and the correlation will persist for a long time. If the particles are small and moving rapidly then the correlation will reduce more quickly (Figure 8.6).²⁵²

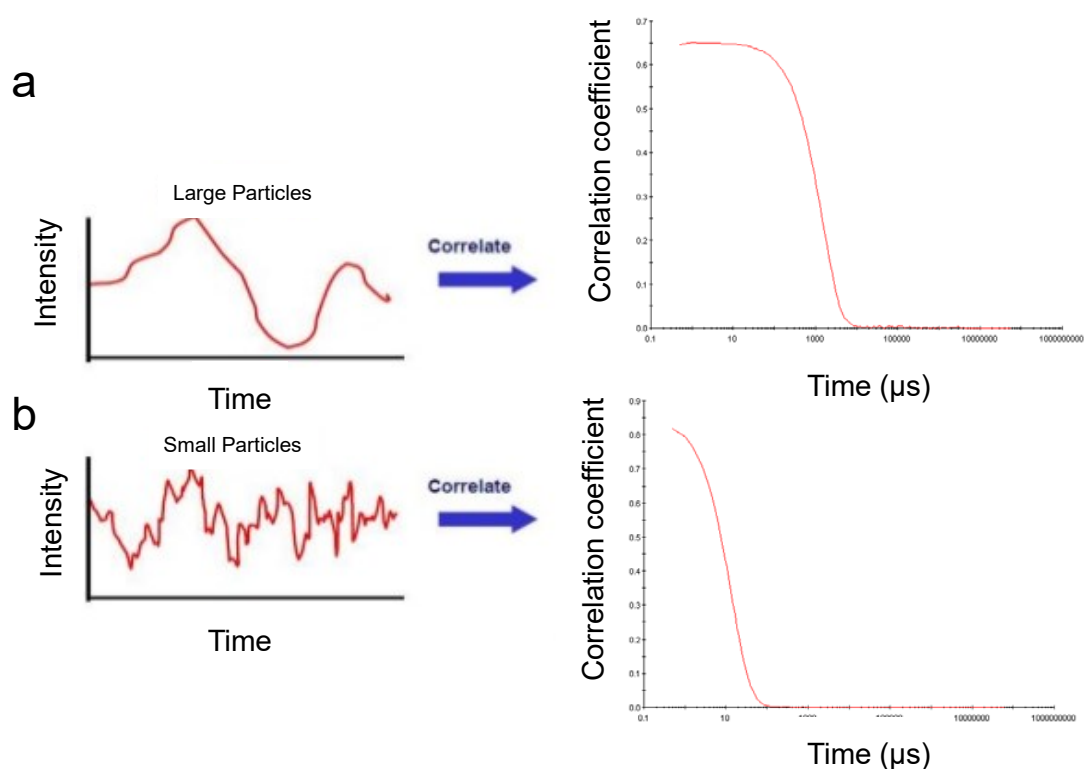


Figure 8.6 Typical correlograms from samples containing (a) Large particles in which the correlation of the signal takes a long time to decay; (b) Small particles in which the correlation of the signal decays more rapidly. Reproduced from Ref. 252.

The particle size is obtained from the correlation function (G) by using various algorithms. The average hydrodynamic radius, R_h , can be estimated by fitting a single exponential to the correlation function (cumulant fit) and the particle size distribution can be obtained by estimating the width of the distribution (Polydispersity index) or fit of a multiple exponential

to the correlation function.²⁵⁰ The size distribution obtained is a plot of the relative light intensities scattered by particles in various size regimes and, hence, called as intensity size distribution. If the distribution of intensity is a single fairly smooth peak, then there is little point in doing the conversion to a volume distribution using the Mie theory. If the optical parameters are correct, this will just provide a slightly different shaped peak. However, if the plot shows a substantial tail or more than one peak, then Mie theory can make use of the input parameter of sample refractive index to convert the intensity distribution to a volume distribution.

The analysis of the time-dependent intensity fluctuation yields the diffusion coefficient of the particles. Further using the Stokes-Einstein equation the size of the particles can be determined:

$$d(H) = \frac{kT}{3\pi\eta D} \quad (8.23)$$

where $d(H)$ is the hydrodynamic particle diameter, D – translational diffusion coefficient, k – Boltzmann constant, T – absolute temperature, and η – viscosity.²⁵²

Typical dynamic light scattering instruments comprises of several main components: a laser as a monochromatic light source, a detector to measure the intensity of scattered light, an attenuator to regulate the intensity of the laser source and amount of scattered light reaching the detector, and a correlator, a digital processing board, which compares the scattering intensity at successive time intervals to derive the rate at which the intensity is varying. The information obtained from a correlator is then passed to a computer where the software will analyse the data and derives the size information.

8.2.5 Gas Adsorption measurements

As a result of more reactive surface atoms, the solid surfaces attract gases, vapours and liquids to balance atomic forces. As a consequence of imbalanced surface energy, gas adsorption takes place where molecules from a gas phase (adsorbate) are taken up by a solid surface (adsorbent).^{253,254} The adsorbed gas molecules temporarily depart from the gas phase and form a film at the surface for a certain period of time and then return to the gas phase. The duration depends on the nature of both adsorbent and the adsorbate.

Adsorption is described through the functions connecting the amount of adsorbate taken up by the adsorbent with the adsorptive equilibrium pressure p , the temperature T , and all other parameters being constant, known as adsorption isotherm. Brunner, Emmet and Teller (BET) analysis provide precise surface area by gas multilayer adsorption measured as a function of relative pressure. An extension of this process results in the condensation of gas in the pores from which the pore structure can be evaluated. As pressure increases, the gas condenses first within the smallest pores followed by the remaining ones. The gas pressure is then incrementally reduced by evaporating the condensed gas from the system. The adsorption and desorption

hysteresis curves reveal the information about the size, volume and area. The pore size distributions are determined according to the Barrett-Joyner-Halenda method (BJH) for mesopores (2-50 nm) and small macropores (>50 nm) from experimental isotherms using the Kelvin model of pore filling. Horvath-Kawazoe technique extracts the micropore (< 2 nm) volume distribution by size from the experimental isotherm. The original H-K method is based on slit-shaped pores. Cylindrical and spherical pores were measured using Saito-Foley and Cheng-Yang methods.^{383,384}

Depending on the structure of solids, adsorption isotherms are classified mainly into six types (Figure 8. 7).³⁸⁵ Type I

isotherms arise due to the monolayer adsorption of adsorbate onto the adsorbent surface and are typical for the microporous solids. This type of behaviour implies to be typical of chemisorption. The strong interaction between the gas molecules and solid layer results in the complete filling of the pores at a relatively low pressure and the plateau indicates the monolayer coverage. Type II or sigmoid isotherms are obtained when the multilayered adsorption of

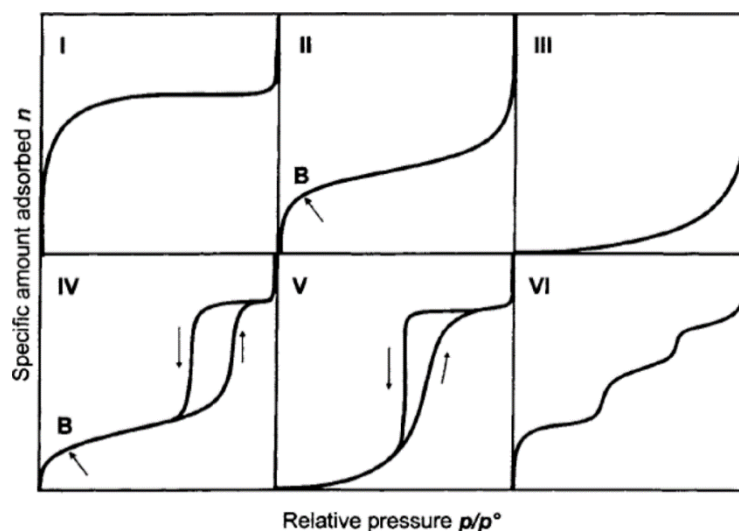


Figure 8. 7 Different types of gas adsorption isotherms. Reproduced from Ref. 385.

gases by nonporous or microporous solids takes place. On the other hand, Type III isotherms given by non-porous or macroporous solids are the result of weak gas-solid interactions. Due to the weak interaction, the gas uptake at low relative pressure is small. But once the molecules become adsorbed, the adsorbate-adsorbate forces will promote further adsorption of molecules resulting in an isotherm which is convex to the pressure axis. Type IV isotherms describe mono and multilayer adsorption plus capillary condensation which are mainly due to the condensation of adsorbates in the small pores of a porous solid at $P < P_0$. A hysteresis loop, which is the main feature of Type IV isotherms, is associated with secondary pore filling process of capillary condensation. Type V isotherms are given by microporous or mesoporous solids and combine features of Type III and Type IV isotherms. Type IV and V isotherms exhibit a hysteresis loop which is a characteristic of highly porous systems.²⁵⁴ Finally, Type VI isotherms are borderline cases between two or more of the ascribed types.

8.2.6 Atomic Force Microscopy (AFM)

In 1986 Gerd Binnig, Calvin Quate and Christoph Gerber invented AFM which uses mechanical springs to sense forces and piezoelectric transducers for scanning.^{256,257} The AFM measures the forces acting on the tip and sample.³⁸⁶

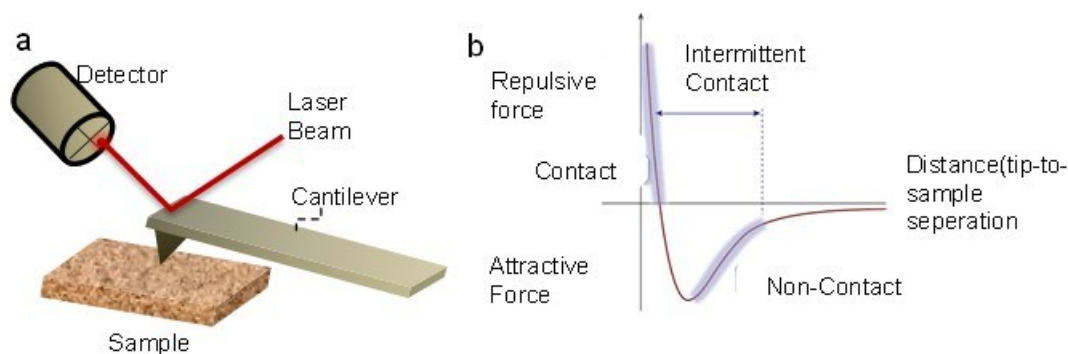


Figure 8.8 (a) Schematic illustration of working principle of an AFM; (b) Typical force-distance curve with corresponding regions of operating AFM modes. Image b reproduced from Ref. 386.

The surface scanning is done with a sharp cantilever tip, which is attached to a spring that deflects in response to the force between tip and sample according to Hooke's law. Due to the attractive or repulsive interatomic interactions between the cantilever tip and the sample surface, the deflection of the cantilever will cause a positive or negative bending of the cantilever. The bending is detected with the help of a laser beam and a photodiode. A constant deflection and a stable contact between the tip and the sample are maintained by a feedback loop that controls the z-position of the tip by a piezo element. The cantilever is made typically from silicon or silicon nitride with spring constants 0.001 N/m to 100 N/m. Its motion from microns to $\approx 0.1 \text{ \AA}$ is measured by the deflection sensor. Depending on the type of interaction and application, the general operation modes of AFM are *contact*, *non-contact* and *tapping modes*.

Contact mode uses the direct interaction of tip with the surface, where the tip scans the surface in raster manner, and the tip deflection at each point is measured by the piezoelectric detector. The tip scans the surface either at a small constant height or under a constant force. In the constant height mode, the height of the tip is fixed whereas in constant force mode the deflection of the cantilever is fixed and the motion of the scanner in the z-direction is recorded.

In non-contact mode, the cantilever is hovered above the sample surface (50 - 150 \AA) and oscillates at a frequency slightly above its resonant frequency with an amplitude of oscillation $< 10 \text{ nm}$. Due to the attractive van der Waals forces between the tip and the sample, the resonant frequency of the cantilever slightly decreases. The feedback loop maintains a constant oscillation frequency by measuring the fluctuations in the sample to tip distance and by adjusting the tip to sample distance.

In *tapping mode*, the cantilever is oscillated at or close to its resonant frequency driven by a piezo-electric crystal. The oscillating tip is brought near the sample until it lightly touches or taps the sample surface. The cantilever oscillation decreases as a result of energy loss which arises due to the contact between the tip and the surface. This reduction in oscillation is sent to the detector and used to identify and measure the sample surface features. Using tapping mode soft and sensitive samples can be measured to produce images with a high resolution.

Phase imaging, an extension of tapping mode, measures the phase lag of cantilever oscillation with the piezo driver instead of resonant oscillation. This mode provides nanometer-scale information about the surface structure and can be used to identify different components in composite materials, the roughness of a surface and distribution and morphology of nanoparticle and polymer on a surface respectively.

8.3 DETERMINATION OF THE CONTENT AND SPECIFIC SURFACE AREA OF GOLD IN Au@SiO₂@PSS CATALYST

In order to normalize the apparent rate constant in terms of surface area or the mass of catalyst, the authors first calculated the weight fraction of gold nanoparticle present in Au@SiO₂@PSS catalyst using ICP-OES. From the technique, the weight fraction of gold was obtained as:

$$\omega_{Au^0/cat} = 0.060 \pm 0.002 \text{ wt. \%} \quad (8.24)$$

As a next step, the content of gold (Au⁰) in moles per unit mass of Au@SiO₂@PSS catalyst was calculated as per the equation given below:

$$m_{Au^0/cat} = \frac{\omega_{Au^0}}{M_{Au^0} \times 100} = \frac{0.060}{197 \times 100} = 3.0 \times 10^{-6} \text{ mmol mg}^{-1} \quad (8.25)$$

Then, the specific surface area of AuNP was calculated based on analysis of TEM images by measuring the size of 400 individual particles (Au@SiO₂ sample):

$$\begin{aligned} S_{AuNP}^* &= \frac{\sum S_{AuNP}}{\sum m_{AuNP}} = \frac{\sum S_{AuNP}}{\rho_{Au} \times \sum V_{AuNP}} = \frac{\sum 4\pi r_{AuNP}^2}{\rho_{Au} \times \sum \frac{4}{3}\pi r_{AuNP}^3} \\ &= \frac{7.9736 \times 10^{-14}}{2.4944 \times 10^{-15}} \end{aligned} \quad (8.26)$$

Specific surface area of gold (Au⁰) per unit mass of Au@SiO₂@PSS catalyst was determined as follows:

$$S^*_{Au^0_{cat}} = \frac{\omega_{Au^0}}{100\%} \times \frac{S^*_{AuNP}}{1000} = \frac{0.060}{100} \times \frac{32.0}{1000} = 1.92 \times 10^{-5} m^2 mg^{-1} \quad (8.27)$$

Finally, the rate constants normalized to the no. of moles and to the surface area of gold nanoparticles can be calculated using eq. 8.25 and eq.8.27 respectively.

$$K_m = \frac{K_{app}}{m_{Au^0}/cat.} \quad (8.28)$$

$$K_s = \frac{K_{app}}{S^*_{Au^0_{cat}}} \quad (8.29)$$

8.4 BLANK EXPERIMENT TO STUDY THE REACTION OF CR + NaBH₄ IN THE ABSENCE OF CATALYST

Figure 8.9 shows the successive spectra of CR+NaBH₄ reaction mixture measured in the absence of Au@SiO₂@PSS catalyst. The spectra were recorded continuously for 60 minutes. The reaction proceeded at a very slow rate in the absence of catalyst when compared to the rate of reaction in presence of the catalyst. The experimental conditions were maintained similar to as described in the case of degradation of Congo Red and NaBH₄ in the presence of the catalyst.

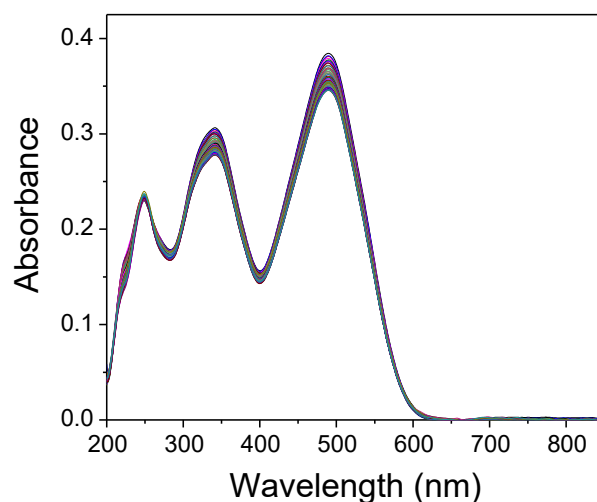


Figure 8.9 Successive UV-Vis spectra of Congo Red and Sodium Borohydride in the absence of catalyst measured for 60 minutes.

8.5 LIST OF ABBREVIATIONS AND SYMBOLS

AFM	Atomic Force Microscope
AgAc	Silver Acetate
AgNP	Silver Nanoparticle/s
Ag@PS- <i>b</i> -P4VP@SiO ₂	Silica deposited block copolymer encapsulated silver nanoparticle
Ag@SiO ₂	Silica shell enclosed silver nanoparticle yolk-shell nanoparticles (nanostructures)
AuNP	Gold Nanoparticle/s
Au@PS- <i>b</i> -P4VP@SiO ₂	Silica deposited block copolymer encapsulated gold nanoparticle
Au@SiO ₂	Silica shell enclosed gold nanoparticle yolk-shell nanoparticles (nanostructures)
BCP	Block Copolymer
CdS	Cadmium Sulfide
CHCl ₃	Chloroform
CR	Congo Red
DLS	Dynamic Light Scattering
d_{app}	Apparent Hydrodynamic Diameter
d_{AuNP}	Diameter of the Gold Nanoparticle
d_{av}	Average Diameter
EtOH	Ethanol
HCl	Hydrochloric acid
H ₂ O	Water (Millipore)
k_{app}	Apparent Rate Constant
K_m	Rate constant normalized to the no. of moles of gold nanoparticles
K_s	Rate constant normalized to the surface area of gold nanoparticles
LCST	Lower Critical Solution Temperature
MB	Methylene Blue
MeOH	Methanol
M_{NP}	Metal Nanoparticle/s
MO	Methyl Orange

mr	Molar Ratio
NaBH ₄ /BH ₄	Sodium Borohydride
NaAuCl ₄ .2H ₂ O	Sodium Tetrachloroaurate (III) Dihydrate
NH ₄ OH	Ammonium Hydroxide
NP	Nanoparticle/s
OlAm	Oleyl Amine
PDI	Poly Dispersity Index
PEO- <i>b</i> -HPP- <i>b</i> -PEO	Poly(ethylene oxide)- <i>block</i> -hexa- <i>p</i> -phenylene- <i>block</i> -poly(ethylene oxide)
PNIPAM- <i>b</i> -P4VP	Poly(N-isopropylacrylamide)- <i>block</i> -poly(4-vinylpyridine)
PS- <i>b</i> -PAA	Poly(styrene)- <i>block</i> -poly(acrylic acid)
PS- <i>b</i> -PEO	Poly(styrene)- <i>block</i> -poly(ethylene oxide)
PS- <i>b</i> -PGA	Poly(styrene)- <i>block</i> -poly(glycolic acid)
PS- <i>b</i> -PI	Poly(styrene)- <i>block</i> -poly(isoprene)
PS- <i>b</i> -PMAA	Poly(styrene)- <i>block</i> -poly(methacrylic acid)
PS- <i>b</i> -PPO- <i>b</i> -PEO	Poly(ethylene oxide)- <i>block</i> -poly(propylene oxide)- <i>block</i> -poly(ethylene oxide)
PS- <i>b</i> -P2VP	Poly(styrene)- <i>block</i> -poly(2-vinylpyridine)
PS- <i>b</i> -P2VP- <i>b</i> -PEO	Poly(styrene)- <i>block</i> -poly(2-vinylpyridine)- <i>block</i> -poly(ethylene oxide)
PS- <i>b</i> -P4VP	Poly(styrene)- <i>block</i> -poly(4-vinylpyridine)
PS- <i>b</i> -P4VP@SiO ₂	Silica shell deposited poly(styrene)- <i>block</i> -poly(4-vinylpyridine) micelle
PSS	Porous Silica Structure
PSSH	Thiol-terminated Polystyrene
QD	Quantum Dots
RPM	Rotations Per Minute
RT	Room Temperature
SEM	Scanning Electron Microscope
SiO ₂	Silica (Silicon dioxide)
TEM	Transmission Electron Microscope
TEOS	Tetra Ethyl Ortho Silicate
TOAB	Tetra Octyl Ammonium Bromide

YS NS	Yolk-Shell Nanostructures
YS NPs	Yolk-Shell Nanoparticles
mM	Millimolar
M	Molar
mL min ⁻¹	Milliliter per minute
L h ⁻¹	Liter per hour
L m ⁻² h ⁻¹	Liter per meter square per hour
mg	Milligrams
nm	Nanometer
4-AP	4-Aminophenol
4-NP	4-Nitrophenol
$m_{\text{Au}}^0/\text{cat}$	Content of gold in moles per unit mass of catalyst
S^*_{AuNP}	Specific surface area of gold nanoparticle
$S^*_{\text{Au}}/\text{cat}$	Specific surface area of gold nanoparticle per unit mass of catalyst
Å	Angstrom
λ	Wavelength
μm	Micrometer
μg	Microgram
χ	Flory Huggins Parameter
φ	Volume fraction
wt. %	Weight percentage
$\omega_{\text{Au0}/\text{cat}}$	Weight fraction of gold nanoparticle per unit mass of catalyst
φ	Volume Fraction

8.6 LIST OF FIGURES

Figure 1.1 TEM images and schematic representation of the common types of nanoparticles: (a) Solid; (b) Hollow; (c) Janus; (d) Core-Shell; (e) Reverse Bumpy Ball; and (f) Yolk-Shells or Nanorattle. Reproduced from Ref. 13.....	3
Figure 1.2 Publications per year for yolk-shell nanoparticles during the period of 2002 to 2015 and list of published documents in journals. Reproduced from Ref. 43.	3
Figure 1.3 Schematic showing the yolk-shell nanoparticle as a nanocatalyst.	5
Figure 2.1 Schematic showing the different types of block copolymers.	8
Figure 2.2 (a) Equilibrium microdomain structures of AB diblock copolymers in bulk: S and S' = body centered cubic spheres, C and C' = hexagonally packed cylinders, G and G' = bicontinuous gyroids, and L = lamellae; (b) Theoretical phase diagram of AB diblock copolymers predicted by the SCMF theory, depending on volume fraction (f) of the blocks and the segregation parameter, χN , where χ is the Flory-Huggins segment-segment interaction energy and N is the degree of polymerization. CPS and CPS' = closely packed spheres; (c) Experimental phase portrait of PI- <i>b</i> -PS copolymers, in which f_A represents the volume fraction of polyisoprene. PL = perforated lamellae. Reproduced from Ref. 50 and 51.....	10
Figure 2.3 Schematic diagram showing various morphologies formed by amphiphilic block copolymers in solution. Reproduced from Ref. 51.	11
Figure 2.4 Schematic representation of A-B diblock copolymer micelle in a solvent selective for one of the blocks and the important characteristics of BCP micelles. Reproduced from Ref. 61.....	12
Figure 2.5 Schematic representation of chain conformations of (a) Linear diblock; (b) Cyclic diblock copolymers; (c, d, e) Linear triblock copolymers in a micellar state. Adapted from Ref. 60 and 70.	14
Figure 2.6 Schematic showing the controlled orientation of block copolymer thin films by introducing selective and neutral nanoparticles. Reproduced from Ref. 106.	19
Figure 2.7 TEM image of (a) PS-coated particles segregated to the centre of the PS domains (light region) in a PS- <i>b</i> -PVP lamellar diblock copolymer phase; (b) PS/PVP coated particles segregated at the interface between PS/PVP blocks. Reproduced from Ref. 100.	20
Figure 2.8 Schematic representation of selective localisation of gold nanoparticle in the core of the micelles (a) As free-standing; (b) Attached to the inner walls of the core; (c) At the interface between PS- <i>b</i> -PAA diblock copolymer and the corresponding TEM images. Reproduced from Ref. 97.....	23

Figure 2.9 Schematic illustrations of the selective incorporation of PS- <i>b</i> -PAA (PS-red and PAA-blue) coated AuNPs into the central portion of the BCP micelles or rods. Reproduced from Ref. 118.....	25
Figure 2.10 Different yolk-shell structures: (a) YS NPs with a single core; (b) YS NPs with multiple cores; (c) YS NPs with multiple shells; (d) YS NPs with a raspberry-like core. Reproduced from Ref. 151.	28
Figure 2.11 Schematic illustration of a localised surface plasmon of a metal sphere. Reproduced from Ref. 209.	30
Figure 2.12 Selective etching strategies for the preparation of yolk-shell nanoparticles. Reproduced from Ref. 151.	32
Figure 2.13 Synthetic procedure and corresponding TEM micrographs (scale bar 100nm) of Au@SiO ₂ yolk-shell nanoparticle. Reproduced from Ref. 184.	33
Figure 2.14 Stepwise synthesis of Au@HMSM yolk-shell nanostructures via a soft-template method. Reproduced from Ref. 215.	34
Figure 4.1 Fabrication of hollow silica nanosphere from PS- <i>b</i> -P2VP- <i>b</i> -PEO micelle template. Reproduced from Ref. 83.	53
Figure 4.2 Schematic showing the synthesis of PS- <i>b</i> -P4VP@SiO ₂ particles.	55
Figure 4.3 SEM micrographs showing the morphologies of PS- <i>b</i> -P4VP@SiO ₂ particles obtained by sol-gel process in methanol at different TEOS: 4VP molar ratios: (a, e) 100mr; (b, f) 400mr; (c, g) 1000mr; (d, h) 4000mr. Scale bars are 1 μm (top) and 100 nm (bottom).	56
Figure 4.4 SEM micrographs showing the silica deposited PS- <i>b</i> -P4VP particle morphology in methanol at different block copolymer concentration: (a, d) 0.1 mg g ⁻¹ ; (b, e) 0.5 mg g ⁻¹ ; (c, f) 2 mg g ⁻¹ . Scale bars 1 μm (top) and 100 nm (bottom).....	57
Figure 4.5 SEM micrographs showing the silica deposited PS- <i>b</i> -P4VP particle morphology in methanol at different reaction time: (a, b) 6 hours; (c, d) 24 hours; (e, f) 48 hours; (g, h) 72 hours; (i, j) 192 hours. Scale bars are 1 μm (left column) and 100 nm (right column).	58
Figure 4.6 (a) Overview SEM; (b) Close view TEM images of PS- <i>b</i> -P4VP@SiO ₂ particles isolated from the reaction mixture after 24 hours of shell formation. Scale bars on image (a) 200 nm; (b) 25 nm.....	59
Figure 4.7 (a) Topography AFM images of PS- <i>b</i> -P4VP@SiO ₂ particles isolated from the reaction mixture after 24 hours of shell formation; (b) Height profile of PS- <i>b</i> -P4VP@SiO ₂ particles across the line on the AFM image (a).	60

- Figure 4.8** (a) Apparent particle size, d_{app} , (rectangles) and PDI (triangles) of PS-*b*-P4VP micelles in methanol (red symbols) and PS-*b*-P4VP@SiO₂ particles (black symbols) measured by intensity and PDI (triangles) as a function of time. The results were obtained by in-situ DLS during the initial period of silica shell formation; (b) Long-time behaviour of d_{app} (rectangles) and PDI (triangles) for PS-*b*-P4VP@SiO₂ particles obtained by DLS during the continuous sol-gel process..... 61
- Figure 4.9** Intensity-average apparent particle size distributions (a) Before; (b-c) After addition of silica sol: (b) After 2 min; (c) After 3h (at a plateau); (d) After 2 days of silica shell formation..... 61
- Figure 4.10** (a) Bright field TEM image; (b-d) Elemental maps of PS-*b*-P4VP@SiO₂ core-shell particles deposited from the reaction mixture on TEM grid immediately after addition of silica sol: (b) Si map; (c) Carbon map; (d) Nitrogen map. Scale bars are 200 nm. 62
- Figure 4.11** Overview (top) and high-magnification TEM images (bottom) of PS-*b*-P4VP@SiO₂ particles deposited from the reaction mixture on TEM grid: (a, b) Immediately after addition of silica sol; (c, d) After 3 hours; (e, f) After 18 hours; (g, h) After 2 days of silica shell formation. Scale bars are 200 nm (top) and 25 nm (bottom).64
- Figure 4.12** Schematics depicting four stages of silica shell formation using acidic sol-gel process and spherical PS-*b*-P4VP micelles as reactive templates. Reproduced from Ref. 322..... 64
- Figure 4.13** Schematic showing (a) Unsupported nanoparticles in dispersion; (b) Nanoparticles attached on the surface of the support; (c) Nanorattles or yolk-shell nanostructures. 66
- Figure 4.14** Yolk-shell nanostructure as a bifunctional heterogeneous catalyst..... 68
- Figure 4.15** Schematic showing the synthesis of Ag@SiO₂ and Au@SiO₂ yolk-shell nanostructures. 69
- Figure 4.16** (a) TEM image; (b) Size distribution of as synthesised AgNPs; (c) UV-Vis spectrum of as synthesised AgNPs in xylene; (d) UV-Vis absorbance spectrum of Ag@PS-*b*-P4VP particles with AgNP of size 12.5 ± 2.7 nm in methanol. 70
- Figure 4.17** (a, b) SEM; (c) TEM micrographs of Ag@PS-*b*-P4VP@SiO₂ particles. The bright spots (indicated by white arrows) in the ESB (b) image and the black spots in the TEM (c) image shows the presence of AgNP inside the silica deposited block copolymer micelles. Scale bars on image (a, b) 100 nm; (c) 50 nm. 71
- Figure 4.18** Successive spectra taken after every minute during borohydride assisted reduction of 4-NP after the addition of Ag@SiO₂ yolk shells showing the decrease in peak intensity of 4-NP with respect to increase in time. All experiments were carried out with initial concentrations $[4-NP]_0 = 0.027$ mmol L⁻¹ and $[NaBH_4]_0 = 0.081$ mol L⁻¹. Amount of Ag@SiO₂ in reaction mixture was: (a) 1.6×10^{-3} mg; (b) 3×10^{-3} mg; (c) 4×10^{-3} mg. The total volume of reaction mixture in the cuvette was 2.2 mL..... 71

- Figure 4.19** (a) TEM image of Ag@PS-*b*-P4VP@SiO₂; (b) Size distribution histogram of AgNPs obtained after 24 hours of silica shell deposition reaction time..... 72
- Figure 4.20** (a) UV-Vis spectra of Ag@PS-*b*-P4VP@SiO₂ particles in reaction mixture taken at different time periods after addition of acidic silica sol to the Ag@PS-*b*-P4VP micellar solution; (b) Relative intensity, A_t/A_0 , of silver plasmon peak at 420 nm versus time obtained upon silica shell deposition..... 73
- Figure 4.21** (a) TEM image of AuNP; (b) UV-Vis spectrum of as synthesised AuNP in H₂O; (c) UV-Vis spectrum of Au@PS-*b*-P4VP in methanol. The scale bar on the image (a) is 20 nm. 75
- Figure 4.22** (a) TEM image of Au@PS-*b*-P4VP@SiO₂; (b) Size distribution histogram of AuNPs inside the Au@PS-*b*-P4VP@SiO₂. The scale bar on the image (a) is 100 nm.... 75
- Figure 4.23** (a) UV-Vis spectra Au@PS-*b*-P4VP@SiO₂ taken at different time periods after addition of acidic silica sol to the Au@PS-*b*-P4VP micellar solution; (b) Relative intensity, A_t/A_0 , of gold plasmon peak at 540 nm versus time obtained upon silica shell deposition. 76
- Figure 4.24** TGA curve showing the weight loss of Au@BCP@SiO₂ measured by heating up to 800 °C in the N₂ atmosphere. 77
- Figure 4.25** (a, b) TEM images of Au@SiO₂ yolk-shell nanoparticles; (c) Size distribution histogram of AuNPs inside Au@SiO₂ yolk-shell nanoparticles. Scale bars on image (a) 100 nm; (b) 50 nm. 77
- Figure 4.26** SEM micrograph showing Au@SiO₂ yolk-shell nanoparticles fused into large aggregates after pyrolysis. Scale bar is 500 nm. 78
- Figure 4.27** (a) N₂ adsorption-desorption isotherms of unpyrolysed Au@PS-*b*-P4VP@SiO₂ (red circles) and pyrolysed Au@SiO₂ yolk-shell nanoparticles (blue circles); corresponding size distributions of (b) Mesopores; (c) Micropores. Filled and unfilled symbols correspond to adsorption and desorption processes respectively..... 79
- Figure 4.28** Mechanism of reduction of 4-nitrophenol by borohydride on the surface of metallic nanoparticles. Reproduced from Ref. 324. 81
- Figure 4.29** (a, b, c) Successive spectra taken after every minute during borohydride assisted the reduction of 4NP after the addition of Au@SiO₂ yolk shells showing the decrease in peak intensity of 4-NP with respect to increase in time; (d, e, f) Shows plots of $\ln(C_t/C_0) \sim \ln(A_t/A_0)$ versus time at different concentrations of Au@SiO₂ catalyst. All experiments were carried out with initial concentrations $[4\text{-NP}]_0 = 0.027 \text{ mmol L}^{-1}$ and $[\text{NaBH}_4]_0 = 0.081 \text{ mol L}^{-1}$. Amount of Au@SiO₂ catalyst in reaction mixture was: (a, d) $0.4 \times 10^{-3} \text{ mg}$; (b, e) $1.0 \times 10^{-3} \text{ mg}$; (c, f) $2.0 \times 10^{-3} \text{ mg}$. Apparent rate constants determined from the slopes of linear fit are: (d) 0.124 min^{-1} ; (e) 0.808 min^{-1} ; (f) 1.391 min^{-1} 82

- Figure 4.30** Plot showing (a) the absorbance spectra of 4-NP + NaBH₄ after addition of recycled catalyst; (b) Conversion of 4-NP to 4-AP in presence of Au@SiO₂ yolk-shell catalyst for 10 recovery cycles..... 83
- Figure 4.31** Schematics showing the preparation of Au@SiO₂@PSS catalyst via block copolymer template approach. 85
- Figure 4.32** (a) SEM image (ESB detector) of Au@PS-*b*-P4VP@SiO₂@PSS sample before pyrolysis: Bright dots pointed with arrows correspond to Au@PS-*b*-P4VP@SiO₂ particles embedded in porous silica support; (b, c) TEM images of Au@SiO₂@PSS catalyst obtained after pyrolysis. Inset on images (a) and (b) show the schematic of corresponding structures. Scale bars on image (a) 400nm; (b) 200 nm; (c) 50 nm..... 86
- Figure 4.33** (a) N₂ adsorption-desorption isotherms of unpyrolyzed (Au@PS-*b*-P4VP@SiO₂@PSS, red circles) and pyrolyzed (Au@SiO₂@PSS, blue squares) samples; corresponding size distributions of (b) Mesopores; (c) Micropores. Filled and unfilled symbols correspond to adsorption and desorption processes, respectively. 87
- Figure 4.34** (a) Successive UV-Vis spectra taken every minute during borohydride reduction of 4-NP after addition of Au@SiO₂@PSS catalyst and 4-NP conversion plot ($A_t/A_0 \sim C_t/C_0$) versus time (inset); (b) Plots of $\ln(C_t/C_0) \sim \ln(A_t/A_0)$ versus time at different concentrations of Au@SiO₂@PSS catalyst. All experiments were carried out with initial concentrations $[4\text{-NP}]_0 = 0.027 \text{ mmol L}^{-1}$ and $[\text{NaBH}_4]_0 = 0.081 \text{ mol L}^{-1}$. $[\text{Au}^0]$ in reaction mixture was: (1) 0.0136 ppm; (2) 0.0273 ppm; (3) 0.0545 ppm; (4) 0.1091 ppm. Apparent rate constants determined from the slopes of linear fit are: (1) 0.0854 min⁻¹; (2) 0.1297 min⁻¹; (3) 0.2881 min⁻¹; and (4) 0.5286 min⁻¹. 88
- Figure 4.35** The comparison of normalised reaction rate constants (a,b) K_m and (c,d) K_s determined for Au@SiO₂@PSS catalyst (red star) with values reported in the literature for analogous catalytic systems: black circles – Lee08;¹⁸⁴ green triangles (left) – Shaik14;³³⁸ green diamond – Chen14;³⁴² blue rectangles – Wu11;¹⁶⁰ pink hexagons – Jeong15;⁴³ cyan triangles (down) – Tan10;²³¹ dark yellow triangles (up) – Mondal15;³³⁹ brown pentagons –Chen11.³⁴¹ 90
- Figure 4.36** Plausible reduction mechanism for Congo Red and Methyl Orange. Reproduced from Ref. 344. 92
- Figure 4.37** Plausible degradation mechanism of Methylene Blue to Leuco-Methylene Blue. Reproduced from Ref. 345..... 93
- Figure 4.38** (a) Successive UV-Vis spectra were taken every minute during borohydride degradation of Congo Red after addition of Au@SiO₂@PSS catalyst and corresponding conversion plot versus time (inset); (b) Plots of $\ln(C_t/C_0)$ versus time obtained at different concentrations of Au@SiO₂@PSS catalyst. All experiments were carried out with initial concentrations $[\text{CR}]_0 = 0.027 \text{ mmol L}^{-1}$ and $[\text{NaBH}_4]_0 = 0.081 \text{ mol L}^{-1}$. $[\text{Au}^0]$ in reaction mixture was: (1) 0.0136 ppm; (2) 0.0273 ppm; (3) 0.0409 ppm; (4) 0.0545 ppm. Apparent

rate constants determined from the slopes of linear fit are: (1) 0.230 min^{-1} ; (2) 0.527 min^{-1} ; (3) 0.710 min^{-1} ; and (4) 1.10 min^{-1} 94

Figure 4.39 The comparison of normalised reaction rate constant, (a, b) K_m ; (c, d) K_s , determined for Au@SiO₂@PSS catalyst (red star) with values reported in the literature for analogous catalytic systems: black cubes - Naik15;³⁴⁸ green circles - R.Rajesh15;³⁴⁹ blue triangles (up) - R.Rajesh14;³⁴⁴ orange diamonds - M.Kumar14.³⁵⁰ 94

Figure 4.40 (a) Successive UV-Vis spectra were taken every minute during borohydride degradation of Methyl Orange in the presence of sodium borohydride after addition of Au@SiO₂@PSS catalyst and corresponding conversion plot versus time (inset); (b) Plots of $\ln(C_t/C_0)$ versus time obtained at different concentrations of Au@SiO₂@PSS catalyst. All experiments were carried out with initial concentrations $[\text{MO}]_0 = 0.027 \text{ mmol L}^{-1}$ and $[\text{NaBH}_4]_0 = 0.081 \text{ mol L}^{-1}$. Amount of catalyst in the reaction mixture was: black squares - 0.0136 ppm; brown squares - 0.0273 ppm; green squares - 0.0409 ppm; and blue squares - 0.0545 ppm..... 96

Figure 4.41 Successive UV-Vis spectra taken every minute during borohydride degradation of Methylene Blue after addition of Au@SiO₂@PSS catalyst and corresponding conversion plot versus time (inset); (b) Plots of $\ln(C_t/C_0)$ versus time obtained at different concentrations of Au@SiO₂@PSS catalyst. All experiments were carried out with initial concentrations $[\text{MB}]_0 = 0.027 \text{ mmol L}^{-1}$ and $[\text{NaBH}_4]_0 = 0.081 \text{ mol L}^{-1}$. Amount of catalyst in the reaction mixture was: black squares - 0.00544 ppm; brown squares - 0.00816 ppm; green squares - 0.0136 ppm; and blue squares - 0.0273 ppm..... 97

Figure 4.42 Schematic showing the preparation of flow-type catalytic system by infiltration of Au@SiO₂ yolk-shells in a porous glass frit..... 99

Figure 4.43 SEM images of the (a) As prepared Au@PS-*b*-P4VP@SiO₂ particles deposited from ethanol; (b) Filtrate collected after infiltration through P4 frit; (c) Filtrate collected after infiltration through the P5 frit. Inset show optical images of (a) As prepared dispersion; (b) Filtrate after infiltration of the feed through P4 frit; (c) Filtrate after infiltration of the feed through the P5 frit..... 100

Figure 4.44 Optical images of (a) Empty P5 frit; (b) P4 frit, (c) P5 frit loaded with Au@SiO₂ yolk-shell nanoparticles..... 100

Figure 4.45 (a) The UV-Vis absorbance spectra of as-prepared Au@PS-*b*-P4VP@SiO₂ feed solution (black), and filtrates collected after infiltration of feed solution into P4 (blue) and P5 (red), respectively; (b) The intensities of plasmon peak of AuNP at 540 nm in feed solution and filtrate collected after infiltration of particles into P4 and P5 filter frits. .. 101

Figure 4.46 Top view optical image of P5 frit after loading of with Au@SiO₂ yolk-shell nanoparticles..... 102

Figure 4.47 Top view SEM images of P5 frit after loading with Au@SiO₂ yolk-shell nanoparticles taken at different magnifications using (a) SE2 detector; (b, c) InLens

- detector; and (d) ESB detector; (c,d) shows the magnified view of the rectangular region in the image (b). Scale bars on image (a) 100 μm ; (b) 2 μm ; (c, d) 1 μm 102
- Figure 4.48** Cross-sectional optical image of P5 frit. The upper pink part shows the loaded Au@SiO₂ particles and the lower white part show the empty frit. 103
- Figure 4.49** Cross-sectional SEM images of P5 frit after loading with Au@SiO₂ yolk-shell nanoparticles taken at different magnifications using InLens (top line) and ESB (bottom line) detectors. Image (c, d) shows the magnified image of the rectangular region in the image (b). Image (e, f) shows the magnified image of the rectangular region in image (d). Scale bars on image (a) 20 μm ; (b) 2 μm ; (c, d) 1 μm ; and (e, f) 200 nm. 103
- Figure 4.50** (a, b) Cross-sectional SEM images and (c, d) EDX gold map of the Au@SiO₂ yolk-shell nanoparticles infiltrated P5 frit indicating the presence of AuNP; (e) EDX spectra took from the three boxed area shown on the corresponding SEM image (b). 104
- Figure 4.51** Top view optical images (a, d) and SEM images of (b, c) P5-0.5; (e, f) P5-2.0 frits after loading with Au@PS-*b*-P4VP@SiO₂ particles respectively; (b, e) InLens detector; (c, f) ESB detector. Scale bars on image (a,d) 2 mm; (b, e) 2 μm ; (c, f) 1 μm 105
- Figure 4.52** Cross-sectional optical (a, d) and SEM images of (b, c) P5-0.5; (e, f) P5-2.0 frits after loading with Au@PS-*b*-P4VP@SiO₂ particles; (b, e) InLens detector; (c, f) ESB detector. Scale bars on image (a, d) 2 mm; (b, c) 2 μm ; (e, f) 1 μm 106
- Figure 4.53** Comparison plot showing the variation in volumetric flux (J) as a function of volumetric flow rates (Q) for: black squares - water passing through empty P5 frit; blue triangles - water passing through P5 frit loaded with Au@SiO₂ yolk-shell particles; red circles - an aqueous solution containing Congo Red (0.067 mM) and sodium borohydride (0.2 M) passing through P5 frit loaded with Au@SiO₂ yolk-shell particles. 108
- Figure 4.54** P5 frit after the continuous passing of CR + NaBH₄ solution for ca. 45 hours. 109
- Figure 4.55** (a) Experimental setup for continuous flow catalysis; (b) Image of the frit holder. The parts are explained as 1 – Feed; 2 – Peristaltic Pump; 3 – Feed Inlet; 4 – Frit Holder; 5 – Outlet. 110
- Figure 4.56** (a) Flow rate vs Flow time (black squares) and mass of AuNPs leached out from the frit (red stars) during continuous flow experiment under a feed of water (blue boxed area) and CR + NaBH₄ reaction mixture (brown boxed area); (b) Volume of the filtrate as function of flow time (black circles) and concentration AuNPs present in the filtrate with respect to corresponding flow time (red triangles) under a feed of water (blue boxed area) and CR + NaBH₄ reaction mixture (brown boxed area). 111
- Figure 4.57** Optical images showing (a) Frit inside the holder; (b) Aqueous solution of CR; aqueous solution CR + NaBH₄ reaction mixture: (c) before passing; (d) after passing through the frit infiltrated with the Au@SiO₂ yolk-shell catalyst The arrows on the image

- (a) point out the crimson coloured CR + NaBH₄ feed drop at the inlet and the colourless reaction mixture coming out of the frit loaded with Au@SiO₂ catalyst. 112
- Figure 4.58** (a) Representative UV-Vis spectra of Congo Red (black) and Congo Red + NaBH₄ reaction mixture after passing through the frit loaded with Au@SiO₂ yolk-shells taken at selected time points; (b) Plot of A_t / A_0 ($\lambda = 499$ nm) versus time obtained during the continuous flow catalysis experiment on degradation of Congo Red. Inset on (b) shows magnified part of initial 50 minutes of continuous flow catalysis experiment. 113
- Figure 4.59** (a) Representative UV-Vis spectra of Methyl Orange (black) and Methyl Orange + NaBH₄ reaction mixture after passing through the frit loaded with Au@SiO₂ yolk-shells taken at selected time points; (b) Plot of A_t / A_0 ($\lambda_{\max} = 464$ nm) versus time obtained during the continuous flow catalysis experiment on degradation of Methyl Orange. Inset on (b) shows magnified part of initial 50 minutes of continuous flow catalysis experiment. Spectra shown as dotted lines on the image (a) correspond to the time period when an increased A_t / A_0 values were observed as compared to its minima, that is starting from 25 minutes of continuous flow experiment. 114
- Figure 4.60** UV-Vis spectra of 4-Nitrophenol (black) and Nitrophenolate (red). The concentration of 4-NP was 0.067 mM whereas the 4-NP: NaBH₄ ratio was 1: 3000.... 116
- Figure 4.61** (a) Representative UV-Vis spectra of 4NP + NaBH₄ reaction mixture after passing through the frit loaded with Au@SiO₂ yolk-shells taken at selected time points; (b) Plot of A_t / A_0 ($\lambda_{\max} = 400$ nm) versus time obtained during the continuous flow catalysis experiment on degradation of 4-NP during the first 65 minutes of continuous flow catalysis experiment. Inset on (b) shows A_t / A_0 time dependency obtained upon prolonged continuous flow experiment. 116
- Figure 5.1** Schematic showing the mechanism of silica shell formation around the PS-b-P4VP micellar templates. 120
- Figure 5.2** (a, b) SEM images showing agglomerated Au@SiO₂ yolk-shell nanoparticles; (c) Bar graph showing the recyclability of Au@SiO₂ yolk-shell nanocatalyst. 121
- Figure 5.3** Fabrication and catalytic activity of Au@SiO₂@PSS catalyst. 122
- Figure 5.4** Image showing the results on catalytic degradation/reduction of Congo Red (CR), Methylene Blue (MB), Methyl Orange (MO), and 4-Nitrophenol (4-NP) using Au@SiO₂@PSS catalyst. 123
- Figure 5.5** Summary showing the continuous flow catalytic system. 124
- Figure 8.1** Schematic representation of (a) Eley-Rideal Mechanism; (b) Langmuir-Hinshelwood Mechanism. Adapted from Ref. 372. 157

Figure 8.2 Variation of rate, r , with a concentration of $[A]$ for bimolecular process via LH mechanism. Reproduced from Ref. 368.....	158
Figure 8.3 (a) Schematic diagram and working principle of SEM; (b) Types of electron-specimen interactions. Reproduced from Ref. 373, 375.	159
Figure 8.4 Schematic showing the working principle of TEM. Fehler! Textmarke nicht definiert.	
Figure 8.5 Absorption spectra of gold and silver nanoparticles of various shapes. Reproduced from Ref. 379, 380.	163
Figure 8.6 Schematics showing different scattering theories for spherical particles Reproduced from Ref. 381.	164
Figure 8.7 Typical correlograms from samples containing (a) Large particles in which the correlation of the signal takes a long time to decay; (b) Small particles in which the correlation of the signal decays more rapidly. Reproduced from Ref. 252.	165
Figure 8.8 Different types of gas adsorption isotherms. Reproduced from Ref. 385.	167
Figure 8.9 (a) Schematic illustration of working principle of an AFM; (b) Typical force-distance curve with corresponding regions of operating AFM modes. Image b reproduced from Ref. 386.	168
Figure 8.10 Successive UV-Vis spectra of Congo Red and Sodium Borohydride in the absence of catalyst measured for 60 minutes.	170
8.7 LIST OF TABLES	
Table 3.1 List of Polymers Used (All polymers were procured from Polymer Source Inc. Canada)	43
Table 3.2 List of Chemicals and Solvents	43
Table 4.1 Summary of the reaction rate constants for catalytic reduction of 4-NP reported in the literature for various Au@SiO ₂ yolk-shell catalysts and some analogues.....	90
Table 4.2 Summary of the reaction rate constants for catalytic reduction of Congo Red and Methyl Orange azo-dyes reported in the literature for various Au and Ag supported catalyst.	95
Table 4.3 Results of ICP-OES analysis of Au@PS- <i>b</i> -P4VP micellar solution, Au@PS- <i>b</i> -P4VP@SiO ₂ feed solution, and the filtrate.	107

8.8 LIST OF PUBLICATIONS

Research Publications:

- A Continuous Flow Type Catalytic System for Effective Waste Water Treatment, **A.Shajkumar**, A.Horechyy, M.Stamm et al., under preparation.
- Silica Supported Au@hollow-SiO₂ particles prepared *via* block copolymer template approach as highly active nanocatalyst. **A. Shajkumar**, B.Nandan, A Horechyy et al., J.Colloids and Interface Science, 2017, 491, 246-254.
- In-situ monitoring of silica shell growth on PS-b-P4VP micelles as templates. A.Horechyy, B.Nandan, **A.Shajkumar** et al., Polymer, 2016, 107, 485-491.

Conferences:

- 09/2016 - Poster Presentation at the 9th ECNP International Conference on Nanostructured Polymers and Nanocomposites, Rome, Italy.
Title: Au@SiO₂@PSS Catalyst Prepared via Block Copolymer Template Approach: An Effective Catalyst for Water Purification.
- 06/2015 - Poster Presentation at European Polymer Congress, Dresden, Germany.
Title: Photochromic Behaviour of Azobenzene/Polymer Mixtures: an Effect of Chemical Architecture and Complexation.
- 09/2014 - Poster presentation at 8th ECNP International Conference on Nanostructured Polymers and Nanocomposites, Dresden, Germany.
Title: Catalytically Active Yolk-Shell Nanostructures Prepared via Self-Assembled Block Copolymer Templates.

9 ACKNOWLEDGEMENTS

First of all, I would like to thank Leibniz-Institut für Polymerforschung Dresden e.V.(IPF) for providing the facilities, finance, and opportunity to do the research that is the core of this thesis. It is my profound privilege to express my feelings of appreciation and deep respect to Professor Dr. Manfred Stamm for giving me the opportunity to pursue PhD under his kind guidance at the IPF. The interactions that I have had with him were very encouraging and helped me in achieving better perspective for science and life in general. His supervision and continuous support helped me throughout this process. I am grateful to Dr. Andriy Horechyy for his scientific guidance and support during the research work. He has always been there to discuss and find fitting solutions to the problem. I want to thank Dr. Petra Uhlmann for her support and her kind words during a difficult phase in my life.

It is beyond words to express my gratitude to Graduate Academy, GFF, and DAAD for providing me with the financial support during the last phase of my PhD work without which it would not have been easy to finish my thesis.

I express my warmest gratitude to Dr. Peter Formanek, Leibniz-Institut für Polymerforschung, for the making the EDX and SEM measurements of the yolk-shell nanoparticles inside the frit possible. I also thank him for introducing with the basics of SEM and TEM. I am very grateful to Dr. Gudrun Auffermann, Max-Planck-Institut für Chemische Physik Fester, Dresden, for carrying out the ICP-OES measurements. I am in short words to pay my gratitude to all the scientific and technical staffs for extending their valuable assistance and their kind support throughout my research. Dr. Andreas Janke, Dr. Mikhail Malanin, and Mrs. Mandy Mende, for introducing with the basics of AFM, UV-Vis, and DLS, respectively. Dr. Victoria Albrecht for N₂ adsorption measurements, Ms. Liane Häussler for TGA measurements, Mr. Hellbach for making the frit and Dr. Alexander Münch for providing the lab facilities for doing the UV-Vis measurements.

I would like to express my heartfelt indebtedness to Ms. Janett Forkel, Ms. Carmen Marx, Ms. Astrid Creutz and all the technical and office staff members for all their contribution related to documentation, supplies and office related help.

I want to especially thank my most cooperative and helpful colleagues (former) and friends in IPF, Dr. Bijay P. Tripathi, Dr. Nidhi C. Dubey, Dr. Gözde Öktem, Dr. Anne Freitag, Dr. Natalya Dolya, Dr. Roman Tkachov, Ms. Alice Rosenthal, Ms. Olga Grätz, and Mr. Yevhen Karpov for all their support and motivation during my research and for all the memorable time, which I will pursue throughout my life.

I want to especially thank my former teachers, mainly Mrs. Anitha Itty, Mrs. Lizy M. Koshy, and Dr. R.S.Rajeev who shed light in my path. I want to thank my B.Tech professor Dr. V.G.Geethamma for discovering the researcher in me. No words can express my gratefulness

Acknowledgements

to my former professor Prof. Dr. Sabu Thomas, who constantly encouraged me to pursue research and gave me the opportunity to start my PhD. I thank you, professor for the constant motivation and the inspiration to dream big.

The part that a family plays in life cannot be expressed by gratitudes, but I would like to take this opportunity to thank my parents Mr. Shajkumar T.N. and Mrs. Usha Kumari K.G. who are pillars of my life and had always been there for me filling my life with positivity and confidence. It was them who are responsible for all my achievements in my life. Their seamless love and constant motivation helped me to stay optimistic and overcome the hard times in my life, especially during my PhD. Achu and Amma I thank you for believing in me when I was not, for not losing hope in me and for cheering me up. I am thankful for the almighty that I am blessed with such wonderful parents who made me who I am today.

I am sincerely grateful to my friend Mr. Rebin Jacob for his willingness to spend his valuable time for my thesis, for his great encouragement and trust in me, as well as for bearing with me at my worst, which has been a priceless support throughout the last years.

This cannot be completed without thanking my wonderful friends especially Anita Sebastian and Parvathi Shaji who always supported me and believed in me. Thank you for cheering me up when I was most distressed. Finally, I owe everything to the Almighty for his endless blessings.

CURRICULUM VITAE

First Name : Aruni
Last Name : Shajkumar
Telephone : +49 15211615182
E-Mail : aruni.shaj@gmail.com

Educational Qualification:

- 2013-2017 Ph.D. in Physical Chemistry and Polymer Physics, Technical University of Dresden, Germany (continue).
- 2011-2013 Master of Science and Technology in Nanoscience and Nanotechnology (M.S.), Mahatma Gandhi University, Kerala, India (CGPA – 8.26/10).
- 2006-2010 Bachelor of Technology in Polymer Science and Technology (B.Tech), Mahatma Gandhi University, Kerala, India (78.4 %).

Fellowship and Academic Achievements:

- 2017 DAAD STIBET-III Matching Funds from Technical University of Dresden, Germany.
- 2017 DAAD Completion and Wrap Up grant from Graduate Academy, Technical University of Dresden, Germany.
- 2016 Interview with the Vatican Radio about the applications of nanoscience and nanotechnology in everyday life.
- 2013 Scholarship for PhD at Leibniz Institute of Polymer Research, Dresden, Germany.
- 2011 Scholarship for M.S. Nanoscience and Nanotechnology at International and Interuniversity Center for Nanoscience and Nanotechnology (IIUCNN), Mahatma Gandhi University, Kerala, India.
- 2010 University 4th for B.Tech in Polymer Science and Technology.

Research Experience:

- 2012-2013 (9 months) Master Dissertation: ‘Monolayer Gold Nanoparticles on Silicon and Glass Substrates for SERS Application’, at Leibniz Institute of Polymer Research, Dresden, Germany.

-
- 2010-2011 (6 months) Junior Research Associate: Topic - 'Synthesis of Graphene and Multi-walled Carbon Nanotubes using CVD'. Quantum Research Corporations, Karnataka, India.
- 2009-2010 (3 months) Bachelor's Thesis: 'Electrostatic Charge Mitigating Polyimide Carbon Nanotube Nanocomposite Film for Space Applications', at Vikram Sarabhai Space Center, Kerala, India.

Research Publications and Conferences:

1. A Continuous Flow Type Catalytic System for Effective Waste Water Treatment, **A.Shajkumar**, A.Horechyy, M.Stamm et al. (under preparation).
2. Silica -supported Au@hollow-SiO₂ particles with outstanding catalytic activity prepared via block copolymer template approach. **A. Shajkumar**, B.Nandan, A Horechyy et al., J.Colloid and Interface Science, 2017, 491, 246-254.
3. In-situ monitoring of silica shell growth on PS-b-P4VP micelles as templates. A.Horechyy, B.Nandan, **A.Shajkumar** et al., Polymer, 2016, 107, 485-491.

Book Chapter:

1. 2015 'Ch.17 - Future of Nanotechnology in Tissue Engineering', in Nanotechnology- Application for Tissue Engineering, S.Thomas and Y.Grohens, Elsevier Publications.

Posters and Oral Presentations:

- 09/2016 Poster Presentation at the 9th ECNP International Conference on Nanostructured Polymers and Nanocomposites, Rome, Italy.
Title: Au@SiO₂@PSS Catalyst Prepared via Block Copolymer Template Approach: An Effective Catalyst for Water Purification.
- 06/2015 Poster Presentation at European Polymer Congress, Dresden, Germany.
Title: Photochromic Behaviour of Azobenzene/polymer Mixtures: an Effect of Chemical Architecture and Complexation.
- 09/2014 Poster Presentation at 8th ECNP International Conference on Nanostructured Polymers and Nanocomposites, Dresden, Germany.
Title: Catalytically Active Yolk-Shell Nanostructures Prepared via Self-Assembled Block Copolymer Templates.
- 01/2012 Oral Presentation at International Conference on Nanomaterials, ICN, Kerala, India.
Title: Monolayer-deposited Gold Nanoparticles on Silicon and Glass Substrates for SERS Applications.

Erklärung gemäß §5 Abs. 1 Punkt 5

§5 Abs. 1 Punkt 5 a

Versicherung

Hiermit versichere ich, dass ich die vorliegende Arbeit ohne unzulässige Hilfe Dritter und ohne Benutzung anderer als der angegebenen Hilfsmittel angefertigt habe; die aus fremden Quellen direkt oder indirekt übernommenen Gedanken sind als solche kenntlich gemacht. Die Arbeit wurde bisher weder im Inland noch im Ausland in gleicher oder ähnlicher Form einer anderen Prüfungsbehörde vorgelegt.

Dresden, ____ . ____ . 2017

Aruni Shajkumar

§5 Abs. 1 Punkt 5 b

Die Dissertation wurde unter wissenschaftlicher Betreuung von Herrn Professor Manfred Stamm und Dr. Andriy Horechyy am Institut für Polymerforschung Dresden e. V. im Zeitraum October 2013 bis September 2017 angefertigt, als eingeschriebener Promotionsstudent an der Technischen Universität Dresden.

§5 Abs. 1 Punkt 5 c

Es hat zuvor kein erfolgloses Promotionsverfahren stattgefunden.

§5 Abs. 1 Punkt 5 d

Ich erkenne die Promotionsordnung der Fakultät Mathematik Naturwissenschaften der Technischen Universität Dresden vom 23.02.2011, zuletzt geändert am 15. 06. 2011 und 18. 06. 2014, an.

Dresden, ____ . ____ . 2017

Aruni Shajkumar